Time Dependent Analysis of $B^0 \to \rho^0\rho^0$ Decays

by

Ilya Leonidovich Osipenkov

B.S. (University of Texas at Austin) 2000

A dissertation submitted in partial satisfaction of the
requirements for the degree of
Doctor of Philosophy

in

Physics

in the

GRADUATE DIVISION
of the
UNIVERSITY OF CALIFORNIA, BERKELEY

Committee in charge:
Professor Yury Kolomensky, Chair
Professor Robert Jacobsen
Professor Stephen Derenzo

Fall 2009

SLAC-R-935
October 2009

Prepared for the Department of Energy under contract number DE-AC02-76SF0015

SLAC National Accelerator Laboratory, 2575 Sand Hill Road, Menlo Park, CA 94025

Time Dependent Analysis of $B^0 \rightarrow \rho^0 \rho^0$ Decays

SLAC-R-935

October 2009

Prepared for the Department of Energy under contract number DE-AC02-76SF0015

SLAC National Accelerator Laboratory, 2575 Sand Hill Road, Menlo Park, CA 94025

by

Ilya Leonidovich Osipenkov

Abstract

Time Dependent Analysis of $B^0 \rightarrow \rho^0\rho^0$ Decays

by

Ilya Leonidovich Osipenkov

Doctor of Philosophy in Physics

University of California, Berkeley

Professor Yury Kolomensky, Chair

The *BABAR* detector at the PEP-II asymmetric-energy e^+e^- collider is located at the Stanford Linear Accelerator Center. It has been gathering data on the $\Upsilon(4S)$ resonance from 2000 until 2007 with the primary objective of studying CP violation in B-meson decays. In this thesis we provide a theoretical overview of how CP violation arises in the context of the Standard Model, why B decays are relevant, and how *BABAR* gathers the necessary data. Specifically, we present the analysis of $B^0 \rightarrow \rho^0\rho^0$ decays in a sample of 465×10^6 $\Upsilon(4S) \rightarrow B\overline{B}$. We measure the corresponding branching fraction $\mathcal{B} = (0.92 \pm 0.32\,(\text{stat.}) \pm 0.14\,(\text{syst.})) \times 10^{-6}$ and the longitudinal polarization fraction $f_L = 0.75^{+0.11}_{-0.14}\,(\text{stat.}) \pm 0.04\,(\text{syst.})$. The evidence for the $B^0 \rightarrow \rho^0\rho^0$ signal has a significance of 3.1 standard deviations (σ), when the systematic uncertainties are included. There is insufficient evidence for B decays into similar modes and the corresponding upper limits are determined to be $\mathcal{B}_{\rho^0 f_0} < 0.34 \times 10^{-6}$, $\mathcal{B}_{f_0 f_0} < 0.16 \times 10^{-6}$, $\mathcal{B}_{\rho^0\pi^+\pi^-} < 8.7 \times 10^{-6}$,

$\mathcal{B}_{\pi^+\pi^-\pi^+\pi^-} < 21.1 \times 10^{-6}$ at the 90% Confidence Level (CL).

We also investigate the proper-time dependence of the longitudinal component in the decay and measure the CP-violating coefficients $S_L = 0.3 \pm 0.7\,(\text{stat.}) \pm 0.2\,(\text{syst.})$ and $C_L = 0.2 \pm 0.8\,(\text{stat.}) \pm 0.3\,(\text{syst.})$. By combining these results with other measurements from the $B \to \rho\rho$ processes and performing an Isospin Analysis, we are able to restrict the unitarity angle α as well as its uncertainty due to penguin contributions, $\Delta\alpha$. Namely, $\alpha = (92.4^{+6.0}_{-6.5})^\circ$ with $-1.8^\circ < \Delta\alpha < 6.7^\circ$ at 1σ CL.

Professor Yury Kolomensky
Dissertation Committee Chair

To the United States of America

Contents

List of Figures

List of Tables

Acknowledgments

I would like to thank the *BABAR* groups at LBNL and UC Berkeley, Saclay, as well as Johns Hopkins University for their efforts on this project and providing me with assistance and advice whenever needed. I would also like to thank the committee members for spending their time to read the manuscript. Particular thanks go out to my adviser, Yury Kolomensky, who gave me the opportunity to work on this analysis and helped me throughout its course.

We are are also grateful for the excellent luminosity and machine conditions provided by our PEP-II colleagues, and for the substantial dedicated effort from the computing organizations that support *BABAR*. The collaborating institutions wish to thank SLAC for its support and kind hospitality. This work was supported by DOE and NSF (USA), NSERC (Canada), IHEP (China), CEA and CNRS-IN2P3 (France), BMBF and DFG (Germany), INFN (Italy), FOM (The Netherlands), NFR (Norway), MIST (Russia), MEC (Spain), and PPARC (United Kingdom). Individuals have received support from the Marie Curie EIF (European Union) and the A. P. Sloan Foundation.

Chapter 1

Introduction

The Standard Model (SM) describes fundamental particles and their interactions (with the exception of gravity). In Chapter 2 we discuss their physics in further details, while focusing on the Electroweak Symmetry. For sufficiently low energy scales ($<\sim$ 250 GeV) it is broken via the Higgs Mechanism and the mixing between quarks is described by the Cabibbo-Kobayashi-Maskawa (CKM) matrix. As there are three generations of quarks, the matrix contains a complex phase, which leads to the violation of Charge-Parity (CP) symmetry. In other words, several types of particles can transform into their antiparticles and vice versa (via the composing quarks oscillating into their conjugates), but the process does not occur at the same rate in both directions. Such an effect was first observed for Kaons by Cronin and Fitch in 1964 [1]. The SM contains only one source of CP violation, which implies that the parameters from the Kaon system can be used to place predictions on decays of other particles. Furthermore, CP asymmetry is required during baryogenisis in the early universe in order to account for the matter-antimatter imbalance (*i.e.* why the universe is composed primarily of matter rather than antimatter) [2]. B-factories were designed to create and analyze the decays of a large number of B-mesons, thus allowing scientists to observe and examine the properties of CP violation in a new sector of physics. Their goal is to perform high precision measurements, which can either verify the SM and determine the CKM matrix elements or reveal violations leading to the discovery of new physics.

BABAR enables such research by generating millions (465×10^6) of $B\overline{B}$ pairs and measuring their decay properties. The experiment consists of the Stanford Linear Accelerator (SLAC), PEP-II storage rings, the detector itself as well as a collaboration of ~ 600 physicists and engineers. The accelerator creates electrons and positrons, which are then stored by PEP-II rings and used to create the $B\overline{B}$ pairs at the collision point. The energy of the e^+e^- pairs is selected so that the interaction occurs on the $\Upsilon(4S)$ resonance, thus maximizing the number of generated pairs. In addition, *BABAR* is an asymmetric B-factory where electrons produced at a higher energy than the positrons (9.1 GeV vs. 3.0 GeV), thus ensuring that the B's are emitted in the direction of the e^- beam. This allows us to measure the time between the decays of B and $\overline{B}$ based on the location of the corresponding decay vertices. As described in Chapter 3, the detector is optimized so that we can pinpoint their locations, fully reconstruct the desired final state ($B \rightarrow \rho^0\rho^0 \rightarrow \pi^+\pi^-\pi^+\pi^-$ in our case) and determine the flavor of the conjugate B (*i.e.* whether it contains a b or a $\bar{b}$ quark).

The goal of our specific analysis is to measure the properties of $B \rightarrow \rho^0\rho^0$ decays. I extracted ~ 100 such events from the $465 \times 10^6 B\overline{B}$ pairs and used them to measure the Branching Fraction, polarization fraction as well as the coefficients (S and C), which parametrize the CP violation for the process. Specifically, I have:

- Examined alternate approaches to selecting the correct event candidate out of a set of repeating ones (and determined that using χ^2_{vtx} optimized the selection, Section 4.4).
- Improved the $B \to D\pi$ veto such that the bachelor pion is selected based on the kinematic expectation, rather than picking the π with the highest momentum (Section 4.3.3).
- Constructed the Probability Density Functions (PDFs) for the signal and all of the relevant backgrounds in each of the observables (Section 4.5).
- Examined, fitted and tested multiple variations of the Charmless background. A detailed study was also performed on how to best combine the modes in the Cocktail when performing the Maximum Likelihood Fit. In addition, we ensured that in the end *Saclay* and *LBNL* fitters have the same configuration (Section 4.6.4).
- Performed an extensive amount of tests to verify the fitter's functionality. Specifically, I validated it by fitting generated Monte Carlo (MC) datasets, cross-fitting with *Saclay* as well as analyzing blind and incomplete (previously unblinded) datasets (Section 4.6).
- Constructed sPlots, Direct Projections, Projection Plots and Likelihood Ratio Plots to check that there were no discrepancies (Section 4.8).
- Performed a host of scans over the range of parameter values to determine the fit bias (Section 4.8.3).

- Studied a number of alternate PDF parameterizations and determined the optimal one for use in the fitter.

- Took errors as well as their correlations from the $B \rightarrow D\pi \rightarrow K\pi\pi\pi$ control sample studies and then determined the systematic uncertainty due to PDF parametrization (through varying each parameter by its error and combining the results, Section 4.9.2).

- Performed several other studies *(e.g.* estimating the uncertainty due to the potential Charmless variation, background CP asymmetries, *etc.*) in order to compute the total Systematic Error (Section 4.9).

A full description of the analysis is given in Chapter 4. In addition to being responsible for the primary fitter, I developed and implemented an approach which uses the Likelihood Discriminant instead of the Neural Net multivariate discriminant (Appendix C). I have also incorporated track based calibration into *BABAR* software (the procedure involved writing and modifying several C++ classes and proxies, as summarized in Appendix B). The results of our research are combined with several other measurements in order to determine the most likely value for the angle α as well as its uncertainty $\Delta\alpha$. The value of the angle is related to the parameters of the CKM matrix, while $\Delta\alpha$ gauges the strength of the Penguin Loop contributions (which could originate from new physics). Thus, by completing the analysis we are verifying the validity of the SM and performing a precision measurement of its parameters.

Chapter 2

Theory

In this section we discuss the significance of $B \to \rho^0\rho^0$ decays from a theoretical perspective and provide an overview of how measurements of their proprieties fit into the greater understanding of Physics. We begin by discussing the Standard Model of Particles And Fields with a particular focus on Electroweak Symmetry Breaking along with the impact it has on the particle content and gauge interactions. Consequently, we proceed to describe the structure of the CKM matrix and CP violation. The significance of B-mesons in general, as well as particular relevance of $B \to \rho\rho$ decays, are discussed in this context.

During the first half of the section we rely heavily on the explanations of the Standard Model, Electroweak Interactions, and the CKM matrix provided in books by *Peskin and Schroeder* [3], *Weinberg* [4], *Jarlskog* [5]. A discussion of B-meson properties uses information from the *BABAR* Physics Book [6] along with subsequent references. The Isospin Analysis follows the template provided by *Gronau and London* [15].

2.1 The Standard Model

In particle physics we describe all (non gravitational) interactions via the Standard Model. It is an $SU(3) \times SU(2) \times U(1)$ gauge theory where the strong and the electroweak forces are quantized as $SU(3)$ and $SU(2) \times U(1)_Y$ theories, respectively [3] (for a detailed discussion of Lie Groups in Particle Theory see *Georgi* [7]). The model has the following particle content:

- quarks (q) - Fermions arranged in three generations (six quarks in total). All are charged under $SU(3)$ and $U(1)_{EM}$, while the left-handed doublets are charged under the $SU(2)$ as well.

- leptons (l) - Three generations of fermions. e-electron, μ-muon, τ-tau are charged under $U(1)_{EM}$. The left handed components together with the corresponding neutrinos form $SU(2)$ doublets.

- gluons (g) - The gauge bosons, which mediate the strong ($SU(3)$) interactions. They are charged under the $SU(3)$.

- photons (γ) - The gauge boson corresponding to the electromagnetic ($U(1)_{EM}$) interactions. It carries no charge.

- $W^{\pm}$ - Charged (under $U(1)_{EM}$) gauge bosons corresponding to the (broken) $SU(2) \times U(1)_Y$ symmetry. Additionally, they interact via $SU(2) \times U(1)_Y$.

- Z^0 - Neutral gauge bosons corresponding to the $SU(2) \times U(1)_Y$ symmetry. They interact via $SU(2) \times U(1)_Y$ as well.

- Higgs Boson (ϕ) - Scalar particle responsible for the Electroweak Symmetry Breaking. It is charged under the $SU(2) \times U(1)_Y$.

The interactions between the fields are shown in Fig. 2.1 and are described by the Lagrangian

$$L_{SM} = L_{QCD} + L_{EW} = L_{QCD} + L(\psi, A_{EW}) + L(\psi, \phi) + L(A_{EW}, \phi) + L(A_{EW}) - V(\phi) \quad (2.1)$$

with the components corresponding to

- L_{QCD} - strong interactions.
- $L(\psi, A_{EW})$ - interactions between the fermions (quarks and leptons) and the electroweak bosons.
- $L(\psi, \phi)$ - interactions between the fermions and the higgs (ϕ). The term is the source of the fermion mass generation, when the Electroweak Symmetry is broken.
- $L(A_{EW}, \phi)$, $L(A_{EW})$ - interactions of the electroweak bosons with the higgs and themselves, respectively.
- $V(\phi)$ - the higgs potential. It serves as a source of the Electroweak Symmetry breaking.

2.1.1 Spontaneous Symmetry Breaking

The higgs field ϕ is in the fundamental representation of $SU(2)$ and has a $U(1)_Y$ charge of 1/2. It can be written as

$$\phi \equiv \begin{pmatrix} \phi^+ \\ \phi^0 \end{pmatrix} \quad (2.2)$$

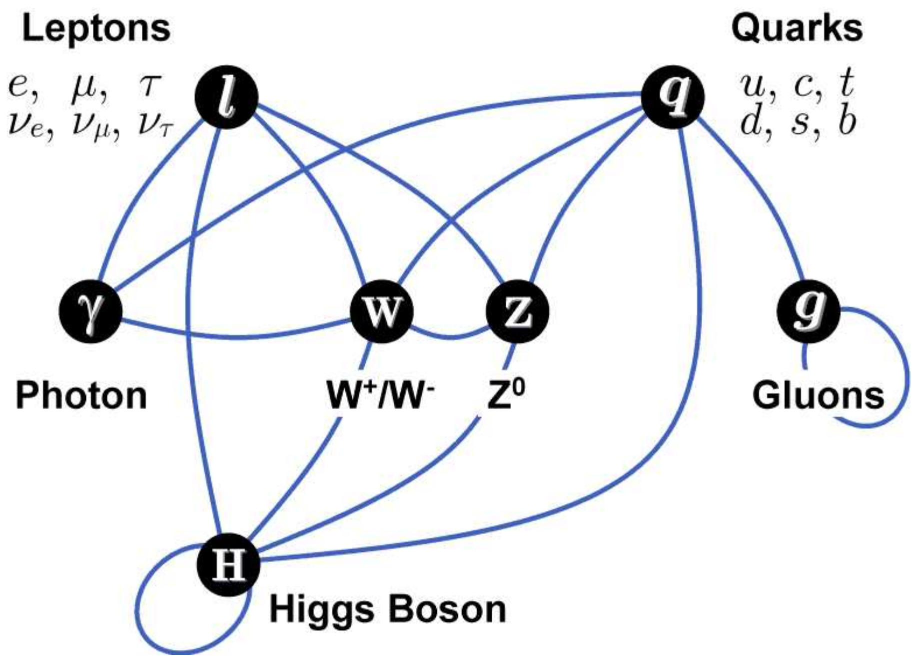

Figure 2.1: *Particle content of the Standard Model Particles [8]. The blue lines denote possible interactions.*

or in terms of real fields $\phi^0 = (\phi_0 + i\phi_3)/\sqrt{2}$, $\phi^+ = (\phi_1 + i\phi_2)/\sqrt{2}$. The higgs potential is

$$V(\phi) = -\frac{\mu^2}{2}\phi^\dagger\phi + \frac{\lambda}{4}(\phi^\dagger\phi)^2, \tag{2.3}$$

which for $\mu^2 > 0$ has a vacuum expectation value (*i.e.* a minimum) at $<\phi>\equiv \nu = \sqrt{\mu^2/\lambda}$. We can perform an $SU(2)\times U(1)_Y$ transformation such that $\phi_1 = \phi_2 = \phi_3 = 0$ and ν is real and positive. Then

$$\phi = \frac{1}{\sqrt{2}}\begin{pmatrix} 0 \\ \nu + H \end{pmatrix} \tag{2.4}$$

where H is the propagating neutral higgs field. The fact that $\nu \neq 0$ means that the $SU(2)\times U(1)_Y$ symmetry has been broken, as L_{SM} will now have several terms not invariant under the above gauge transformation.

Consequently, the interaction of the higgs and the $SU(2)\times U(1)_Y$ fields yields a (nonzero) vector meson mass term in the interaction

$$L(A_{EW},\phi) = -\frac{1}{2}|(\partial_\mu - i\vec{A_\mu}\cdot\vec{t^\phi} - iB_\mu y^\phi)\phi|^2, \tag{2.5}$$

where $\vec{A_\mu}$, B_μ are the $SU(2)$, $U(1)_Y$ gauge fields with their couplings $\vec{t^\phi} = \frac{g}{2}\vec{\tau}$, $y^\phi = -\frac{g'}{2}I$

$$\vec{\tau} \equiv \left[\begin{pmatrix} 0 & 1 \\ 1 & 0 \end{pmatrix}, \begin{pmatrix} 0 & -i \\ i & 0 \end{pmatrix}, \begin{pmatrix} 1 & 0 \\ 0 & -1 \end{pmatrix}\right],\ I \equiv \begin{pmatrix} 1 & 0 \\ 0 & 1 \end{pmatrix}.$$

It contains a term dependent on $<\phi>$

$$-\frac{1}{2}|(\vec{A_\mu}\cdot\vec{t^\phi} + B_\mu y^\phi) <\phi> |^2 = -\frac{1}{2}\left|(\frac{g}{2}(\vec{A_\mu}\cdot\vec{\tau} - \frac{g'}{2}B_\mu)\begin{pmatrix} 0 \\ \nu \end{pmatrix}\right|^2 = \tag{2.6}$$

$$= -\frac{\nu^2 g^2}{4}W^\dagger_\mu W^\mu - \frac{\nu^2(g^2+g'^2)}{4}Z_\mu Z^\mu.$$

As can be seen, the charge eigenstates

$$W^+_\mu \equiv W_\mu = (A^1_\mu + iA^2_\mu)/\sqrt{2}, \tag{2.7}$$

$$W^-_\mu \equiv W^\dagger_\mu = (A^1_\mu - iA^2_\mu)/\sqrt{2}$$

acquire a mass $m_W = \nu|g|/2$, while the neutral boson $Z_\mu = \cos(\theta_W)A^3_\mu + \sin(\theta_W)B_\mu$ gets a mass $m_Z = \nu\sqrt{g^2+g'^2}/2$. The angle θ_W is known as the *weak mixing angle* and is defined via

$$\sin(\theta_W) = \frac{g'}{\sqrt{g^2+g'^2}},\ \cos(\theta_W) = \frac{g}{\sqrt{g^2+g'^2}}. \tag{2.8}$$

The fourth gauge boson $A_\mu = -\sin(\theta_W)A^3_\mu + \cos(\theta_W)B_\mu$ is the photon. It remains massless and the $U(1)_{EM}$ symmetry is preserved. In summary, below the TeV scale the higgs coupling constant μ^2 becomes greater than 0 thus leading to the spontaneous breaking of the $SU(2)\times U(1)_Y$ down to its $U(1)_{EM}$ subgroup. In the process the electroweak fields acquire nonzero masses.

2.1.2 Fermion Masses

Now, let us take a look at the interaction between the higgs and the fermions. The portion of Eq. (2.1) describing the quark interactions can be written as

$$L(\psi,\phi)_q = -\sum_{i,j=1}^{3}\{G_{ij}\overline{(U^i,D^i)_L}\begin{pmatrix}\phi^+\\ \phi^0\end{pmatrix}D_R^j + \tag{2.9}$$

$$+F_{ij}\overline{(U^i,D^i)_L}\begin{pmatrix}\phi^{0*}\\ -\phi^{+*}\end{pmatrix}U_R^j + \text{hermitian conjugate } (h.c.)\},$$

where $\vec{U},\vec{D}$ each represent three independent quark fields with charge $2e/3, -e/3$; G_{ij}, F_{ij} are the corresponding coupling constants; while the subscripts L and R denote the left-handed $SU(2)$ doublets and right-handed singlets, respectively. A very similar term $L(\psi,\phi)_l$ describes the lepton sector, with $\vec{U}\to\vec{E}, \vec{D}\to\vec{\nu}$ (where $\vec{E},\vec{\nu}$ represent the corresponding lepton fields) and $G_{ij}, F_{ij}\to G^l_{ij}, F^l_{ij}$. Once the electroweak symmetry is broken, the higgs field corresponds to the one given by Eq. (2.4). Then the above Lagrangian can be written as

$$L(\psi,\phi)_q = -\sum_{i,j=1}^{3}\{M^D_{ij}\overline{D^i_L}D^j_R + M^U_{ij}\overline{U^i_L}U^j_R + h.c.\}(1+\frac{1}{\nu}h) \tag{2.10}$$

with $M^D = \nu G/\sqrt{2}$, $M^U = \nu G\sqrt{2}$. These matrices are complex and contain off-diagonal terms. However, we can perform a unitary transformation on the quark fields:

$$U_L \to V_{uL}U_L,\ U_R\to V_{uR}U_R,\ D_L\to V_{dL}D_L,\ D_R\to V_{dR}U_R, \tag{2.11}$$

where $V_{uL}, V_{uR}, V_{dL}, V_{dR}$ are complex unitary (3×3) matrices and are chosen such that

$$M^U_{diag} = V_{uL}M^UV^\dagger_{uR},\ M^D_{diag} = V_{dL}M^DV^\dagger_{dR} \tag{2.12}$$

are diagonal and real. In other words, the above transformation takes us to the mass eigenbasis, which we normally work with. Here the quark fields represent the usual three generations (*i.e.* $\vec{U} = (u, c, t)$, $\vec{D} = (d, s, b)$).

2.2 The CKM Matrix

2.2.1 Charged Current Interaction

The interaction between fermions and the electroweak bosons ($L(\psi, A_{EW})$) contains the quark - $SU(2)$ gauge boson term

$$L(\psi, A_{EW})_q = -\frac{1}{2} g \sum_{i=1}^{3} \overline{(U_L^i, D_L^i)} \gamma^\mu \vec{A_\mu} \cdot \vec{\tau} \begin{pmatrix} U_L^i \\ D_L^i \end{pmatrix} + h.c. \tag{2.13}$$

Once the electroweak symmetry is broken the interaction between charged bosons $W^\pm$ (defined in terms of $\vec{A_\mu}$ via Eq. (2.7)) is expressed as

$$L_W = -\frac{1}{2} g \sum_{i=1}^{3} \overline{U_L^i} \gamma^\mu W_\mu^+ D_L^i + h.c. \tag{2.14}$$

In the quark mass basis, given by the transformation in Eq. (2.11), the Lagrangian is

$$\begin{aligned} L_W &= -\frac{1}{2} g \sum_{i,j,k=1}^{3} \overline{U_L^j} \gamma^\mu W_\mu^+ V_{uL}^{ji} V_{dL}^{\dagger ik} D_L^k + h.c. = \\ &= -\frac{1}{2} g \sum_{j,k=1}^{3} \overline{U_L^j} \gamma^\mu W_\mu^+ V^{jk} D_L^k + h.c., \end{aligned} \tag{2.15}$$

where $V = V_{uL} V_{dL}^\dagger$ is a 3×3 matrix, also known as the CKM (Cabibbo-Kobayashi-Maskawa) matrix. It describes the mixing between the three generations of quarks during weak interactions and is the source of CP violation.

2.2.2 CKM Matrix Structure

Technically, V is a complex $N \times N$ $(N = 3)$ matrix and therefore contains $2N^2$ parameters. However, since the CKM matrix is constructed as a product of unitary matrices ($V = V_{uL}V_{dL}^{\dagger}$ as defined in Eqs. (2.11), (2.15)) it is itself unitary:

$$VV^{\dagger} = 1. \tag{2.16}$$

This fact reduces the number of independent parameters to N^2. Furthermore, it implies that $N(N-1)/2 = 3$ of them can be represented as angles (representing rotations in N-dimensional Euclidean space) and the remaining $N(N+1)/2 = 6$ as phases [9]. Because the phases of the quark fields are arbitrary, they can always be rotated as

$$u_L \to e^{i\phi(u)}u_L,\ d_L \to e^{i\phi(d)}d_L, etc. \tag{2.17}$$

We use this procedure to to eliminate $2N - 1 = 5$ of the 6 CKM phases (and in the process multiply V by an otherwise irrelevant sixth phase). Thus, the CKM matrix is parametrized by a combination of three angles $\theta_{12}, \theta_{13}, \theta_{23}$ and a phase δ :

$$V = \begin{pmatrix} V_{ud} & V_{us} & V_{ub} \\ V_{cd} & V_{cs} & V_{cb} \\ V_{td} & V_{ts} & V_{tb} \end{pmatrix} = \tag{2.18}$$

$$= \begin{pmatrix} c_{12}c_{13} & s_{12}c_{13} & s_{13}e^{-i\delta} \\ -s_{12}c_{23} - c_{12}s_{23}s_{13}e^{-i\delta} & c_{12}c_{23} - s_{12}s_{23}s_{13}e^{-i\delta} & s_{23}c_{13} \\ s_{12}s_{23} - c_{12}c_{23}s_{13}e^{-i\delta} & -c_{12}s_{23} - s_{12}c_{23}s_{13}e^{-i\delta} & c_{23}c_{13} \end{pmatrix},$$

where $c_{ij} = \cos\theta_{ij}$, $s_{ij} = \sin\theta_{ij}$. Note that for just two generations of quarks, the above procedure eliminates all of the phases and all but one angle. The mixing matrix is then simply

$$\begin{pmatrix} \cos\theta_c & \sin\theta_c \\ -\sin\theta_c & \cos\theta_c \end{pmatrix}, \tag{2.19}$$

otherwise known as the Cabibbo matrix [10]. For three generations, unitarity of the CKM matrix implies several relations between its elements, including

$$V_{id}V_{is}^* = V_{ud}V_{us}^* + V_{cd}V_{cs}^* + V_{td}V_{ts}^* = 0, \tag{2.20}$$

$$V_{is}V_{ib}^* = V_{us}V_{ub}^* + V_{cs}V_{cb}^* + V_{ts}V_{tb}^* = 0, \tag{2.21}$$

$$V_{id}V_{ib}^* = V_{ud}V_{ub}^* + V_{cd}V_{cb}^* + V_{td}V_{tb}^* = 0. \tag{2.22}$$

In addition, there is a natural hierarchy describing the interactions between the generations:

$$|V| \simeq \begin{pmatrix} 0.975 & 0.221 & 0.003 \\ -0.221 & 0.975 & 0.040 \\ 0.009 & 0.039 & 0.999 \end{pmatrix}. \tag{2.23}$$

Thus, it is convenient to use the Wolfenstein Parameterization [11] where

$$V = \begin{pmatrix} 1-\frac{\lambda_w^2}{2} & \lambda_w & A\lambda_w^3(\rho - i\eta) \\ -\lambda_w & 1-\frac{\lambda_w^2}{2} & A\lambda_w^2 \\ A\lambda_w^3(1-\rho-i\eta) & -A\lambda_w^2 & 1 \end{pmatrix}. \tag{2.24}$$

The above holds up to $O(\lambda_w^4)$ for $\lambda_w = \sin\theta_c =\simeq 0.22$ (where θ_c is the Cabibbo angle used in Eq. (2.19)) or to all orders for $s_{12} = \lambda_w$, $s_{23} = A\lambda_w^2$, $s_{13}e^{-i\delta} = A\lambda_w^3(\rho - i\eta)$ [12].

2.2.3 CP Violation and the Unitarity Triangle

There are three possible discrete symmetries of the Standard Model Lagrangian Eq. (2.1): Parity (P), Time Reversal (T) and Charge Conjugation (C). Parity reverses the handedness of space by taking $(t, \vec{x}) \rightarrow (t, -\vec{x})$. Time reversal interchanges the forward and backward light-cones through $(t, \vec{x}) \rightarrow (-t, \vec{x})$. Charge conjugation interchanges particles with their antiparticles. It is observed experimentally and incorporated into L_{SM} that each of the three symmetries is preserved under the strong and electromagnetic interactions. Plus, it can be shown that any local Lorentz Invariant Lagrangian field theory has the combination CPT as its exact symmetry (all experimental observations to date are consistent with this statement) [3].

However, the weak interactions violate P and C separately, while their behavior under the action of the combination CP warrants a closer examination. Specifically, under the CP conjugation the individual terms in the Lagrangian transform into their hermitian conjugates:

$$\bar{\psi}_i \psi_j \rightarrow \bar{\psi}_j \psi_i, \tag{2.25}$$

$$\bar{\psi}_i \gamma^\mu W_\mu (1 - \gamma_5) \psi_j \rightarrow \bar{\psi}_j \gamma^\mu W_\mu (1 - \gamma_5) \psi_j \, etc.,$$

with the complete set of transformation rules is described in the literature (*e.g.* [3]). As a result, the term describing the weak interactions of quarks (Eq. 2.15) transforms as

$$L_W = -\frac{1}{2} g (V_{jk} \bar{U}_j \gamma^\mu W^+_\mu (1 - \gamma_5) D_k + V^*_{jk} \bar{D}_k \gamma^\mu W^-_\mu (1 - \gamma_5) U_j) \rightarrow \tag{2.26}$$

$$\rightarrow -\frac{1}{2} g (V_{jk} \bar{D}_k \gamma^\mu W^-_\mu (1 - \gamma_5) U_j + V^*_{jk} \bar{U}_j \gamma^\mu W^+_\mu (1 - \gamma_5) D_k).$$

If we make the approximation that there are only two generations of quarks or if the theory contains another symmetry, which allows us to remove the phase in Eq. (2.18) (such as making an estimate that two quarks of the same charge have the same mass), then V is real and the CP transformation leaves L_W unchanged. However, in the Standard Model the presence of the complex phase (δ) means that in general $V_{ij} \neq V_{ij}^*$ and the CP symmetry is violated by weak interactions.

Furthermore, relations (2.20)-(2.22) contain three complex numbers, which add up to 0, and therefore can be represented as triangles in the complex plane (Fig. 2.2). They provide an understanding of decays in the Kaon, B_s and B systems, respectively. While all three of these triangles are equal in area, the ones corresponding to Kaons and B_s-mesons are nearly flat, with two sides much longer than the third. In order to observe CP violation in these systems, one would have to analyze the processes related to the short sides, which are very rare. On the other hand, the triangle corresponding to B decays is relatively open (shown in detail in Fig. 2.3). Specifically, we rescale the Unitarity Triangle by dividing

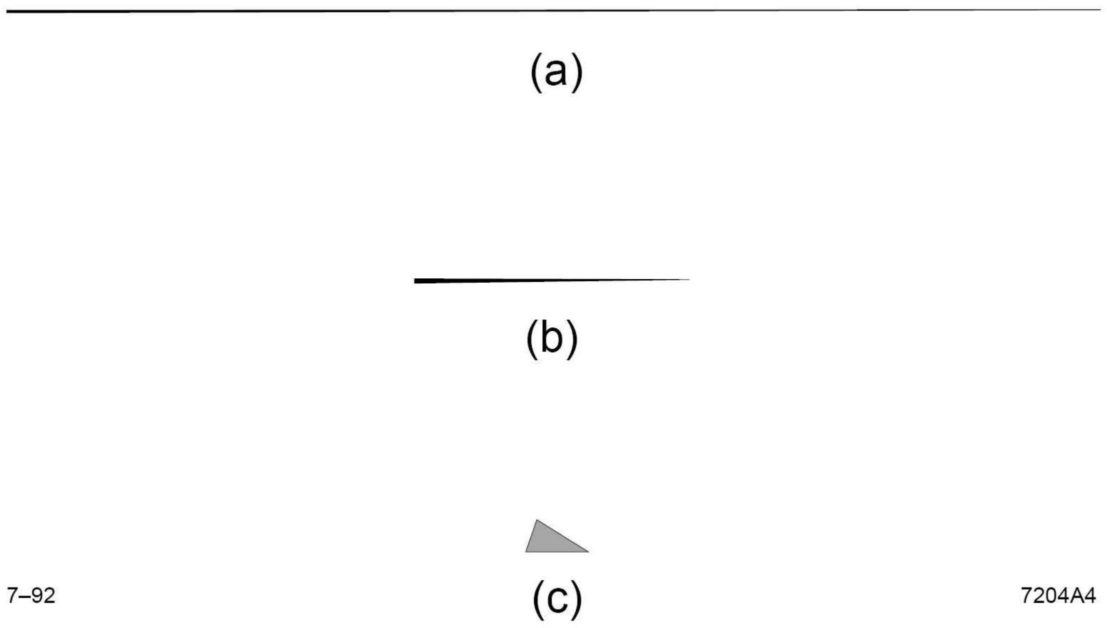

Figure 2.2: *Three Unitarity Triangles for the a) Kaon b) B_s and c) B_d systems [6].*

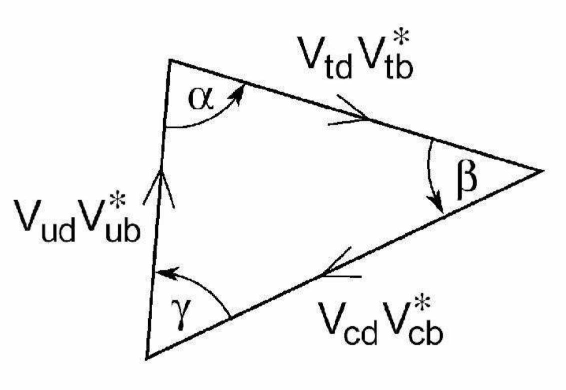

Figure 2.3: *Unitarity Triangles corresponding to the B system [6].*

each side by $V_{cd}V_{cb}^*$, thus ensuring that one of the sides (formerly the $V_{cd}V_{cb}^*$ side) has a magnitude 1 and is aligned with the real axis. The result is shown in Fig. 2.4 with the unitarity angles are defined as

$$\alpha \equiv -arg\left[\frac{V_{td}V_{tb}^*}{V_{ud}V_{ub}^*}\right], \tag{2.27}$$

$$\beta \equiv -arg\left[\frac{V_{cd}V_{cb}^*}{V_{td}V_{tb}^*}\right], \tag{2.28}$$

$$\gamma \equiv -arg\left[\frac{V_{ud}V_{ub}^*}{V_{cd}V_{cb}^*}\right]. \tag{2.29}$$

Their values are measured to be $\alpha \sim 90^0$, $\beta \sim 20^0$, $\gamma \sim 70^0$ [13]. If the Standard Model is correct, then $\alpha+\beta+\gamma = 180^0$. The resultant (large) CP asymmetries in B decays are measured in *BABAR* in order to verify the validity of the model and look for any physics beyond it. An overview of the measurements involved, along with how they are combined to place restrictions on the parameters of the CKM matrix, is given in Appendix A.

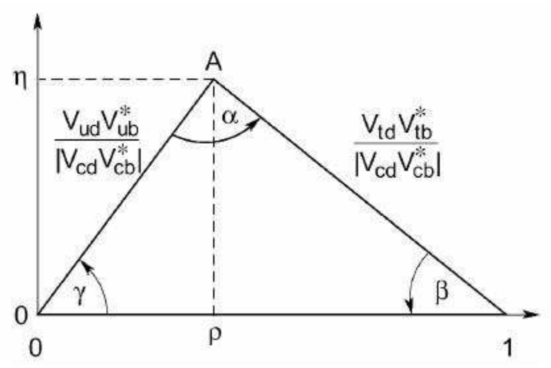

Figure 2.4: *Unitarity Triangle rescaled by* $V_{cd}V_{cb}^*$ *[6].*

2.3 B-Mesons

2.3.1 Eigenstates

The B mesons are flavor eigenstates. Specifically, the $\Upsilon(4S)$ decays into a $B^0 = (\bar{b}d)$ and a $\overline{B}^0 = (b\bar{d})$. Since the constituent quarks are not mass eigenstates, neither are B^0 and $\overline{B}^0$. They are able to oscillate into one another, as is described by the Feynman diagrams in Fig. 2.5.

The light (B_L) and heavy (B_H) mass eigenstates are linear combinations of the

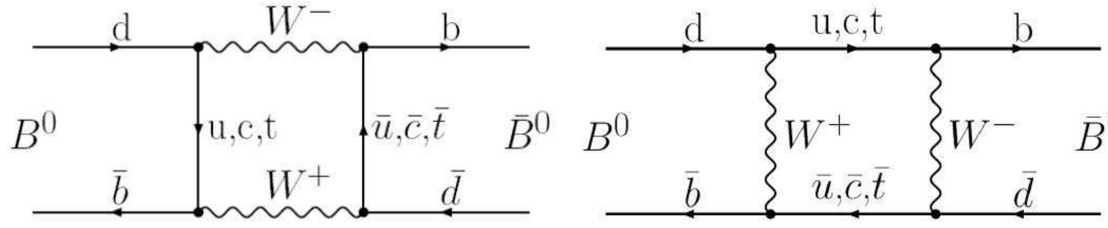

Figure 2.5: *Leading order Standard Model Feynman Diagrams for* B^0*-*$\overline{B}^0$ *mixing.*

flavor states

$$|B_L>= p|B^0> +q|\overline{B}^0>, \tag{2.30}$$

$$|B_H>= p|B^0> -q|\overline{B}^0>,$$

where normalization (coupled with the fact that $< B^0|\overline{B}^0>= 0$) requires

$$|p|^2 + |q|^2 = 1. \tag{2.31}$$

Because these are mass eigenstates, the action of the Hamiltonian leaves them invariant:

$$H|B_{L,H}>= (M_{L,H} - \frac{i}{2}\Gamma_{L,H})|B_{L,H}> \tag{2.32}$$

and solving for the eigenvalues yields a series of relations between the above parameters.

Furthermore, the action of CP transforms B^0 and $\overline{B}^0$ into one another:

$$CP|B^0>= e^{2i\xi_B}|\overline{B}^0>,\ CP|\overline{B}^0>= e^{-2i\xi_B}|B^0>, \tag{2.33}$$

where b-flavor conservation in strong interactions allows us to redefine the phase ξ_B [14]. If CP were a good symmetry of the theory, then $|B_L>$ and $|B_H>$ would be CP eigenstates. For the B system the CP violation is pronounced (with $|p| \sim |q|$ due to interference). It can be observed by analyzing decay amplitudes into final CP states $|f>$

$$A_f \equiv< f|H|B^0>, \tag{2.34}$$

$$\bar{A}_f \equiv< f|H|\overline{B}^0>,$$

and the quantity

$$\lambda = \frac{q\bar{A}_f}{pA_f}, \tag{2.35}$$

which is independent of the phase conventions. Whenever $\lambda \neq 1$, CP is not an exact symmetry.

2.3.2 Time Dependent Formalism

The decay of $\Upsilon(4S)$ produces B^0 and $\overline{B}^0$ in a coherent state. In other words, while the particles oscillate into one another there is always one B^0 and one $\overline{B}^0$ in the system (until a decay occurs). The full two-B state can be written as [6]:

$$S(t_f,t_b) = \frac{1}{\sqrt{2}} e^{-i(M-i\Gamma/2)(t_f+t_b)} \{\cos[\Delta m_B(t_f-t_b)/2](B^0_f\overline{B}^0_b - \overline{B}^0_f B^0_b) + \tag{2.36}$$

$$-i\sin[\Delta m_B(t_f-t_b)/2](\frac{p}{q}B^0_f B^0_b - \frac{q}{p}\overline{B}^0_f\overline{B}^0_b)\}\sin(\theta_f),$$

where the subscripts f and b refer to the Bs flying off in the forward and backward directions (with respect to the e^- beam), θ is the angle they make with the beam, $t_{f,b}$ are the proper decay times for each B (until one meson decays, $t_f = t_b$), $\Delta m_B \equiv M_H - M_L$ with M_H,M_L defined via Eq. (2.32) [6]. Subsequently, the amplitude for one of the B's to decay to a final state f_1 (at time t_1) and the other B to decay to a state f_2 (at time t_2) is

$$A(t_1,t_2) = \pm\frac{1}{\sqrt{2}} e^{-i(M-i\Gamma/2)(t_1+t_2)} \{\cos[\Delta m_B(t_1-t_2)/2](A_1\bar{A}_2 - \bar{A}_1 A_2) + \tag{2.37}$$

$$-i\sin[\Delta m_B(t_1-t_2)/2](\frac{p}{q}A_1 A_2 - \frac{q}{p}\bar{A}_1\bar{A}_2)\}\sin(\theta_1),$$

where $A_i(\bar{A}_i)$ is the amplitude for $B^0(\overline{B}^0)$ to decay to the state f_i and $+,-$ signs correspond to the cases where $t_1 = t_{f,b}$, $t_2 = t_{b,f}$.

When measuring the CP asymmetries at *BABAR* we focus on situations where one of the B-mesons decays into a CP eigenstate (denoted f_{CP}) at time t_f. We are able to determine the b-flavor of the other B by examining its decay products, which is commonly referred to as the 'tagged' B (with decay time t_{tag}), and since we know its flavor $A_{tag} = 0$ or $\bar{A}_{tag} = 0$. The rate for producing a CP and a tagged state then becomes [6]

$$R(t_{tag},t_{CP}) = \frac{Ce^{-\Gamma(t_{tag}+t_{CP})}|\bar{A}_{tag}|^2|A_{f_{CP}}|^2}{1+|\lambda_{f_{CP}}|^2}\times \tag{2.38}$$

$$\times\left\{1 \pm \frac{1-|\lambda_{f_{CP}}|^2}{1+|\lambda_{f_{CP}}|^2}\cos[\Delta m_B(t_{CP}-t_{tag})] \mp \frac{2Im(\lambda_{f_{CP}})}{1+|\lambda_{f_{CP}}|^2}\sin[\Delta m_B(t_{CP}-t_{tag})]\right\}.$$

The $+\cos$ ($-\cos$) applies to the case where the $\overline{B}^0$ (B^0) is the the tagged particle [6]. The quantity $\lambda_{f_{CP}}$ is defined in Eq. (2.35) and can be written as

$$\lambda_{f_{CP}} \equiv \frac{q\bar{A}_{f_{CP}}}{pA_{f_{CP}}} = \eta_{f_{CP}}\frac{q\bar{A}_{\bar{f}_{CP}}}{pA_{f_{CP}}}, \tag{2.39}$$

where $\eta_{f_{CP}} = \pm 1$ is the CP eigenvalue of the state f_{CP}. Furthermore, we can use the fact that $|q/p| = 1$ to express the asymmetry for the decay rates as

$$a_{f_{CP}}(t) \equiv \frac{\Gamma(B^0(t)\to f_{CP}) - \Gamma(\overline{B}^0(t)\to f_{CP})}{\Gamma(B^0(t)\to f_{CP}) + \Gamma(\overline{B}^0(t)\to f_{CP})} = \tag{2.40}$$

$$= \frac{1-|\lambda_{f_{CP}}|^2}{1+|\lambda_{f_{CP}}|^2}\cos(\Delta m_B t) - \frac{2Im(\lambda_{f_{CP}})}{1+|\lambda_{f_{CP}}|^2}\sin(\Delta m_B t) =$$

$$= C_{CP}\cos(\Delta m_B t) - S_{CP}\sin(\Delta m_B t),$$

where $t = t_{CP} - t_{tag}$. Moreover, $a_{f_{CP}}$ is a physical quantity, which we extract from the data via a *BABAR* analysis and use to measure the Unitarity Angles.

2.4 The $\rho\rho$ System

Measuring the properties of $B \to \rho\rho$ decays helps us examine the structure of the CKM Matrix and search for contributions due to new physics. Specifically, there are six amplitudes for three final states:

$$A^{+-} \equiv A(B^0 \to \rho^+\rho^-),\ \bar{A}^{+-} \equiv A(\overline{B}^0 \to \rho^+\rho^-), \tag{2.41}$$

$$A^{+0} \equiv A(B^+ \to \rho^+\rho^0),\ \bar{A}^{-0} \equiv A(B^- \to \rho^-\rho^0),$$

$$A^{00} \equiv A(B^0 \to \rho^0\rho^0),\ \bar{A}^{00} \equiv A(\overline{B}^0 \to \rho^0\rho^0),$$

with $\rho^0 \to \pi^+\pi^-$, $\rho^\pm \to \pi^\pm\pi^0$. The $\rho^+\rho^-$ and $\rho^0\rho^0$ are CP eigenstates. As a result, the decay rates into those states are given by Eq. (2.38) to be

$$R(B^0 \to \rho^+\rho^-, \rho^0\rho^0) \propto 1 - C^{+-,00}\cos(\Delta m_B t) + S^{+-,00}\sin(\Delta m_B t), \tag{2.42}$$

$$R(\overline{B}^0 \to \rho^+\rho^-, \rho^0\rho^0) \propto 1 + C^{+-,00}\cos(\Delta m_B t) - S^{+-,00}\sin(\Delta m_B t),$$

where the proportionality coefficient is $\frac{1}{2}|A^{+-,00}|^2 e^{-\Gamma t}/(1+|\lambda_{+-,00}|^2)$ in all four cases. S and C are expressed in terms of the amplitudes as [6]:

$$C^{+-,00} = \frac{1-|\lambda_{+-,00}|^2}{1+|\lambda_{+-,00}|^2} = \frac{|A^{+-,00}|^2 - |\bar{A}^{+-,00}|^2}{|A^{+-,00}|^2 + |\bar{A}^{+-,00}|^2}, \tag{2.43}$$

$$S^{+-,00} = \frac{2Im(\lambda_{+-,00})}{1+|\lambda_{+-,00}|^2} = \frac{2|A^{+-,00}|^2}{|A^{+-,00}|^2 + |\bar{A}^{+-,00}|^2} Im\left(e^{-2i\phi_M}\frac{\bar{A}^{+-,00}}{A^{+-,00}}\right),$$

where we used the definition (2.35) along with the fact that $q/p = e^{-2i\phi_M}$ [15]. Physically, C represents interference between tree level decays and 'Penguin' loop corrections (Fig. 2.6). In the limit where they are negligible $|A| = |\bar{A}|$, which implies $C = 0$. S, on the other hand, measures the effect of CP violation due to interference (via mixing) between A and $\bar{A}$, with the corresponding leading order diagrams shown in Fig. 2.5.

Also note that, unlike the $B \to \pi\pi$ decays, there are always at least two charged particles in the final state for the $B \to \rho\rho \to \pi\pi\pi\pi$ processes. This allows us to reconstruct the decay vertices for each of the B's (as described in Section 4.1.3). We then extract the time difference $t_{CP} - t_{tag}$ between the decays and fit for the parameters S and C in Eq. (2.38). Therefore, it is possible to fully analyze CP properties of the system by measuring the constants for each of the relevant processes (listed in Eq. (2.41)).

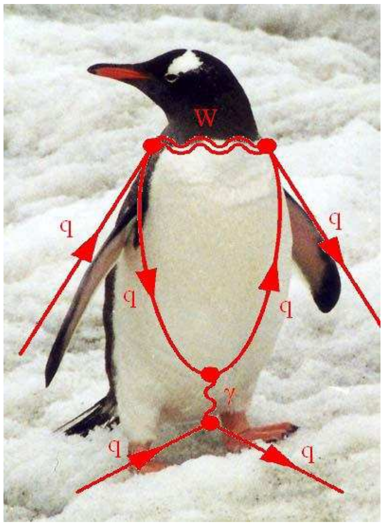

Figure 2.6: *A representation of the 'Penguin' diagram. It is a 1-Loop correction to the Tree-Level photon exchange between two quarks (or creation of a $q\bar{q}$ pair).*

2.4.1 Isospin Properties

We can relate the above amplitudes and coefficients to each other and the unitarity angles by examining the isospin properties of the system. We start by noting that because ρ is a vector-meson, the final $\rho\rho$ state can be in either S, P or D-wave. As a result, it is possible for it to have either *longitudinal* or *transverse* polarization[1]. While the transverse component has both CP-even and CP-odd portions, the longitudinal part has to be even under CP conjugation [16]. By Bose statistics the final state has to be symmetric, thus only the even isospin configurations ($I = 0, 2$) are allowed. Hence, we have two independent decay amplitudes A_0 and A_2 for $B \to \rho\rho$ decays into isospin eigenstates (along with two more for $\overline{B}$'s). The situation is completely analogous to the $B \to \pi\pi$ decays described

---

[1] The helicity angle $\theta_{1,2}$ is defined as the angle that the π^+ makes with the direction of the ρ^0 momentum (in the B^0 rest frame) measured in the ρ^0 rest frame, as shown in Fig. 2.7. The longitudinal component of the distribution has the angular dependence of $\cos^2\theta_1 \cos^2\theta_2$, and the transverse part is parametrized by $\sin^2\theta_1 \sin^2\theta_2$.

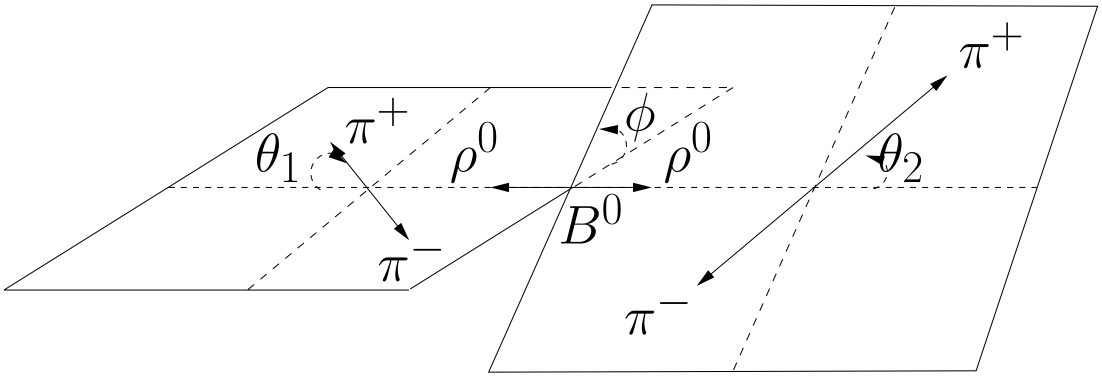

Figure 2.7: *Helicity angles θ_1, θ_2 and ϕ (which is subsequently integrated over) for the $B^0 \to \rho^0\rho^0$ decay. The two planes correspond to the ρ^0 rest frames [17].*

in [15]. Performing isospin decomposition and evaluating the Clebsch-Gordan coefficients yields

$$(1/\sqrt{2})A^{+-} = A_2 - A_0,\ A^{00} = 2A_2 + A_0,\ A^{+0} = 3A_2 \tag{2.44}$$

with similar relations for the $\overline{B}$ decays. The six amplitudes in Eq. (2.41) can then be expressed in terms of each other via the triangle relations

$$(1/\sqrt{2})A^{+-} + A^{00} = A^{+0} \tag{2.45}$$

and

$$(1/\sqrt{2})\bar{A}^{+-} + \bar{A}^{00} = \bar{A}^{-0}, \tag{2.46}$$

represented geometrically in Fig. 2.8.

Furthermore, the triangle relations can be used to express the coefficient $Im(\lambda)$, appearing in the definition of S in Eq. (2.43), in terms of the amplitudes and α. In order to do so, we need to recognize the following facts:

1. The amplitudes for decays of B vs. $\overline{B}$ into $I = 2$ state have the same strong phase

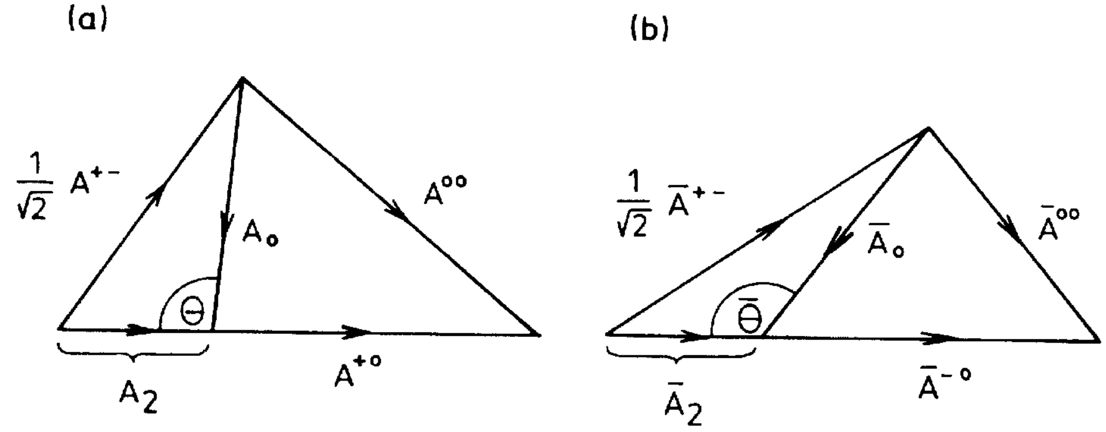

Figure 2.8: *Decay amplitudes represented as triangles in the complex plane for a) $B \to \rho\rho$, b) $\overline{B} \to \rho\rho$ decays [15].*

(δ_2), are related to each other by the sign change in the CKM phase ϕ_t and only have the tree level contribution [15]:

$$A_2 = |A_2| e^{i(\delta_2 + \phi_t)},\ \bar{A}_2 = |A_2| e^{i(\delta_2 - \phi_t)}. \tag{2.47}$$

2. The phases are the angles of the Unitarity Triangle, with $\phi_M = \beta$ (given $\lambda_f = e^{-2i\phi_M}\overline{A_f}/A_f$ for a CP final state f), $\phi_t = \gamma$ and $\phi_M + \phi_t = \pi - \alpha$ [18].

3. The angles θ and $\bar{\theta}$ are expressed in terms of the amplitudes via straightforward geometry from Fig. 2.8 as

$$\cos\theta = \frac{1}{2}\frac{|A_0|^2 + |A_2|^2 - |A^{+-}|^2/2}{|A_0 A_2|}. \tag{2.48}$$

4. There is a sign ambiguity for both θ and $\bar{\theta}$, since each triangle can be reflected over the x-axis with the relations 2.45-2.46 still holding.

After some algebra we obtain the expressions

$$Im(\lambda_{+-}) = Im(e^{-2i\phi_M}\bar{A}^{+-}/A^{+-}) = Im\left(e^{2i\alpha}\frac{1-|\bar{z}|e^{\pm i\bar{\theta}}}{1-|z|e^{\pm i\theta}}\right), \tag{2.49}$$

$$Im(\lambda_{00}) = Im(e^{-2i\phi_M}\bar{A}^{00}/A^{00}) = Im\left(e^{2i\alpha}\frac{1+|\bar{z}|e^{\pm i\bar{\theta}}/2}{1+|z|e^{\pm i\theta}/2}\right), \tag{2.50}$$

where $z \equiv A_0/A_2$, $\bar{z} \equiv \bar{A}_0/\bar{A}_2$ and the sign of θ need not correspond to the sign of $\bar{\theta}$ (*i.e.* there is a four-fold ambiguity due to the fact that the above equations still hold if one, but not necessarily the other, triangle is reflected).

2.4.2 $B \to \rho^+\rho^-$ Decays

The $\rho^+\rho^-$ state is a CP eigenstate. B decays into it proceed via Tree Level and Penguin processes shown in Fig. 2.9. Since the tree diagram is *not* color suppressed, the Branching Fraction for $B \to \rho^+\rho^-$ is relatively large (25.5×10^{-6} [20]). On the other hand, the leading (strong) Penguins are suppressed. If we make the approximation where their contribution to the decay amplitudes is neglected, then $Im(\lambda_{+-}) = \sin(2\alpha)$. In addition the coefficients S^{+-} and C^{+-}, defined in Eq. (2.43), are related each other as

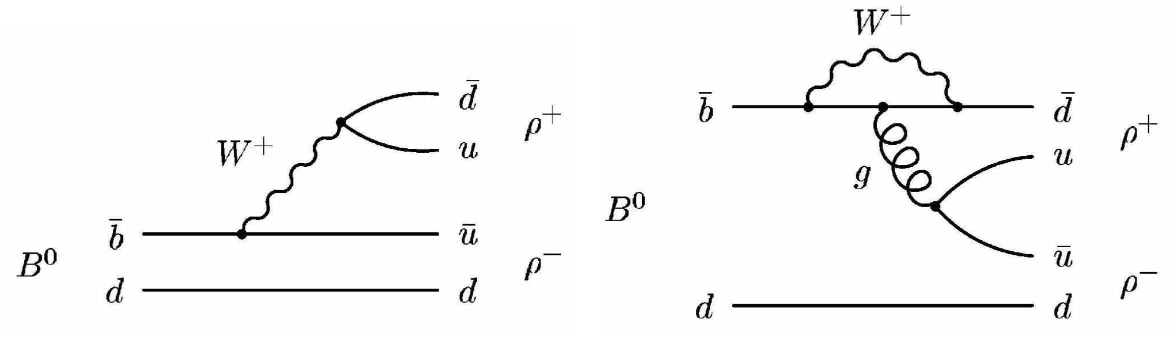

a) b)

Figure 2.9: *Feynman Diagrams describing the $B^0 \to \rho^+\rho^-$ decay. Shown are: a) Tree Level process, b) (Strong) Penguin Loop Corrections [20].*

$S^{+-} = -\sqrt{1-(C^{+-})^2}\sin(2\alpha)$. Thus, we define the quantity $\alpha_{eff} \simeq \alpha$ by

$$S^{+-} = -\sqrt{1-(C^{+-})^2}\sin(2\alpha_{eff}). \tag{2.51}$$

Analysis of the CP asymmetries and decay rates for $B^0, \overline{B}^0 \to \rho^+\rho^-$ decays should yield its value.

2.4.3 $B^0 \to \rho^0\rho^0$ Decays

The $\rho^0\rho^0$ state is a CP eigenstate as well. It is produced from the $B^0, \overline{B}^0$ mesons via Tree Level and Penguin processes shown in Figs. 2.10, 2.11. Unlike the case of $\rho^+\rho^-$, the Tree Level decays are color suppressed and the process is not useful in measuring α directly. However, since the Penguins are expected to make a significant contribution ($\sim 20\%$), the decay allows us to obtain the limit on Penguin Contributions, parametrized as

$$\Delta\alpha = \alpha - \alpha_{eff}. \tag{2.52}$$

The Strong Penguins provide the largest corrections to the amplitudes, but their impact is more easily accounted for in the context of isospin analysis. Specifically, when the Electroweak Penguins are neglected $|A^{+0}| = |\bar{A}^{-0}|$. The two isospin triangles (Fig. 2.8) can then be superimposed, as shown in Fig. 2.12. Note, that now

$$S^{+-,00} = -\sqrt{1-(C^{+-,00})^2}\sin(2\alpha + \kappa^{+-,00}), \tag{2.53}$$

while we still retain the four-fold ambiguity with $\kappa^{+-} = \pm(\phi \pm \bar{\phi})$ for positive ϕ,$\bar{\phi}$.

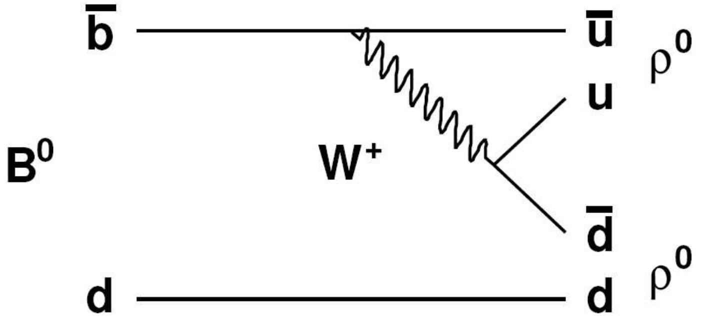

Figure 2.10: *Tree Level diagram for $B \to \rho^0\rho^0$ decays.*

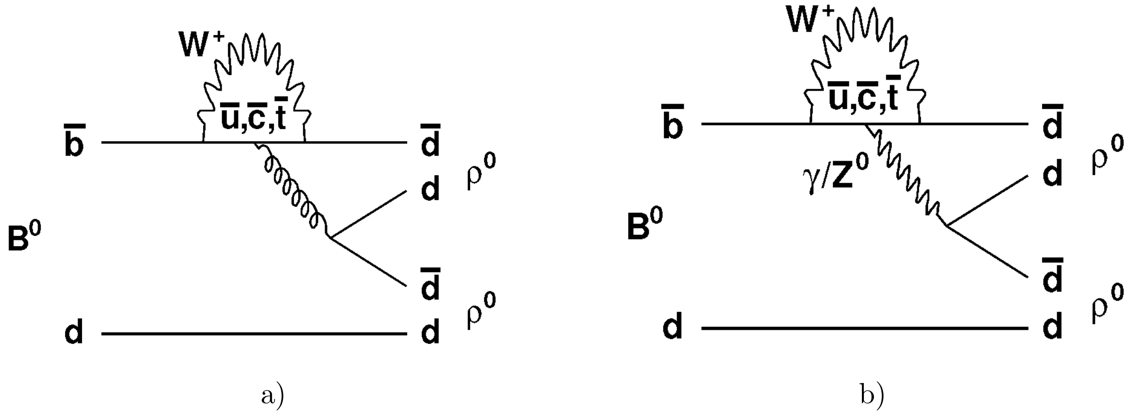

a)

b)

Figure 2.11: *a) Strong and b) Electroweak Penguin contributions to the $B \to \rho^0\rho^0$ amplitudes.*

2.4.4 Measuring α

While in theory it is possible to obtain α from the relation between S and C, we wish to use all of the available information in order to obtain the strongest possible constraint. Namely, there are 7 parameters: the three branching ratios $B_L^{+-}, B_L^{\pm 0}, B_L^{00}$ for the decays into longitudinal final states; and the four corresponding CP parameters $S_L^{+-}, C_L^{+-}, S_L^{00}, C_L^{00}$; which can be expressed in terms of the four amplitudes $A_0, A_2, \bar{A}_0, \bar{A}_2$.

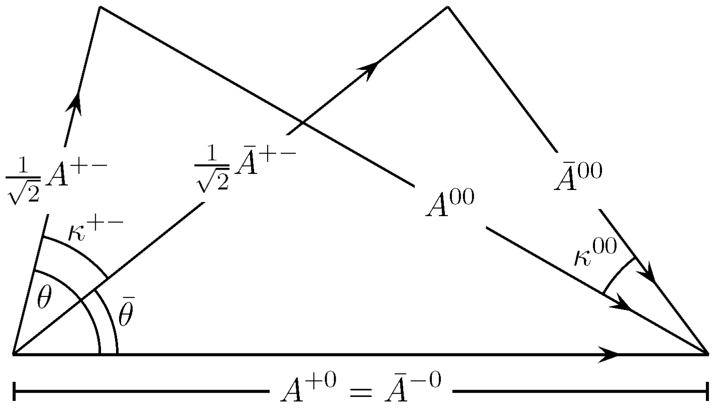

Figure 2.12: *Isospin triangles for* $B^0 \to \rho\rho$ *and* $\overline{B}^0 \to \rho\rho$ *aligned with each other for* $|A^{+0}| = |\bar{A}^{-0}|$.

Thus, we form a χ^2 measure:

$$\chi^2(\alpha) = \sum_{i=+-,00} \left(\frac{(\tilde{S}^i - \sqrt{1-(C^i)^2}\sin(2\alpha+\kappa^i))^2}{\sigma^2(\tilde{S}^i)} + \frac{(\tilde{C}^i - C^i)^2}{\sigma^2(\tilde{C}^i)} \right) + \tag{2.54}$$

$$+ \sum_{i=+-,\pm0,00} \left(\frac{(\tilde{B}^i_L - B^i_L)^2}{\sigma^2(\tilde{B}^i_L)} \right) + \textit{correlation terms},$$

where we employed the relation 2.53 between S and C and used $\tilde{X}$ to denote the measured value for X. In order to determine α, we perform a scan over all values, while minimizing χ^2 with respect to the four amplitudes (or equivalently $|z|, |\bar{z}|, \theta, \bar{\theta}$ defined in Eqs. (2.49), (2.50)). In the end we are able to measure α and restrict $\Delta\alpha$ at the desired Confidence Level, as discussed in Section 4.11.1.

Chapter 3

The Experiment

In this section we provide an overview of the *BABAR* experiment and how it is used to measure properties of $B \rightarrow \rho^0\rho^0$ decays. As such, we discuss the specific components involved starting with the SLAC (Stanford Linear Accelerator) complex and proceed to describe each of the *BABAR* subsystems. Particular attention is paid to how they are relevant to reconstructing the $\pi^+\pi^-\pi^+\pi^-$ final state, locating the decay vertices and determining the flavor of the conjugate B.

3.1 Decay Overview

Out of the 465×10^6 $\Upsilon(4S) \rightarrow B\overline{B}$ events we extract ~ 100 $B^0, \overline{B}^0 \rightarrow \rho^0\rho^0 \rightarrow \pi^+\pi^-\pi^+\pi^-$ decays and examine their CP properties. A representation of such a decay, with a focus on components essential for reconstruction, is shown in Fig. 3.1. The detector is setup to collect information, which enables us to:

a) Identify the pions composing the $\pi^+\pi^-\pi^+\pi^-$ final state and measure the corre-

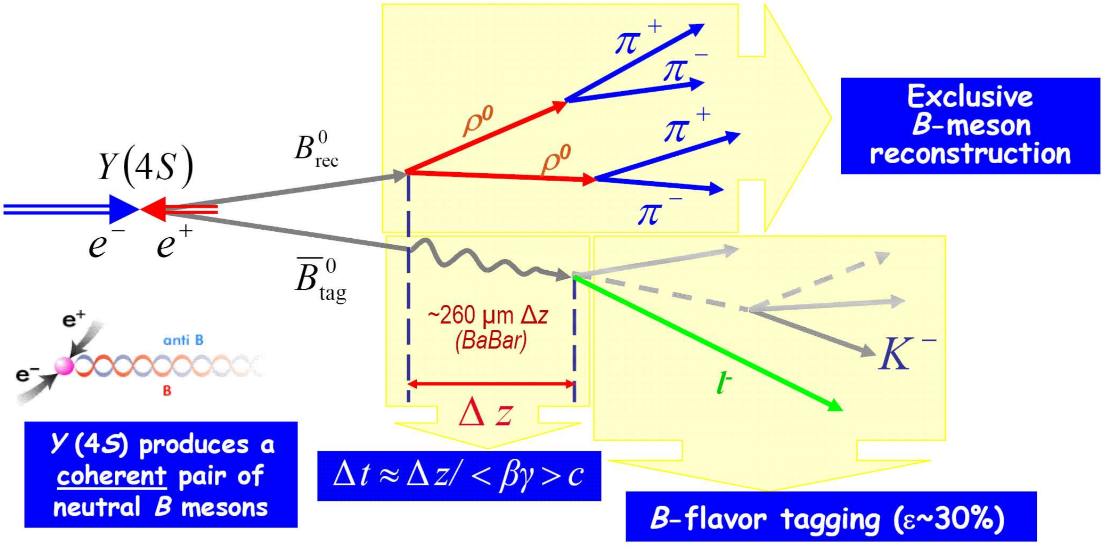

Figure 3.1: *A representation of* $\Upsilon(4S) \rightarrow B^0\overline{B}^0$ *with* $B^0 \rightarrow \rho^0\rho^0$ *decay along with the components essential for reconstruction at BABAR.*

sponding momenta. Note that this knowledge allows us to effectively identify the ρ^0 resonances by examining the reconstructed masses of the $\pi^+\pi^-$ pairs (in the mass range of $0.55 < m_{\pi\pi} < 1.05$ GeV).

b) Measure the B^0_{rec} (*i.e.* the B^0, which decays into $\rho^0\rho^0$) decay vertex location from the charged pion tracks.

c) Measure the decay vertex location for the conjugate ($\overline{B}^0_{tag}$) from its byproducts.

d) Identify these byproducts. Then use the information to determine whether the conjugate was a B^0 or a $\overline{B}^0$ (*e.g.* a negatively charged lepton indicates that it was a $\overline{B}^0$).

Based on the location of the vertices we extract the time between the decays of the two B's ($\Delta t \approx \Delta z/\beta\gamma c$). We also recognize that the wave-function for the B^0 is a linear combination of B^0 and $\overline{B}^0$ states, where the oscillations between the two occur with a frequency of $\Delta m_B/2$, Eq. (2.36). Thus the b-flavor information for the conjugate (at the time of its decay) can be used to compute the probability of it being a B^0 (or $\overline{B}^0$) when B^0_{rec} decayed into two ρ^0's. Because $\Upsilon(4S)$ produces a coherent $B\overline{B}$ state, B^0_{rec} has the opposite flavor of $\overline{B}^0_{tag}$. By combining the above information, we are able to measure the Branching Fraction and the CP coefficients for the decay.

3.2 The Collider

In addition to *BABAR* the experiment consists of the Linear Accelerator (linac) and the PEP-II (Positron-Electron Project II) storage rings, shown in Fig. 3.2. The electrons are produced at the main injector site and accelerated to the energy of 9 GeV. During the process some are diverted toward the positron source, where the e^+ beam is created and boosted up to 3.1 GeV by the linac. Here, a series of klystrons generate the microwaves, while the waveguides feed them into the accelerator's copper structure, Fig. 3.3. The microwaves create oscillating electric fields, which in turn accelerate e^+,e^- bunches comprising the beams. The linac is then utilized as an injector for PEP-II.

The Positron-Electron Project Upgrade (PEP-II) is described in detail in the Conceptual Design Report [41]. The function of its storage rings is to store and deliver the beams to *BABAR*. Specifically, PEP-II consists of the High Energy Storage Ring (HER), which contains the 9 GeV electrons, and a Low Energy Storage Ring (LER), which contains the 3.1 GeV positrons. The main components are:

- Magnets, which guide and focus the beams in the storage rings.

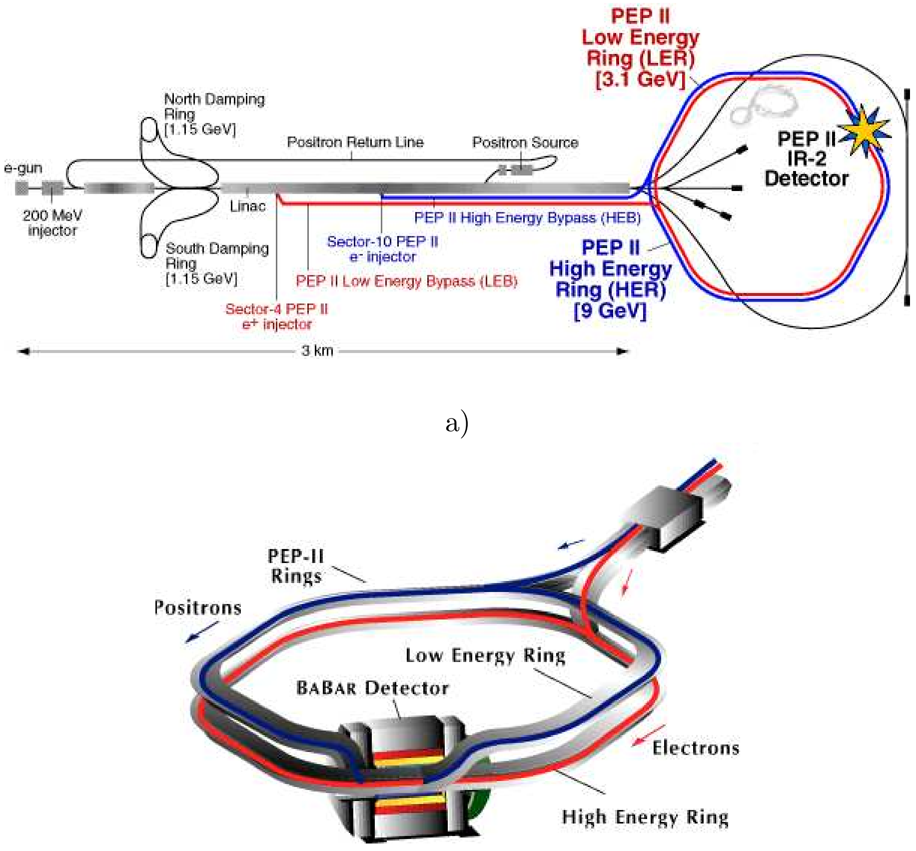

a)

b)

Figure 3.2: *a) SLAC and b) the PEP-II storage ring [39].*

- The vacuum system, which is designed to maintain a low background gas pressure in spite of high thermal loads due synchrotron-radiation.

- RF cavities, which compensate for the synchrotron energy loss by accelerating the beams.

- Electronics and support equipment, such as power supplies, control system, *etc.*

Overall, PEP-II was required to achieve [41]:

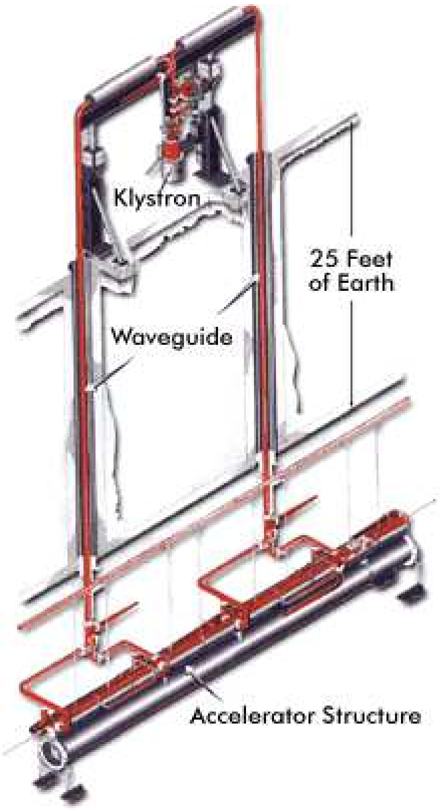

Figure 3.3: *Representation of a section of the linac [40].*

- Beam energies of 9 GeV (HER) and 3.1 GeV (LER).
- Beam currents of 0.99 A (HER) and 2.14 A (LER).
- Bunch length of 1 cm.
- Beam emittances of approximately 50 $\mathrm{nm} \cdot \mathrm{rad}$ (HER) and 66 $\mathrm{nm} \cdot \mathrm{rad}$ (LER).
- Beam energy spread of $\sigma_E/E \leq 1 \times 10^{-3}$.

The data taking began in 1999 and ended in April 2008, with Runs 1-6 dedicated to doing (mainly) B-physics on the $\Upsilon(4S)$ resonance, while Run 7 focused on searches for new physics at $\Upsilon(3S)$, $\Upsilon(2S)$ energies. The Integrated Luminosity is shown in Fig. 3.4.

3.3 *BaBar*

The primary goal of the *BABAR* detector is to verify the Standard Model picture of CP violation (described in Section 2.2) by examining B-meson decays. The detector is designed to allow us to extract CP asymmetries for a variety of processes (with an overview is given in Appendix A), including $B \to \rho^0\rho^0$ and use the information to constrain the CKM parameters, while verifying the model's consistency. As was already mentioned, PEP-II is

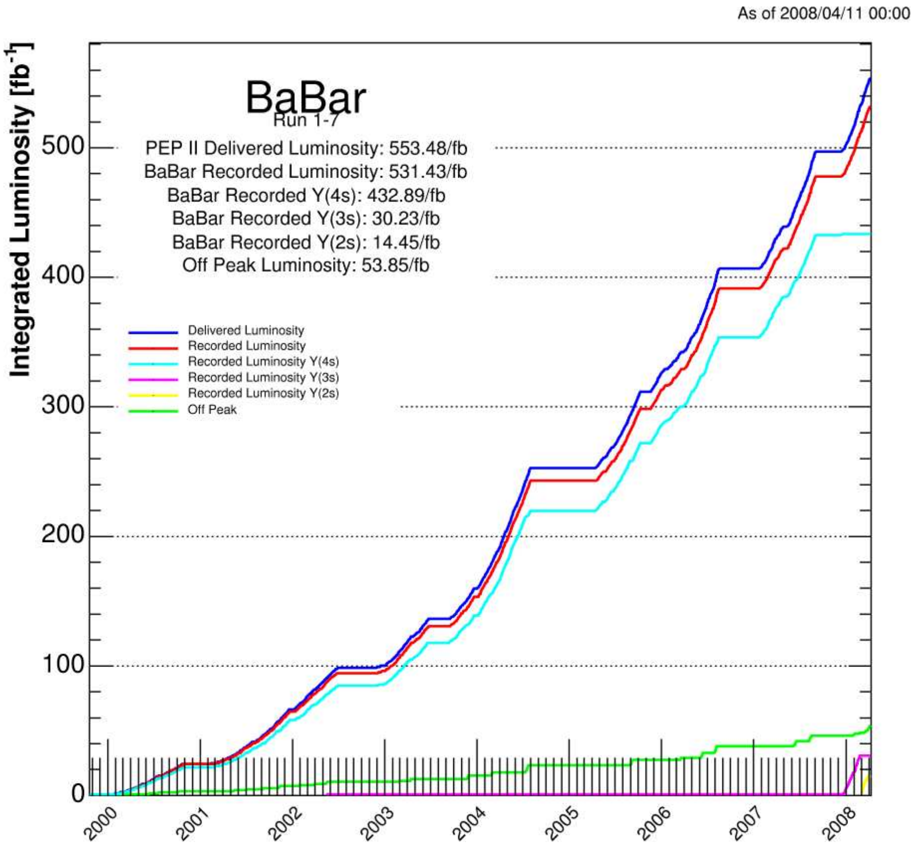

Figure 3.4: *Integrated Luminosity recorded by BABAR [38].*

an asymmetric B factory, where collisions between 9 GeV e^- and 3.1 GeV e^+ take place. The energy of the beams is chosen to be on $\Upsilon(4S)$ resonance, *i.e.* $e^+e^- \to \Upsilon(4S) \to B\overline{B}$ with $\sqrt{s} = 10.58$ GeV. While in the center of mass frame the B mesons are essentially at rest, the fact that the energies of the e^+ and e^- beams are not equal implies that the mesons will be moving (in the e^- direction) in the lab frame. As a result we can measure their decay lengths and compute the corresponding decay times.

In addition to determining the proper time of the B^0 decay, it is necessary to fully reconstruct the exclusive final state as well as detect the b flavor of the conjugate B^0 (*a.k.a.* tagging) in order to observe the CP asymmetries. When constructing the detector, the component subsystems were designed with these goals in mind, as described in detail in the Technical Design Report [37] (with updates listed in Section 3.2 of the Physics Book [6]) and shown Fig. 3.5. In our analysis we examine the data gathered by *BABAR* on the $\Upsilon(4S)$ resonance ($\sqrt{s} \simeq \mathrm{M}_{\Upsilon(4S)}$), denoted as Run 1-6 in Fig. 3.4. Here, the main features and advantages (of running on the resonance in an e^+e^- environment) are:

- A high signal-to-background ratio ($\sigma_{b\bar{b}}/\sigma_{TOT} \simeq 0.28$).
- Beam optics elements placed very closely to the interaction region in order to achieve high luminosities.
- Clean events (mean charge multiplicity ~ 11) with low interaction rates (physics rate ~ 10 Hz).
- Absence of fragmentation products, due to annihilation of e^+e^- pairs.
- Knowledge of both the exact 4-momentum of the $B\overline{B}$ system as well as of the mo-

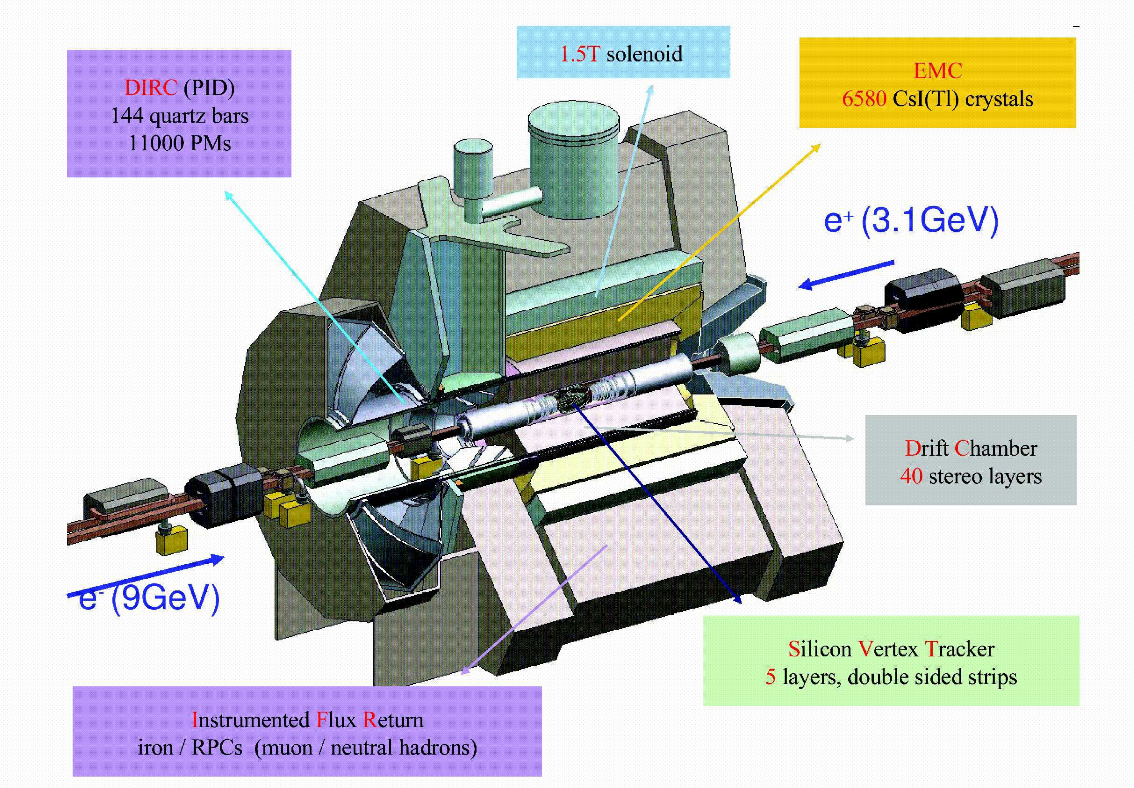

Figure 3.5: *The BABAR Detector.*

mentum magnitudes for each of the B's in the center-of-mass (COM) frame.

- Asymmetric detector setup designed to maximize acceptance in the COM system.
- Excellent vertex resolution in the z-direction (*i.e.* the direction of travel of the B mesons), with a focus on discrimination of b quark vertices as well as minimizing multiple scattering.
- Ability to do tracking over a wide range of momenta ($\sim 50 - 4000$ MeV).
- Capacity to detect neutrals (photons, π^0's) over a wide range as well as effectively identify and discriminate between the various types of particles in the detector.

In addition, the machine was able to operate at a previously unprecedented luminosity ($\sim 10^{34}$ cm^{-2}s^{-1}) with the integrated luminosity shown in Fig. 3.4.

3.4 Subsystems

When making the above measurements, the Silicon Vertex Tracker (SVT) is used to determine the vertex location (*a.k.a.* vertexing), the Drift Chamber (DCH) is used measure the track curvature in the magnetic field in order to evaluate the pion momenta, while all of the *BABAR* subsystems are employed in Particle Identification (PID).

3.4.1 Silicon Vertex Tracker

The main objective of *BABAR*, as well as our analysis, is to measure CP asymmetries by observing B decays. Thus, it is necessary to reconstruct the B decay vertices as precisely as possible. As a result, we place the detector components as closely to the interaction point as possible. Specifically, in order to do CP violation physics, it is necessary to measure the separation (Δz) between the two vertices with a precision of better than one half the mean separation (*i.e.* $\sim 250\mu$m) or single vertex separation better than 80μm at PEP-II [42]. This goal is readily achieved by a silicon micro-strip detector, with the resolution as a function of angle shown in Fig. 3.6. The cross-sectional views of the Silicon Vertex Tracker are shown in Fig. 3.7. Its main features are [37]:

- An asymmetric design which provides us with maximum forward coverage by placing support components in the backward region. The SVT effectively covers the polar angles of 20.1° to 150.2°.

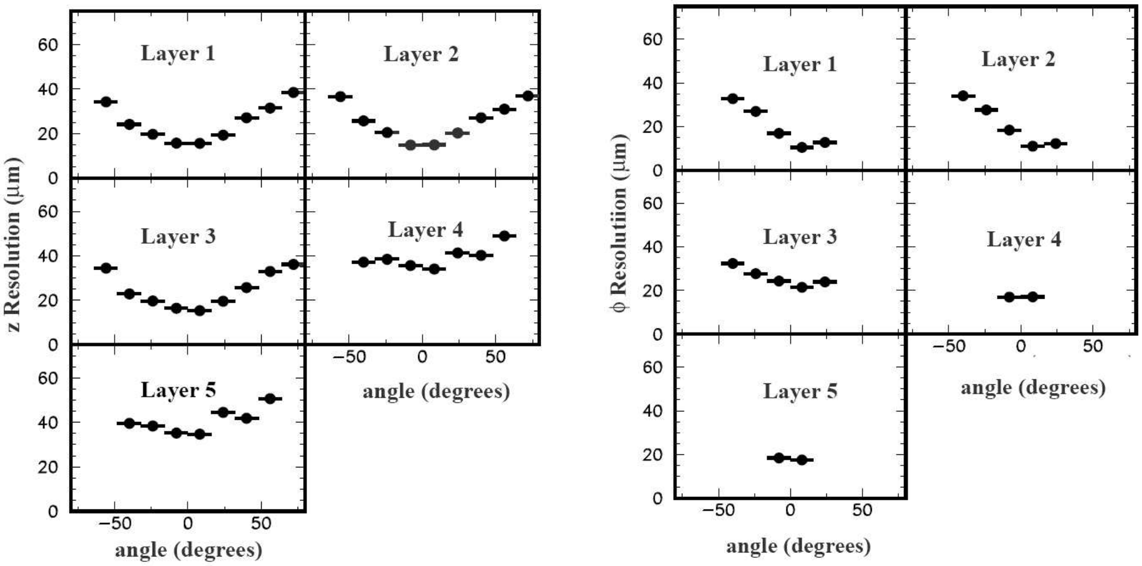

a) b)

Figure 3.6: *SVT hit resolution (for each of the five layers) as a function of the track incidence angle in the: a) z view, b) ϕ view [45].*

- Five concentric cylindrical layers of double-sided silicon strip detectors, AC coupled with plysilicon bias resistors [43].
- Strips oriented in both the ϕ (circular) and z (beam) directions in order to ensure a more complete vertex reconstruction in 3D.
- A total of 340 silicon detectors covering an area of 0.94 m^2 with $\sim 150,000$ readout channels.

In addition to reconstructing B^0 vertices, the SVT is used for reconstruction of charged tracks. It is the only tracking device for particles with transverse momenta less than 100 MeV/c, which do not reach the Drift Chamber. It useful in gathering track information up to $p_t \simeq$180 MeV/c, when DCH reaches its full efficiency. Additionally, the SVT provides theta angle for DIRC θ_c, Section 3.4.5; and (as discussed in Appendix B) we have worked

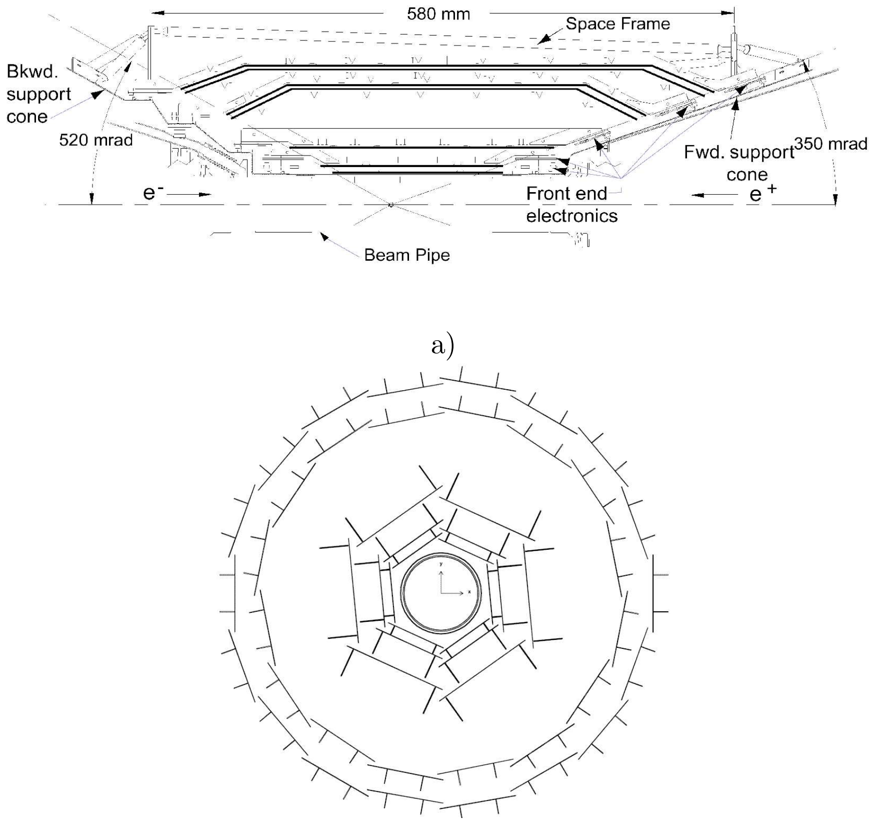

a)

b)

Figure 3.7: *Cross-sectional view of the SVT: a) Parallel to the beam axis b) Perpendicular to the beam axis [37].*

on obtaining momentum (and consequently PID) information from the SVT hits alone.

3.4.2 The Drift Chamber

The Drift Chamber is the main tracking device in *BABAR*. In our analysis we use it to measure the trajectories for each of the pions in the $\pi^+\pi^-\pi^+\pi^-$ final state. A side view of the detector is shown in Fig. 3.8.

It ensures high reconstruction efficiency (for tracks with $p_t > 100$ MeV/c) by

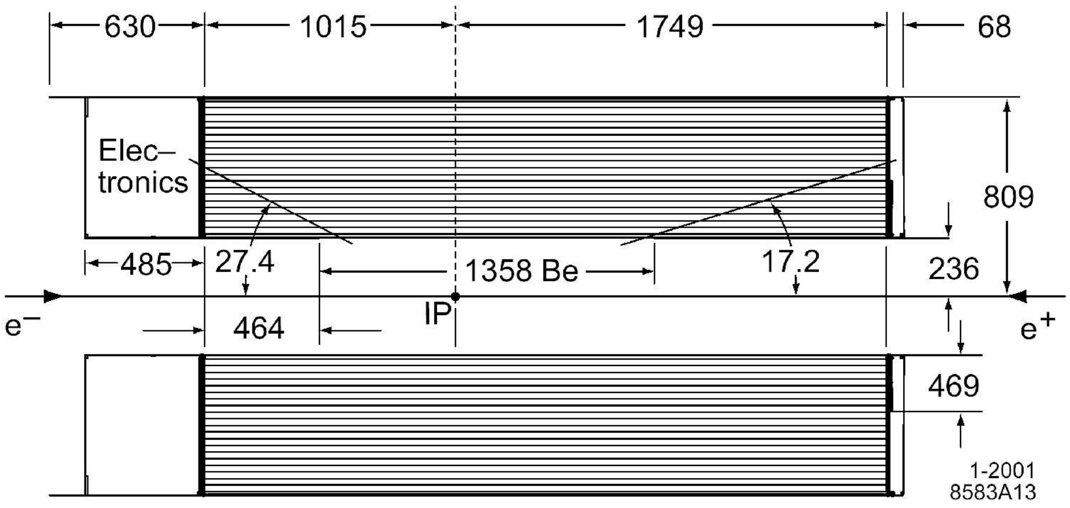

Figure 3.8: *Longitudinal view of the DCH [37].*

providing up to 40 coordinate measurements per track. The main features are [37]:

- It is a 280 cm long cylinder with an inner and outer radii of 23.6 cm and 80.9 cm, respectively, along with aluminum end-plates.
- An 80 : 20 Helium:Isobutane gas mixture filling the cylinder.
- 40 layers of drift cells (arranged in 10 superlayers with 4 layers each), as shown in Fig. 3.9(a).
- Drift cells made up of 120 μm or 80 μm gold-plated aluminum field wires (which generate the electric fields) and 20 μm gold-plated tungsten-rhenium sense wires (which pickup the charged particles), as shown in Fig. 3.9(b).

The DCH is placed in a 1.5T solenoid magnetic field. This field remains constant (within a few percent) across the tracking volume, which simplifies track finding and fitting. Overall,

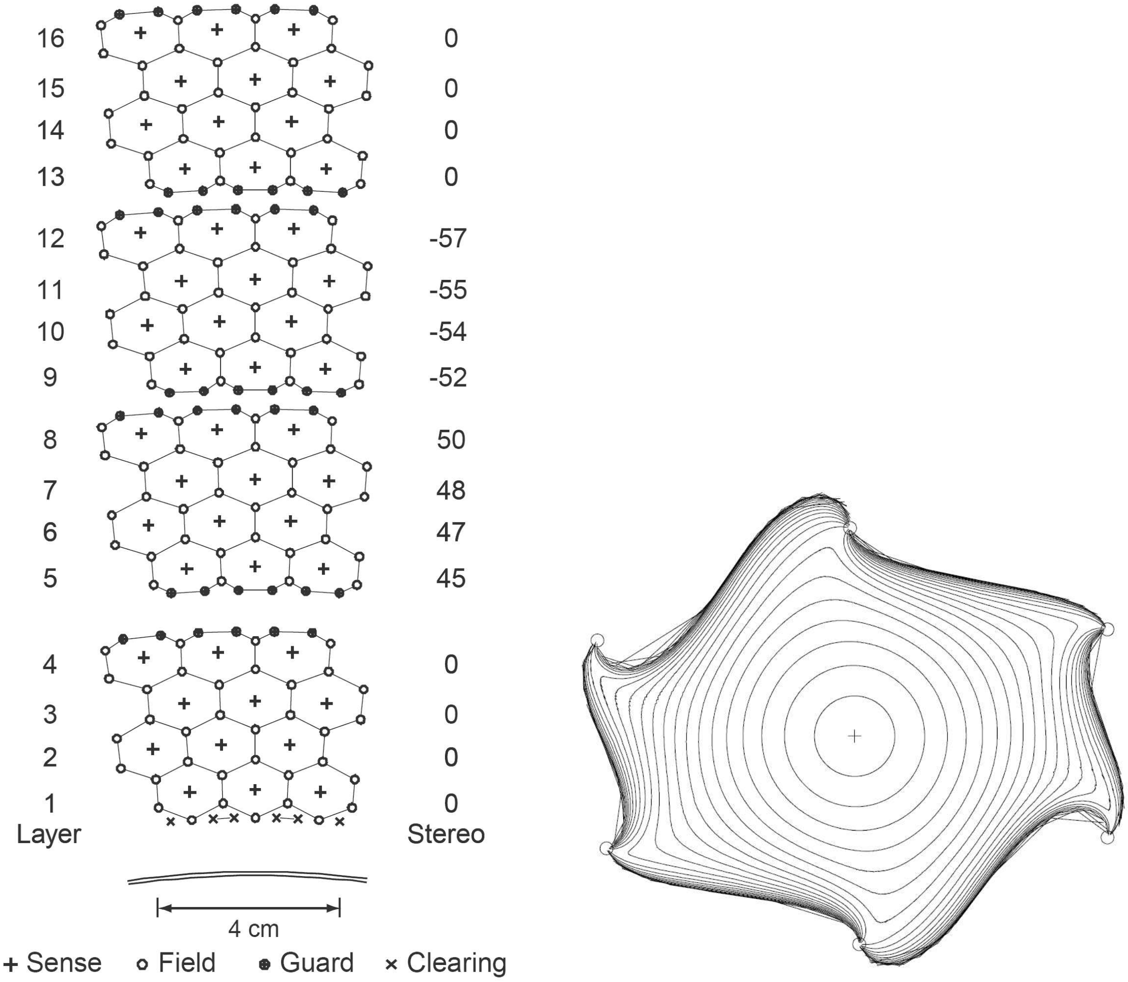

(a) (b)

Figure 3.9: *a) Cell layout in the Drift Chamber (for the four innermost superlayers) [45]. b)Typical DCH cell. The lines are* 50 ns *isochrones (i.e. it takes an ionized particle* 50 ns *to travel between the two of them) [37].*

the Drift Chamber has met the performance goals of providing a spatial resolution better than 140 μm (averaged over a typical cell) and supplying PID (from ionization energy loss measurements) for low momentum tracks with a resolution of 7% [37].

3.4.3 Solenoid Magnet

In order to measure particle momenta (as well as charges) it is necessary to have curved tracks and obtain the kinematic information from the corresponding curvature. The *BABAR* magnet system creates the required field in SVT and DCH. Its main features are [37], [45]:

- A superconducting solenoid placed outside the Electromagnetic Calorimeter (Fig. 3.5), which consists of magnetic coils along with the necessary cryostat assembly.
- A series of dipole and quadrapole magnets located inside the solenoid. Their function is to maintain the large field in the longitudinal (1.5T) as well as limit the fluctuations in the radial (< 0.25T) directions, while minimizing disturbance of operation of the PEP-II beam elements.
- An offset of the central point (by 370mm) in the e^- direction intended to optimize detector acceptance at unequal beam energies.
- Functionality as a hadron absorber (assisting with hadron-muon separation).
- Serving as structural support for inner detector components as well as a design which allows it to survive accelerations due to an earthquake without serious damage.
- A detailed mapping of the magnetic field (with a precision of 0.2mT) [46].

We maintain a relatively constant field over the tracking volume (Fig. 3.10). Overall, the system has performed without problems since its commissioning.

3.4.4 The Electromagnetic Calorimeter (EMC)

The EMC is designed to measure the energy and position of e^-, γ, π^0 and η's. Specifically, as these particles pass through it they generate electromagnetic showers, which are then absorbed by the CsI(TI) crystals. The corresponding energy and angular resolution are measured to high efficiency.

The detector is shown in Fig. 3.11. It consists of the cylindrical barrel (5,760 crystals arranged in 48 rings) plus the forward endcap (820 crystals in 8 rings), and covers the polar angle of 15.8^o to 141.8^o [45]. The supports and electronics are attached at the outer radius with only a thin gas seal at the front, in order to minimize pre-showering. Furthermore, the CsI(TI) crystals have been shaped and arranged in order to minimize the effects of shower leakage, with a typical setup shown in Fig. 3.12.

The energy and angular resolutions are parametrized as [45]:

$$\frac{\sigma_E}{E} = aE^{1/4} \oplus b, \tag{3.1}$$

$$\sigma_\theta = \sigma_\phi = cE^{1/2} + d,$$

where $\oplus$ denotes the quadrature sum, E is the energy measured in GeV, σ refers to the rms error and a, b, c, d are parametrization constants used to describes detector effects such as fluctuations in photon statistics, non-uniformity in light collection at varying energies, uncertainties in calibrations, *etc.* The resolution for the EMC is shown in Fig. 3.13 with the parameters fitted to be $a = (2.32 \pm 0.30)\%$, $b = (1.85 \pm 0.12)\%$, $c = (3.87 \pm 0.07)$ mrad, $d = (0.00 \pm 0.04)$ mrad.

3.4.5 Detector of Internally Reflected Cerenkov Radiation (DIRC)

The DIRC is used in PID, primarily to distinguish between pions, kaons and protons (and is used for electrons, as well). The detector measures track velocity based on the Cherenkov angle. That information is then combined with momentum measurements (from other *BABAR* components), which allows us to extract the particle mass thus identifying its type.

More specifically, when a charged particle passes through an object with a velocity higher than the speed of light in the material, it produces Cherenkov radiation. The corresponding angle can be related to the index of refraction of the object ($n = 1.473$ for fused silica) by

$$\cos\theta_c = 1/n\beta, \tag{3.2}$$

where $\beta = v/c$. In Fig. 3.14 we provide a schematic view of how radiation is generated along the track trajectory, transported through the silicon bar via total internal reflection (note that the angle is preserved upon each reflection), travels through the purified water and is then picked up by the Photomultiplier Tubes (PMTs).

We use fused, synthetic silica bars as radiators (as well as light pipes) in the DIRC. They are placed in 12 bar boxes (12 bars per box), as shown in Fig. 3.15(b). A schematic view of the detector is given in Fig. 3.15(a). Furthermore, DIRC is designed to measure both the position as well as the arrival time of the PMT signals, which enables us to deal with ambiguities in the signal association and high background rates. Overall, the performance of the detector is close to expectations [47] with sample resolutions shown in Fig. 3.16.

3.4.6 Instrumented Flux Return (IFR)

The IFR is designed for high efficiency muon identification and for detection of neutral hadrons, which were able to penetrate the inner subdetectors in *BABAR* (in addition, it serves as a flux return for the magnetic solenoid). It (Fig. 3.17(a)) uses the steel flux return of the magnet as a muon filter and hadron absorber. Single gap resistive plate chambers (RPCs) are used as detectors Fig. 3.17(b) [48]. They are arranged in 19 layers along the barrel, 18 layers in the endcaps, as well as two layers between the EMC and the magnet cryostat (in order to detect particles exiting the EMC) [45]. The RPCs rely on capacitive readout strips to detect streamers from ionizing particles.

Overall, the IFR was constructed with large solid angle coverage, good efficiency and high background rejection rates (for muon momenta down to 1 GeV/c) in mind. The detector efficiency, along with the $\pi^{\pm}$ misidentification probability, is shown in Fig. 3.18. Over time the IFR has undergone a series of modifications where the rapidly aging RPCs were either upgraded or replaced with Limited Streamer Tubes in order to avoid the loss of as well as improve the efficiency [44].

3.5 Data Acquisition

In this section we describe how the readings gathered by the above detectors are converted into data on disk [45]. The general overview is provided in Fig. 3.19. As can be seen, the procedure begins with Front-End Electronics (FEE) which processes and digitizes the analog signals collected by *BABAR*. They are sent to the Level 1 (L1) trigger system, which interprets the incoming detector signals, reduces beam-induced background down to an acceptable level and sends the event information to Level 3 (L3) trigger. It in turn selects the events of interest and places them in the Intermediate Event Store.

Specifically, the L1 system consists of three subsections. The Trigger Processor collects summary data on the position and energy of the particles from the DCH, EMC and IFR triggers. It then processes the data to form specific triggers. They are then delivered to the Fast Control and Timing System (FCTS). The FCTS can mask or prescale the triggers and if a valid one remains, an L1 accept command is issued to send the event to L3. These actions are performed by L1 hardware, which is housed in five 9U VME crates. The resulting output rate is ≤ 2 kHz with a maximum response latency (for a given collision) of 12 μs.

This output is then processed by the L3 software, which performs the second stage rate reduction, as well as flags special events (needed for luminosity determination, diagnostics and calibration). L3 is a set of event selection filters, which have full access to L1 data. They function by refining and augmenting the selection methods (*e.g.* improving DCH vertex resolution, providing for greater background rejection in the EMC, *etc.*). The system runs within the Online Event Processing framework, where its output rate is typically less than 120 Hz, which prevents overloads to the downstream storage and processing capacity. A typical event display is shown in Fig. 3.20. While *BABAR* was operational, both L1 and L3 systems have met their original design goal of 99% triggering efficiencies at 3×10^{33} cm^{-2}s^{-1} luminosity. In the end, the Data Acquisition process produced events required for our analysis of $B^0 \to \rho^0\rho^0$ decays.

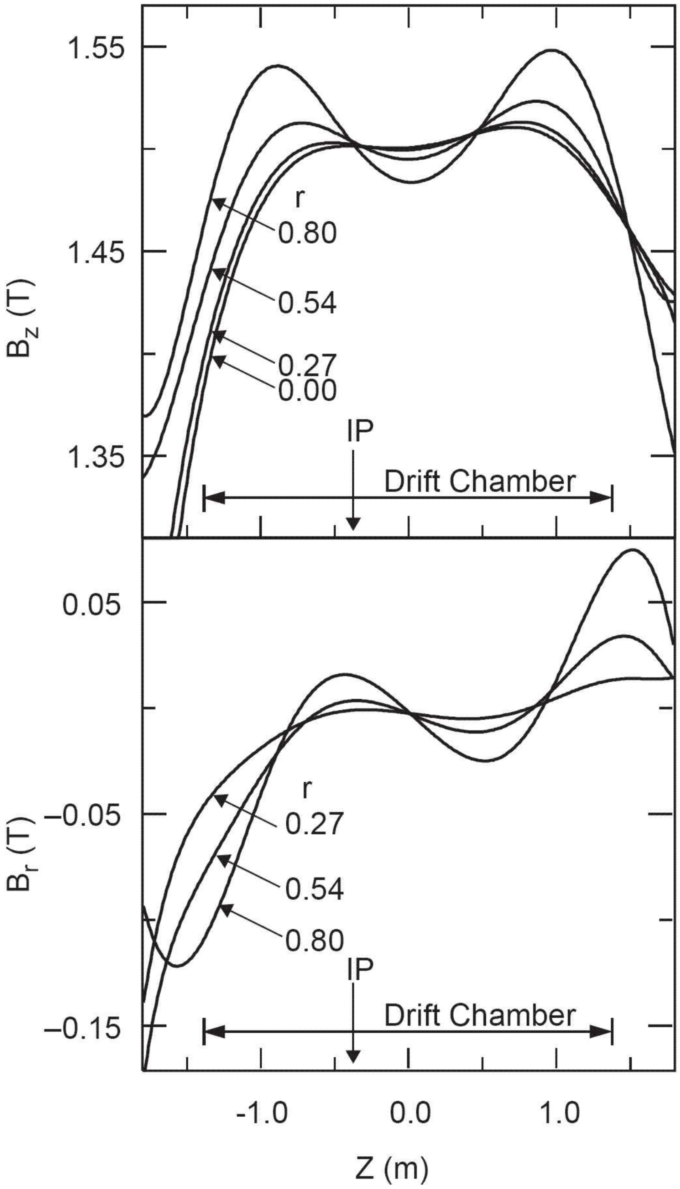

Figure 3.10: *The magnetic field in the longitudinal (B_z) and radial (B_r) directions as a function of z for various distances (r) from the beam [45]. The span of the Drift Chamber and the interaction point (IP) are denoted.*

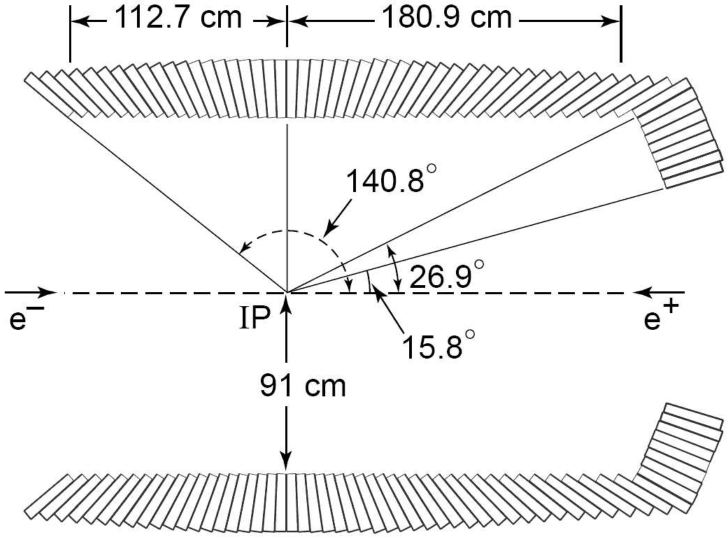

Figure 3.11: *A sideview of the Electromagnetic Calorimeter [37].*

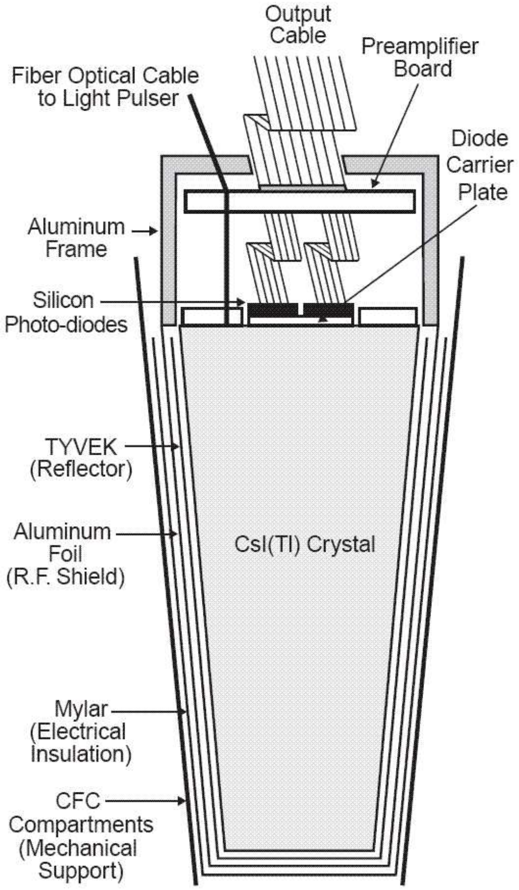

Figure 3.12: *A schematic view of the wrapped CSI(TI) EMC crystal for the front-end readout package mounted on the rear face [45].*

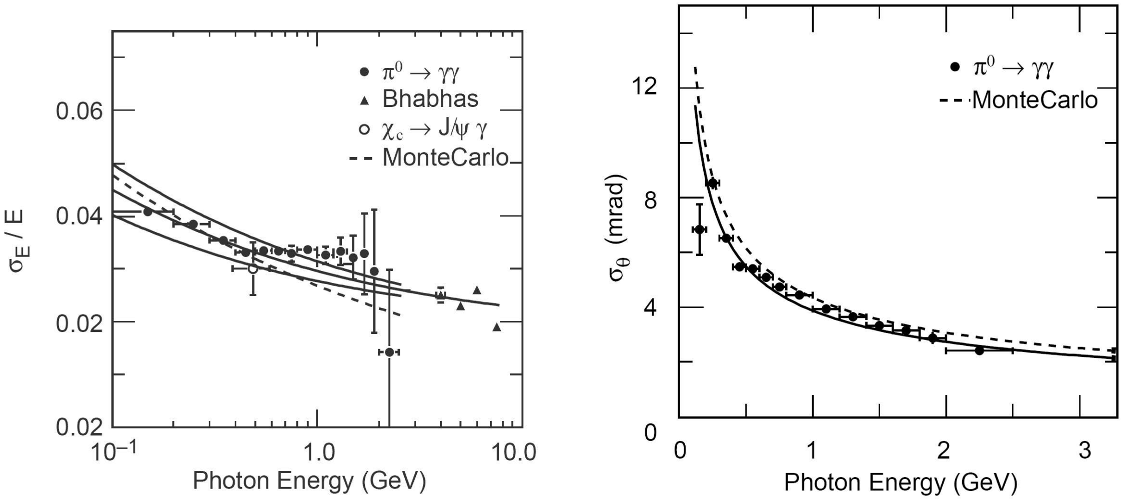

a) b)

Figure 3.13: *a) Energy resolution from various processes and b) angular resolution from (photons from)* π^0 *decays for the EMC [45].*

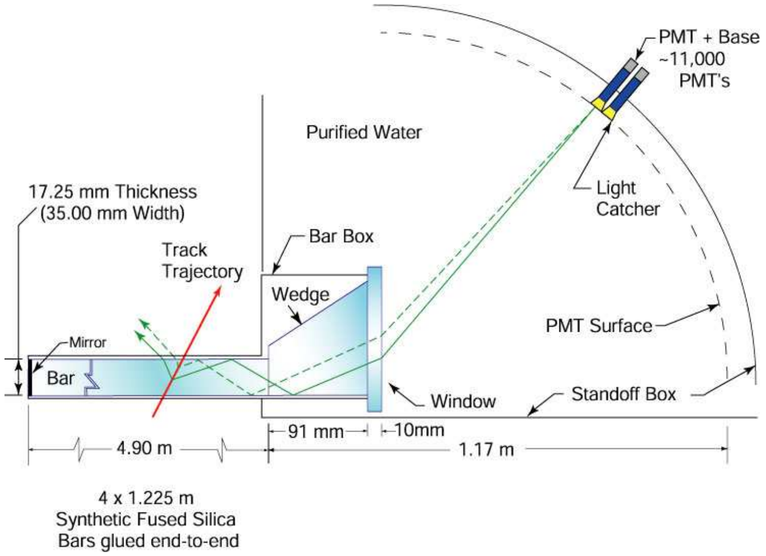

Figure 3.14: *A schematic view of the DIRC [44]*

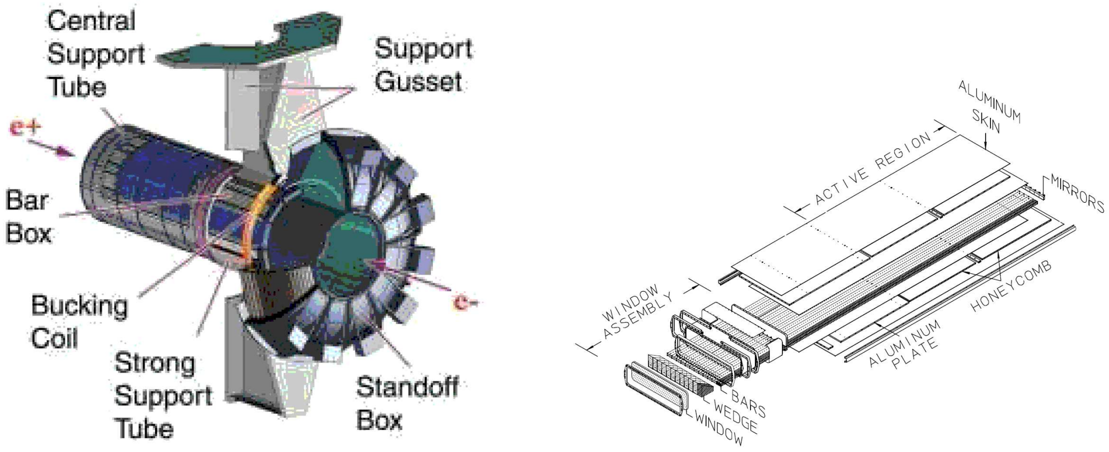

(a) (b)

Figure 3.15: *Schematic views of a) DIRC, b) component barboxes [45].*

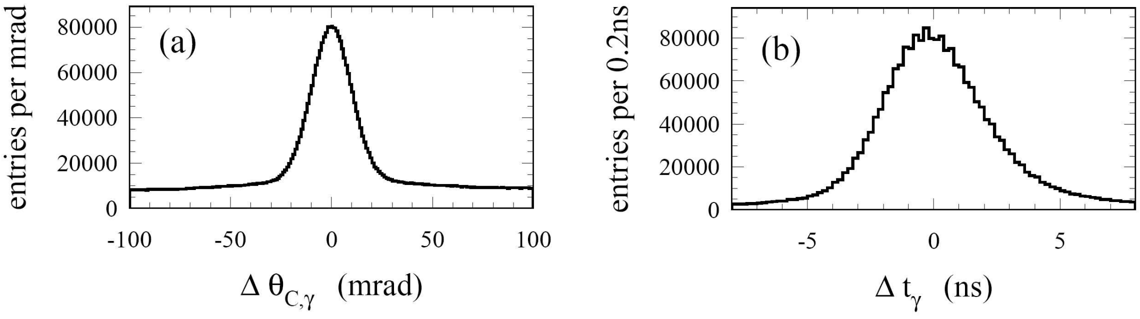

a) b)

Figure 3.16: *DIRC resolution: a) the difference between measured and expected Cherenkov angle for single photons b) measured and expected photon arrival time (for single muons in* $\mu^+\mu^-$ *events) [45].*

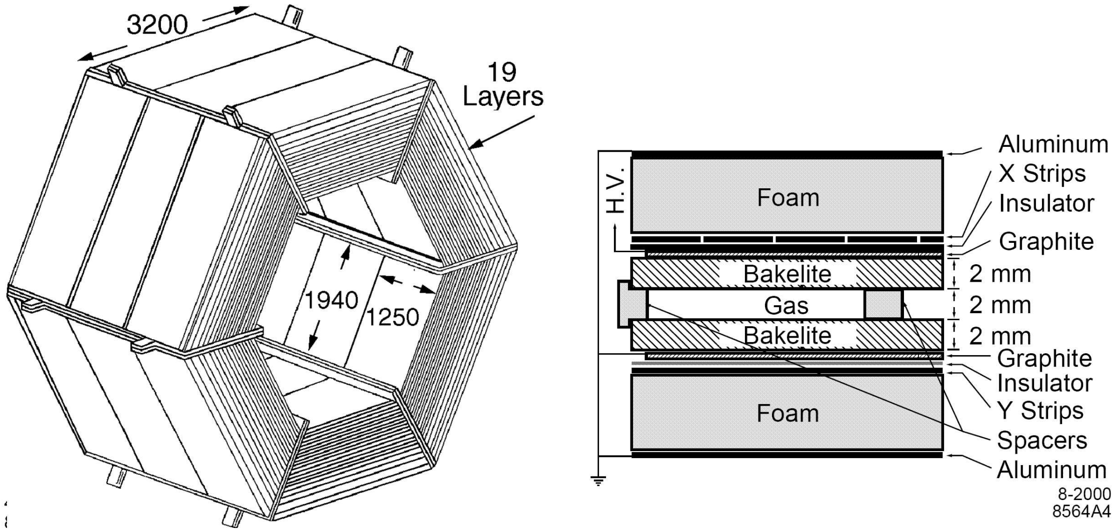

(a) (b)

Figure 3.17: *OFT: a) barrel, b) RPC cross section [45].*

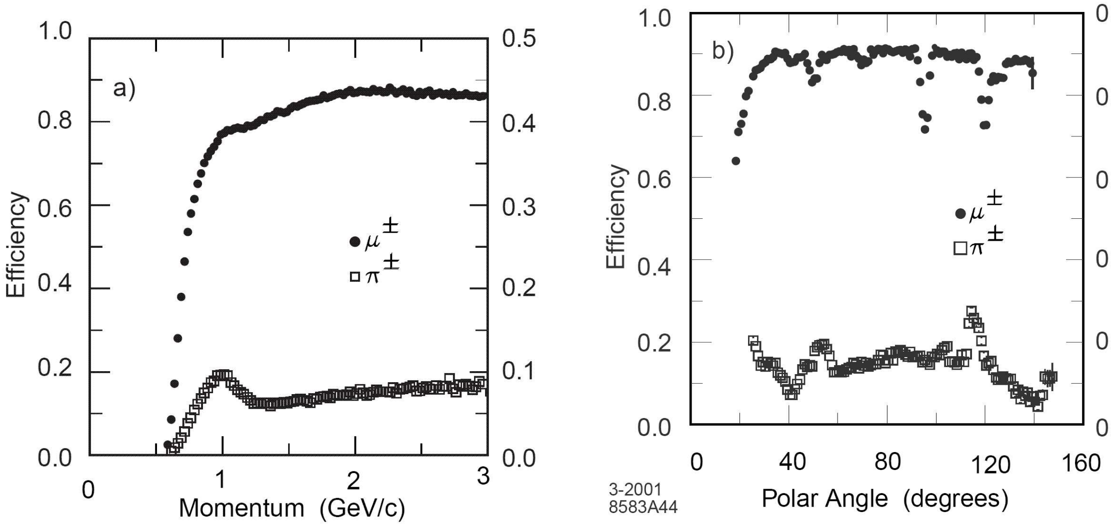

a) b)

Figure 3.18: *IFR muon efficiency and pion misidentification probability as a function of: a) particle momentum b) polar angle (in the laboratory frame) [45].*

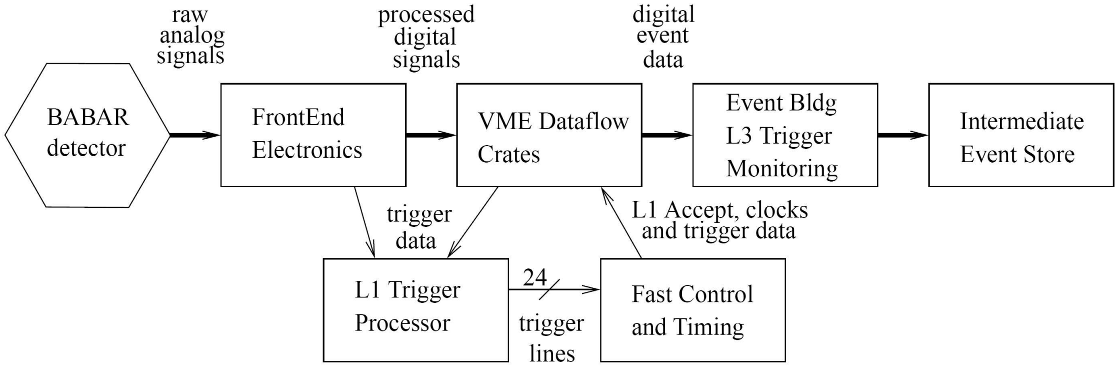

Figure 3.19: *A schematic of the Data Acquisition process in BABAR [45].*

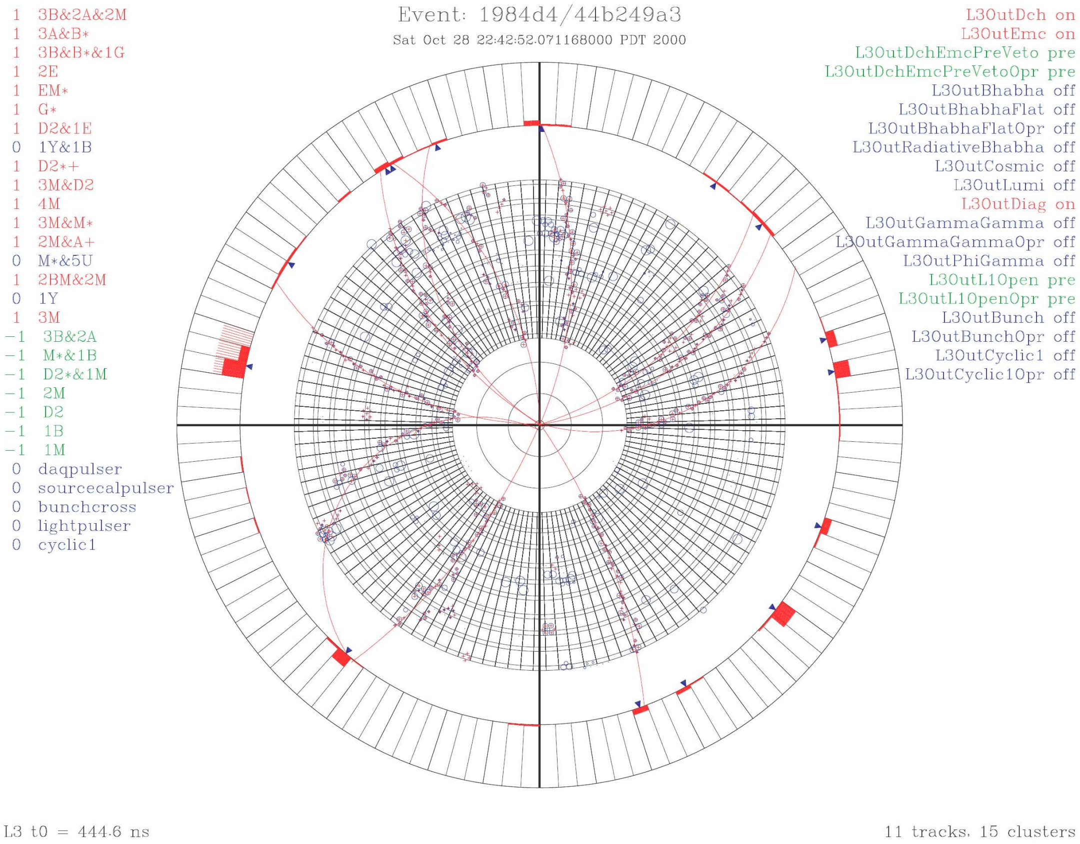

Figure 3.20: *A Level 3 event display. The small circles and small crosses in the DCH volume are DCH hits and TSF segment hit wires respectively. The filled EMC crystals represent energy deposit from L3 EMC clusters while the small triangles just inside the EMC indicate the location of the cluster centroid [45].*

Chapter 4

Analysis

The purpose of this Chapter is to describe how we get from the data collected by *BABAR* to the measurements of the branching fraction ($\mathcal{B}$), longitudinal polarization fraction and the *CP*-violating coefficients for $B^0 \rightarrow \rho^0\rho^0$ decays. We discuss the observables used along with the cuts placed on them, how the fitter is constructed, how it is validated, which systematics come into play, what the results are and ultimately how they are relevant in the determination of the unitarity angle α. The content is similar to what is discussed in the supporting documents plus published articles [49]-[52].

When performing the analysis, the objective is to extract ~ 100 $B \rightarrow \rho^0\rho^0 \rightarrow \pi^+\pi^-\pi^+\pi^-$ events from the data gathered by *BABAR*, in order to measure their properties. First, we filter out (a large part of) the non-B events and reconstruct tracks, clusters, vertices, corresponding 4-vectors, flavor of the b quark and identify the particles involved (Section 4.1), while corresponding Monte Carlo is generated. A set of loose cuts is then placed in order to select the B decays with a $\pi^+\pi^-\pi^+\pi^-$ final state. In addition to $B \rightarrow \rho^0\rho^0$

there are a number of processes with a similar final state which make it past these cuts; and we select a set of observables in order to extract the signal (Section 4.3.2). A series of cuts are then placed on them, but several particularly problematic background modes remain. Therefore we use Monte Carlo (or sideband data for the continuum) to construct the Probability Density Functions for each mode (or a combination of similar modes) in each variable. These functions are then combined to form a Maximum Likelihood Fit (Section 4.5), which is applied to the data within our window of cuts, thus distinguishing the signal from the backgrounds. We then examine the selected $B \to \rho^0\rho^0$ events, measure the corresponding Branching Ratios as well as CP coefficients, and use the results to obtain a more precise value of $\Delta\alpha$.

4.1 Event Selection

In this section we describe how the data (stored on tape by L3 trigger) is filtered, how the objects of interest are reconstructed, and eventually how the `ntuples` containing possible signal events are generated.

4.1.1 Reconstruction

Prior to undergoing reconstruction the triggered data is filtered against 'undesirable' events. The first step of the process is performed by the `DigiFilter`, which primarily removes calibration events (*e.g.* the copious Bhabhas emitted at small polar angles) [57]. The result is then sent to the `BGFilter`.

The BGFilter

This program is a part of the partial reconstruction process. Here, the DCH information is used to identify tracks based on transverse momentum (> 0.1 GeV/c), number of hits, as well as the separation from the interaction point. Clusters in the EMC are then identified and matched to the tracks. Information on their energy, momentum and shape is combined to compute R_2 (R_2^{ch}), the ratios of zeroth to second Fox-Wolfram moments [59] for neutral (charged) clusters. A series of tags is then applied in order to distinguish events of interest. Specifically, we select:

- Multi-Hadron events (`BGFMultiHadron` tag);
- Neutral Multi-Hadron events (`BGFNeutralHadron`);
- $e^+e^- \to \mu^+\mu^-$ events (`BGFMuMu`);
- $e^+e^- \to \tau^+\tau^-$ events (`BGFTau`);
- Two Prong events (`BGFTwoProng`);
- Two Photon events $e^+e^- \to \gamma\gamma$ (`BGFGammaGamma`);
- Radiative Bhabha events (`BGFRadBhabha`);
- $e^+e^- \to \phi\gamma$ events (`BGFPhiGamma`);
- Neutral Two Photon events (`BGFAllNeutralTwoPhoton`);
- Virtual Compton Scattering events (`BGFVirtualComptonScattering`).

The above are identified using Fox-Wolfram moments, energy, momentum as well as vertex information. The process is described in detail in [60]. Roughly 35% of the L3 events pass these filters.

Full Reconstruction

Once we have filtered out (a significant portion of) the non-B events, we reconstruct the rest. The first part of the process involves a more detailed reconstruction of tracks. The ϕ and z hits in the SVT are combined to form space points, while the detector algorithm does a search for good tracks (requiring hits in at least four out of five layers) [6]. Independently, the drift chamber algorithm identifies straight-line track segments and combines them to form a helical track. Pattern recognition algorithms match the two sets. They are then fitted with a simple helices (ignoring interactions with the material) and assigned a set of track parameters (based on a weighted average of the two input tracks). The Kalman fitter can be used to perform fits to more accurate track models, based on the mass hypothesis (*i.e.* the assumption of particle mass).

The second part of the process involves the EMC. As (both neutral and charged) particles interact with the calorimeter, they leave energy deposits in the CsI crystals. The reconstruction algorithm generates a list of crystals where these deposits exceed a given amount (~ 0.5MeV). We then form clusters, defined as sets of adjacent crystals with the sum of their energies above a certain threshold (nominally 20MeV), and identify individual bumps (energy deposits likely to have been left by a single particle) within each cluster. These are matched to previously identified tracks based on ϕ and z coordinates near the point of entry to the EMC. In the end, the above data is used to remove a number of probable non-B events and generate track as well as cluster information for the rest.

4.1.2 PID

In addition to reconstructing clusters and tracks, it is essential to identify the corresponding particles. While the primary B-meson decay in our analysis involves charged pion byproducts, correct identification of all particle types is necessary to perform proper tagging (Section 4.1.4) of the other B. To this end *BABAR* subdetectors provide complementary information. The SVT and DCH record the specific energy loss (dE/dx) information as charged particles pass through the silicon strips and the gas mixture. The DIRC extracts velocity data based on the Cherenkov angle and records the number of Cherenkov photons. The EMC provides cluster shape, energy and position measurements, which differ between electrons, muons and hadrons. Likewise, the hits along with their pattern in the IFR are used to distinguish between hadrons and muons. Below we provide a summary of how each B decay byproduct is identified [6]:

- $\pi^{\pm}$, $K^{\pm}$: Via dE/dx information in the SVT plus DCH, via the Cherenkov angle, as well as the number of photons in the DIRC, and with the help of cluster energy plus shower shape in the EMC.
- Protons : From dE/dx measurements at lower momenta ($\sim\leq$ 1GeV/c) and via DIRC (based on the angle plus photon count) for higher energies.
- $e^{\pm}$: Predominantly from the energy deposited in the EMC, but with the help from DIRC and dE/dx measurements.
- $\mu^{\pm}$: From patterns of interaction with the iron in the IFR at higher momenta. The

DIRC is used for $p \sim 500\text{MeV/c}$, while energy loss in the SVT is useful for very low momentum muons ($p \sim 100\text{MeV/c}$).

- π^0, γ : Based on cluster energy and distribution in the EMC.
- K^0_L : Mainly from hits in the IFR chambers, with the interactions starting in the EMC about half of the time.

Results from all *BABAR* components are combined to optimize the accuracy of the PID information.

4.1.3 Vertexing

The Vertexing process takes the tracks and assigns a (three-dimensional) interaction or decay point to them. To first order the charged tracks are helices in a uniform magnetic field and neutral tracks are straight lines. We minimize the sum of the squares of the distance of closest approach for each point in order to find the interaction (or decay) vertex. However, there are a number of complications.

First, the travel path for neutrals lacks precise spatial information, as it is obtained from energy deposits in the EMC. Likewise, for charged particles, the non-uniformities in the magnetic field, along with the presence of the material, distort the helical tracks. Due to their curvature, finding the point of closest approach is a nonlinear problem, which is dealt with by linearizing and iterating to obtain a solution. There are several approaches ranging from making a 'reasonable guess' for the starting point [61] to analytically solving the equations of motion in order to determine it [62]. In general, we identify three types of vertices for $B\overline{B}$ decays:

1. Primary Vertex : The location where $\Upsilon(4S)$ decays into $B\overline{B}$ often needs to be estimated with more precision than the e^+e^- interaction point (150μm in the x, 6μm in the y, 1cm in the z direction). For each event the fit removes tracks associated with particles decaying far from the interaction point by requiring an impact parameter of less than 1mm in the $x-y$ plane. For $B\overline{B}$ events we account for the fact that both B's travel in the z direction by adjusting the vertex location to be the midway point between the two B decays.

2. B_{CP} Vertex : We select the final state tracks (in our case the four $\pi^{\pm}$ tracks), which are most likely to originate from the B-meson.

3. B_{tag} Vertex : It is reconstructed from the remaining tracks either by pinpointing the vertex (when there's more than one track) or by identifying the point closest to the B_{CP} Vertex (when there's just one track). When there's a lepton track from a $B \rightarrow Xl\nu$ decay we take the point closest to the beam-spot and (possibly) take the average of the z coordinate with the location obtained by using one of the first two methods. A number of cuts are applied to the track momenta, impact parameters, *etc.* The details of the B_{tag} reconstruction are provided in [63] with more recent updates given in [20].

In addition, kinematic constraints (*e.g.* masses, momenta, *etc.*) are combined with the spatial ones via kinematic fitting [64]. The procedure not only provides improved track parameters, but allows us to use the knowledge of momenta and masses to match daughters to their parent particles. As such, it resolves ambiguities and improves the accuracy of the vertexing process.

4.1.4 Tagging

Tagging is how we identify whether B_{tag} is a B^0 or a $\overline{B}^0$, or more precisely how we identify the probability that it is a B^0 vs. a $\overline{B}^0$ (as well as several other parameters) based on the decay products. The current Tag04 approach is described in [65]. The algorithm uses a Neural Network (NN) to process relevant information and create a subtagger, which identifies the particular physics of the process. Namely, we look at properties of the emerging particles (*i.e.* what kind of particle is it, what is its momentum, how many particles there are, *etc.*) and use them to determine the quark content at the vertex. For example, leptons originate from semileptonic B decays giving us the best information on whether the source was a b or a $\bar{b}$ (based on whether the lepton is negatively or positively charged, respectively). Distinguishing between pions and kaons with various kinematic properties further allows us to pinpoint the decay types (*e.g.* a slow pion track along with an oppositely charged kaon indicates a $D^{*\pm}$ decay). Detailed information on the tags used, as well as what type of process each one selects is provided in [66]. The input parameters for the NN are [6]:

- P_l^* , the lepton momentum in the $\Upsilon(4S)$ center of mass system.
- M_{recoil}, the recoil mass of the lepton.
- P_{miss}, the missing momentum of the event.
- θ_{miss} in the B^0 Center of Mass System (CMS), the angle between the lepton direction and the missing momentum of B_{tag}.
- θ_{min} in the B^0 CMS, the angle between the the direction of the reconstructed virtual W and the particle closest to this direction. The direction of the virtual W is

approximated by the sum of the lepton and missing momenta.

- E_{90}^{W} , the energy in the B^0 CMS in the 90 degree cone defined around of the direction of the reconstructed virtual W.

- $Asym$, the asymmetry in the B^0 CMS between the projection with respect to the lepton direction of the sum of all the particle momenta in the lepton hemisphere, and the projection of the sum of the other particles' momenta.

- Q^2, the invariant mass of the virtual W from the lepton momentum and the reconstructed neutrino momentum.

- $Q_l Q_K$, the product of the charge of the lepton and that of the kaon.

- $Q_{l1} Q_{l2}$, the product of the charges of the two leptons.

- N_{imp}, the number of tracks in the event with impact parameter $\geq$ 1mm in the transverse plane.

- M_{miss}, the missing mass of the tagging B^0.

A larger Neural Network is then used to combine the subtaggers to create a generic $BtgTag$ (as well as a $LeptonTag$), which is optimized to distinguish between B^0 and $\overline{B}^0$. The effectiveness of this tag is shown in Fig. 4.1. As a result we obtain seven output categories:

1. *Lepton* : Leptons with $|btgtag| > 0.8$ and $LeptonTag > 0.7$.

2. $Kaon1$: Fast kaons with $|btgtag| > 0.8$ and $LeptonTag < 0.7$.

3. $Kaon2$: Slower kaons with $0.6 < |btgtag| < 0.8$.

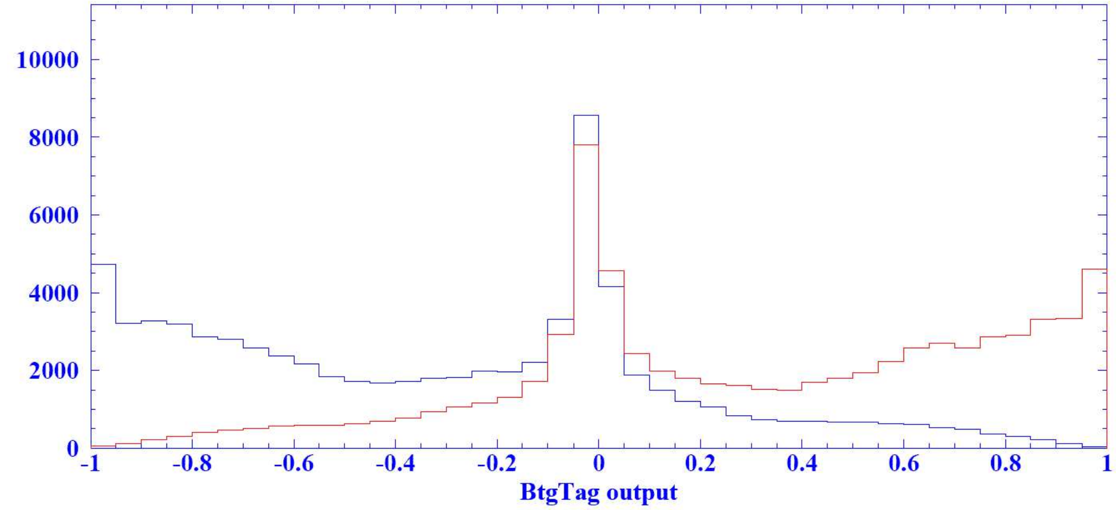

Figure 4.1: *BtgTag for Monte Carlo events. The blue (peaking near* -1*) and red (peaking near* 1*) histograms denote* B^0 *and* $\overline{B}^0$*, respectively [65].*

4. *KaonPion* : Either kaons or pions with $0.4 < |btgtag| < 0.6$.

5. *Pion* : Pions with $0.2 < |btgtag| < 0.4$.

6. *Other* : Another particle (*e.g.* e^-, p^+) with $0.1 < |btgtag| < 0.2$.

7. *NoTag* : Insufficient information with $|btgtag| < 0.1$ or when there is no tag.

The difference in values between the signal (b or $\bar{b}$) vs. all events in our dataset (dominated by charm decays), for each category, is shown in Fig. 4.2. In addition, a number of parameters, which depend on these tagging categories, are determined either by the B Tagging Group [55] or during the course of our analysis (for a detailed discussion see Section 4.5.1).

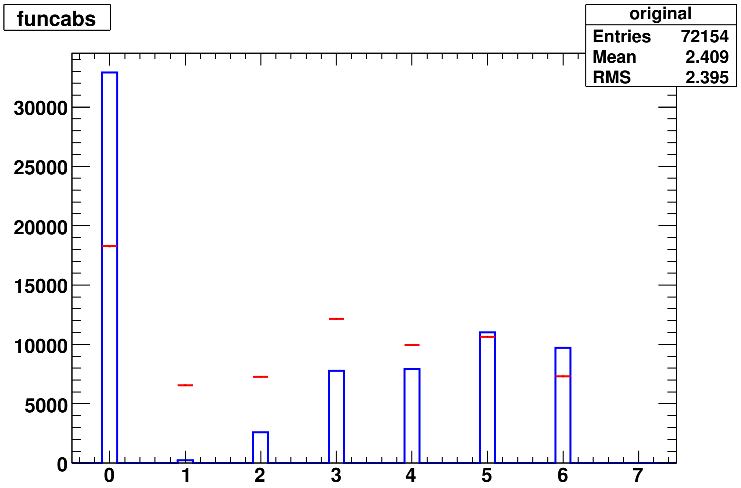

Figure 4.2: $B^0 \rightarrow \rho^0\rho^0$ *Longitudinal Signal MC (red dots) vs. the data (blue histograms), scaled to have the same event count, for each tagging category.*

4.1.5 Skimming

The fully processed data (stored in the `AllEventsSkim` files) consists of clusters, tracks, corresponding events, along with associated information which includes their positions and 4-vector momenta. Each event also has multiple (over 100) tags, which are used to select the desired topology out of the full set. This procedure is referred to as Skimming. In the case of $\rho^0\rho^0$ decays we rely on the `BFourHHHH` skim, where the final state contains four charged hadrons. The specific details along with the software involved are discussed in [67], [68]. The general approach is to select what are likely to be $B^0 \rightarrow \rho^0\rho^0 \rightarrow \pi^+\pi^-\pi^+\pi^-$ decays and then place additional cuts on the kinematic variables to ensure that we indeed have such an event. These cuts are $|m_{\rm ES}^{corr} - E_{beamCM}| < 0.100$ GeV/c^2, $|\Delta E| < 0.310$ GeV, $|\cos\theta_T| < 0.8$, where their physical significance along with the definition of the variables is provided in Section 4.3. Overall, the skim contains $\sim 1.3\%$ of $B^0\overline{B}^0$, which are stored as readily accessible `.root` file(s) [69].

4.1.6 Monte Carlo Simulation

Prior to fitting the actual data, we use Monte Carlo (MC) to model the distributions in each variable. Naturally, there is a procedure for generating and selecting the desired MC events similar to the one described above [70]. The first step is to generate the desired events, while correctly modeling the underlying physics. This is accomplished by smearing the beam energies and location of the interaction point [71], then using the `EvtGen` generator [72] to run the simulation. A (relatively) complete table of decays (stored in the `DECAY.DEC` file) is used in the process. Next, energy deposits, along with their locations, made by the would be particles are simulated via the `Geant4` framework [72]. The generated structures (GHits) are digitized into signals, which look like actual data collected by detector components. We overlay various backgrounds on top of them (accomplished by `SimApp`). The final step mirrors the process of event selection (described above) for the MC. In the end we obtain 'skims' for the $\rho^0\rho^0$ signal, as well as for each of the backgrounds we intend to model.

4.2 The Data Sample

We work with the data sample in CM2 format reconstructed with Release 22 [53]. The full (`AllEventsSkim`) dataset has a luminosity of 426fb^{-1}, where there are 468×10^6 $e^-e^+ \rightarrow \Upsilon(4S) \rightarrow B\overline{B}$ decays with the remaining events mainly originating from the continuum (*i.e.* not $B\overline{B}$ decays). After selecting the `BFourHHHH` skim (Section 4.1.5) we identify and place cuts on the observables m_{ES}, ΔE, $eShape$, m_1, m_2, $\cos\theta_1$, $cos\theta_2$, Δt, $\sigma_{\Delta t}$ order to eliminate the backgrounds. The final dataset contains 6.9×10^4 continuum and 2.4×10^3 $B\overline{B}$ (with ~ 100 $B \to \rho^0\rho^0$) events.

Several other event sources are needed throughout the analysis. Namely, we use data from the $B^0 \to D^-\pi^+$ decay to optimize the D-Veto process (Section 4.3.3) as well as for Control Sample Studies (Section 4.4.2). Off-peak data (*i.e.* events collected when e^+e^- collision energy is set 40MeV below the $\Upsilon(4S)$ resonance) is required in order to pick the best candidate selection algorithm (Section. 4.4) and train Shape Discriminants (Appendix C). Naturally, we use MC to model the distributions (in each observable) for the problematic backgrounds, which made it past the direct cuts, in order to distinguish them from the signal. The relevant modes, along with the number of generated events, are listed in Table 4.1. The specifics of the observables and corresponding fit shapes are discussed below.

4.3 Observables

4.3.1 General Requirements

Our objective is to select observables, which allow us to distinguish $B^0 \to \rho^0\rho^0$ decays from the backgrounds. The general requirements are:

- Four charged tracks, which are likely to be pions and are arranged into two pairs (corresponding to the ρ^0's).
- Like the charges, the four momenta and positions for the tracks should add up to

Table 4.1: *Monte Carlo modes used during the* $\rho^0\rho^0$ *analysis. The CP coefficients for the signal modes are* $S = 0.0$, $C = 0.0$ *unless stated otherwise.*

Mode	# of events produced	reference
$B \to \rho^0\rho^0$ Longitudinal ($S = -0.4$)	350k	SP-2396
$B \to \rho^0\rho^0$ Longitudinal ($S = -0.0$)	175k	SP-7331
$B \to \rho^0\rho^0$ Longitudinal ($S = -0.2$)	175k	SP-7332
$B \to \rho^0\rho^0$ Longitudinal ($S = -0.4$)	175k	SP-7333
$B \to \rho^0\rho^0$ Longitudinal ($S = -0.6$)	175k	SP-7334
$B \to \rho^0\rho^0$ Transverse	350k	SP-2397
$B \to \rho^0\rho^0$ Transverse	175k	SP-7335
$\rho^0 f_0$	175k	SP-4756
$f_0 f_0$	350k	SP-5074
$\rho^0\pi^+\pi^-$	1503k	SP-2487
$\pi^+\pi^-\pi^+\pi^-$	1053k	SP-4870
$a_1\pi$	4923k	SP-1012
$f_0 K^{*0}$	175k	SP-3359
$\rho^0 K^{*0}$-long	350k	SP-2359
$\rho^0 K^{*0}$-tran	350k	SP-2360
$\rho^0\rho^+$-long	1402k	SP-2390
$\eta' K$	1402k	SP-1508
$\rho^0\pi^+$	1053k	SP-1220
$\rho^+\rho^-$-long	3518k	SP-2498
$\rho^+\pi^-$	1754k	SP-1228
$\rho^-\pi^+$	1754k	SP-1229
$a_1^+ f_0$	704k	SP-5073
$a_1^0\pi^+$	878k	SP-4156

those of the B^0.

- Spherical symmetry, which can be used to distinguish them from the more jetty continuum events.

- Appropriate kinematics each pair of pions. Namely they should appear to be originating from a ρ^0 in their mass as well as angular distributions.

Afterward, we place a series of cuts designed to eliminate most of the backgrounds, but keep a sufficient window to pick up signal events as well as retain enough continuum events to model its distributions (we also cut off the difficult to model edge effects in the process).

4.3.2 Detailed Examination

The observables used in our analysis are:

1. Kinematic Observables

Two (nearly) independent variables are used to kinematically identify the B meson candidates.

- $m_{\mathrm{ES}} = [(s/2 + \mathbf{p}_i \cdot \mathbf{p}_B)^2/E_i^2 - \mathbf{p}_B^2]^{1/2}$: the energy-substituted B-meson mass, reconstructed from beam values. Here we also minimize variations of the end point by making the shift

$$m_{\mathrm{ES}}^{corr} = m_{\mathrm{ES}} - \sqrt{s}/2 + 5.29\,\mathrm{GeV}/c^2,$$

  where $\sqrt{s}$ is the *reported* value of the center-of-mass energy (the remaining fluctuations are accounted for by Control Sample Studies: Section 4.4.2) and working with $m_{\mathrm{ES}} \equiv m_{\mathrm{ES}}^{corr}$ throughout the analysis.

- $\Delta E = (E_i E_B - \mathbf{p}_i \cdot \mathbf{p}_B - s/2)/\sqrt{s}$: the difference between the reconstructed energy of the B candidate and beam parameters in the Center of Mass System (CMS).

$(E_i, \mathbf{p}_i)$ is the initial state four-momentum, obtained from the beam momenta. $(E_B, \mathbf{p}_B)$ is the four-momentum of the reconstructed B candidate. The signal peaks at the B mass for m_{ES}, and we place a cut of $5.245 < m_{\mathrm{ES}} < 5.29$ GeV/c^2 to select the events of interest (*i.e.* the ones where all four pions originate from the same B). Likewise, ΔE peaks near zero for the signal, while we restrict $|\Delta E| < 0.085$ GeV to remove events with extra or missing π's (peaking for $|\Delta E| \sim 0.15$).

Even with the restrictions above there are still instances ($\sim 10\%$) where one of the pions originates from the wrong B. These are referred to as Self Cross Feed (SXF) events. They may make it past the selection process, but are readily distinguishable based on the shapes of the m_{ES} and ΔE distributions.

2. Invariant Masses

The reconstructed invariant masses of the two pion pairs.

- m_1
- m_2

We select a window of $0.55 < m_1, m_2 < 1.05\ \mathrm{GeV}/c^2$, which allows us to pick up the peaks in $\rho^0 \to \pi^+\pi^-$ (and $f_0 \to \pi^+\pi^-$) distributions, while cutting out the remaining resonances. The pairing (based on the azimuthal angle of the ρ^0's in the detector) has no impact on analysis, since we treat the two observables in a symmetric fashion. The kinematic range for the masses is wide enough to retain sidebands for later fitting, but sufficiently narrow so that a wrong association between the pions (when pairing π^+ with π^-) occurs less than 0.02% of the time.

3. Angular Observables

The B meson is a vector-vector (VV) final state, whose angular distribution is a combination of S, P, and D-wave contributions with unknown relative amplitudes. Thus, we can describe it via the helicity angles (defined in Section 2.4.1)

- $\cos\theta_1$
- $\cos\theta_2$,

which are defined by the direction of the two-body ρ^0 decay axis in the ρ^0 rest system relative to the ρ^0 momentum in the B^0 rest frame [49]. It is also possible to define the azimuthal equivalent $\phi = \phi_1 - \phi_2$ in the same way. But since this angle does not provide significant background suppression, we integrate over it (to a good approximation there are no acceptance effects for this observable). The distribution, as a function of the angular observables, is then given by

$$\frac{1}{\Gamma}\,\frac{d^2\Gamma}{d\cos\theta_1\;d\cos\theta_2} = \frac{9}{4}\left[\cos^2\theta_1\cos^2\theta_2 f_L + \frac{1}{4}\sin^2\theta_1\sin^2\theta_2\,(1-f_L)\right], \tag{4.1}$$

where f_L is the fraction of the Longitudinally Polarized ρ^0's. The cuts of $|\cos\theta_1|$,$|\cos\theta_2| < 0.98$ remove the detector acceptance effects as well as the backgrounds (primarily $B^0 \to a_1^{\pm}\pi^{\mp}$), which exponentially peak near $\cos\theta = 1$.

4. Event Shape Observables

In order to reject the dominant quark-antiquark continuum background we construct variables based on the geometric shape of the events ('jetty' for continuum vs. symmetric for B decays). They are combinations of the following nine variables:

- $L_0^{charged}$, $L_0^{neutral}$, $L_2^{charged}$, $L_2^{neutral}$: The four Legendre monomials, split for charged and neutral particles.
- $\sum_r p_T$: The sum of the transverse momenta of all particles in the rest of the event, calculated with respect to the B direction.
- $\cos\theta_{BT}$: The cosine of the angle between the B thrust (*i.e.* the direction which maximizes the sum of the longitudinal momenta of the particles) and the z axis.
- $\cos\theta_B$: Cosine of the B direction with respect to the beam.

- $\cos\theta_T$: The cosine of the angle between the thrust of the rest of the event and the B thrust. Note that we require $|\cos\theta_T| < 0.8$ during skimming, to explicitly remove the more jetty (mostly) continuum events.
- χ^2_{vtx} : The vertex chi-squared, computed for 4 charged tracks (5 degrees of freedom). More precisely, we use their vertex convergence probability

  $$p_{\mathrm{vtx}} = -\log(Prob(\chi^2_{\mathrm{vtx}}, 5))$$

  when forming the discriminants. Additionally, when there are multiple candidates for the same event, we use χ^2_{vtx} to select the best one, as described in Section 4.4. We also require that $\chi^2_{\mathrm{vtx}} < 15$, which corresponds to the vertex convergence probability of about 1%. It is loose enough to a have large signal efficiency with a small systematic uncertainty, while providing significant suppression of backgrounds with tracks from displaced vertices.

The above observables are combined to construct either a neural net multivariate discriminant (*eShape*) or a likelihood-based discriminant (*likeShape*). The specifics of how this is accomplished as well as comparison studies between the two are provided in Appendix C. In the end, there is a very strong (> 95%) correlation between the two discriminants, and we only use one of them when performing the fit (*eShape* for the publications [51],[52]). The cut $|eShape| < 2$ is designed to remove outliers.

5. B-Flavor Tagging

As was discussed in Section 4.1.4, during the analysis we obtain information on the flavor of the conjugate B. It is parametrized via the variable

- Tag : This is a discrete variable, which we place in one of seven possible categories described in Section 4.1.4. The typical efficiencies are given in Table. 4.2.

In addition to being essential for the measurements of CP parameters, the tagging information is used directly for background suppression. The signal and several backgrounds have differing efficiency values (due to variations in quark content between $B\overline{B}$ vs. continuum events as well as due to track mismatches between B vs. $\overline{B}$ vertices), and the fitter distinguishes between them based on the corresponding values.

6. Time Dependent Variables

In order to extract CP properties for the process we perform a time dependent fit, which uses

- Δt : the time difference between the decays of B and $\overline{B}$;
- $\sigma(\Delta t)$: event-by-event error estimate for Δt.

The requirements of $|\Delta t| < 15$ ps, $0.1 < \sigma(\Delta t) < 2.5$ ps remove the edge effects. The construction of the Full Time Dependent(TDCP) Maximum Likelihood Fit is described in detail in Section 4.5.1.

4.3.3 D-Veto

Additionally, we explicitly veto the most dangerous B backgrounds with a possible 4-track final state: $B^0 \to D^-\pi^+$ and $D^{*-}\pi^+$, by cutting on the reconstructed charmed meson mass. The procedure includes an improvement over the previous analyses. Namely, for $B^0 \to D^-\pi^+$ we identify the bachelor pion as the pion with the momentum closest to the kinematically required value of 2.3 GeV, rather than the pion with the highest

Table 4.2: *Tagging Categories along with corresponding efficiencies for Signal* $B^0 \to \rho^0\rho^0$ *(taken from BReco samples), Continuum Background (fitted for during our analysis) and Charmless component (taken from MC).*

Category	Signal	Continuum	Charmless(MC)
Lepton	0.088 ± 0.001	0.003 ± 0.500	0.003 ± 0.500
Kaon 1	0.109 ± 0.001	0.004 ± 0.500	0.073 ± 0.500
Kaon 2	0.173 ± 0.001	0.108 ± 0.500	0.171 ± 0.500
Kaon-Pion	0.136 ± 0.001	0.110 ± 0.500	0.149 ± 0.500
Pion	0.142 ± 0.001	0.153 ± 0.500	0.149 ± 0.500
Other	0.095 ± 0.001	0.135 ± 0.500	0.108 ± 0.500
Untagged	0.257 ± 0.001	0.456 ± 0.500	0.318 ± 0.500

momentum (in the B frame). For the other three particles, we apply the following cuts against $D^- \to K^+\pi^-\pi^-$:

- $|m_{K\pi\pi} - m_{D^+}| > 13.2$ MeV;
- $|m_{K\pi\pi} - m_{D^+}| > 40$ MeV if the candidate kaon is in the `NotAPion` LH PID selector list;
- $|m_{\pi\pi\pi} - m_{D^+}| < 13.2$ MeV against $D^- \to \pi^+\pi^-\pi^-$.

The D^- veto disproportionately removes events with a helicity $\cos\theta_{\text{hel}}$ values of ~ 0.85 for one of the ρ^0 candidates. As a result we observe a 'dip' in the efficiency, which is taken into account by the helicity acceptance function (*e.g* Fig. D.13). The improvement in the rejection of the $B^0 \to D^-\pi^+$ background is summarized in Fig. 4.3, while overall algorithm efficiencies are given in the Table 4.3.

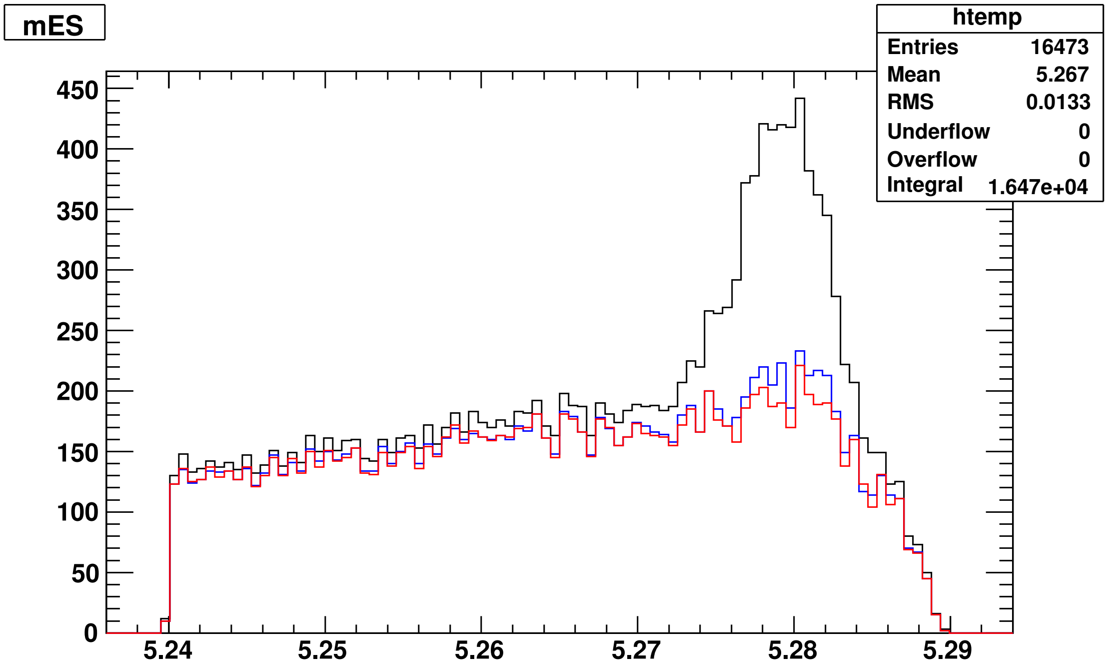

Figure 4.3: *D-veto Comparison. The black line denotes the background without the D-veto. The blue line and red lines represent the background after the old and improved D-veto algorithms, respectively.*

Table 4.3: *Efficiency computation in the study of D-veto. Longitudinally polarized signal is used.*

Method	Signal Efficiency	Background Efficiency	$\epsilon_{sig}/\sqrt{\epsilon_{bkgr}}$
No D-Veto	1.000	1.000	1.000
Old D-Veto	0.942	0.661	1.159
Improved D-Veto	0.933	0.627	1.178

4.4 Best Candidate Selection

Upon applying the cuts, we are still left with multiple candidates for a number of events ($\sim$ 5%). In the prior analysis [73], the candidate was chosen at random, and there are several options for improving on that approach. As such, we tested the possible selection methods in order to determine the best alternative. Specifically, we looked at the

Table 4.4: *Comparison of Selection Method Efficiencies. Here Efficiency=(Number of Remaining True Events)/(Number of Initial True Events). The Total Efficiency is computed by applying the selection method to the entire signal, while the Algorithm Efficiency is computed by applying the selection method only to the events with multiple candidates.*

Selection Method	Total Efficiency	Algorithm Efficiency
Random Selection	0.87	0.37
χ^2_{vtx} Selection	0.92	0.58
$\chi^2_{\Delta E} + \chi^2_{m1} + \chi^2_{m2}$	0.97	0.85
$\chi^2_{\Delta E} + \chi^2_{m1} + \chi^2_{m2} + \chi^2_{\text{vtx}}$	0.97	0.85

effect of choosing a candidate with the smallest χ^2_{vtx}, the smallest $\chi^2_{\Delta E} + \chi^2_{m1} + \chi^2_{m2}$ (*i.e.* χ^2 for $\Delta E = 0$ and $m = m_\rho$) or the smallest $\chi^2_{\Delta E} + \chi^2_{m1} + \chi^2_{m2} + \chi^2_{\text{vtx}}$. By analyzing signal MC, we computed and compared the resulting efficiencies, as shown in Table 4.4.

The studies indicate that:

1. Using $\chi^2_{\Delta E} + \chi^2_{m1} + \chi^2_{m2}$ to select the event has the highest efficiency of selecting true signal events.

2. It also has an increased systematic error due the bias of the background (*e.g.* off-resonance) distributions that must be taken into account. The bias comes from a change in the shape of the background distributions to more signal-like (*i.e.* the process generates peaks in the signal region or even shape discontinuity at the best value). Plus, potentially dangerous correlations could be introduced.

3. Fitting the variables (after the selection process) with a Background PDF (Probability Density Function), we can observe how much of that is taken up by the Signal PDF. In Figs. 4.4, 4.5 we show the ΔE distributions for the off-resonance events with two or more reconstructed B candidates, after the best candidate selection based on the smallest $\chi^2_{\Delta E} + \chi^2_{m1} + \chi^2_{m2}$ was applied.

4. As can be seen, the peaking introduced in the off-resonance ΔE distribution, by selecting the best candidate based on a variable that includes ΔE, is highly pronounced. This generates a fake signal-like component in the continuum background, where its uncertainty (the error in the parameter a) will contribute to the overall systematic error.

5. With the use of estimated values for the number of signal and continuum background events, we can show that the increase in the systematic error outweighs the gains in statistics by over three orders of magnitude.

Thus, using the smallest $\chi^2_{\Delta E} + \chi^2_{m1} + \chi^2_{m2}$ to select the best candidate is not an effective approach. The parameter $\chi^2_{\rm vtx}$ is independent of ΔE (and other fit parameters) and relying on it does not introduce any systematic bias to the variables used in the likelihood fit, while improving efficiency (when compared to the random selection), as shown in Table. 4.4. Hence, when there are multiple candidates for an event, we select the one with the smallest $\chi^2_{\rm vtx}$.

4.4.1 Summary Of Cuts

Cuts on all of the observables are summarized in Table. 4.5. For comparison, we show the (longitudinal) signal MC events overlayed on top of the full (continuum dominated) dataset, after the cuts have been applied: Fig. 4.6. The selection efficiency and the fraction of the self-crossfeed (SXF) events (*i.e.* events reconstructed with one pion not originating from the correct B vertex) are summarized in Table 4.6.

We use the `BToHHHHUser` *BABAR* package to implement these cuts and reduce the

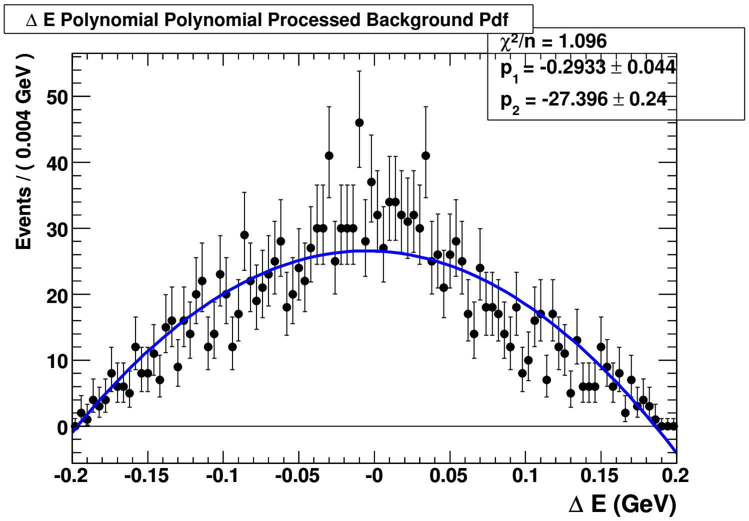

Figure 4.4: ΔE *distributions for the off-resonance events with two or more reconstructed* B *candidates after the best candidate selection based on the smallest* $\chi^2_{\Delta E} + \chi^2_{m1} + \chi^2_{m2}$ *is applied. It is fitted with a standard second order polynomial (a.k.a. the background fit).*

Table 4.5: *Selection Cuts.*

$5.245 < m_{\mathrm{ES}}^{corr} < 5.29$ GeV/c^2
$\lvert\Delta E\rvert < 0.085$ GeV
$0.55 < m_1, m_2 < 1.05$ GeV/c^2
$\lvert eShape\rvert < 10$ (with $\lvert\cos\theta_T\rvert < 0.8$)
$\lvert\cos\theta_1\rvert, \lvert\cos\theta_2\rvert < 0.98$
$\chi^2_{\mathrm{vtx}} < 15$
$\lvert\Delta t\rvert < 15$ ps
$0.1 < \sigma(\Delta t) < 2.5$ ps
PID not kaon, not electron LH tight
D-veto as in 4.3.3.

skims down to small ntuples (produced in Release `analysis-42`). They are then analyzed in `root` using the `RooFit` [74] and `RooRarFit` [75] toolkits. Several backgrounds (discussed in Section 4.5.2) similar to the signal remain after the cuts are applied and have to be distinguished based on the PDF shapes for the observables.

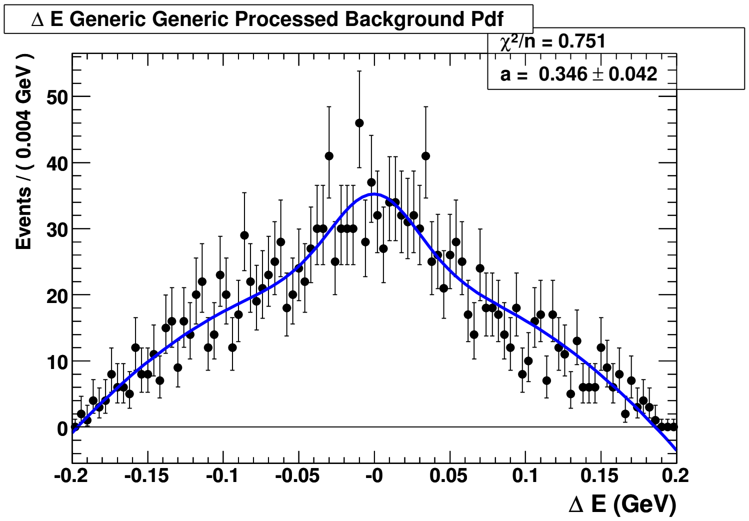

Figure 4.5: ΔE *distributions for the off-resonance events with two or more reconstructed* B *candidates after the best candidate selection based on the smallest* $\chi^2_{\Delta E} + \chi^2_{m1} + \chi^2_{m2}$ *is applied. It is fitted with a combination of signal and background PDFs* $(1-a)*BkgrPDF + a*SigPDF$.

Table 4.6: *Efficiency for* $B^0 \to \rho^0\rho^0$ *sample, for the data.*

Longitudinal (True+SXF)	25.86%
SXF fraction	17.57%
Transverse (True+SXF)	30.23%
SXF fraction	3.16%

4.4.2 Control Sample Studies

The Monte Carlo is not an exact match to the data, and we rely on $B^0 \to D^-\pi^+ \to (K^+\pi^-\pi^-)(\pi^+)$ control samples to account for the discrepancies. In addition to validating that there is a reasonable match between the two, the following corrections are made:

1. Corrections to the parameters themselves. These are needed due to the the fact that the MC is an imperfect model, as well as due to the fact that detector performance changes over time. Specifically, for the average values of m_{ES} and ΔE we not only

observe a discrepancy between data and MC, but also a significant systematic difference in between Runs 1-5 and Run 6. The subsequent studies are split as Runs 1-5 vs. Run 6, with different values for the signal and signal-like m_{ES}, ΔE means.

2. Corrections to the parameter errors. Due to the large amount of Monte Carlo for numerous modes, when fitting it with a PDF we tend to underestimate their size. As a (conservative) solution we add in quadrature the errors obtained from fitting the control samples with those obtained from the MC. Since we are using the same control sample to correct multiple PDFs, the newly created correlations must be taken into account during error analysis.

Specifically, we make the corrections for m_{ES}, ΔE, *eShape* and *likeShape* in *BABAR* Analysis-42 package, Release 22. We use the Crystal-Ball Shape to describe the signal m_{ES} PDF, while a Two-Gauss is used for the ΔE (the functional form for these distributions is given in Section 4.5.3). A tail Crystal-Ball parameter is added to account for any detector effect and is fixed (to the value in MC data) in the fit to the on-peak data. The results are given in Table 4.7.

For the Event Shape Observables, we study both *eShape* as well as *likeShape*. These discriminants are fitted with a combination of (potentially) asymmetric gaussians. The parameters are statistically consistent between the MC, Runs 1-5 data and Run 6 data. The results of the studies are shown in Tables 4.8, 4.9 with the correlations provided in Tables 4.10, 4.11.

Table 4.7: *Summary of results in the analysis of decay* $B^0 \to D^-\pi^+ \to (K^+\pi^-\pi^-)(\pi^+)$*. PDF parameters are presented for* m_{ES} *and* ΔE *in data and MC.*

Dataset	m_{ES} (MeV)	$\sigma_{m_{ES}}$ (MeV)	ΔE (MeV)	$\sigma_{\Delta E}$ (MeV)
Monte Carlo	5279.560 ± 0.023	2.519 ± 0.023	-1.113 ± 0.275	18.811 ± 0.314
Runs 1-5-OnPeak Runs 1-5 to MC Shift	5279.160 ± 0.024 -0.400	2.605 ± 0.023 -	-4.909 ± 0.217 -3.796	20.129 ± 0.198 -
Runs 1-6-OnPeak Runs 1-6 to MC Shift	5279.020 ± 0.023 -0.540	2.631 ± 0.021 -	-4.735 ± 0.207 -3.362	20.326 ± 0.189 -
Run 5-OnPeak Run 5 to MC Shift	5278.760 ± 0.042 -0.800	2.688 ± 0.034 -	-4.770 ± 0.364 -3.657	20.702 ± 0.336 -
Run 6-OnPeak Run 6 to MC Shift	5277.830 ± 0.077 -1.730	2.653 ± 0.058 -	-2.745 ± 0.697 -1.632	20.372 ± 0.625 -

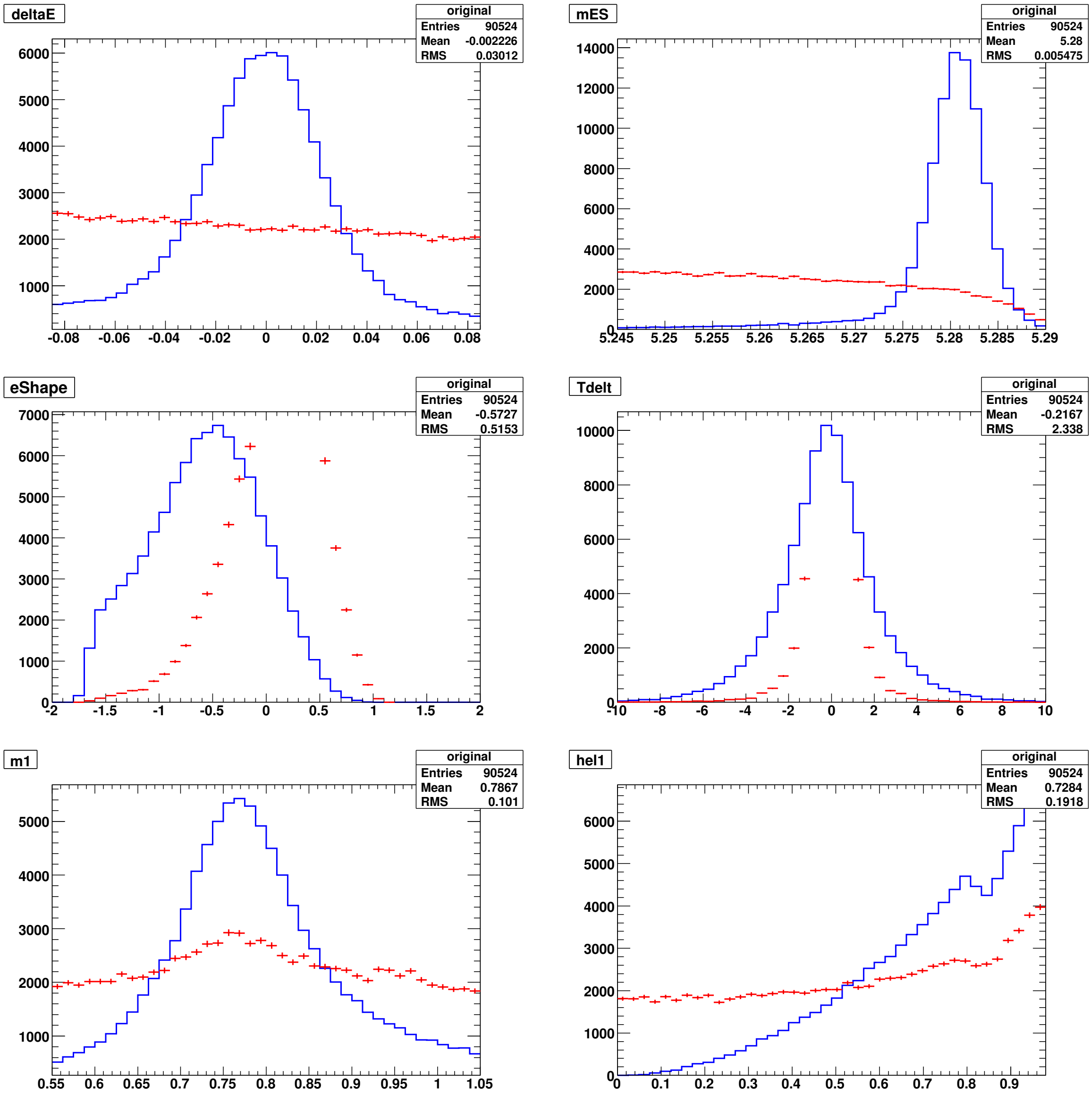

Figure 4.6: $B^0 \rightarrow \rho^0\rho^0$ *Longitudinal Signal MC (blue lines) vs. the data (red dots) scaled to have the same event count, for each of the observables. Note that there are* ~ 100 *signal events and* ~ 70000 *background event in the full dataset, after all of the cuts have been made.*

Table 4.8: *eShape validation for* $B^0 \to D^-\pi^+ \to (K^+\pi^-\pi^-)(\pi^+)$*. The sum of 2 BGGauss and one Gaussian is used for the signal, while one BGGauss is used for the continuum. (BGGauss is a bifurcated gaussian, where the* σ_R *on the right is not the same as* σ_L *on the left.) We compare the core BGGauss parameters between the MC and Runs 1-6/Runs 1-5 OnPeak Data. All of the parameters are floated in the fit, and they are statistically consistent between MC and data.*

Comp	Var	Monte Carlo	Runs 1-6 OnPeak	Runs 1-5 OnPeak
BGGauss1	μ_1	-0.479 ± 0.030	-0.486 ± 0.031	-0.511 ± 0.034
	σ_{L1}	0.348 ± 0.008	0.331 ± 0.016	0.320 ± 0.018
	σ_{R1}	0.326 ± 0.019	0.325 ± 0.020	0.329 ± 0.023
	f_1	0.711 ± 0.072	0.715 ± 0.045	0.709 ± 0.053
BGGauss2	μ_2	-1.148 ± 0.045	-1.114 ± 0.048	-1.116 ± 0.047
	σ_{L2}	0.162 ± 0.019	0.164 ± 0.022	0.153 ± 0.022
	σ_{R2}	0.410 ± 0.156	0.378 ± 0.145	0.362 ± 0.151
	f_2	0.134 ± 0.069	0.126 ± 0.047	0.115 ± 0.043
Gauss3	μ_3	0.102 ± 0.013	0.093 ± 0.030	0.063 ± 0.035
	σ_3	0.208 ± 0.005	0.213 ± 0.013	0.224 ± 0.014

Table 4.9: *likeShape validation for* $B^0 \to D^-\pi^+ \to (K^+\pi^-\pi^-)(\pi^+)$*. Two-Gaussian PDFs are used for both the signal and continuum background. We compared the core BGGauss parameters between the MC and Runs 1-6/Runs 1-5 OnPeak Data by floating all of the parameters in the fit. MC and data parameters are statistically consistent.*

Var	Monte Carlo	Runs 1-6 OnPeak	Runs 1-5 OnPeak
μ_C	0.763 ± 0.005	0.769 ± 0.013	0.762 ± 0.014
σ_C	1.281 ± 0.004	1.305 ± 0.013	1.309 ± 0.014
μ_T	1.204 ± 0.019	1.121 ± 0.032	1.116 ± 0.035
σ_T	0.493 ± 0.017	0.470 ± 0.035	0.482 ± 0.036
f_C	0.885 ± 0.006	0.867 ± 0.016	0.858 ± 0.017

Table 4.10: *Correlations of the eShape parameters* μ_1, σ_{L1}, σ_{R1}, μ_2, σ_{L2}, σ_{R2}, μ_3, σ_3, f_1 *and* f_2 *for the full (Runs 1-6-OnPeak-R22d-v07) dataset.*

	μ_1	σ_{L1}	σ_{R1}	μ_2	σ_{L2}	σ_{R2}	μ_3	σ_3	f_1	f_2
μ_1	1.00									
σ_{L1}	0.609	1.00								
σ_{R1}	-0.350	-0.207	1.00							
μ_2	0.658	0.020	-0.257	1.00						
σ_{L2}	0.538	-0.098	-0.209	0.964	1.00					
σ_{R2}	0.440	0.430	-0.254	-0.004	0.087	1.00				
μ_3	0.755	0.474	0.156	0.455	0.378	0.070	1.00			
σ_3	-0.702	-0.440	-0.138	-0.416	-0.345	-0.064	-0.928	1.00		
f_1	-0.308	0.012	0.612	-0.282	-0.236	-0.745	0.259	-0.249	1.00	
f_2	0.692	0.211	-0.342	0.520	0.434	0.814	0.278	-0.254	-0.822	1.00

Table 4.11: *Correlations of the likeShape signal fit parameters* μ_C, σ_C, μ_T, σ_T *and* f_C *for the full dataset.*

	μ_C	σ_C	μ_T	σ_T	f_C
μ_C	1.00				
σ_C	-0.315	1.00			
μ_T	-0.125	-0.402	1.00		
σ_T	0.199	0.573	-0.547	1.00	
f_C	0.298	-0.744	0.499	-0.812	1.00

4.5 Maximum Likelihood Fit

4.5.1 TDCP Maximum Likelihood Fit

We perform an extended maximum likelihood fit for the observables listed in Section 4.3. The actual variables used are: m_{ES}, ΔE, neural network output *eShape* (or alternatively the likelihood discriminant *likeShape*), reconstructed masses (m_1, m_2), helicity angles ($\cos\theta_1$, $\cos\theta_2$) of the two vector mesons, time difference Δt, the corresponding event-by-event error $\sigma(\Delta t)$, and the flavor tag (the PDFs are split into the 7 tagging categories defined in Section 4.1.4). When fitting the data, we split m_{ES} and ΔE shifts between Runs 1-5 and Run 6 datasets, as suggested by the control sample studies (Section 4.4.2). Additionally, we can classify the events into several categories of signal and background samples based on similar efficiencies (described in detail in Section 4.5.2). The likelihood function is then written as:

$$-ln\ L_j = \sum_{tagcat\ i} [\epsilon^{sig}_{tag_i} \sum_{signal_K} N_{sig_k} \mathcal{P}_{sig_k}(\vec{x}_j;\vec{\alpha}) + N_{cont}\epsilon^{cont}_{tag_i}\mathcal{P}_{cont}(\vec{x}_j;\vec{\alpha}) \tag{4.2}$$
$$+N_{Chls}\epsilon^{Chls}_{tag_i}\mathcal{P}_{Chls}(\vec{x}_j;\vec{\alpha}) + N_{B\overline{B}}\epsilon^{B\overline{B}}_{tag_i}\mathcal{P}_{B\overline{B}}(\vec{x}_j;\vec{\alpha})],$$

where we used the fact that multiple signal modes have the same efficiencies $\epsilon^{sig}_{tag_i}$. $\mathcal{P}_i(\vec{x}_j;\vec{\alpha})$ is the Probability Density Function for the measured variable $\vec{x}_j$ of a candidate j in category i, N_i are the corresponding yields (generally extracted from the fit) and the parameters $\vec{\alpha}$ describe the expected distributions of the measured variables in each category. Our overall goal was to:

1. Determine the event yields for signal events (*i.e.* determine the number of longitudinal and the number of transverse events, or alternatively determine the total number of

events along with the polarization fraction $f_L = N_{Long}/(N_{Long} + N_{Tran}))$.

2. Fit for the C and S parameters of the $\rho^0\rho^0$ category, using the PDFs in Δt.

The Δt distribution is described by [54]:

$$F^{\rho^0\rho^0}_{Q_{tag}}(\Delta t_m) \sim \frac{e^{-|\Delta t_t|/\tau}}{4\tau} \times \{1 - Q_{tag}\Delta w + Q_{tag}\mu(1-2\omega) + \tag{4.3}$$

$$+ (Q_{tag}(1-2w) + \mu(1 - Q_{tag}\Delta\omega))\,[S\sin(\Delta m_d \Delta t_t) - C\cos(\Delta m_d \Delta t_t)]\} \otimes R(\Delta t_t, \Delta t_m),$$

where Δt_t is the true time between the B decays, Δt_m is the measured time, $\otimes$ denotes convolution, $Q_{tag} = 1(-1)$ when the tagging meson B^0_{tag} is a $B^0(\bar{B}^0)$, τ is the mean B^0 lifetime, Δm_d is the mass difference between the two B^0 mass eigenstates, and the mistag parameters w and Δw are the average and the difference, respectively, of the probabilities that a true B^0 is incorrectly tagged as a $\bar{B}^0$ or vice versa; μ is the tag efficiency difference between B^0 and $\bar{B}^0$ [50]. The Δt resolution function is the sum of three gaussians, scaled by the Δt error for two of them:

$$R(\Delta t, \sigma_{\Delta t}) = f_{core} G(\Delta t, \mu_{core}\sigma_{\Delta t}, \sigma_{core}\sigma_{\Delta t}) \tag{4.4}$$

$$+ f_{tail} G(\Delta t, \mu_{tail}\sigma_{\Delta t}, \sigma_{tail}\sigma_{\Delta t}) + f_{out} G(\Delta t, \mu_{out}, \sigma_{tail}),$$

where $\Delta t = \Delta t_t - \Delta t_m$ and $G(\mu, \sigma)$ is a gaussian distribution with the mean μ and standard deviation σ.

For the $\rho^0\rho^0$ and other signal-like modes, the mistag parameters (w, Δw, μ) as well as the resolution parameters (μ_c, σ_c) are the same as those computed by the B Tagging Group [55] for the *BABAR* control samples. They are given in Table 4.12 for Monte Carlo and Table 4.13 for the data. The standard values for the remaining resolution parameters

Table 4.12: *MC Mistag Fractions (the parameters for the resolution gaussians are in* ps*).*

Category	ω	$\Delta\omega$	μ	μ_c	σ_c
Lepton	0.070	0.0289	0.0334	-0.03	0.98
Kaon1	0.083	0.0202	0.0253	-0.27	1.09
Kaon2	0.171	0.0122	0.0254	-0.28	1.20
KaonPion	0.310	-0.0155	0.0362	-0.27	1.12
Pion	0.348	0.0723	0.0225	-0.26	1.12
Other	0.390	0.0462	0.0102	-0.25	1.07
NoTag	0.5	0.0	0.1000	-0.23	1.11

Table 4.13: *Data Mistag Fractions (the parameters for the resolution gaussians are in* ps*).*

Category	ω	$\Delta\omega$	μ	μ_c	σ_c
Lepton	0.029	0.0018	-0.0039	-0.07	1.02
Kaon1	0.053	-0.0001	-0.0002	-0.16	1.16
Kaon2	0.145	0.0039	0.0066	-0.20	1.14
KaonPion	0.233	-0.0063	0.0021	-0.19	1.14
Pion	0.326	0.05101	-0.0246	-0.25	1.10
Other	0.415	0.03789	0.0174	-0.18	1.07
NoTag	0.5	0.0	-0.0039	-0.20	1.12

are listed in Table 4.14. These are taken from Tag04 MC [65] as a default, but fitted to the MC when necessary.

It is possible for the continuum to contain states with nonzero CP coefficients (mainly coming from detector and interaction effects) and therefore have an asymmetry be-

Table 4.14: *Standard Resolution Parameters (the parameters for the resolution gaussians are in* ps*).*

Parameter	MC	Data
σ_t	3.0	3.0
σ_o	8.0	8.0
μ_t	-1.18	-1.05
μ_o	0.0	0.0
$frac_c$	0.889	0.879
$frac_o$	0.0041	0.0034

tween B^0 and $\bar{B}^0$ tagged events. We parametrize its time distribution by the *CP*-asymmetric PDF $f(\Delta t) = (1 \pm A_{CP})$, convoluted with the standard Resolution Function. The corresponding asymmetry parameters are determined from the side-band data ($m_{ES} < 5.27$ GeV) and are listed in Table 4.15.

4.5.2 Component Overview

Prior to performing a maximum likelihood fit on the data we have to construct PDFs (Probability Density Functions) for the following component modes:

- Primary Signal mode: $B^0 \rightarrow \rho^0\rho^0$. As a consequence of the spin of the ρ^0, the signal PDF is decomposed in a longitudinal and a transverse part, with each portion containing a True and a SXF component:

$$\mathcal{P}_{\rho^0\rho^0} = f_L \left[(1 - SXF_L)\mathcal{P}_L^{True} + SXF_L\mathcal{P}_L^{SXF}\right] + (1 - f_L)\left[(1 - SXF_T)\mathcal{P}_T^{True} + SXF_T\mathcal{P}_T^{SXF}\right]$$

- Secondary Signal modes with the same final state: $B^0 \rightarrow \rho^0 f_0$ and $B^0 \rightarrow f_0 f_0$.

- Non-resonant modes with the same final state: $B^0 \rightarrow \rho^0\pi^+\pi^-$ and $B^0 \rightarrow \pi^+\pi^-\pi^+\pi^-$.

- $B^0 \rightarrow a_1^{\pm}\pi^{\mp}$, consisting of three separate components:

$$\mathcal{P}_{a1\pi} = \left[(1 - f_{SXF} - f_{quasitrue})\mathcal{P}_{true} + f_{quasitrue}\mathcal{P}_{quasitrue} + f_{SXF}\mathcal{P}_{SXF}\right],$$

Table 4.15: *Continuum CP Asymmetry.*

Category	A_{CP}
Lepton	0.008 ± 0.089
Kaon1	0.005 ± 0.025
Kaon2	-0.003 ± 0.014
KaonPion	0.021 ± 0.014
Pion	-0.051 ± 0.012
Other	-0.070 ± 0.012
NoTag	0.0

where the *quasitrue* component consists of four tracks originating from the same B^0, but with ρ^0 reconstructed using an incorrect one.

- Signal-Like Charmless modes: $B^0 \to \rho^0 K^{*0}$ and $B^0 \to f_0 K^{*0}$, where $K^{*0} \to K^\pm \pi^\mp$. We have a significant number of these decays (~ 50 events for $\rho^0 K^{*0}$ vs. ~ 100 for $\rho^0\rho^0$) and with the exception of $K^\pm$ being misidentified as a $\pi^\pm$ they are very similar to the signal.

- SXF-Like Charmless cocktail: events with at least one fake or one missing charged track. It contains a combination of $\rho^0\rho^+$ (longitudinal), $\eta' K$, $\rho^0\pi^+$, $\rho^+\rho^-$ (longitudinal), $\rho^+\pi^-$, $\rho^-\pi^+$, $a_1^+ f_0$ and $a_1^0\pi^+$ modes parametrized as a single PDF. These decays resemble the SXF, rather than true signal, but are sufficiently abundant (~ 600 events) to pose problems when fitting.

- B background: All remaining$B$ decay modes (dominated by open charm $b \to c$ transitions).

- Continuum Background: Events originating from non-$B\overline{B}$ decays (mainly from $c\bar{c}$).

The expected yields for $a_1\pi$, Signal-Like and SXF-Like Charmless modes for the data are listed in Table 4.16.

The correlations between observables are sufficiently small ($< 15\%$) to be neglected (*e.g* the correlations for longitudinal signal events are listed in Table 4.17). The total PDF for every category can be defined as the product of the individual PDFs, and we can use Eq. (4.2) to describe the overall likelihood. However, in many cases topological correlations prevent this simple factorization. For example, the order of the reconstructed

Table 4.16: *Expected Charmless and $a_1\pi$ Branching Ratios (BR's) and yields for the Full Dataset.*

Mode	Efficiency (%)	$BR \times 10^6$	Expected Events
$a_1\pi$	2.8	19.9 ± 1.8	254 ± 24
f_0K^{*0}	3.3	1.7 ± 0.7	26 ± 18
ρ^0K^{*0}-long	3.2	2.1 ± 0.7	31 ± 11
ρ^0K^{*0}-tran	4.1	1.6 ± 1.1	30 ± 20
$\rho^0\rho^+$-long	1.5	15.2 ± 3.0	104 ± 20
$\eta'K(\eta' \to \rho^0\gamma)$	0.4	20.6 ± 1.1	38 ± 2
$\rho^0\pi^+$	0.6	8.7 ± 1.1	23 ± 3
$\rho^+\rho^-$-long	0.2	23.0 ± 3.2	18 ± 2
$\rho^+\pi^-$	0.3	12.0 ± 1.2	17 ± 2
$\rho^-\pi^+$	0.3	12.0 ± 1.2	16 ± 2
$a_1^+f_0$	0.3	10.0 ± 10.0	12 ± 12
$a_1^0\pi^+$	1.0	11.1 ± 2.8	50 ± 13

mesons in $B^0 \to \rho^0 f_0(980)$ decay (where if the first pair of pions forms a ρ^0 meson, the second forms f_0, and vice versa) is nontrivial and prevents us from factorizing $\mathcal{P}(m_1, m_2)$ as $\mathcal{P}(m_1) \times \mathcal{P}(m_2)$ ($\mathcal{P}(m_1, m_2) = \mathcal{P}(m_1^{f_0}, m_2^{\rho^0}) + \mathcal{P}(m_1^{\rho^0}, m_2^{f_0})$ in this case). The other instances include $B^0 \to a_1^{\pm}\pi^{\mp}$ decays, where the mass and helicity density functions have to be explicitly split into three components, helicity PDF for the signal $B^0 \to \rho^0\rho^0$ decays, which depends on the fraction f_L of the longitudinally-polarized decays, *etc.* In these cases the PDFs are parameterized as sums of appropriate products of factorisable PDFs.

Time-Dependent Fit Model

For the time-dependent component, we fit the B decay components (signal and background) with the *CP*-Model PDF, described in Eq. (4.3), convoluted with the Resolution Function of Eq. (4.4). In RooFit [74] this is referred to as the `RooBCPGenDecay` model. When performing a *CP*-symmetric fit to obtain the yields, we use `RooDecay` model

Table 4.17: *Correlation coefficients for (true) longitudinal* $B^0 \to \rho^0\rho^0$ *decays.*

	$m_{\rm ES}$	ΔE	m_1	m_2	$\lvert\cos\theta_1\rvert$	$\lvert\cos\theta_2\rvert$	$eShape$	Btag
$m_{\rm ES}$	1.00	-0.13	0.00	0.00	0.00	0.00	0.00	-0.01
ΔE	-0.13	1.00	0.02	0.01	0.00	0.00	-0.01	0.00
m_1	0.00	0.02	1.00	0.01	-0.01	-0.01	0.00	-0.01
m_2	0.00	0.01	0.01	1.00	0.00	-0.01	0.00	0.01
$\lvert\cos\theta_1\rvert$	0.00	0.00	-0.01	0.00	1.00	0.01	0.01	-0.01
$\lvert\cos\theta_2\rvert$	0.00	0.00	-0.01	-0.01	0.01	1.00	0.00	0.00
$eShape$	0.00	-0.01	0.00	0.00	0.01	0.00	1.00	0.00
Btag	-0.01	0.00	-0.01	0.01	-0.01	0.00	0.00	1.00

with the same time resolution function. Furthermore, for the continuum PDF we replace the CP-Model PDF with $f(\Delta t) = (1 \pm A_{CP})$ and convolute it with the standard resolution function (with the parameters and the values of A_{CP} determined from fitting to the sideband $m_{ES} < 5.27$ GeV).

4.5.3 PDF Construction

The backgrounds listed in Section 4.5.2 make it past the selection cuts (Table 4.5). These events can be distinguished from the signal based on the shape of their distributions in (at least some) of the observables. Thus, a large part of the analysis work involves constructing these PDFs with a minimal number of parameters (to reduce the systematics), while retaining the accuracy of the model.

Since the analysis is statistically limited (*i.e.* we have insufficient data for most of the modes) we rely on simulated events when constructing the PDFs. For the continuum, the Monte Carlo is not fully reliable; plus we have a much larger data sample. The corresponding PDFs are fitted to the sideband data ($m_{ES} < 5.27$ GeV or $-0.05 < \Delta E < 0.05$ GeV). More complex parameterizations generally arise for the mass-helicity functions, where the topology prevents factorization; as well as the time dependent component, where it is necessary to vary parameters based on the Tag value. The specifics of these parameterizations are discussed below. We show the fits in Appendix D and summarize them in Table. 4.18. Specific functions used are:

- Gauss - Standard Gaussian.
- 2G - A sum of two Standard Gaussians.
- 3G - A sum of two Asymmetric Gaussians and a Standard Gaussian.
- Pol(n) - Polynomial of order n.
- CB - Crystal Ball Function, which we use to parametrize m_{ES} for the Self Cross Feed (SXF) like backgrounds. CB$(x;\alpha,n,\bar{x},\sigma)$ is

  $$e^{-\frac{(x-\bar{x})^2}{2\sigma^2}}$$

  for $\frac{x-\bar{x}}{\sigma} > -\alpha$ and

  $$(\frac{n}{|\alpha|})^n e^{-\frac{|\alpha|^2}{2}}(\frac{n}{|\alpha|} - |\alpha| - \frac{x-\bar{x}}{\sigma})^{-n}$$

  for $\frac{x-\bar{x}}{\sigma} \leq -\alpha$, where $\alpha, n, \bar{x}, \sigma$ are coefficients obtained from the fit [81].
- Arg - Argus Function, which we use to parametrize m_{ES} for Continuum like backgrounds. Arg$(x;b,E_c)$ is

  $$x\sqrt{1-(x/E_c)^2}e^{b(1-(x/E_c)^2)},$$

  where $E_c = 5.29\text{MeV/c}^2$ is the cutoff energy and b is a coefficient determined from the fit [82].

- $M_{\rho,f,bkg}$ - Mass Funcition. We use a relativistic Breit-Wigner (BW) to parametrize the mass of ρ^0, f_0. BW$(x; m_{\rho^0}, \Gamma_0, r)$ is

  $$\frac{x m_{\rho^0}\Gamma}{(x^2 - m_{\rho^0}^2)^2 + m_{\rho^0}^2\Gamma^2}$$

  with

  $$\Gamma = \Gamma_0 \frac{m_{\rho^0}}{x}\left(\frac{x^2 - 4m_\pi^2}{m_{\rho^0}^2 - 4m_\pi^2}\right)^{3/2}\left(\frac{4/r^2 + m_{\rho^0}^2 - 4m_\pi^2}{4/r^2 + x^2 - 4m_\pi^2}\right),$$

  where $m_\pi = 0.14\mathrm{GeV/c^2}$ is the pion mass, while the parameters m_{ρ^0}, Γ_0, r are determined from the fit. The background mass PDF can usually be described by a polynomial.

- $H_{\rho,f,bkg}$ - Helicity Function. The helicity for ρ^0 is distributed as $\cos^2\theta$ ($\sin^2\theta$) for the longitudinally (transversely) polarized decays. The f_0 distribution is flat in $\cos\theta$, while backgrounds have a steeply increasing component (toward $\cos\theta = 1$). For all processes we multiply the above by resolution functions in order to account for detector effects as well as the impact of D-Veto (described in Section. 4.3.3).

- $Tmh(a,b) \equiv M_a(m_1)M_b(m_2)H_a(\theta_1)H_b(\theta_2) + M_a(m_2)M_b(m_1)H_a(\theta_2)H_b(\theta_1)$ - A symmetrized mass helicity function used to account for the fact that there are two kinds of reconstructed 'particles' (a,b) in the decay. For example, the mass-helicity distribution for $B^0 \to \rho^0 f_0(980)$ True Signal is

  $$Tmh(\rho^0, f_0) = M_\rho(m_1)M_f(m_2)H_\rho(\theta_1)H_f(\theta_2) + M_\rho(m_2)M_f(m_1)H_\rho(\theta_2)H_f(\theta_1).$$

- BGD(S,C) - the `RooBCPGenDecay` model described in Sections 4.5.1 and 4.5.2, which is a function of the CP coefficients S, C. The remaining parameters are listed in Tables 4.13, 4.14.

- BGD(S,C,μ_C,σ_C) - BGD(S,C) with the mean and σ for the central gaussian of the resolution function fitted to MC (of the component in question).
- F - Any remaining (and generally more complex) PDF, which is described in the text below.

Furthermore, a number of PDF components have the same functional form (and parameters). In this case, we refer to an already fitted component in parentheses. For example, Table. 4.18 we describe the m_{ES} entry for $f_0 f_0$ True is 2G(SigT). Thus the m_{ES} distribution for $f_0 f_0$ is identical to the m_{ES} distribution for the Sig True and is described by a sum of two Gaussian functions.

Table 4.18: *Functional Form for the PDFs used in the Maximum Likelihood Fit.*

Mode	$m_{\rm ES}$	ΔE	$eShape$	mass-helicity	Δt
Sig True	2G	2G	3G	$F_{\rho\rho}$	$F^{\Delta t}_{\rho\rho}$
Sig SXF	CB	Pol(2)	3G	$F_{\rho,bkg}$	$F^{\Delta t}_{\rho,bkg}$
f_0f_0 True	2G(Sig)	2G	3G(Sig)	$\mathrm{M}_{f_0}(m_1)\mathrm{M}_{f_0}(m_2)\mathrm{H}_{f_0}(\theta_1)\mathrm{H}_{f_0}(\theta_2)$	BGD(0,0)
f_0f_0 SXF	CB(SigSXF)	Pol(2)	3G	$Tmh(f_0,bkg)$	BGD(0,0)
ρ^0f_0 True	2G	2G	3G(Sig)	$Tmh(\rho^0,f_0)$	BGD(0,0)
ρ^0f_0 SXF	CB	Pol(2)	3G(SigSXF)	$F^{SXF}_{\rho^0,f_0}$	BGD(0,0)
$a_1\pi$ True	2G	2G	3G(Sig)	$Tmh(\rho^0,bkg))$	BGD($S_{a_1\pi}$,$C_{a_1\pi}$)
$a_1\pi$ QT	2G($a_1\pi$T)	2G	3G(Sig)	$Tmh(\sim\rho^0(a_1),\sim\rho^0(B^0))$	BGD($S_{a_1\pi}$,$C_{a_1\pi}$)
$a_1\pi$ SXF	Arg+2G	Gauss	F^{eShape}	$F^{SXF}_{a_1\pi}$	BGD($S_{a_1\pi}$,$C_{a_1\pi}$,μ_C,σ_C)
$\rho^0\pi^+\pi^-$	2G(Sig)	2G(∼Sig)	3G(Sig)	$Tmh(\rho^0,bkg)$	BGD(0,0)
$\pi^+\pi^-\pi^+\pi^-$	2G(Sig)	2G(∼Sig)	3G(Sig)	$\mathrm{M}_{bkg}(m_1)\mathrm{M}_{bkg}(m_2)\mathrm{H}_{bkg}(\theta_1)\mathrm{H}_{bkg}(\theta_2)$	BGD(0,0)
ρ^0K^{*0}	2G(Sig)	2G	3G	$F_{\rho^0K^{*0}}$	BGD(0,0,μ_C,σ_C)
f_0K^{*0}	2G(Sig)	2G	3G(ρ^0K^{*0})	$Tmh(f_0,K^{*0})$	BGD(0,0,μ_C,σ_C)
Chls	Arg+2G	Pol(0)	F^{eShape}_{Chls}	F_{Chls}	BGD(0,0,μ_C,σ_C)
$B\overline{B}$	Arg+Gauss	Pol(2)	3G	$F_{B\overline{B}}$	BGD(0,0,μ_C,σ_C)
Continuum	Arg	Pol(2)	3G	$F_{\rm qq}$	$F^{\Delta t}_{\rm qq}$

$B^0 \to \rho^0\rho^0$ PDF

The $B^0 \to \rho^0\rho^0$ helicity PDF is parametrized as:

$$\mathcal{P}^{\mathrm{hel}}_{\mathrm{sig}}(\theta_1,\theta_2,f_L) = \left(\frac{1}{4}\cdot(1-f_L)\cdot\sin^2\theta_1\sin^2\theta_2 + f_L\cdot\cos^2\theta_1\cos^2\theta_2\right)\cdot\mathcal{G}(\theta_1,\theta_2),$$

where f_L is the fraction of the longitudinal polarization and $\mathcal{G}(\theta_1,\theta_2)$ is a function we constructed to parametrize the effects of detector acceptance and D-Veto:

$$F_{\rho\rho} = M_\rho(m_1)M_\rho(m_2)\left(f_L H_\rho^{Long}(\theta_1)H_\rho^{Long}(\theta_2) + (1-f_L)H_\rho^{Tran}(\theta_1)H_\rho^{Tran}(\theta_2)\right) \tag{4.5}$$

The time-dependent component is described by the model

$$F^{\Delta t}_{\rho\rho} = f_L BGD(S_{CP},C_{CP}) + (1-f_L)BGD(0,0), \tag{4.6}$$

where S_{CP}, C_{CP} are the CP coefficients to be extracted from the fit (Note that the transversely-polarized component is not a CP eigenstate and therefore has $S = C = 0$). Thus, the total PDF for $B^0 \to \rho^0\rho^0$ True Signal is:

$$\mathcal{P}_{\mathrm{SigT}}(\vec{x};\vec{\alpha}) = \mathcal{P}_{\mathrm{SigT}}(\Delta t,\sigma_{\Delta t})\cdot\mathcal{P}_{\mathrm{SigT}}(m_{ES})\cdot\mathcal{P}_{\mathrm{SigT}}(\Delta E)\cdot\mathcal{P}_{\mathrm{SigT}}(eShape)\cdot \tag{4.7}$$

$$\mathcal{P}_{\mathrm{SigT}}(Tag)\cdot\mathcal{P}_{\mathrm{SigT}}(m_1)\cdot\mathcal{P}_{\mathrm{SigT}}(m_2)\cdot\mathcal{P}^{\mathrm{hel}}_{\mathrm{SigT}}(|\cos\theta_1|,|\cos\theta_2|,f_L)$$

In addition, we have the Self Cross Feed (SXF) component, which is defined as $B^0 \to \rho^0\rho^0 \to \pi^+\pi^-\pi^+\pi^-$ events reconstructed by picking up the wrong pion (and using it to reconstruct either of the ρ^0's). In this case, the mass-helicity distribution is described by the equivalent of Eq. (4.5) as

$$F_{\rho,bkg} = M_\rho(m_1)M_{bkg}(m_2)\left(f_L H_\rho^{Long}(\theta_1)H_{bkg}(\theta_2) + (1-f_L)H_\rho^{Tran}(\theta_1)H_{bkg}(\theta_2)\right) \tag{4.8}$$

$$+M_\rho(m_2)M_{bkg}(m_1)\left(f_L H_\rho^{Long}(\theta_2)H_{bkg}(\theta_1) + (1-f_L)H_\rho^{Tran}(\theta_2)H_{bkg}(\theta_1)\right)$$

and the time-dependent component becomes

$$F^{\Delta t}_{\rho,bkg} = f_L BGD(S_{CP}, C_{CP}, \mu_C, \sigma_C) + (1 - f_L) BGD(0, 0, \mu_C, \sigma_C), \tag{4.9}$$

where μ_C,σ_C are the same for the two components (but different from the True Signal). The total PDF (equivalent of Eq. (4.7)) is expressed as

$$\mathcal{P}_{\rm SigSXF}(\vec{x};\vec{\alpha}) = \mathcal{P}_{\rm SigSXF}(\Delta t, \sigma_{\Delta t}) \cdot \mathcal{P}_{\rm SigSXF}(m_{ES}) \cdot \mathcal{P}_{\rm SigSXF}(\Delta E) \cdot \tag{4.10}$$

$$\mathcal{P}_{\rm SigSXF}(eShape) \cdot \mathcal{P}_{\rm SigT}(Tag) \cdot \mathcal{P}^{m,\rm hel}_{\rm SigSXF}(m_1, m_2, |\cos\theta_1|, |\cos\theta_2|, f_L)$$

$B^0 \to f_0(980) f_0(980)$ PDF

For the $B^0 \to f_0(980) f_0(980)$ decays there is only one polarization (unpolarized), since $f_0(980)$ is a pseudoscalar. Hence, the PDFs take a much simpler form:

$$\mathcal{P}_{\rm f_0f_0True}(\vec{x};\vec{\alpha}) = \mathcal{P}_{\rm Sig_{00}}(\Delta t, \sigma_{\Delta t}) \cdot \mathcal{P}_{\rm SigT}(m_{ES}) \cdot \mathcal{P}_{\rm f_0f_0True}(\Delta E) \cdot \mathcal{P}_{\rm SigT}(eShape) \cdot \tag{4.11}$$

$$\mathcal{P}_{\rm SigT}(Tag) \cdot \mathcal{P}_{\rm f_0T}(m_1) \cdot \mathcal{P}_{\rm f_0T}(m_2) \cdot \mathcal{P}_{\rm f_0T}(|\cos\theta_1|) \cdot \mathcal{P}_{\rm f_0T}(|\cos\theta_2|),$$

$$\mathcal{P}_{\rm f_0f_0True}(\vec{x};\vec{\alpha}) = \mathcal{P}_{\rm Sig_{00}}(\Delta t, \sigma_{\Delta t}) \cdot \mathcal{P}_{\rm SigSXF}(m_{ES}) \cdot \mathcal{P}_{\rm f_0f_0SXF}(\Delta E) \cdot \mathcal{P}_{\rm f_0f_0SXF}(eShape) \cdot \tag{4.12}$$

$$\mathcal{P}_{\rm SigT}(Tag) \cdot Tmh(f_0, bkg),$$

where Sig_{00} denotes the signal distribution with $S = C = 0$ (*i.e.* $\mathcal{P}_{\rm Sig_{00}}(\Delta t, \sigma_{\Delta t})$ =BGD(0,0)).

$B^0 \to \rho^0 f_0(980)$ PDF

The $B^0 \to \rho^0 f_0(980)$ decay differs from $B^0 \to \rho^0\rho^0$ by the fact that there is an $f_0(980)$ instead of a ρ resonance. There is equal probability that the first pair of pions forms a ρ^0 or f_0. Thus the PDFs are:

$$\mathcal{P}_{\rm f_0\rho^0T}(\vec{x};\vec{\alpha}) = \mathcal{P}_{\rm Sig_{00}}(\Delta t, \sigma_{\Delta t}) \cdot \mathcal{P}_{\rm f_0\rho^0T}(m_{ES}) \cdot \mathcal{P}_{\rm f_0\rho^0T}(\Delta E) \cdot \mathcal{P}_{\rm SigT}(eShape) \cdot \mathcal{P}_{\rm SigT}(Tag) \cdot \tag{4.13}$$

$$[\mathcal{P}_{\rm SigT}(m_1)\cdot\mathcal{P}_{\rm f_0}(m_2)\cdot\mathcal{P}_{\rm SigT}(|\cos\theta_1|)\cdot\mathcal{P}_{\rm f_0}(|\cos\theta_2|)+\mathcal{P}_{\rm SigT}(m_2)\cdot\mathcal{P}_{\rm f_0}(m_1)\cdot\mathcal{P}_{\rm SigT}(|\cos\theta_2|)\cdot\mathcal{P}_{\rm f_0}(|\cos\theta_1|)]$$

and

$$\mathcal{P}_{\rm f_0\rho^0SXF}(\vec{x};\vec{\alpha}) = \mathcal{P}_{\rm Sig_{00}}(\Delta t,\sigma_{\Delta t})\cdot\mathcal{P}_{\rm f_0\rho^0SXF}(m_{ES})\cdot\mathcal{P}_{\rm f_0\rho^0SXF}(\Delta E)\cdot\mathcal{P}_{\rm SigSXF}(eShape)\cdot \tag{4.14}$$

$$\mathcal{P}_{\rm SigT}(Tag)\cdot F^{SXF}_{\rho^0,f_0},$$

where $F^{SXF}_{\rho^0,f_0} = ((1-f_{\rho^0})Tmh(f_0,bkg)+f_{\rho^0}Tmh(\rho^0,bkg))$.

$B^0 \to a_1^{\pm}\pi^{\mp}$ PDF

The decay occurs as $B^0 \to a_1^{\pm}\pi^{\mp} \to \rho^0\pi^{\pm}\pi^{\mp} \to \pi^+\pi^-\pi^{\pm}\pi^{\mp}$. The corresponding PDF has a True component, where the ρ^0 is reconstructed correctly; plus a Quasi-True component, where one of the pions used to reconstruct ρ^0 comes from either the decay of the a_1 or B^0 (and the other comes from the ρ^0). They are:

$$\mathcal{P}_{\rm a_1\pi T}(\vec{x};\vec{\alpha}) = \mathcal{P}_{\rm a_1\pi}(\Delta t,\sigma_{\Delta t})\cdot\mathcal{P}_{\rm a_1\pi T}(m_{ES})\cdot\mathcal{P}_{\rm a_1\pi T}(\Delta E)\cdot \tag{4.15}$$

$$\mathcal{P}_{\rm SigT}(eShape)\cdot\mathcal{P}_{\rm SigT}(Tag)\cdot Tmh(\rho^0,bkg))$$

and

$$\mathcal{P}_{\rm a_1\pi QT}(\vec{x};\vec{\alpha}) = \mathcal{P}_{\rm a_1\pi}(\Delta t,\sigma_{\Delta t})\cdot\mathcal{P}_{\rm a_1\pi T}(m_{ES})\cdot\mathcal{P}_{\rm a_1\pi QT}(\Delta E)\cdot \tag{4.16}$$

$$\mathcal{P}_{\rm SigT}(eShape)\cdot\mathcal{P}_{\rm SigT}(Tag)\cdot Tmh(\sim\rho^0(a_1),\sim\rho^0(B^0)),$$

where $\sim$ indicates a ρ^0 reconstructed with the wrong pion (selected from the right B^0). Likewise, there is a corresponding Self Cross Feed component, where any one of the three types of pions (coming from ρ^0, directly from a_1, or directly from B^0) has been selected incorrectly:

$$\mathcal{P}_{\mathrm{a_1\pi SXF}}(\vec{x};\vec{\alpha}) = \mathcal{P}_{\mathrm{a_1\pi}}(\Delta t,\sigma_{\Delta t})\cdot\mathcal{P}_{\mathrm{a_1\pi SXF}}(m_{ES})\cdot\mathcal{P}_{\mathrm{a_1\pi SXF}}(\Delta E)\cdot \tag{4.17}$$

$$\mathcal{P}_{\mathrm{a_1\pi SXF}}(eShape)\cdot\mathcal{P}_{\mathrm{SigT}}(Tag)\cdot F^{SXF}_{a_1\pi},$$

where

$$F^{SXF}_{a_1\pi} = f_\rho Tmh(\rho^0,bkg))+(1-f_\rho-f_{bkg})Tmh(bkg_1,bkg_2)+f_{bkg}\mathrm{M}_{bkg}(m_1)\mathrm{M}_{bkg}(m_2)\mathrm{H}_{bkg}(\theta_1)\mathrm{H}_{bkg}(\theta_2),$$

$$F^{eShape}_{a_1\pi} = 3\mathrm{G}(\mathrm{Sig}) + 3\mathrm{G}(\mathrm{SigSXF}) + 3\mathrm{G}(B\overline{B}). \tag{4.18}$$

Furthermore, the CP coefficients for this mode are nonzero, and we use $S_{a_1\pi} = 0.38\pm0.20$, $C_{a_1\pi} = -0.12\pm0.18$ from the *BABAR* $B^0\to a_1\pi$ measurement [56].

$B^0\to\rho^0\pi^+\pi^-$ PDF

This process is distinguished from the signal by the fact that the two of the four pions originate directly from the B^0 rather than a ρ^0. Thus, other than in the mass-helicity component, the PDF is very similar to the signal:

$$\mathcal{P}_{\rho^0\pi^+\pi^-}(\vec{x};\vec{\alpha}) = \mathcal{P}_{\mathrm{Sig_{00}}}(\Delta t,\sigma_{\Delta t})\cdot\mathcal{P}_{\mathrm{SigT}}(m_{ES})\cdot\mathcal{P}_{\sim\mathrm{SigT}}(\Delta E)\cdot\mathcal{P}_{\mathrm{SigT}}(eShape)\cdot \tag{4.19}$$

$$\mathcal{P}_{\mathrm{SigT}}(Tag)\cdot Tmh(\rho^0,bkg),$$

where $\sim SigT$ denotes a distribution that has the same functional form and most of the parameters as the True Signal. Also note that while the Monte Carlo simulates ρ^0 as unpolarized, we fit the data with the (physical) longitudinal ρ^0 helicity distribution.

$B^0 \to \pi^+\pi^-\pi^+\pi^-$ PDF

In this case B^0 decays directly to $\pi^+\pi^-\pi^+\pi^-$, without any ρ^0 resonances. The PDFs are flat in helicity (with the exception of the acceptance function) as well as polynomial (*i.e.* background-like) in mass, but otherwise resemble the signal:

$$\mathcal{P}_{\pi^+\pi^-\pi^+\pi^-}(\vec{x};\vec{\alpha}) = \mathcal{P}_{\mathrm{Sig}_{00}}(\Delta t, \sigma_{\Delta t}) \cdot \mathcal{P}_{\mathrm{SigT}}(m_{ES}) \cdot \mathcal{P}_{\sim\mathrm{SigT}}(\Delta E) \cdot \mathcal{P}_{\mathrm{SigT}}(eShape) \cdot \tag{4.20}$$

$$\mathcal{P}_{\mathrm{SigT}}(Tag) \cdot \mathcal{P}_{\pi^+\pi^-\pi^+\pi^-}(m_1) \cdot \mathcal{P}_{\pi^+\pi^-\pi^+\pi^-}(m_2) \cdot \mathcal{P}_{\mathrm{Sig}_{\mathrm{Tran}}}(|\cos\theta_1|) \cdot \mathcal{P}_{\mathrm{Sig}_{\mathrm{Tran}}}(|\cos\theta_2|),$$

where $\sim SigT$ once again denotes a distribution that has the same functional form and most of the parameters as the True Signal, while Sig_{Tran} refers to the Transverse Signal component.

Charmless PDF

The Charmless background is a combination of modes (listed in Table. 4.16), which bear some similarity to the signal. It consists of signal-like modes $\rho^0 K^{*0}$, $f_0 K^{*0}$ (where $K^* \to K\pi$ with the K being misidentified as a π), as well as the SXF-like cocktail (denoted $Chls$). The PDF is:

$$\mathcal{P}_{\mathrm{FullCharmless}}(\vec{x};\vec{\alpha}) = \frac{1}{N_{\rho^0 K^{*0}} + N_{f_0 K^{*0}} + N_{Chls}} \tag{4.21}$$

$$\left(N_{\rho^0 K^{*0}} \mathcal{P}_{\rho^0 \mathrm{K}^{*0}}(\vec{x};\vec{\alpha}) + N_{f_0 K^{*0}} \mathcal{P}_{\mathrm{f_0 K}^{*0}}(\vec{x};\vec{\alpha}) + N_{Chls} \mathcal{P}_{\mathrm{Chls}}(\vec{x};\vec{\alpha})\right),$$

where we fix $N_{\rho^0 K^{*0}} = 62$, $N_{f_0 K^{*0}} = 26$ (based on the Branching Fraction estimates [58]), while allowing N_{Chls} to float in the fit to the data. The corresponding PDFs are:

$$\mathcal{P}_{\rho^0 \mathrm{K}^{*0}}(\vec{x};\vec{\alpha}) = \mathcal{P}_{\rho^0 \mathrm{K}^{*0}}(\Delta t, \sigma_{\Delta t}) \cdot \mathcal{P}_{\mathrm{SigT}}(m_{ES}) \cdot \mathcal{P}_{\rho^0 \mathrm{K}^{*0}}(\Delta E) \cdot \tag{4.22}$$

$$\mathcal{P}_{\rho^0\mathrm{K}^{*0}}(eShape)\cdot\mathcal{P}_{\mathrm{SigT}}(Tag)\cdot F_{\rho^0K^{*0}},$$

$$\mathcal{P}_{\mathrm{f_0K^{*0}}}(\vec{x};\vec{\alpha})=\mathcal{P}_{\mathrm{f_0K^{*0}}}(\Delta t,\sigma_{\Delta t})\cdot\mathcal{P}_{\mathrm{SigT}}(m_{ES})\cdot\mathcal{P}_{\mathrm{f_0K^{*0}}}(\Delta E)\cdot \tag{4.23}$$

$$\mathcal{P}_{\rho^0\mathrm{K}^{*0}}(eShape)\cdot\mathcal{P}_{\mathrm{SigT}}(Tag)\cdot Tmh(f_0K^{*0}),$$

$$\mathcal{P}_{\mathrm{Chls}}(\vec{x};\vec{\alpha})=\mathcal{P}_{\mathrm{Chls}}(\Delta t,\sigma_{\Delta t})\cdot\mathcal{P}_{\mathrm{Chls}}(m_{ES})\cdot\mathcal{P}_{\mathrm{Chls}}(\Delta E)\cdot \tag{4.24}$$

$$\mathcal{P}_{\mathrm{Chls}}(eShape)\cdot\mathcal{P}_{\mathrm{Chls}}(Tag)\cdot F_{Chls}.$$

For ρ^0K^{*0} we account for the Longitudinal and Transverse components of polarization in the mass-helicity distribution:

$$F_{\rho^0K^{*0}}=f_{\rho^0K^{*0}-Long}Tmh(\rho^0_{Long},K^{*0})+(1-f_{\rho^0K^{*0}-Long})Tmh(\rho^0_{Tran},K^{*0}). \tag{4.25}$$

The SXF-like cocktail mass-helicity requires a more complex parametrization with components containing a peak resembling ρ^0, a peak resembling f_0 and a continuum-type background:

$$F_{Chls}=f_{\sim\rho}Tmh(\sim\rho^0,bkg)+ \tag{4.26}$$

$$(1-f_{\sim\rho}-f_{cont})Tmh(\sim f_0,bkg)+f_{cont}\mathrm{M}_{cont}(m_1)\mathrm{M}_{cont}(m_2)\mathrm{H}_{cont}(\theta_1)\mathrm{H}_{cont}(\theta_2),$$

$$F^{eShape}_{Chls}=3\mathrm{G}(\mathrm{SigSXF})+3\mathrm{G}(B\overline{B}) \tag{4.27}$$

$B\overline{B}$ PDF

The $B\overline{B}$ background is a combination of all remaining B decays. When constructing its PDF, we account for resonance production as well as the significant correlations between mass and helicity component (on the other hand, correlations between the first and second reconstructed ρ^0 are negligible):

$$\mathcal{P}_{\mathrm{B\bar{B}}}(\vec{x}_j;\vec{\alpha})=\mathcal{P}_{\mathrm{B\bar{B}}}(\Delta t,\sigma_{\Delta t})\cdot\mathcal{P}_{\mathrm{B\bar{B}}}(m_{ES})\cdot\mathcal{P}_{\mathrm{B\bar{B}}}(\Delta E)\cdot\mathcal{P}_{\mathrm{B\bar{B}}}(eShape)\cdot\mathcal{P}_{\mathrm{B\bar{B}}}(Tag)\cdot F_{B\overline{B}},$$

where

$$F_{B\bar{B}} = \mathcal{P}_{\mathrm{B\bar{B}}}(m_1, |\cos\theta_1|) \cdot \mathcal{P}_{\mathrm{B\bar{B}}}(m_2, |\cos\theta_2|), \tag{4.28}$$

$$\mathcal{P}_{\mathrm{B\bar{B}}}(m_i, |\cos\theta_i|) = f^{\mathrm{B\bar{B}}}_{\rho^0} \cdot \mathcal{P}^{\rho^0}_{\mathrm{B\bar{B}}}(m_i) \cdot \mathcal{P}^{\rho^0}_{\mathrm{B\bar{B}}}(|\cos\theta_i|) + (1 - f^{\mathrm{B\bar{B}}}_{\rho^0}) \cdot \mathcal{P}^{\mathrm{comb}}_{\mathrm{B\bar{B}}}(m_i) \cdot \mathcal{P}^{\mathrm{comb}}_{\mathrm{B\bar{B}}}(|\cos\theta_i|).$$

Continuum PDF

The continuum consists of jetty events, which are mainly distinguished from the B-decays via the Neural Net variable *eShape*. However, we must properly account for the topological structure in the mass-helicity component, which consists of ρ^0, K^{*0}, f_0-type events as well as non-resonant continuum. The total PDF is written as:

$$\mathcal{P}_{\mathrm{qq}}(\vec{x};\vec{\alpha}) = \mathcal{P}_{\mathrm{qq}}(\Delta t, \sigma_{\Delta t}) \cdot \mathcal{P}_{\mathrm{qq}}(m_{ES}) \cdot \mathcal{P}_{\mathrm{qq}}(\Delta E) \cdot \mathcal{P}_{\mathrm{qq}}(eShape) \cdot \mathcal{P}_{\mathrm{qq}}(Tag) \cdot F_{\mathrm{qq}}, \tag{4.29}$$

where $F^{\Delta t}_{qq} = \mathcal{P}_{\mathrm{qq}}(\Delta t, \sigma_{\Delta t})$ is $(1 \pm A_{CP})$ convoluted with a standard resolution function, as described in section 4.5.2. Also note that $\mathcal{P}_{\mathrm{qq}}(m_{ES})$ is obtained from the ΔE sideband ($-0.5 < \Delta E < 0.5$ GeV), while all other components are fitted to the m_{ES} sideband ($m_{ES} <$ 5.27 GeV). Since there are significant correlations between mass and helicity components for each reconstructed ρ^0 (but not between the two reconstructed ρ^0's), $F_{\mathrm{qq}} = F^1_{\mathrm{qq}} \cdot F^2_{\mathrm{qq}}$.

$$F^i_{\mathrm{qq}} = f^{\mathrm{qq}}_{\rho^0,\sim K} \cdot \mathcal{P}^{\rho^0,\sim K}_{\mathrm{qq}}(m_i, |\cos\theta_i|) + \tag{4.30}$$

$$f^{\mathrm{qq}}_{\sim f_0} \cdot \mathcal{P}^{\sim f_0}_{\mathrm{qq}}(m_i, |\cos\theta_i|)(1 - f^{\mathrm{qq}}_{\rho^0,\sim K} - f^{\mathrm{qq}}_{\sim f_0})\mathcal{P}^{\mathrm{comb}}_{\mathrm{qq}}(m_i, |\cos\theta_i|),$$

where $\sim$ denotes a distribution at the location of the resonance, but with some parameters allowed to float. The $\mathcal{P}$'s account for the mass-helicity correlations and cannot be factorized. All of the PDFs are shown in Appendix D.

4.5.4 Fit On Data

Upon constructing all of the PDFs, we combine them and perform a fit on the data. Since the MC (or sideband) may not be a perfect match to it, a number of parameters are allowed to float in the process. In order to obtain the final values for the yields and CP coefficients, we go through the following steps:

1. *CP-Symmetric* (Mass-Helicity) Yield Fit - Here we use the Δt variables and the flavor tagging categories, but not the *sign* of the flavor tag. Some (10) of the mass-helicity parameters as well as the yields are allowed to float.
2. *CP-Symmetric* (*eShape*) Yield Fit - Once the mass-helicity parameters have been determined, we repeat the above procedure allowing 10 m_{ES}, ΔE and *eShape* parameters to float.
3. *CP* (Δt) Fit - Full *CP* fit with fixed S and C. The resolution parameters for the Continuum ($\mu_c^{Bkg}(Tag)$, $\sigma_c^{Bkg}(Tag)$) as well as the lifetimes $\tau_{B\overline{B}}$, τ_{Chls} are fitted for.
4. Full *CP* Fit - The final *CP* fit for the yields of $\rho^0\rho^0$, $\rho^0 f_0$, $f_0 f_0$, $a_1\pi$, Chls, $B\overline{B}$ and the continuum, plus S_L, C_L fitted for.

The above steps are repeated as necessary, but correlations between observables are fairly small and we do not have any difficulties getting the fit to converge.

4.6 Fit Validation

Validating the fit is a continuous process where the fitter grows in complexity and the *BABAR* dataset gets bigger over time. It consists of a series of steps, which generally rely upon and serve as an enhancement to the previous ones, as outlined in [49], [50]. Below we present a streamlined version, which is used to validate the final fit (on the complete dataset).

4.6.1 Validation Procedure

We use MC to verify convergence and measure the fit bias via the following procedure:

1. Generate Toy Monte Carlo events for the Continuum and $B\overline{B}$ backgrounds from PDF (*i.e.* it would be impractical to run the full simulation for this many events, thus we generate the events from the fitted PDFs).
2. Generate randomly-distributed TaggingCategory and FlavorSign variables for these components.
3. Construct 100 datasets by embedding all other modes from the fully reconstructed MC within the generated Continuum and $B\overline{B}$ backgrounds.
4. Perform a Maximum Likelihood Fit on each dataset (first fit for the yields and then for S, C).

4.6.2 Basic Fitter

The first step is verify that the Basic Fitter (*i.e.* without the non-resonant (NR) modes $\rho^0\pi^+\pi^-$, $\pi^+\pi^-\pi^+\pi^-$; which cause most of the convergence problems) converges and returns the correct values. The input yields are based on the measured branching ratios [21], while $S = -0.4$ and $C = 0.0$ are the values of the CP coefficients in the generated

Table 4.19: *Test results for the Basic Fitter.*

Parameter	Given	Fitted	RMS
$N_{\rho^0\rho^0-\mathrm{Long}}$	56	54.4 ± 2.3	23.4
$N_{\rho^0\rho^0-\mathrm{Tran}}$	29	26.6 ± 1.4	13.6
$N_{Continuum}$	6.230×10^4	$6.246 \times 10^4 \pm 26$	256
S	-0.4	-0.52 ± 0.12	1.00
C	0.0	0.07 ± 0.10	0.89
S-Pull	0.0	-0.11 ± 0.11	0.99
C-Pull	0.0	0.17 ± 0.14	1.19
Convergence	100	75	
$N_{\rho^0 f_0}$	6	10.9 ± 2.1	21.3
$N_{f_0 f_0}$	6	3.5 ± 0.8	8.5
$N_{a_1\pi}$	226	282.7 ± 5.2	51.8
$N_{Charmless}$	246	206.5 ± 8.9	89.1
$N_{B\overline{B}}$	2698	2523 ± 15	153

Monte Carlo (in Section 4.8.3 we study the effects of varying the Signal Yields, S and C). The given values, along with the fit results, are summarized in Table 4.19. A particular fit is defined to have converged when $|S_{fitted} - S_{expected}| < 2.55$, $|C_{fitted} - C_{expected}| < 1.95$ (*i.e.* we eliminate the fits where the S or C values hit their limits). Histograms of Signal, S, C and their pulls are shown in Fig. E.1 (Pull≡(Fitted Value - Expected Value)/Error). All yields and parameters are within the expected range. We conclude that this fitter is capable of both successfully isolating $\rho^0\rho^0$ events in the available data and determining corresponding S, C values.

4.6.3 Full Fitter Verification

The Full Fitter contains the NR ($\rho^0\pi^+\pi^-$, $\pi^+\pi^-\pi^+\pi^-$) modes. These decays are particularly problematic because of their similarity to the Signal, with the main distinctions coming from the mass-helicity distributions. The $\rho^0\pi^+\pi^-$ Monte-Carlo corresponds to the unpolarized configuration (*i.e.* the ρ^0 has a uniform helicity distribution), which is not physical. Thus we assume the $\rho^0 \to \pi^+\pi^-$ are in S-wave and perform each test after changing the helicity PDF to be longitudinal. All parameters are fitted to the MC and then the true ρ^0 helicity PDF is multiplied by $\cos^2\theta$ (such $\rho^0\pi^+\pi^-$ events have to be generated from their PDF). We perform the validations for the following configurations:

- The NR yields are at their upper limits of 26 $\rho^0\pi^+\pi^-$, 30 $\pi^+\pi^-\pi^+\pi^-$ events (corresponding to $BR(\rho^0\pi\pi) = 5\times10^{-6}$, $BR(4\pi) = 9\times10^{-6}$). The results are shown in Table 4.20 and Fig. E.2.

- The NR yields are at their lower limit (0 $\rho^0\pi^+\pi^-$, 0 $\pi^+\pi^-\pi^+\pi^-$ events) with their fitted yields restricted to their physical values (*i.e.* greater than zero). The results are shown in Table 4.21 and Fig. E.3.

- The NR yields are at their lower limit (0 $\rho^0\pi^+\pi^-$, 0 $\pi^+\pi^-\pi^+\pi^-$ events) without any restrictions on their fitted yields. The results are shown in Table 4.22 and Fig. E.4.

These tests demonstrate that even when the NR Yields allowed to float, there is no significant bias in the yields, polarizations, S or C exhibited by any of the fitters. When we require the Non-Resonant Yields to be above 0 there is a bias and an asymmetry in the Pulls, as a result of the correlations with the NR modes (Fig E.3). However, if the NR Yields aren't restricted, there is no (statistically significant) bias in the Pulls or their RMS (Fig. E.4). Thus, we allow the NR yields to fluctuate below 0 when fitting the data.

Table 4.20: *Test results for the Full Fitter, where* $\rho^0\pi^+\pi^-$ *and* $\pi^+\pi^-\pi^+\pi^-$ *are at their upper limit.*

Parameter	Given	Fitted	RMS
$N_{\rho^0\rho^0-\mathrm{Long}}$	56	60.4 ± 3.1	30.9
$N_{\rho^0\rho^0-\mathrm{Tran}}$	29	30.4 ± 1.9	19.1
$N_{\rho^0\pi^+\pi^-}$	26	11.1 ± 4.7	47.4
$N_{\pi^+\pi^-\pi^+\pi^-}$	30	30.2 ± 3.2	32.3
$N_{Continuum}$	6.230×10^4	$6.25 \times 10^4 \pm 26$	255
S	-0.4	-0.37 ± 0.12	1.06
C	0.0	-0.05 ± 0.09	0.78
S-Pull	0.0	0.14 ± 0.11	0.98
C-Pull	0.0	0.01 ± 0.11	0.93
Convergence	100	77	
$N_{\rho^0 f_0}$	6	12.9 ± 2.6	26.3
$N_{f_0 f_0}$	6	2.8 ± 1.0	10.4
$N_{a_1\pi}$	226	288.8 ± 5.9	58.6
$N_{Charmless}$	246	198.4 ± 9.1	91.3
$N_{B\overline{B}}$	2698	2521 ± 15	152

4.6.4 Comparison With The Saclay Fitter

As an additional crosscheck, the *Saclay* group constructed its own fitter (using the same PDFs with a different fitting code), and we compared the two by studying how each fits the Monte-Carlo events generated by the other team. Specifically, each group constructed 100 toy datasets, where the Continuum and $B\overline{B}$ events were generated from their PDFs and everything else was directly embedded (subject to Poisson smearing). When fitting, we restricted $-2 < C_{LBNL} < 2$, $-3 < S_{LBNL} < 3$, $-2 < C_{Saclay} < 2$, $-3 < S_{Saclay} < 3$, and made the plots by symmetrically cutting off the outliers (*i.e.* $-1.95 < C < 1.95$, $-2.95 < S < 2.15$). The results for Full Run 1-6 tests are shown in Fig. E.5 and Fig. E.6. We observed a good agreement between the two fitters.

Table 4.21: *Test results for the Full Fitter with zero expected events for* $\rho^0\pi^+\pi^-$ *and* $\pi^+\pi^-\pi^+\pi^-$ *modes. The Fitted NR Yields are restricted to be above* 0.

Parameter	Given	Fitted	RMS
$N_{\rho^0\rho^0-\text{Long}}$	56	$54.8^{+2.3}_{-2.7}$	$^{+23.4}_{-26.9}$
$N_{\rho^0\rho^0-\text{Tran}}$	29	$27.2^{+1.1}_{-1.3}$	$^{+11.1}_{-13.5}$
$N_{\rho^0\pi^+\pi^-}$	0	0	–
$N_{\pi^+\pi^-\pi^+\pi^-}$	0	0	–
$N_{Continuum}$	6.230×10^4	$6.246 \times 10^4 \pm 26$	256
S	-0.4	-0.50 ± 0.12	1.00
C	0.0	0.05 ± 0.11	0.91
S-Pull	0.0	-0.07 ± 0.11	0.93
C-Pull	0.0	0.13 ± 0.13	1.14
Convergence	100	73	
$N_{\rho^0 f_0}$	6	6.5 ± 2.2	22.2
$N_{f_0 f_0}$	6	3.2 ± 0.9	8.9
$N_{a_1\pi}$	226	280.8 ± 5.3	52.7
$N_{Charmless}$	246	209.3 ± 9.1	90.8
$N_{B\bar{B}}$	2698	2521 ± 15	154

4.6.5 Blind Fit

We apply the full fitter to the our dataset, while blinding the signal yields along with S, C. This is done both with and without the non-resonant modes present. The results are shown in Table 4.23, with the correlations between the yields given in Table 4.24. Note that even-though we list the 'values' for S and C, they are still blind, but the offset is the same for the NR Yields > 0 and Unrestricted NR cases (*i.e.* the blinding procedure shifts the values for S and C, but it does so in the same manner for all fits).

We compare the yields to their expected values. The results are consistent with the Toy Validation (Table 4.19), once the increase in the size of the dataset(from 65637 to 72154

Table 4.22: *Test results for the Full Fitter with zero expected events for* $\rho^0\pi^+\pi^-$ *and* $\pi^+\pi^-\pi^+\pi^-$ *modes.*

Parameter	Given	Fitted	RMS
$N_{\rho^0\rho^0-\mathrm{Long}}$	56	59.9 ± 3.1	30.6
$N_{\rho^0\rho^0-\mathrm{Tran}}$	29	29.7 ± 1.9	19.1
$N_{\rho^0\pi^+\pi^-}$	0	-10.8 ± 4.8	48.4
$N_{\pi^+\pi^-\pi^+\pi^-}$	0	-4.1 ± 3.6	36.4
$N_{Continuum}$	6.230×10^4	$6.246 \times 10^4 \pm 26$	256
S	-0.4	-0.43 ± 0.11	0.98
C	0.0	0.06 ± 0.10	0.86
S-Pull	0.0	-0.02 ± 0.11	0.98
C-Pull	0.0	0.14 ± 0.13	1.14
Convergence	100	79	
$N_{\rho^0 f_0}$	6	12.8 ± 2.5	25.4
$N_{f_0 f_0}$	6	3.8 ± 0.9	8.9
$N_{a_1\pi}$	226	286.4 ± 5.3	53.3
$N_{Charmless}$	246	202.1 ± 9.2	91.7
$N_{B\overline{B}}$	2698	2529 ± 16	155

events) is taken into account. The only troubling portion is the Charmless, which is ~ 400 events higher than the expected value. However, this is a common feature which has always been present in the fitter, and it is explained by the high degree of correlation between Charmless and $B\overline{B}$ components (and to a lesser extent $a_1\pi$). Moreover, the Charmless PDF does not include some of the poorly known multi-body charmless final states (their PDFs are also SXF-like, and are consumed by the combination of the Charmless and $B\overline{B}$ yields in the data fit). Overall, the blind fit results are what we expected and do not reveal any defects in the fitter.

Table 4.23: *Blind Results of the fit on The Full Fit.*

Parameter	NR Yields > 0	Unrestricted NR
$N_{\rho^0\rho^0}$	X ± 29.1	X ± 35.3
$f_L(\rho^0\rho^0)$	X ± 0.149	X ± 0.151
$C_L(\rho^0\rho^0)$	-0.04 ± 0.87	0.06 ± 0.82
$S_L(\rho^0\rho^0)$	-0.07 ± 0.87	-0.03 ± 0.72
$N_{\rho^0 f_0}$	X ± 17.7	X ± 21.7
$N_{f_0 f_0}$	X ± 0.03	X ± 7.8
$N_{\rho^0\pi^+\pi^-}$	X ± 3.0	X ± 29.7
$N_{\pi^+\pi^-\pi^+\pi^-}$	X ± 2.4	X ± 39.3
$N_{a_1\pi}$	272.1 ± 52.7	280.7 ± 52.5
N_{Chls}	694 ± 98.5	681.6 ± 98.3
N_{BBbar}	2134 ± 158	2144 ± 158
$N_{Continuum}$	68874 ± 286	68872 ± 287

Table 4.24: *Relevant Correlation Coefficients for The Full Fit.*

Parameter	$f_L(\rho^0\rho^0)$	N_{BBbar}	$N_{Continuum}$	N_{Chls}	$N_{a_1\pi}$	$N_{\rho^0\rho^0}$
$f_L(\rho^0\rho^0)$	1.000	0.001	0.018	-0.027	-0.178	0.187
N_{BBbar}	0.001	1.000	-0.369	-0.369	-0.162	-0.047
$N_{Continuum}$	0.018	-0.369	1.000	0.068	0.012	0.004
N_{Chls}	-0.027	-0.369	0.068	1.000	-0.300	-0.016
$N_{a_1\pi}$	-0.178	-0.162	0.012	-0.300	1.000	-0.243
$N_{\rho^0\rho^0}$	0.187	-0.047	0.004	-0.016	-0.243	1.000

4.7 Results

We now perform the full fit (without blinding) and summarize the results in Table 4.25. We also compute the likelihood (L) for yields near the fitted values for $\rho^0\rho^0$, $\rho^0\pi^+\pi^-$, $\pi^+\pi^-\pi^+\pi^-$ and display the scans for $NLL = -2Ln(L/L_0)$ in Fig. 4.7. Assuming a gaussian distribution for the likelihood

$$L(Y) = L_0 e^{-\frac{1}{2}(\frac{Y-Y_0}{\sigma})^2}, \tag{4.31}$$

Table 4.25: *Unblinded Values for the Full Fit. The third column gives the values for the fit when the likeShape variable is used instead of eShape (for a description and comparison between the two see Appendix C).*

Parameter	Fitted Value	Fitted Using *likeShape*
$N_{\rho^0\rho^0}$	$107.0^{+35.3}_{-34.3}$	$88.1^{+33.6}_{-32.3}$
$f_L(\rho^0\rho^0)$	$0.712^{+0.129}_{-0.151}$	$0.699^{+0.148}_{-0.187}$
S_L	$0.26^{+0.67}_{-0.73}$	$0.31^{+0.80}_{-0.87}$
C_L	$0.20^{+0.82}_{-0.70}$	$0.48^{+1.14}_{-0.81}$
$N_{\rho^0 f_0}$	$10.2^{+21.7}_{-20.1}$	$0.6^{+20.0}_{-17.9}$
$N_{f_0 f_0}$	$4.4^{+7.8}_{-4.9}$	$4.3^{+7.1}_{-4.4}$
$N_{\rho^0\pi^+\pi^-}$	$-23.5^{+39.3}_{-35.2}$	$-2.8^{+39.6}_{-36.2}$
$N_{\pi^+\pi^-\pi^+\pi^-}$	$3.7^{+29.7}_{-25.3}$	$8.9^{+28.1}_{-23.9}$

where Y is the event yield, Y_0 is its most probable (*i.e.* fitted) value and sigma is the error;

$NLL = 1$ corresponds to a 1σ deviation, $NLL = 2$ corresponds to 2σ, *etc.*

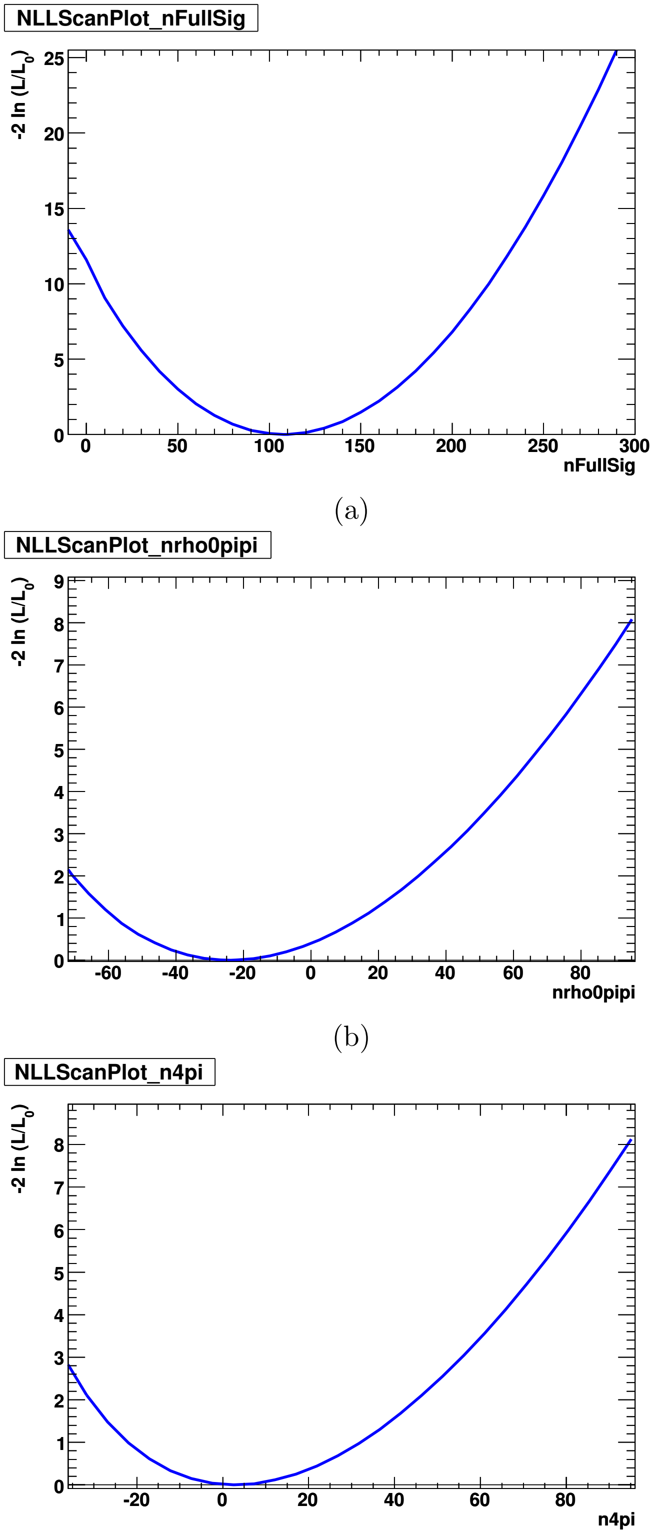

(a)

(b)

(c)

Figure 4.7: *Likelihood Scans (i.e. the NLL values vs. corresponding yields) for a)* $\rho^0\rho^0$, *b)* $\rho^0\pi^+\pi^-$ *and c)* $\pi^+\pi^-\pi^+\pi^-$.

4.8 Validation II

Once the fit results have been obtained, we construct and examine a series of projections to ensure validity of the fit. In addition, we vary the parameter values about the fitted results in order to account for any additional bias.

4.8.1 Projections

sPlots

We implement the technique developed by *Pivk and Diberder* [76] to construct sPlot projections. When making an sPlot for a particular variable (x) we:

1. Perform fits needed to obtain PDF distributions in all other variables as well as to get the yields for each particle species present.
2. Use the likelihoods to construct the sWeights and determine how much background is present in each bin.
3. Plot the difference between the total and the background (along with the corresponding errors).

The approach is designed to reproduce the true distributions for x. Statistical uncertainties cause fluctuations (especially when subtracting a large number of background events) and the projected event count may turn out to be negative for a particular bin. Resulting sPlots for the Continuum, Signal, Charmless, $B\overline{B}$ and $a^1\pi$ are given in Figs. E.7-E.11.

Direct Projections

In order to verify the accuracy of the fit, we construct projections via Toy Monte-Carlo (in order to save processing time). Namely, we use the parameters from the fit to the data to generate toy MC for all components, and then plot it on top of the data (while normalizing the event counts to be the same). The results are shown in Fig. E.12, where we embed 100× more MC than the expected yields.

Projection Plots

We also construct projection plots for the Signal, as shown in Fig. E.13. These are made by placing a likelihood cut designed to enhance the signal to background ratio and projecting the multidimensional fit onto its parameters (*i.e.* we plot events with $\mathcal{L}_{sig}/\mathcal{L}_{bkg} > 0.95$).

Likelihood Ratios

Fig. 4.8 shows the likelihood ratio $\mathcal{L}_{\rm sig}/\sum_i \mathcal{L}_i$, where likelihoods $\mathcal{L}_i$ include all signal and background PDFs. This ratio peaks at 1 for signal events (Fig. 4.8(b) and is highly peaked near zero for the backgrounds. The $\chi^2/n_{df} = 1.20$ for the total PDF fit, thus we conclude that there is a strong agreement between to the data and the fitter output (*i.e.* the resulting values for the floated parameters as well as the yields).

4.8.2 Fits With $m_{ES} > 5.25, 5.26$

We examine the effects of having a large range of m_{ES} values in the Sideband Data by repeating the fit for $5.25 < m_{ES} < 5.29$ and $5.26 < m_{ES} < 5.29$. We then compare the

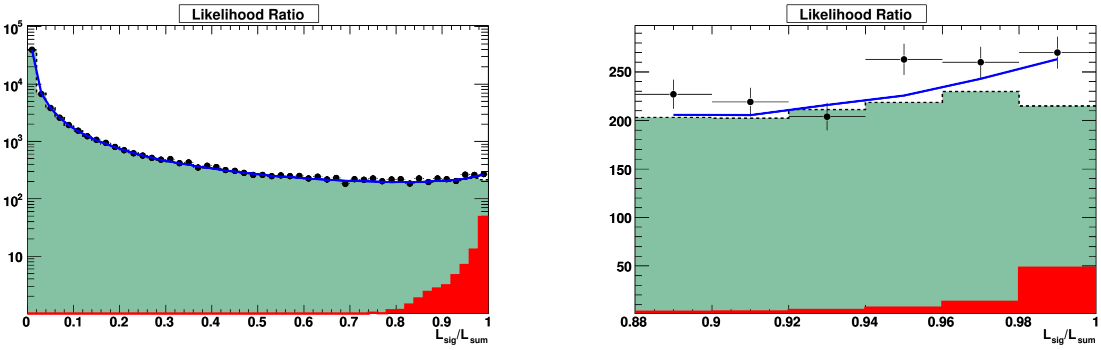

(a) (b)

Figure 4.8: *Likelihood ratio $\mathcal{L}_{\rm sig}/\sum_i \mathcal{L}_i$, where likelihoods $\mathcal{L}_i$ include all signal and background PDFs. The points correspond to the data, blue curve corresponds to the full PDF, shaded teal histogram and black dashed line corresponds to the sum of background PDFs, and red histogram corresponds to the signal contribution. Full range (a) and a zoom-in into the signal region (b) are shown.*

Table 4.26: *Fit Results for the Full Dataset.*

Parameter	Default Values	Values for $m_{ES} > 5.25$	Values for $m_{ES} > 5.26$
$N_{\rho^0\rho^0}$	108.9±31.8	108.0±31.9	108.1±33.6
$f_L(\rho^0\rho^0)$	0.684±0.133	0.723±0.132	0.671±0.138
S_L (blind)	-0.03 ± 0.74	-0.05 ± 0.71	-0.04 ± 0.76
C_L (blind)	0.03 ± 0.74	0.06 ± 0.70	0.05 ± 0.76
$N_{\rho^0 f_0}$	11.3±19.2	8.1±19.5	14.3±20.6
$N_{f_0 f_0}$	4.2±5.8	3.0±5.4	4.7±6.5
$N_{\rho^0\pi^+\pi^-}$	-31.9±31.0	-43.4±30.4	-34.0±34.6
$N_{\pi^+\pi^-\pi^+\pi^-}$	-1.7±22.6	18.8±26.6	-2.7±24.8
$N_{a_1\pi}$	279.7±52.2	278.7±52.1	263.6±50.6
N_{Chls}	669.3±95.6	632.6±93.0	546.2±86.0
N_{BBbar}	2330±149	2121±141	1766±128
$N_{Continuum}$	68701±282	58899±262	39964±217

results to the Default Fit ($5.245 < m_{ES} < 5.29$), as summarized in Table 4.26. Other than the expected drops in the number of Continuum, $B\overline{B}$ and Charmless events, there are no (statistically significant) discrepancies.

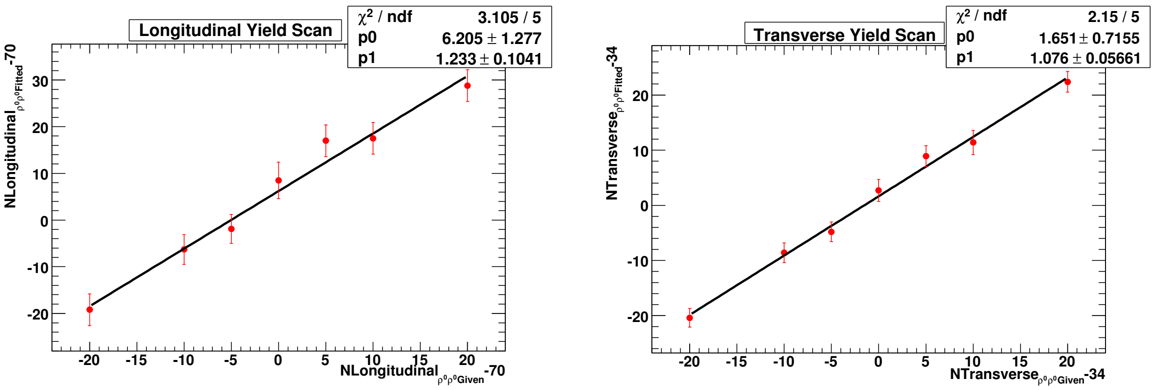

(a) (b)

Figure 4.9: *Yield Scans around* $nSigL = 70$ *and* $nSigT = 34$.

4.8.3 Fit Bias

In order to account for fit bias we construct and fit MC datasets (via the procedure described in Section 4.6.1), where the embedded values progressively differ from the fitted results.

Yield Scans

First, we check whether the fit bias depends on the number of generated signal events. We start with 70 longitudinal events and 34 transverse events (close to the results of the ML fit), and vary each component around this value. The results are shown in Fig. 4.9. The fitter bias is 6.2 ± 1.3 for longitudinal events, 1.7 ± 0.7 for transverse events and is roughly independent of the yield.

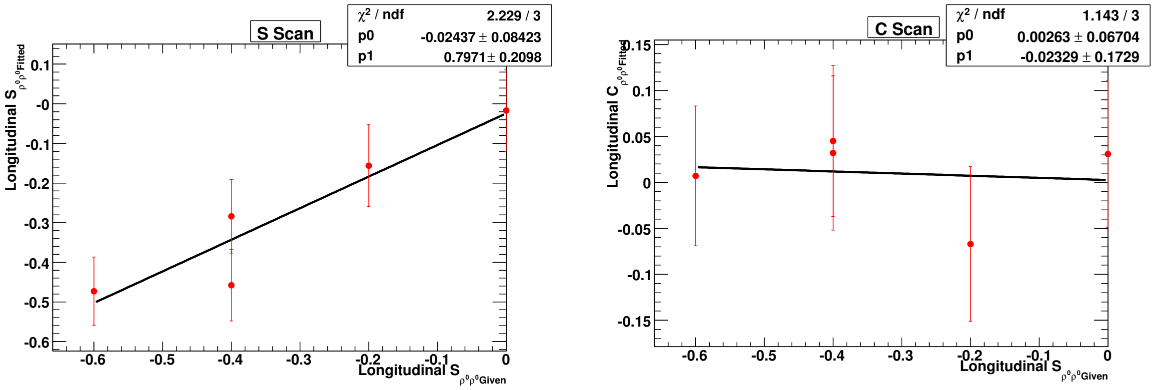

Figure 4.10: *$S_{fitted} - S_{expected}$ and C as a function of $S_{expected}$.*

S,C Scans With Embedded MC

As a next step, we check that varying the values of S or C doesn't introduce bias to the fit. The full MC has $C = 0$ and we construct fits of S and C as a function of S, shown in Fig. 4.10. The bias in S and C is negligible (-0.024 ± 0.084 for S and 0.003 ± 0.067 for C), and its uncertainty is propagated into the systematic errors.

S, C Scans With PDF-Generated MC

Due to insufficient amount of MC (for the desired S, C values) we perform scans with signal events generated from their PDFs. Once again, we plot the fitted S and C as a function of their expected values, shown in Fig. 4.11. The bias is minimal: 0.068 ± 0.033 for S and 0.035 ± 0.022 for C.

NR Scans

We also analyze how sensitive the fit is to the variations in the yields for Non-Resonant modes. Thus, we add 0-90 $\rho^0\pi\pi$ (toy) MC events to our dataset. The fitted

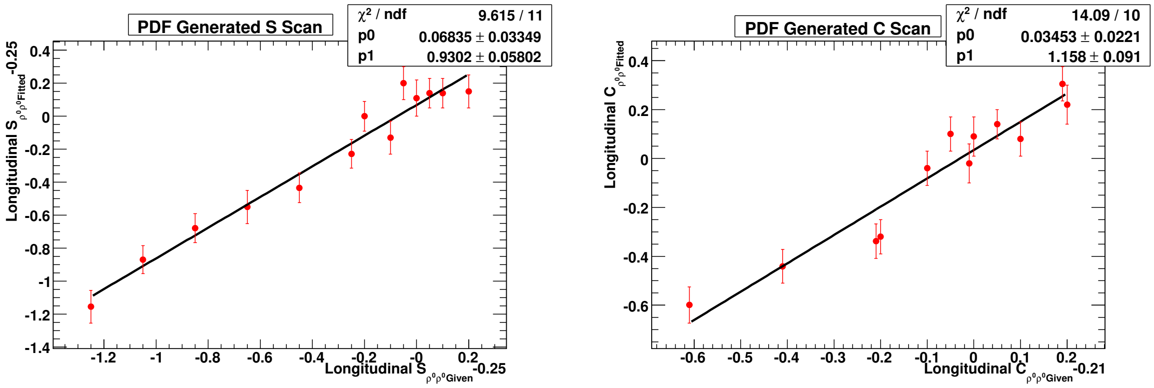

Figure 4.11: $S_{fitted} - S_{expected}$ *and* C *as a function of* $S_{expected}$.

signal and $\rho^0\pi\pi$ yields are shown in Figs. 4.12(a),(b). We then repeat the procedure for the 4π mode, as shown in Fig. 4.12(c),(d). Since the datasets are correlated, it is inappropriate to take the errors directly from the ML fits. Instead we recognize that there should be a linear increase in the yield and estimate it such that $\chi^2/n_{df} = 1$ for the (first order) polynomial fit to the yields (*i.e.* when performing these tests we are interested in how much the $\rho^0\rho^0$ changes, when additional NR events are added, rather than its overall value). As expected, there is a corresponding increase in the fitted yields for the NR modes, while the Signal Yield remains statistically consistent (within 2σ) with the original value of 106 events.

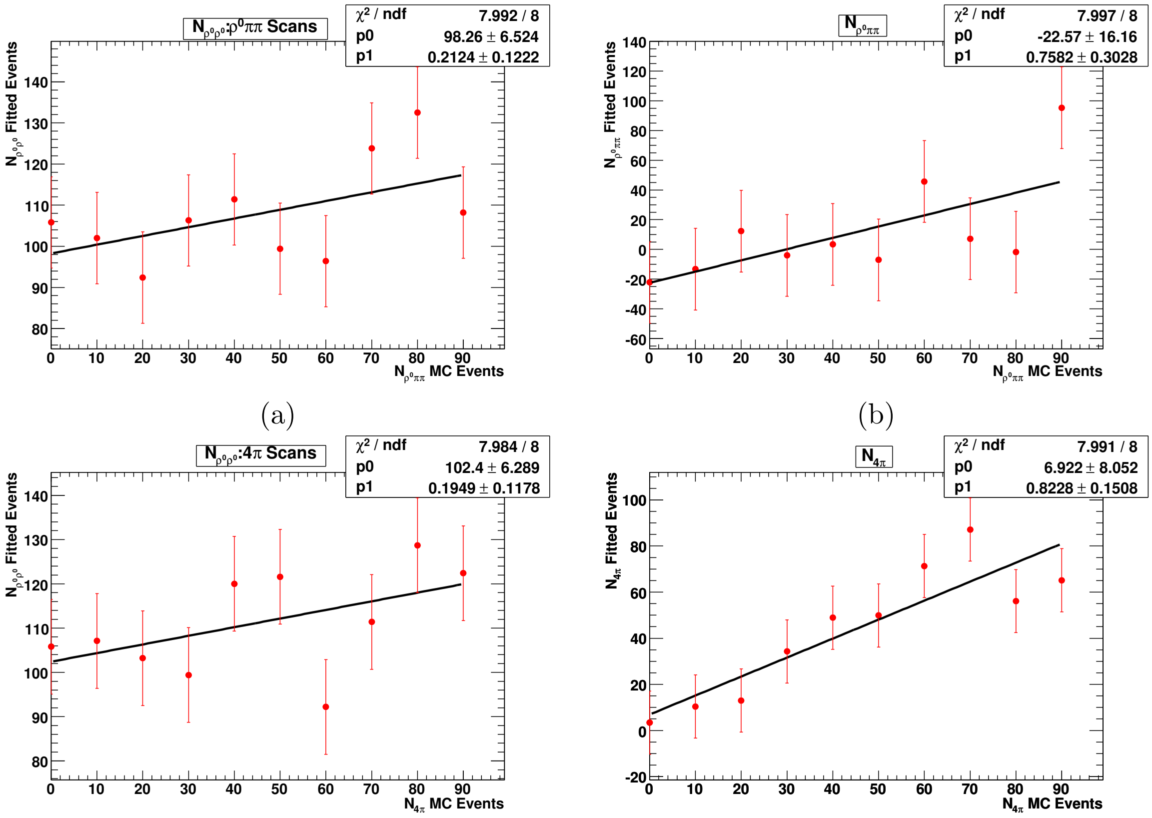

(a) (b)

(c) (d)

Figure 4.12: *Non-Resonance Scans. Shown are Signal Yield a), $\rho^0\pi\pi$ Yield b) as a function of $\rho^0\pi\pi$ MC events and Signal Yield c), 4π Yield d) as a function of 4π MC events.*

4.9 Systematic Uncertainties

In addition to fitting for the BR's and CP parameters, we must estimate the systematic error associated with each measurement. There are a number of uncertainties, approximations and simplifications throughout the analysis. In this section we examine how each of them affects the final results.

4.9.1 Reconstruction Systematics

First, there are standard systematic uncertainties arising mainly from modeling of the reconstruction efficiencies. The significant ones are [49],[50]:

- $\underline{B \text{ counting}}$: The uncertainty on the Branching Fractions resulting from the fact that we do not know the exact number of $\Upsilon(4S)$'s, which decayed into $B^0\overline{B}^0$ pairs. It is estimated to be 1.1% [77].
- $\underline{\text{Tracking efficiency}}$: It is estimated to be 0.36% per track [78] or a total systematic uncertainty of 1.4%.
- $\underline{\text{PID efficiency}}$: Control sample studies show an agreement between data and MC within 0.5% per track. This estimate agrees with the ones made by the PID group [79] and gives us total systematic uncertainty of 2.0%.
- $\underline{\rho^0 \text{ and } f_0 \text{ lineshape}}$: We vary the parameters by 5 MeV. For the f_0 lineshape the parameters from E791 [80] are used.
- $\underline{\text{Vertex } \chi^2 \text{ cut}}$: The relative efficiency between data and Monte Carlo has been studied on control samples. No significant difference was found. Therefore, we apply no

correction and assign a conservative 2% systematic error.

- Selection cuts : The uncertainties due to track multiplicity and thrust angle cuts are estimated to be 1% (for each cut).

- Value of f_L : Since we float f_L value in the ML fit, there is no model uncertainty. Because the efficiencies for the longitudinal and transverse components differ, the statistical error on f_L propagates to the uncertainty in the average selection efficiency (and therefore the branching fraction). However, this uncertainty is statistical in nature and is included in the (statistical) error on $\mathcal{B}$.

- Fit bias : As was discussed in Section 4.8.3, we use toy studies to determine the average bias to the fitted signal yield as well as the CP parameters and correct for it. Naturally, there is an error associated with that correction (listed in Tables 4.30, 4.31), which must be taken into account.

- Charmless Branching Ratios : The Charmless cocktail consists of multiple modes, with only the overall SXF-Like Charmless Yield varied during the fit to the data. Thus, we vary the event yield for each component mode and analyze the impact on the signal (*i.e.* we treat the yields as individual parameters and apply the techniques discussed in Section 4.9.2).

- SXF rate : The $\rho^0\rho^0$ PDF includes a fraction of self-crossfeed (SXF) events. It is obtained from the MC and fixed in the fit to the data. The associated associated systematic errors are listed in Table 4.27.

Table 4.27: *Errors from the $\rho^0\rho^0$ SXF rate uncertainty.*

variable	$\Delta N_{\rho^0\rho^0}$	Δf_L	ΔS_L	ΔC_L	$\Delta N_{\rho^0 f_0}$	$\Delta N_{f_0 f_0}$
SxF	0.37	0.00	0.00	0.00	0.01	0.07

4.9.2 PDF Parameters

For each PDF parameter, there is an uncertainty which translates into an error on the extracted quantities. We take this error to be either the value returned by the fit to the MC or the error from the fit combined in quadrature with the value obtained from the Control Sample Studies (Section 4.4.2). The contribution of the PDF uncertainties to the systematic error is determined by running an independent fit to the data for each of the (~ 400) parameters, while smearing it by $\pm 1\sigma$. The errors are then taken as the difference in signal yield from the original fit to data. They are combined, while taking into account parameter correlations. The impact on the yields is summarized in Table 4.28.

A similar procedure is performed to extract the systematic uncertainties of S_L and C_L due to the variation of the *CP* content of the B backgrounds. Here, we use the measured values of *CP* asymmetries, whenever appropriate. If the measurements are not available for a *CP* eigenstate, we take $S = C = 0$ with an uncertainty of $1/\sqrt{3}$. The results are given in Table 4.29.

Table 4.28: *Contribution of The PDF Parameter Uncertainties (in events for yields and in absolute units for f_L^{raw}). Error on C and S due to the variation of fit yields is for informational purposes only; the final fit is done with yields and CP parameters floated simultaneously.*

Parameter	$B \to \rho^0\rho^0$	$B \to f_0 f_0$	$B \to \rho^0 f_0$	f_L^{raw}	$B \to \rho^0\pi^+\pi^-$	$B \to 4\pi$	S	C
mES	0.63	0.25	0.42	0.00	0.78	1.15	0.00	0.00
ΔE	0.18	0.23	0.47	0.00	1.25	3.16	0.00	0.01
eShape	3.02	0.95	2.52	0.01	3.67	2.65	0.02	0.04
mass-helicity	2.14	1.87	1.63	0.01	4.29	2.95	0.02	0.02
BBbar	1.29	0.94	1.04	0.01	0.66	1.41	0.01	0.01
Continuum	–	–	–	–	–	–	0.02	0.01
Tag Cats	0.91	0.47	0.49	0.00	1.32	1.33	0.01	0.01
Δt	0.37	0.29	0.46	0.00	0.82	1.43	0.02	0.05
Fit Yields	–	–	–	–	–	–	0.08	0.01
S and C	–	–	–	–	–	–	0.22	0.26
Total	4.57	2.54	3.56	0.03	7.11	7.56	0.23	0.27

Table 4.29: *Systematic uncertainties due to variations of S and C of the B backgrounds.*

Parameter	S	C	$S-err$	$C-err$
Chls	0.08	0.01	0.15	0.01
BBbar	0.06	0.12	0.10	0.10
$a_1\pi$	0.12	0.16	0.20	0.18
$\rho^0\rho^0_{Tran}$	0.07	0.08	0.58	0.58
$\rho^0 f_0, f_0 f_0$	0.03	0.05	0.58	0.58
$\rho^0\pi\pi, 4\pi$	0.13	0.13	0.58	0.58
$\rho^0 K^{*0}, f_0 K^{*0}$	0.02	0.03	0.10	0.20
Total	0.22	0.26	–	–

4.9.3 Interference

Throughout the analysis we assumed a direct relation between the Branching Ratio and the Amplitude ($i.e.$ $\mathcal{B}_{\rho^0\rho^0} = |\mathcal{A}_{\rho^0\rho^0}|^2$). However, the situation is complicated by similar decays into the same final state, where the BR measurement picks up portions of the interference term. For example, if the final $\pi^+\pi^-\pi^+\pi^-$ state could only be reached via the $B^0 \to \rho^0\rho^0 \to \pi^+\pi^-\pi^+\pi^-$ or $B^0 \to \rho^0\pi^+\pi^- \to \pi^+\pi^-\pi^+\pi^-$ then the overall $\mathcal{B}_{4\pi}$ would be given by

$$\mathcal{B}_{4\pi} = |\mathcal{A}_{\rho^0\rho^0} + \mathcal{A}_{\rho^0\pi\pi}|^2 = |\mathcal{A}_{\rho^0\rho^0}|^2 + 2Re(\mathcal{A}_{\rho^0\rho^0}\mathcal{A}^*_{\rho^0\pi\pi}) + |\mathcal{A}_{\rho^0\pi\pi}|^2.$$

While we are interested in and use the Monte Carlo to model the PDFs for $\mathcal{B}_{\rho^0\rho^0} = |\mathcal{A}_{\rho^0\rho^0}|^2$ ($\mathcal{B}_{\rho^0\pi\pi} = |\mathcal{A}_{\rho^0\pi\pi}|^2$), a portion of the interference term $2Re(\mathcal{A}_{\rho^0\rho^0}\mathcal{A}^*_{\rho^0\pi\pi})$ will resemble $B^0 \to \rho^0\rho^0$ ($B^0 \to \rho^0\pi^+\pi^-$). Specifically, this will occur when $\pi^+\pi^-$ appear to be originating from a ρ^0 resonance ($i.e.$ when ρ^0 decays look 'flat' in the mass distribution). These events are picked up by the fitter, thus adding an uncertainty to the measurement.

We estimate this error by simulating the events (via `EvtGen`) and examining the impact. The procedure (described in more detail in Appendix D of [50]) involves:

- Inputs of BR's and *CP* coefficients for the relevant processes. We either take them from prior measurements [51]-[56] and our measurement, or (for $S_{\rho^0\rho^0}$, $C_{\rho^0\rho^0}$) treat them as input parameters.
- Properly modeling and symmetrizing the amplitudes.
- Taking the Bayesian approach and generating (mostly gaussian) priors for the input parameters.
- Extracting the error from the RMS in the difference between the resultant parameters with vs. without the interference effects.

The uncertainty is proportional to the square-root of the two Branching Ratios (*e.g.* as a result of interference with $B^0 \to \rho^0\pi^+\pi^-$, $\Delta\mathcal{B}_{\rho^0\rho^0} \sim \sqrt{\mathcal{B}_{\rho^0\rho^0}\mathcal{B}_{\rho^0\pi\pi}}$). Thus, interference with the $a_1\pi$ has the strongest impact on the signal measurement with the complete results summarized in Table 4.30.

4.9.4 Summary of Systematic Uncertainties

We summarize the errors on the yields and the *CP* parameters Tables 4.30-4.31, respectively. The interference effects and possible PDF shape variations are the largest sources of systematic uncertainty.

Table 4.30: *Summary of systematic errors in the measurement of the branching fractions and polarization.*

Source	$B \to \rho^0\rho^0$		$B \to \rho^0 f_0$		$B \to f_0 f_0$		$B \to \rho^0\pi\pi$		$B \to 4\pi$		
	frac	evts	frac	evts	frac	evts	frac	evts	frac	evts	f_L
	Multiplicative (*i.e.* $\to 0$ as $N_{\rho^0\rho^0} \to 0$)										
Number of B mesons	1.1%	–	1.1%	–	1.1%	–	1.1%	–	1.1%	–	–
Track multiplicity cut	1.0%	–	1.0%	–	1.0%	–	1.0%	–	1.0%	–	–
Thrust angle cut	1.0%	–	1.0%	–	1.0%	–	1.0%	–	1.0%	–	–
Vertex requirement	2.0%	–	2.0%	–	2.0%	–	2.0%	–	2.0%	–	–
PID cut	2.0%	–	2.0%	–	2.0%	–	2.0%	–	2.0%	–	–
Track finding	1.4%	–	1.4%	–	1.4%	–	1.4%	–	1.4%	–	–
MC statistics	<1%	–	<1%	–	<1%	–	<1%	–	<1%	–	< 0.01
	Additive										
PDF variation	–	4.6	–	3.6	–	2.5	–	7.1	–	7.6	0.03
Fit bias	–	2.0	–	2.5	–	0.9	–	4.8	–	3.6	0.009
Charmless BR	–	2.2	–	2.9	–	0.3	–	0.2	–	1.9	0.00
Interference	–	14.3	–	10.5	–	6.0	–	15.3	–	6.2	0.03
Total	15.7		11.7		6.6		17.5		10.6		0.048

Table 4.31: *Summary of systematic errors on S and C .*

Source	S	C
PDF variation	0.23	0.27
Fit bias	0.03	0.02
Charmless BR	0.01	0.01
$a_1\pi$ interference	0.04	0.04
Total	0.24	0.27

4.10 Results

4.10.1 Branching Ratios

The results of the fit on the full dataset (465×10^6 $\Upsilon(4S)$ decays) have been provided in Table 4.25. We account for fit bias, which is determined in Section 4.8.3 (or directly from Table 4.22 for non-signal modes). Using the efficiency values from Table 4.6, we then determine the physical yields and polarization, as listed in Table 4.32.

Table 4.32: **Analysis Results**. We list event yields; fraction of longitudinal polarization (f_L); selection efficiency (Eff) corresponding to measured polarization; branching fractions ($\mathcal{B}$); branching fraction upper limits (UL) at 90% CL; and significance $\mathcal{S}$, including systematic uncertainties. First uncertainty is statistical and second is systematic.

Mode	Yield	f_L	Eff (%)	$\mathcal{B}$ (10^{-6})	UL (10^{-6})	$\mathcal{S}$ (σ)
$B^0 \to \rho^0\rho^0$	$99^{+35}_{-34} \pm 15$	$0.75^{+0.11}_{-0.14} \pm 0.04$	23.28 ± 0.07	$0.92 \pm 0.32 \pm 0.14$	-	3.1
$B^0 \to \rho^0 f_0 \to \rho^0[\pi^+\pi^-]_{f_0}$	$3^{+22}_{-20} \pm 5$	-	24.16 ± 0.09	$0.03^{+0.20}_{-0.18} \pm 0.05$	< 0.34	
$B^0 \to f_0 f_0 \to [\pi^+\pi^-]_{f_0}[\pi^+\pi^-]_{f_0}$	$6^{+8}_{-5} \pm 2$	-	27.22 ± 0.07	$0.05^{+0.06}_{-0.04} \pm 0.02$	< 0.16	
$B^0 \to \rho^0\pi^+\pi^-$	$-12^{+39}_{-35} \pm 9$	-	1.68 ± 0.01	$-1.2^{+5.0}_{-4.5} \pm 1.1$	< 8.7	
$B^0 \to \pi^+\pi^-\pi^+\pi^-$	$8^{+30}_{-25} \pm 6$	-	0.55 ± 0.01	$3.2^{+11.7}_{-9.8} \pm 3.4$	< 21.1	

Note that the upper limits on the Non Resonant modes are consistent with the Belle analysis [84], which scans over a larger mass window ($0.55 < m_{\pi\pi} < 1.70$ GeV/c^2). In conclusion, we show evidence for $B \to \rho^0\rho^0$ decays, while obtaining upper limits for the rest of the signal-like modes.

4.10.2 CP Parameters

We fit the proper-time distribution on the data sample and obtain the CP-violating parameters (for the longitudinally polarized $B^0 \to \rho^0\rho^0$ events) to be:

$$S_L^{00} = 0.3 \pm 0.7 \text{ (stat.)} \pm 0.2 \text{ (syst.)},$$

$$C_L^{00} = 0.2 \pm 0.8 \text{ (stat.)} \pm 0.3 \text{ (syst.)},$$

with a correlation of 0.035 between the two coefficients. Projection plots for the time dependent component as well as the asymmetry (defined in Eq. (2.40)) are given in Figs. 4.13, 4.14. In the end, we see some effects from the CP violation (resulting in S,$C \neq 0$), but measuring them at the 3σ level would require a significantly larger data sample.

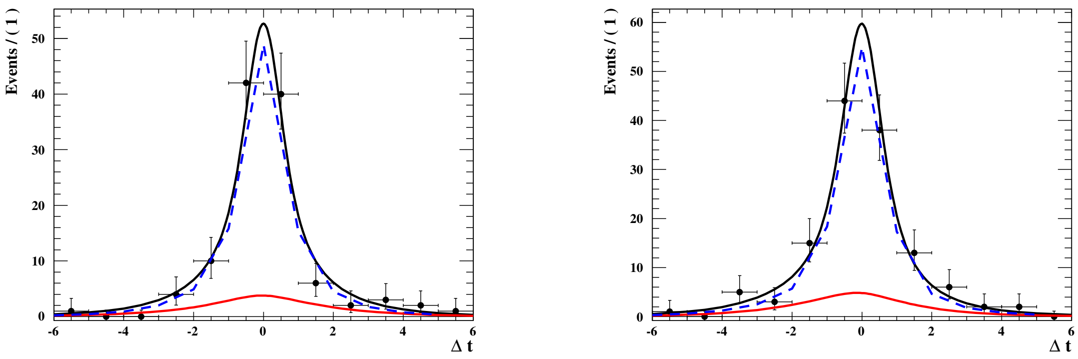

a)

b)

Figure 4.13: *Projection Plots for the time dependent component of a)*B^0 *b)*$\overline{B}^0$*-tagged events. Solid black line represents the full fit, solid red line shows the* $B^0 \to \rho^0\rho^0$ *component, and the blue hashed line represents the sum of all background components. We apply a likelihood cut of* $\mathcal{L}_{\rho^0\rho^0}/\mathcal{L}_{\rm total} > 0.99$ *in order to enhance the signal component. A larger value of* S *would shift the signal mean away from* 0*, while an increase in* C *would result in a more pronounced peak.*

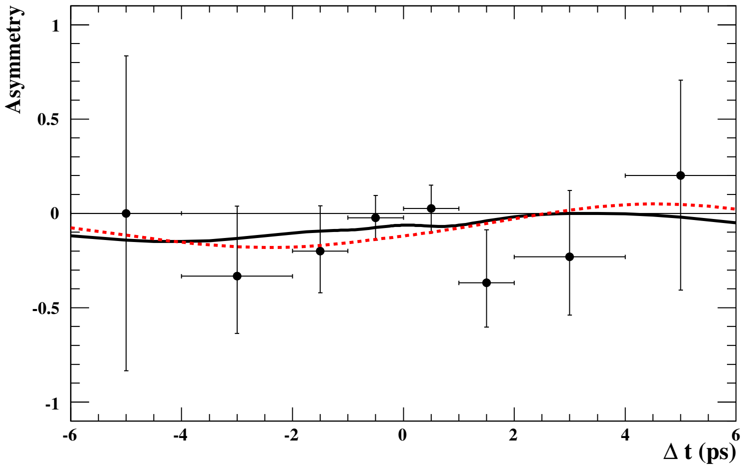

Figure 4.14: *CP Asymmetry. Solid black line represents the full fit, while the dashed red line shows the* $B^0 \to \rho^0\rho^0$ *component. We apply a likelihood cut of* $\mathcal{L}_{\rho^0\rho^0}/\mathcal{L}_{\rm total} > 0.99$ *in order to enhance the signal component. A larger value of* C *shifts the* x *intercept away from* 0*, while an increase in* S *would result in more pronounced signal peaks.*

4.11 Implications For α

4.11.1 Determining α

In the Section 2.4 we gave a general description of how to obtain α from a set of measured quantities. Now, we implement the method by incorporating our results, along with those of $B \to \rho^+\rho^0$ [19] and $B \to \rho^+\rho^-$ [20] analyses. To recap, we construct a χ^2 discriminant, as defined by Eq. (2.54):

$$\chi^2(\alpha) = \sum_{i=+-,00} \left(\frac{(\tilde{S}^i - \sqrt{1-(C^i)^2}\sin(2\alpha+\kappa^i))^2}{\sigma^2(\tilde{S}^i)} + \frac{(\tilde{C}^i - C^i)^2}{\sigma^2(\tilde{C}^i)} \right) +$$

$$+ \sum_{i=+-,\pm 0,00} \left(\frac{(\tilde{B}^i_{Tot} - B^i_{Tot})^2}{\sigma^2(\tilde{B}^i_{Tot})} + \frac{(\tilde{f}^i_L - f^i_L)^2}{\sigma^2(\tilde{f}^i_L)} \right) + \textit{correlation terms},$$

input the measured quantities (denoted by ∼ and listed in Table. 4.33) and scan over all values of α, while minimizing with respect to the remaining parameters. There are only four independent variables (besides α): the amplitudes A_0, A_2, $\bar{A}_0$, $\bar{A}_2$ for B, $\overline{B}$ to decay to the $I = 0$, $I = 2$ states. The Branching Ratios can be expressed in terms of them via Eq. (2.44); noting that since we are dealing with longitudinal components, only the measured value for the B_T appears during this analysis. In other words

$$B^i_{Tot} = B^i_L + \tilde{B}^i_T = |A^i_L|^2 + \tilde{B}^i_T,$$

where $i = +-, \pm 0, 00$. The amplitudes A^i_L are related to these variables via Eq. (2.44), while $C^{+-,00}$ is given by Eq. (2.43). By utilizing Figs. 2.8, 2.12 we compute

$$\kappa^{+-} \equiv \theta - \bar{\theta} = \cos^{-1}\left(\frac{1}{2}\frac{|A_0|^2 + |A_2|^2 - |A^{+-}|^2/2}{|A_0 A_2|}\right) - \cos^{-1}\left(\frac{1}{2}\frac{|\bar{A}_0|^2 + |A_2|^2 - |\bar{A}^{+-}|^2/2}{|\bar{A}_0 A_2|}\right), \tag{4.32}$$

$$\kappa^{00} = \cos^{-1}\left(\frac{1}{2}\frac{|A_0|^2 + |A^{+0} - A_2|^2 - |A^{00}|^2/2}{|A_0(A^{+0} - A_2|)}\right) - \cos^{-1}\left(\frac{1}{2}\frac{|\bar{A}_0|^2 + |A^{+0} - A_2|^2 - |\bar{A}^{00}|^2/2}{|\bar{A}_0(A^{+0} - A_2|)}\right),$$

Table 4.33: *Measured values for the parameters used to scan for the most probable value of α [19], [20], Section 4.10.*

Parameter	Value	Uncertainty
S^{00}	0.3	0.7
C^{00}	0.2	0.9
S^{+-}	-0.17	0.21
C^{+-}	0.01	0.16
$\mathcal{B}_{\rho^0\rho^0}(\times 10^6)$	0.92	0.35
$\mathcal{B}_{\rho^+\rho^0}(\times 10^6)$	16.8	3.2
$\mathcal{B}_{\rho^+\rho^-}(\times 10^-)$	25.5	4.4
$f_L^{\rho^0\rho^0}$	0.75	0.15
$f_L^{\rho^+\rho^0}$	0.90	0.05
$f_L^{\rho^+\rho^-}$	0.99	0.04

similarly to Eq. (2.48). Note that A_0, $\bar{A}_0$ are allowed to be negative (A_2, $\bar{A}_2 > 0$) and the sign of θ is the same as the sign of A_0, which incorporates the four-fold sign ambiguity.

The above approach is based on the assumption that the uncertainties are Gaussian-distributed and that we can neglect $I = 1$ isospin contributions, electroweak loop amplitudes, non-resonant, as well as isospin-breaking effects [52]. The results of the scan are shown in Fig. 4.15. There are three possible solutions (*i.e.* minima in the C.L.), all of which point to $\Delta\alpha$ near zero. Based on the analysis of the $\rho\rho$ system, we conclude that the (slightly) preferred one is $\Delta\alpha = 13^\circ$. More precisely $|\Delta\alpha| < 15.7^\circ$ (17.6°) at the 68% (90%) Confidence Level (CL) and $\alpha = (82.6^{+32.6}_{-6.3})^\circ$ at the 68% CL.

4.11.2 The CKM Picture

In addition to our results, a number of other measurements are used to place further limits on α. Specifically, by combining the observations from the $B \to \rho\rho$ with those from $B \to \rho\pi$ as well as $B \to \pi\pi$ decays the UTFit (CKMfitter) collaboration determined

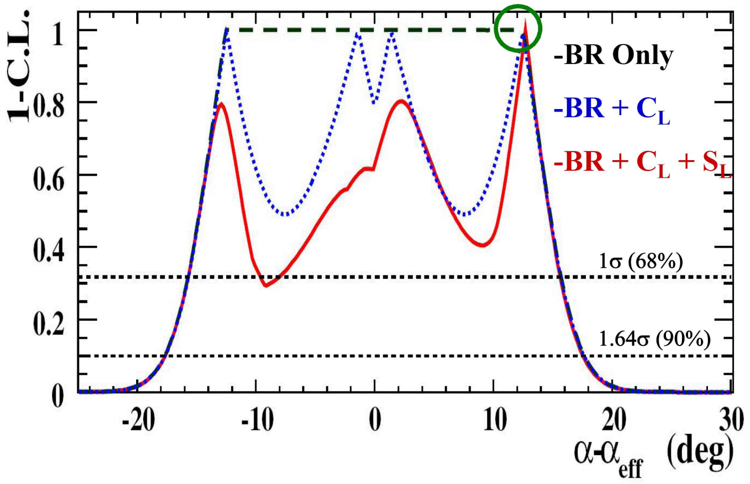

Figure 4.15: *Confidence Level on $\Delta\alpha = \alpha - \alpha_{\rm eff}$, as determined from the isospin analysis. The black (long-dashed) curve is obtained using only the BR information from $B^0 \rightarrow \rho^0\rho^0$ decays (along with all of the other information for the $\rho\rho$ system). The blue (dotted) curve corresponds to the isospin analysis without S_L^{00}, while the red (solid) curve includes all of the information in the fit.*

α to be $(91\pm8)^\circ$ $((81^{+17}_{-5})^\circ)$ at the 1σ level. We describe the details of how these results are combined in Appendix A.2 with the Probability Density scans and constraints on the CKM parameters shown in Fig. 4.16. These restrictions are then combined with the all other results via the approach described in Appendix A.4 and shown in Fig. A.12. The CKM parameters are determined by the CKMfitter (UTFit) to be $\bar{\eta} = 0.341^{+0.048}_{-0.034}$, $\bar{\rho} = 0.139^{+0.073}_{-0.052}$, $(\bar{\eta} = 0.342^{+0.044}_{-0.040}$, $\bar{\rho} = 0.154^{+0.066}_{-0.065})$ at the 3σ level [24], [23].

4.11.3 Further Measurements

Since we completed our analysis, there has been an update to the measurement of the branching fraction (as well as the polarization fraction) for the $B \rightarrow \rho^+\rho^0$ decays [83]. Its most probable value increased from $(16.8\pm3.2)\times10^{-6}$ to $(23.7\pm2.0)\times10^{-6}$. The impact is displayed in Fig. 4.17. After forming the $\chi^2(\alpha)$ discriminant and scanning over its values (*i.e.* repeating the procedure described in Section 4.11.1 with the new results) two of the three peaks are excluded due to the increase in $\mathcal{B}_{\rho^+\rho^0}$. In the end $-1.8^\circ < \Delta\alpha < 6.7^\circ$ with $\alpha = (92.4^{+6.0}_{-6.5})^\circ$ at the 1σ level.

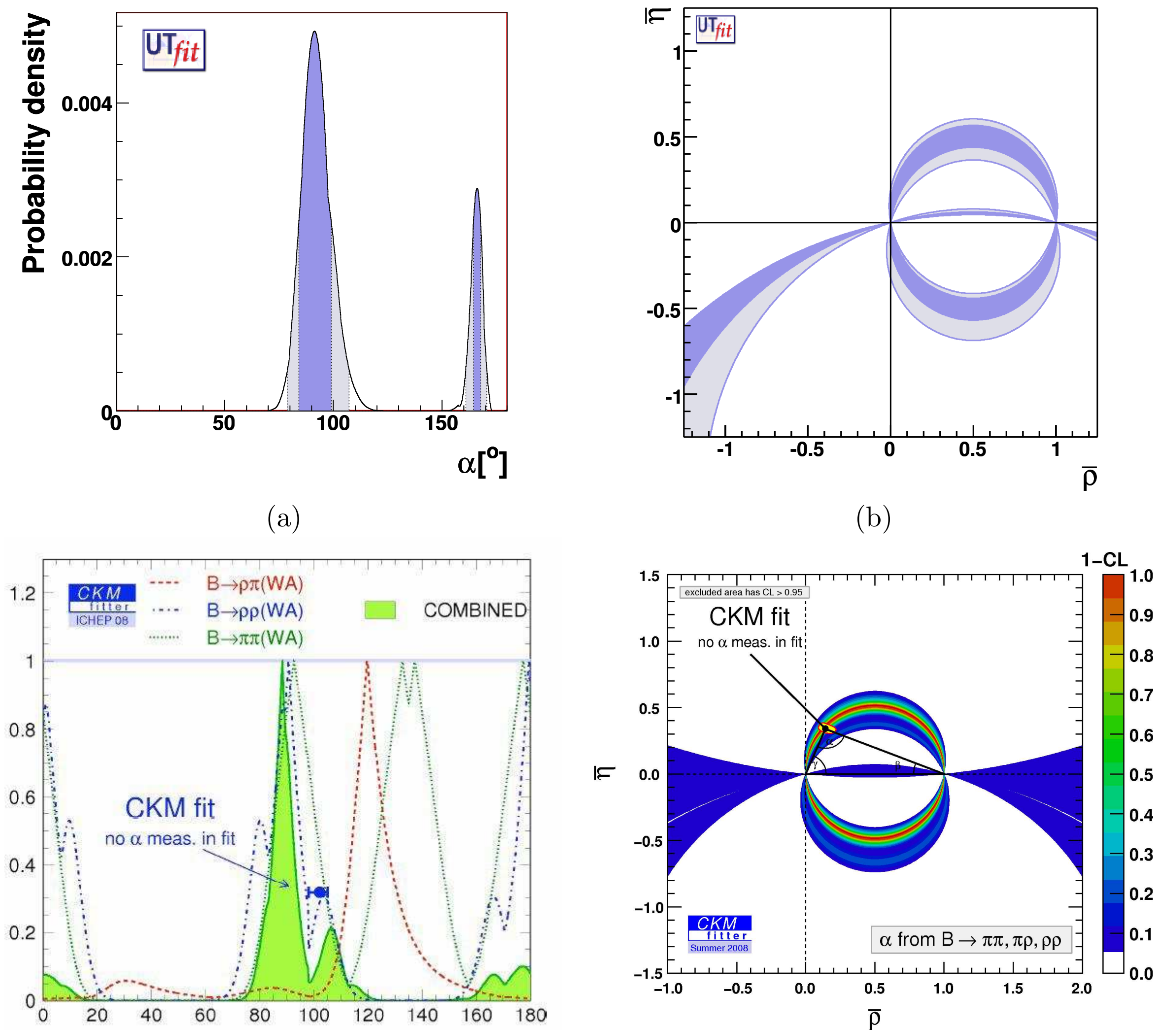

(a) (b)

(c) (d)

Figure 4.16: *α measurements from $B \to \pi\pi$, $B \to \rho\pi$, $B \to \rho\rho$ channels: a),c) Probability Density Distribution; b),d) CKM Parameters $\bar{\eta}$ vs. $\bar{\rho}$ [23], [24]. For the UTFit, the values outside the darkly and lightly shaded regions are excluded at 68% and 95% CLs, respectively. For the CKM fitter, the shaded regions denote a 95% CL, while the blue bar denotes the estimated value from all other measurements. Specifics of how the measurements are combined by the UTFit and CKM fitter collaborations are discussed in Appendix A.4.*

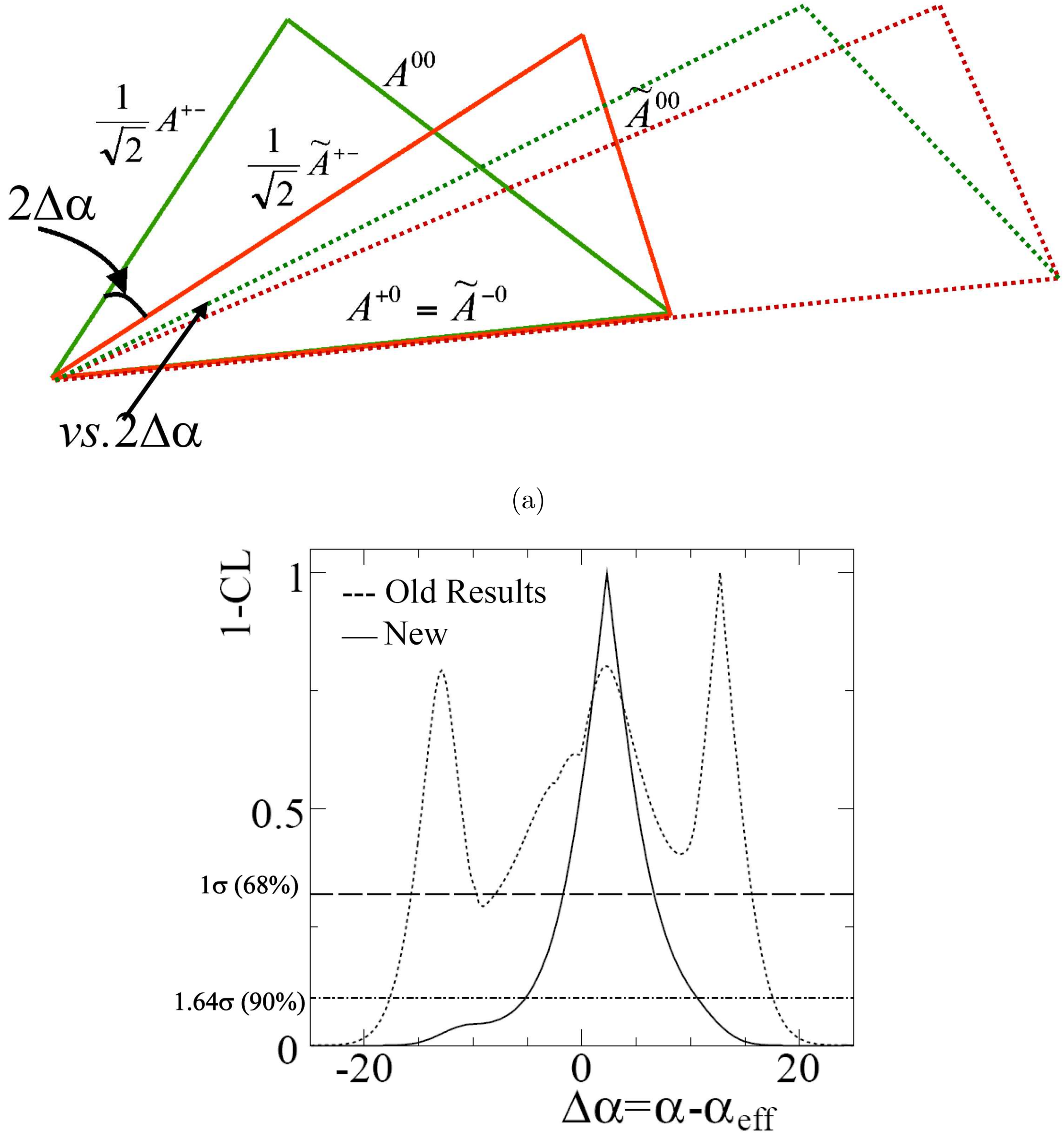

(a)

(b)

Figure 4.17: *Impact of the change in the value of $\mathcal{B}_{\rho^+\rho^0}$ [83]: a) A diagram showing the decrease in $\Delta\alpha$ due to the sides of the isospin triangles becoming longer (solid lines represent the old result, while the dashed lines represent the new one) b) Confidence Level on $\Delta\alpha$ (the dashed line represents the old α scan, while the solid line represent the new one).*

Chapter 5

Conclusion

In this thesis we presented an analysis of $B \to \rho^0\rho^0$ decays. We gave an overview of the Standard Model, described how B-meson decays are relevant in the context of CP Violation, shown how the *BABAR* detector (along with its component subsystems) gathers the necessary data and provided a description of how that data is processed in order to extract the results. We observed the Branching Fraction and the fraction of longitudinal polarization to be

$$\mathcal{B}_{\rho^0\rho^0} = (0.92 \pm 0.33 \pm 0.14) \times 10^{-6}, \tag{5.1}$$

$$f_L = 0.75 \pm 0.14 \pm 0.05.$$

This was the first analysis to find evidence for $B \to \rho^0\rho^0$ decays. The significance (statistical+systematic) of our final result is 3.1σ. When the Likelihood Discriminant is used in place of the Neural Net, $\mathcal{B}_{\rho^0\rho^0} = (0.78 \pm 0.31 \pm 0.13) \times 10^{-6}$, at 3.0σ. There was no significant evidence for B decays to other signal-like modes. The corresponding upper limits (at 90%

CL) are:

$$\mathcal{B}_{\rho^0 f_0} < 0.34 \times 10^{-6},$$

$$\mathcal{B}_{f_0 f_0} < 0.16 \times 10^{-6},$$

$$\mathcal{B}_{\rho^0 \pi^+ \pi^-} < 8.7 \times 10^{-6},$$

$$\mathcal{B}_{\pi^+ \pi^- \pi^+ \pi^-} < 21.1 \times 10^{-6}.$$

Our results are statistically consistent with all other measurements, including those made by Belle [84].

We also measured the CP coefficients to be

$$S = 0.3 \pm 0.7 \pm 0.2,$$

$$C = 0.2 \pm 0.8 \pm 0.3.$$

Even-though the error on these measurements is too great to claim evidence for nonzero values (*i.e.* CP violation in the system), the information is combined with the Branching Fraction values as well as results from other analyses to determine the value of α (Section 4.11.1). Namely, we performed a scan over α, while attempting to minimize $\chi^2(\alpha)$, (Fig. 4.15) and obtained the result of

$$\alpha = (82.6^{+32.6}_{-6.3})^\circ,$$

$$|\Delta\alpha| < 15.7^\circ$$

at the 1σ level. With the updated $B \rightarrow \rho^+ \rho^0$ decay parameters the values become $\alpha = (92.4^{+6.0}_{-6.5})^\circ$, $-1.8^\circ < \Delta\alpha < 6.7^\circ$ [83]. In the end, our observations are fully consistent with other measurements at the B-factories (Fig. A.12) as well as with the Standard Model picture of CP violation [23].

The results are statistically dominated and could be improved by gathering additional data. There are currently several proposals to build SuperB factories at KEK and Frascati, which would operate at luminosities of $10^{35}(\mathrm{cm}^2\mathrm{s})^{-1}$ and $10^{36}(\mathrm{cm}^2\mathrm{s})^{-1}$, respectively. The presented analysis techniques are well developed and can be readily implemented for those experiments, when they come online. However, the current generation of B-factories is unlikely to replicate or supersede the above results and they are expected to be the standard for the next decade.

Bibliography

[1] Cronin and Fitch Experiment with Kaons,

http://hyperphysics.phy-astr.gsu.edu/HBASE/Particles/cronin.html.

J.H. Christenson, J.W. Cronin, V.L. Fitch, R. Turlay, Phys. Rev. Lett. **13**, 138 (1964).

[2] A. D. Sakharov, Violation of CP invariance, C asymmetry, and baryon asymmetry of the universe, Soviet Physics Journal of Experimental and Theoretical Physics (JETP) **5**, 24-27 (1967).

[3] M. E. Peskin and D. V. Schroeder, An Introduction to Quantum Field Theory, (Addison-Wesley Publishing Company, 1995).

[4] S. Weinberg, The Quantum Theory of Fields II, (Cambridge University Press, 1996).

[5] C. Jarlskog, CP Violation, (World Scientific Publishing Co. Pte. Ltd., 1989).

[6] *BABAR* Collaboration, P. F. Harrison and H. R. Quinn, Physics at an Symmetric B Factory.

[7] H. Georgi, Lie Algebras in Particle Physics, (Perseus Books, 1999).

[8] The Standard Model,

S.Weinberg, Phys. Rev. Lett. **19**, 1264 (1967);

A. Salam, Elementary Particle Theory, (Almquist and Wiksells, Stockholm, 1969);

S.L. Glashow, J. Iliopoulos, and L. Maiani, Phys. Rev. **D2**, 1285 (1970).

http://www.answers.com/topic/standard-model.

[9] F.D.Murnaghan, The Unitary and Rotation Groups, (D.C.Spartan, 1962).

[10] N. Cabibbo, Phys. Rev. Lett. **10**, 531 (1963); M. Kobayashi and T. Maskawa, Prog. Theor. Phys. **49**, 652 (1973).

[11] L.Wolfenstein, Phys. Rev. Lett. **51**, 1945 (1983).

[12] L. G. Buras, M. E. Lautenbacher and G. Ostermaier, Phys. Rev. D **50**, 3433 (1994).

[13] M. Bona *et al.*, J. High Energy Phys. **0610**, 081 (2006).

[14] W. Grimus, Fortschr. Phys. **36**, 201 (1988).

[15] M. Gronau and D. London, Phys. Rev. Lett. **65**, 3381 (1990).

[16] R. Aleksan *et al.*, Phys. Lett. B **356**, 95 (1995).

[17] A. Breon, P. Giraud, G. Graziani, A. Gritsan, L. Mir, C. Yeche, *BABAR* Analysis Document 914 (2004).

[18] C. O. Dib, I. Dunietz, F. J. Gilman, and Y. Nir, Phys. Rev. D **41**, 1522 (1990).

[19] *BABAR* Collaboration, B. Aubert *et al.*, Phys. Lett. **97**, 261801 (2006).

[20] *BABAR* Collaboration, B. Aubert *et al.*, Phys. Rev. D **76**, 052007 (2007).

[21] Heavy Flavor Averaging Group: http://www.slac.stanford.edu/xorg/hfag ; E. Barberio *et al.*, Averages of b-hadron and c-hadron Properties at the End of 2007, arXiv:hep-ph/0808.1297.

[22] M. Ciuchini, M. Pierini, L. Silvestrini, Phys. Rev. Lett. **95**, 221804 (2005), arXiv:hep-ph/0507290v3.

[23] UTfit Collaboration: M. Bona *et al.*, arXiv:hep-ph/0606167v2 ; Updated results and plots are available at http://www.utfit.org.

[24] CKMfitter Group (J. Charles *et al.*), Eur. Phys. J. C41, 1-131 (2005), arXiv:hep-ph/0406184 ; Updated results and plots are available at http://ckmfitter.in2p3.fr.

[25] *BABAR* Collaboration, B. Aubert *et al.*, Phys. Rev. D **71**, 032005 (2005); Belle Collaboration, R. Itoh, Y. Onuki, Phys. Rev. Lett. **95**, 091601 (2005).

[26] A. Bondar, T. Gershon, P. Krokovny, Phys. Lett. B **624**, 1-10 (2005).

[27] H. R. Quinn and A. E. Snyder, Phys. Rev. D **48**, 2139 (1993); M. Ciuchini, M. Pierini, L. Silvestrini, Phys. Rev. D **74**, 051301 (2006).

[28] M. Gronau and D. Wyler, Phys. Lett. B **265**, 172 (1991).

[29] D. Atwood, I. Dunietz and A. Soni, Phys. Rev. Lett. **78**, 3257 (1997).

[30] A. Giri, Y. Grossman, A. Soffer, J. Zupan, Phys. Rev. D **68**, 054018 (2003).

[31] For a recent discussion, see M. Neubert and B. Stech, CERN-TH/97-99 (1997), hep-ph/9705292 or A. J. Buras and M. Lindner, World Scientific, Singapore (1998).

[32] R. Fleischer, Int. Jour. Mod. Phys. **A12**, 2459 (1997).

[33] O. Long, M. Baak, R. N. Cahn, D. Kirkby, Phys. Rev. D **68**, 034010 (2003).

[34] M. Ciuchini, *et al.*, arXiv:hep-ph/0012308v3.

[35] A. Hocker, *et al.*, Eur. Phys. J. C **21**, 225-259 (2001).

[36] M. Battaglia, *et al.*, arXiv:hep-ph/0304132v2.

[37] *BABAR* Collaboration, Technical Design Report, SLAC-REP-372 (1995).

[38] Data Quality Group,

http://www.slac.stanford.edu/BFROOT/www/Computing/DataQuality/.

[39] *BABAR* Detector Image Gallery,

http://www.slac.stanford.edu/BFROOT/www/Detector/Images/Images.html.

[40] Linac Description,

http://www2.slac.stanford.edu/vvc/accelerators/structure.html.

[41] PEP-II, An Asymmetric B Factory: Conceptual Design Report, SLAC-R-418 (June 1993),

http://www.slac.stanford.edu/pubs/slacreports/slac-r-418.html.

[42] A. Snyder, The Effect of Vertex Cuts on CP Reach, *BABAR* Note 177 (1994).

[43] D. Barbieri *et al.*, Silicon Sensors for the BABAR Vertex Tracker, Il Nuovo Cimento A**112**, (1999) Issue 0102, p.113.

[44] The *BABAR* Detector,

http://www.slac.stanford.edu/BFROOT/www/doc/workbook/detector/detector.html.

[45] *BABAR* Collaboration, B. Aubert *et al.*, Nucl. Instrum. Methods Phys. Res., Sect. **A479**, 1 (2002).

[46] C. Newman-Holmes, E.E. Schmidt, R. Yamada, Nucl. Instrum. Methods **A274**, 443 (1989).

[47] R. Aleksan *et al.*, Nucl. Instr. Methods A**397** (1997) 261.

[48] R. Santonico, R. Cardarelli, Nucl. Instr. Methods A**187** (1981) 377.

[49] M. Escalier, Y. Gao, A. Gritsan, Yu. Kolomensky, L. Mir, I. Osipenkov, G. Vasseur, C. Yeche, *BABAR* Analysis Document 1478 (2006).

[50] S. Emery, M. Escalier, L. Esteve, Y. Gao, A. Gritsan, Yu. Kolomensky, L. Mir, I. Osipenkov, G. Vasseur, C. Yeche, *BABAR* Analysis Document 1701 (2008).

[51] *BABAR* Collaboration, B. Aubert *et al.*, Phys. Rev. Lett. **98**, 111801 (2007).

[52] *BABAR* Collaboration, B. Aubert *et al.*, Phys. Rev. D **78**, 071104(R) (2008).

[53] Release 22 Datasets,

http://www.slac.stanford.edu/BFROOT/www/Computing/DataQuality/

datasets/R22-Skims/R22fSkims-v11.html.

[54] M. Gronau, J. Zupan. Phys. Rev., **D73**, 057502 (2006).

[55] *B* Tagging Group,

http://www.slac.stanford.edu/BFROOT/www/Physics/

Tools/Tagging/Main/index.html.

[56] *BABAR* Collaboration, B. Aubert *et al.*, Phys. Rev. Lett. **98**, 181803 (2007).

[57] Background Filter Information,

http://www.slac.stanford.edu/BFROOT/www/doc/

workbook/eventinfo/TagInfo/BGF+DigiF_Flags.html.

[58] *BABAR* Collaboration, B. Aubert *et al.*, Phys. Rev. Lett. **97**, 201801 (2006).

[59] G.C. Fox and S. Wolfram, Nucl. Phys. **B149**, 413 (1979).

[60] R. Bartoldus *et al.*, *BABAR* Analysis Document 194 (2002).

[61] P. Billoir and S. Qian, Nucl. Instr. Methods **A311**, 139 (1992).

[62] E. Dedrick, J. M. LoSecco and W. D. Shephard, Analytic Vertex Estimation, *BABAR* Note 378 (1997).

[63] A. Forti, F. Lanni and F. Palombo, Measurement of the CKM Alpha Angle in the Processes $B_d^0 \to a_1^{\mp}\pi^{\pm} \to \pi^+\pi^-\pi^+\pi^-$, *BABAR* Note 423 (1998).

[64] J. M. LoSecco, Kinematic Fitting for *BABAR*, *BABAR* Note 352 (1997).

[65] D. Lange, G. Sciolla, M.C. Simani, Y. Zheng, *BABAR* Analysis Document 729 (2004).

[66] D. Lange, G. Sciolla, M.C. Simani, Y. Zheng, *BABAR* Analysis Document 730 (2004).

[67] A. Gritsan, *BABAR* Analysis Document 156 (2001).

[68] A. Gritsan, *BABAR* Analysis Document 312 (2001).

[69] Skims in *BABAR*,

http://www.slac.stanford.edu/BFROOT/www/Physics/skims/skims.html.

[70] Simulation and Reconstruction,

http://www.slac.stanford.edu/BFROOT/www/doc/workbook/simreco/simreco.html.

[71] D.Wright, BEGET: The B-Factory Event Generator Version 21, *BABAR* Note 149 (1994).

[72] GEANT4:

S. Agostinelli *et al.*, Nuclear Instruments and Methods in Physics Research **A506**, 250 (2003).

http://www.slac.stanford.edu/BFROOT/www/Physics/

Tools/generators/GenFwkInt/GenFwkInt.html.

[73] *BABAR* Collaboration, B. Aubert *et al.*, Phys. Rev. Lett. **94**, 131801 (2005).

[74] RooFit tools, http://roofit.sourceforge.net/.

[75] RooRarFit tools, http://rarfit.sourceforge.net/.

[76] M. Pivk and F.R. Le Diberder, ${}_s\mathit{Plot}$: a statistical tool to unfold data distributions, arXiv:physics/0402083v3.

[77] Measurement of the Number of $\Upsilon(4S)$ Mesons Produced in Run 1 (B Counting), *BABAR* Analysis Document 134.

[78] D. Lopes Pegna *et al.*, Tracking efficiency systematics for R22, v03.

[79] PID Tools Group,

http://www.slac.stanford.edu/BFROOT/www/Physics/Tools/Pid/

PidOnMc/pidonmc.html.

[80] E.M. Aitala *et al.*, E791 Collaboration. Phys. Rev. Lett. **86**,765 (2001).

[81] J. E. Gaiser, Charmonium Spectroscopy from Radiative Decays of the J/Ψ and Ψ', SLAC-R-255 (1982).

[82] H. Albrecht *et al.*, Phys. Lett. **B241**, 278 (1990).

[83] *BABAR* Collaboration, B. Aubert *et al.*, Improved Measurement of $B \to \rho^+\rho^0$ and Determination of the CKM Angle α, arXiv:hep-ex/0901.3522v1.

[84] Belle Collaboration, Phys. Rev. **D77**, 111102 (2008).

[85] K. Hagiwara *et al.*, Phys. Rev. **D66**, 010001 (2002).

[86] *BABAR* Collaboration, A.Telnov, *BABAR* Analysis Document 1500 (2007).

[87] Release 24 Computing,

http://www.slac.stanford.edu/BFROOT/www/Computing/R24-main-monitoring-page.html

Appendix A

Unitarity Angle Measurements

The unitarity angles α, β, γ, defined in terms of the CKM matrix elements in Eq. (2.27), describe the amount of CP violation in the B_d system. If the Standard Model is correct, then $\alpha + \beta + \gamma = 180^\circ$ and the unitarity triangle (shown in Figs. 2.3, 2.4) is closed. As such, the bulk of the work at B-factories is geared toward isolating the relevant decays and measuring each of these angles. In the end the individual results are combined to produce a picture of how consistent the experimental results are with the Standard Model.

A.1 Measuring β

The value for the angle $\beta \equiv -arg\left[\frac{V_{cd}V_{cb}^*}{V_{td}V_{tb}^*}\right]$ is obtained primarily from $B \to J/\Psi K^0$ (*i.e.* $b \to c\bar{c}s$) decays, shown in Fig. A.1. The decay mode $B \to J/\Psi K_S^0$ has a large Branching Fraction ($(863 \pm 35) \times 10^{-6}$ [21]) and once the other modes are taken into account, the analysis has a small theoretical uncertainty [22] (hence it is often referred to as 'The Golden Mode').

The CP violation in the process occurs as a result of the interference between direct decays (Fig. A.1) and mixing (Fig. 2.5) followed by the direct decay. As such,

$$\lambda(B \to J/\Psi K_S^0) = -\left(\frac{V_{tb}^* V_{td}}{V_{tb} V_{td}^*}\right)\left(\frac{V_{cs}^* V_{cb}}{V_{cs} V_{cb}^*}\right)\left(\frac{V_{cd}^* V_{cs}}{V_{cd} V_{cd}^*}\right),$$

where the first term comes from the mixing, the second from the ratio of the amplitudes $A(\overline{B} \to J/\Psi K_S^0)/A(B \to J/\Psi K_S^0)$, the third originates from $K^0 - \bar{K}^0$ mixing with λ defined in Eq. (2.35). The corrections to the weak phase are doubly Cabibbo suppressed [23], which implies that $|\lambda| \simeq 1$. Thus, the CP coefficients defined in Eq. (2.40) are $S_{CP} = Im(\lambda) = \sin 2\beta$, $C_{CP} = 0$ and the physically measured asymmetry, to a good approximation ($O(\lambda_w^4)$, with λ_w given by Eq. (2.24)), is

$$a_{CP} = -\sin 2\beta \sin(\Delta m_B t). \tag{A.1}$$

Once the theoretical error is accounted for [22], $\sin 2\beta = 0.668 \pm 0.028$ at the 95% Confidence Level (CL) [23] with the Probability Density shown in Fig. A.2. Moreover, as each measurement is made, the results constrain the CKM parameters ρ and η, which

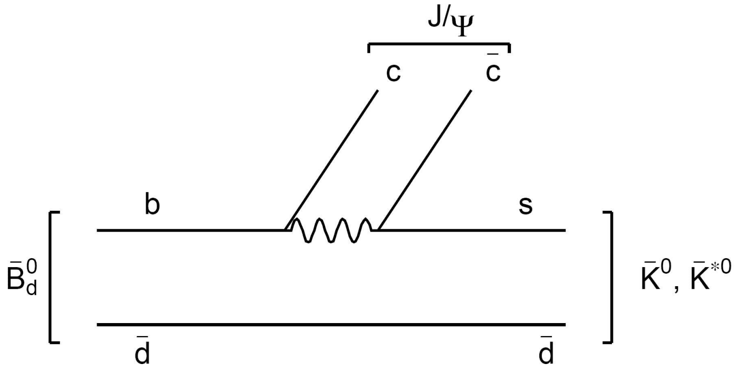

Figure A.1: *Dominant diagram for the* $\overline{B}^0 \to$ *charmonium+*K *decay [6]. The process is used to measure* $\sin 2\beta$.

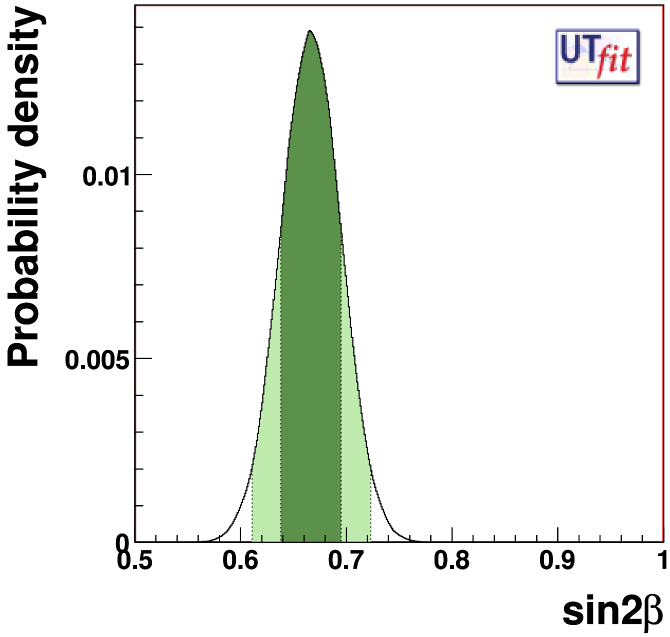

Figure A.2: *Probability Density Distribution as a function of* $\sin 2\beta$*, from* $B \rightarrow J/\Psi K^0$*, as obtained by the UTFit Collaboration [23]. The values outside the darkly and lightly shaded regions are excluded at* $68\%(1\sigma)$ *and* 95% *levels, respectively. Specifics of how the measurements are combined by the UTFit Collaboration and the scan is obtained are discussed in Section A.4.*

parametrize the amount of CP violation in the Standard Model (Eq. (2.24)). For $\sin 2\beta$ the constraints are shown in Fig. A.3.

In addition to $\sin 2\beta$, it is possible to measure $\cos 2\beta$ at B-factories. This is accomplished either by performing a time-dependent analysis together with an angular analysis of a Vector-Vector final state for $B \rightarrow J/\Psi K_S^{*0}$ decays [25], or by using a Dalitz approach, which extracts the value from the interference between B^0 and $\overline{B}^0$ amplitudes [26]. The results of the two methods are then combined, as shown in Fig. A.4. While the constraints are not nearly as strong as the ones coming from the $\sin 2\beta$, the combination of

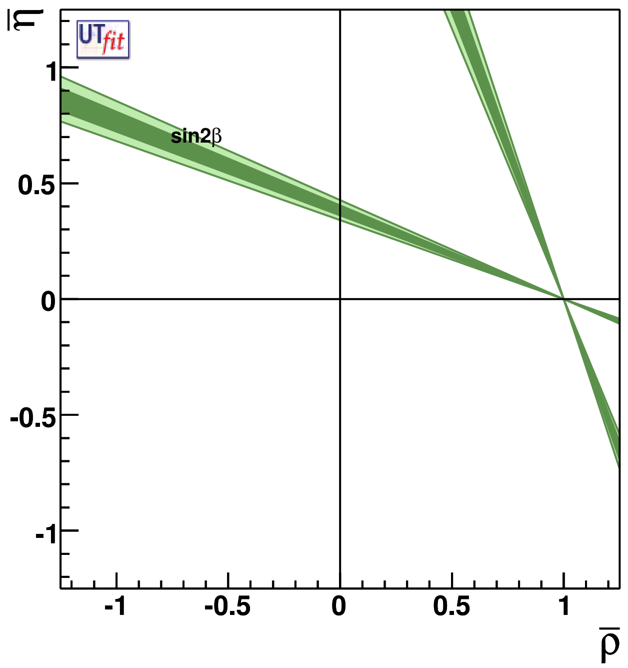

Figure A.3: *Restrictions on CKM parameter* $\bar{\eta}$ *vs.* $\bar{\rho}$ *given by the* $\sin 2\beta$ *measurements (from* $B \to J/\Psi K^0$ *decays) [23]. The values outside the darkly and lightly shaded regions are excluded at* 68% *and* 95% *CLs, respectively.*

two measurements excludes the 'steeper' of the two cones in Fig. A.3.

A.2 Measuring α

The angle $\alpha \equiv -arg\left[\frac{V_{td}V_{tb}^*}{V_{ud}V_{ub}^*}\right]$ is extracted from $b \to u\bar{u}d$ decays. Specifically, the relevant processes are $B \to \pi\pi$, $B \to \rho\pi$, $B \to \rho\rho$ with the leading order diagram shown in Fig. A.5(a). The CP violation occurs primarily via usual mixing (shown in Fig. A.5(b)). The combination of the two effects yields a phase of $\alpha = 180° - \beta - \gamma$; or more precisely $\alpha_{measured} = 180° - \beta - \gamma + \alpha_{NonSM}$, where α_{NonSM} is the potential contribution from Non Standard Model physics.

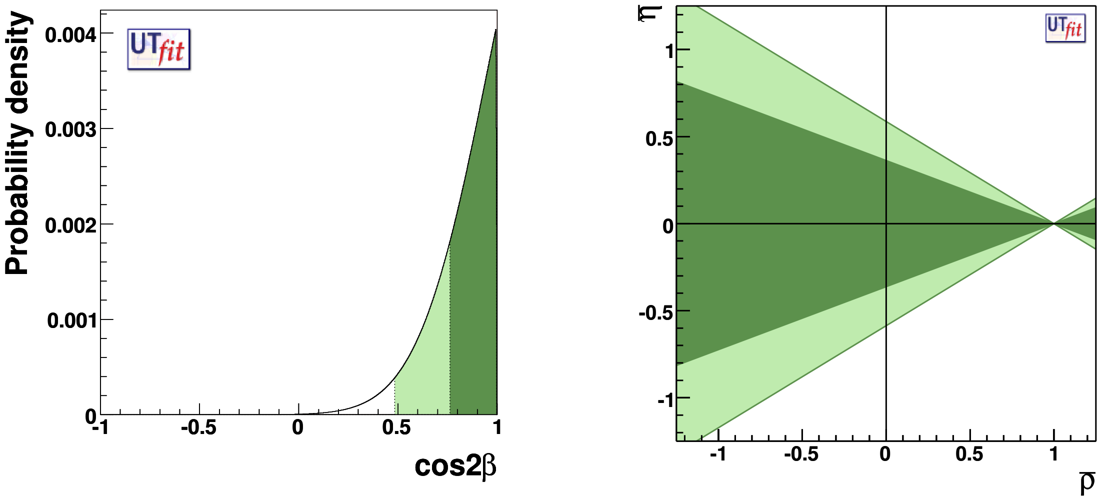

a) b)

Figure A.4: *Results of the* $\cos 2\beta$ *measurements combined via UTFit [23] for a) The Probability Density b) The CKM Parameters* $\bar{\eta}$ *vs.* $\bar{\rho}$*. The values outside the darkly and lightly shaded regions are excluded at* 68% *and* 95% *levels, respectively.*

However, unlike $\sin 2\beta$ measurements, here the impact of the (Penguin) loop corrections must be accounted for. When a decay proceeds to a CP final state (*i.e.* $B \to \pi\pi$, $B \to \rho\rho$) we use isospin analysis developed by Gronau and London [15], with a detailed

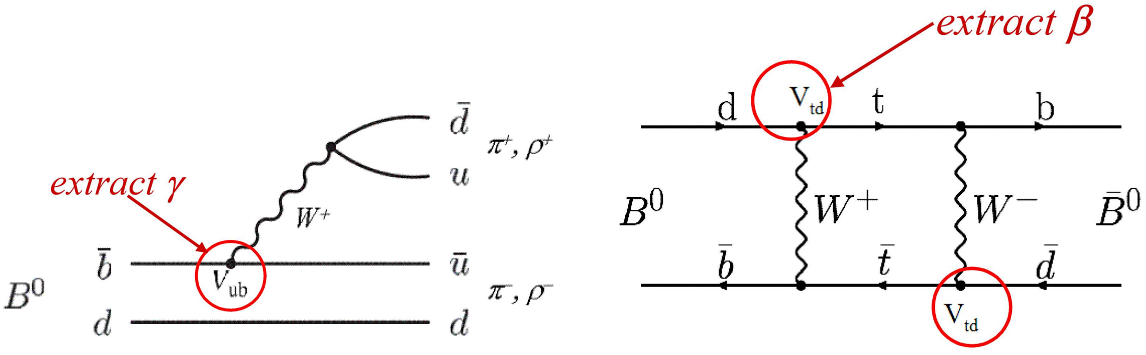

(a) (b)

Figure A.5: *Processes used in the measurement of* α*: a)*$b \to u\bar{u}d$ *decays, b)*B^0*-*$\overline{B}^0$ *mixing.*

discussion of the procedure given in Section 2.4.1. In the case of $B \to \rho\pi$, a Dalitz analysis is used to extract both the absolute values and the phases for the tagged decay amplitudes [27]. The Probability Density scans for the processes are shown in Fig. A.6. The $B \to \rho\rho$ channel gives the strongest constraints on α, with a detailed discussion of the analysis given in Section 4.11. All three results are combined by the UTFit [23] and CKMfitter [24] collaborations to give $\alpha = (92 \pm 7)^\circ$ and $\alpha = (81.1^{+17.5}_{-4.9})^\circ$, respectively. The combined Probability Density scans, along with the constraints on the CKM parameters coming from these measurements, are shown in Fig. 4.16.

A.3 Measuring γ

The angle $\gamma \equiv -arg\left[\frac{V_{ud}V^*_{ub}}{V_{cd}V^*_{cb}}\right]$ is measured by analyzing $B \to DK$ decays and comparing V_{ub} with V_{cb} mediated transitions, as shown in Fig. A.7. At leading order, γ is extracted via the Gronau, London, Wyler method [28], which relates the amplitudes for

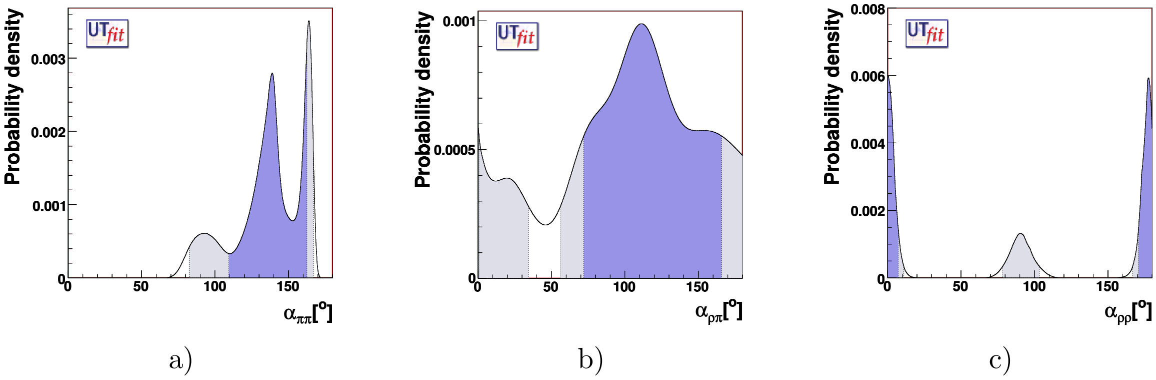

a) b) c)

Figure A.6: *Probability Density Distribution as a function of α for: a)$B \to \pi\pi$, b)$B \to \rho\pi$, c)$B \to \rho\rho$. The values outside the darkly and lightly shaded regions are excluded at 68% and 95% levels, respectively [23].*

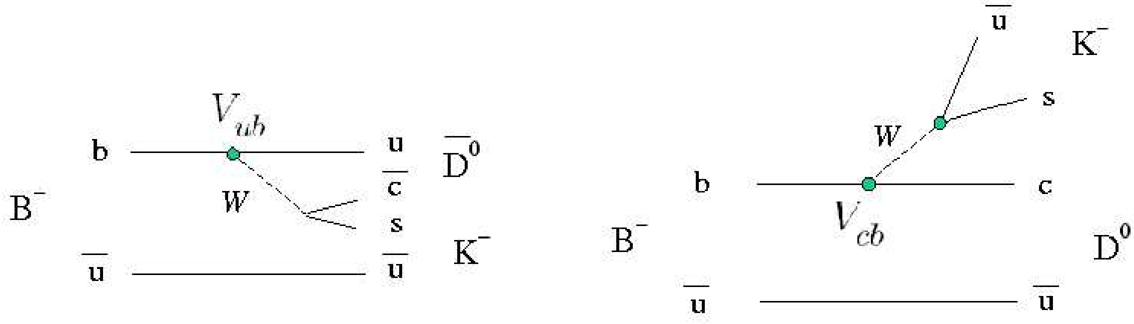

(a) (b)

Figure A.7: *$B \to DK$ decays used to measure γ. Tree level amplitudes for a) Color-allowed, V_{ub} mediated, b) Color-suppressed , V_{cb} mediated transitions [23].*

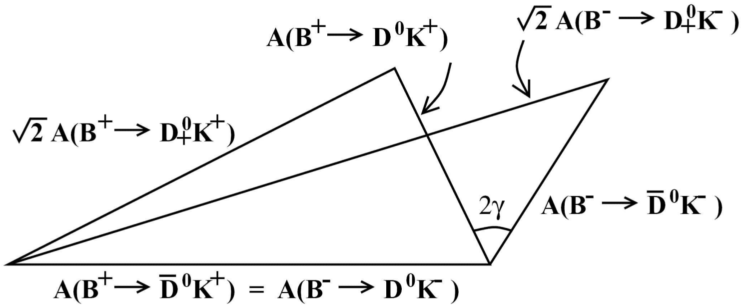

Figure A.8: *Triangle relations for $B^{\pm} \to DK^{\pm}$ decays [6].*

$B^{\pm} \to DK^{\pm}$ decays to each other by exploiting the isospin properties of the system. The relation between the amplitudes and the angle is represented by two triangles in the complex plane (Fig. A.8). Upon performing a time dependent analysis, we extract the value for γ in terms of the ratio of the amplitudes for V_{ub} and V_{cb} transitions along with the difference between their strong phases.

However, in practice there are several complications to the above approach. First, $|A(B^- \to \bar{D}^0K^-)|/|A(B^- \to D^0K^-)| \simeq 0.08$ [31] due to both CKM and color suppression.

Thus, the triangles in Fig. A.8 become squashed, causing large uncertainties on 2γ. Moreover, both D^0 and $\bar{D}^0$ can decay to the $K^+\pi^-$ final state, which results in large interference effects for the related branching fractions ($B^- \to \bar{D}^0 K^-$ vs. $B^- \to D^0 K^-$) as well as the $\bar{D}^0$ hadronic tags. But following the formalism of Atwood, Dunietz, Soni [29], the interference effects for doubly Cabbibo suppressed decays (*e.g.* $D^0 \to K^+\pi^-$, $D^0 \to K\pi\pi$) are included. Furthermore, using the Dalitz (*a.k.a.* Giri, Grossman, Soffer, Zupan) approach [30], the full sub-resonance structure of both Cabbibo allowed and Cabbibo suppressed three-body decays is taken into account. Comparison between the methods is shown in Figs. A.9, A.10. Combined Probability Density scans along with the resultant constraints on the CKM parameters are shown in Fig. A.10. In the end, γ is still not constrained nearly as strongly as $\sin 2\beta$ or α, with its value estimated at the 95% CL to be $(78 \pm 12)^\circ$, $(-102 \pm 16)^\circ$ by the UTFit [23] and $(70^{+27}_{-29})^\circ$ by the CKMfitter [24] collaborations.

In addition to measuring γ from $B \to DK$ processes, it is also possible to obtain the value for $\sin(2\beta + \gamma)$ using $B \to D^{(*)}\pi$ decays. The idea is that $\bar{b} \to \bar{u}c\bar{d}$, $b \to c\bar{u}d$ transitions have no (Penguin) loop corrections and can be expressed as hadronic matrix elements of a low-energy effective Hamiltonian [32]. The product of the observables $\lambda_f \lambda_{\bar{f}}$, defined by Eq. (2.35), is $\lambda(B \to f)\lambda(B \to \bar{f}) = e^{-2i(2\beta+\gamma)}$ [6] (Section 7.6.1). Once the impact of tag-side interference is taken into account [33], a time-dependent CP analysis is performed. As a result, $2\beta + \gamma = (\pm 90 \pm 32)^\circ$ [23] and (taking the $B \to DK$ data into account) $\gamma = (76^{+16}_{-23})^\circ$ [24] at the 95% CL. The resulting Probability Density scans and constraints on the CKM parameters are shown in Fig. A.11.

A.4 Combining The Measurements

As we have discussed, the measurements are combined by the UTFit [23] and the CKMfitter [24] groups. The main difference between the two sets of results is how theoretical inputs are treated. Namely, UTFit uses the Bayesian approach, which makes no (formal) distinction between experimental and theoretical parameters [34]. On the other hand, the CKMfitter implements Rfit, which combines the inputs in a frequentist fashion [35]. In this case, the theoretical uncertainties have no statistical meaning (*i.e.* the theoretical and statistical errors are added in quadrature, with the likelihood function corresponding to the product of two uncertainties). The two approaches assume different input likelihoods for

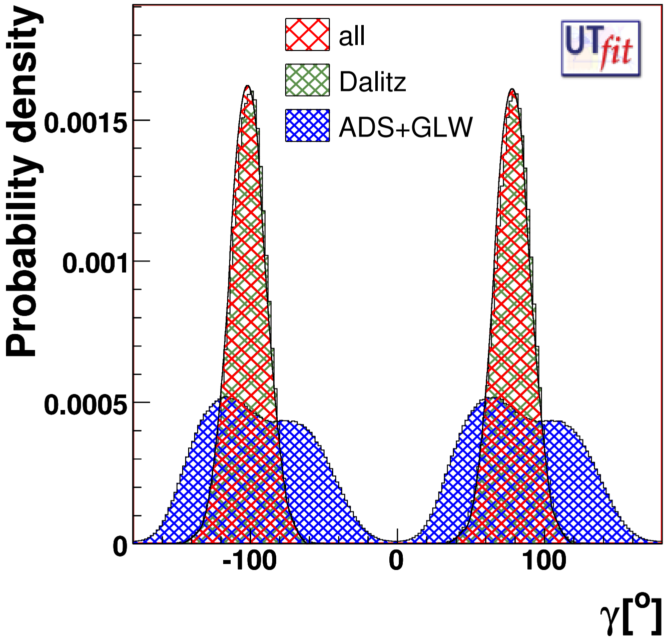

Figure A.9: *Comparison of the Probability Density Distribution of γ obtained by the GLW+ADS [28], [29] vs. GGSZ Dalitz [30] methods (made by the UTFit Collaboration [23]).*

the same set of parameters [36]. Specifically, in addition to the measurements of α, β, γ discussed above, the two groups utilize information from:

- Unitarity Triangle sides.
- B_s decays.
- CKM matrix elements.
- Rare branching fractions (*e.g.* $B \rightarrow \tau\nu$, $B \rightarrow \mu^+\mu^-$, *etc.*).
- Theory.

The combination of constraints on the CKM parameters from all of the inputs is shown in Fig. A.12, which are determined by the CKMfitter (UTFit) to be $\bar{\eta} = 0.341^{+0.032}_{-0.025}$, $\bar{\rho} = 0.139^{+0.053}_{-0.040}$, ($\bar{\eta} = 0.342^{+0.029}_{-0.027}$, $\bar{\rho} = 0.154 \pm 0.044$) at the 95% CL [24], [23]. There are no statistically significant deviations from the Standard Model.

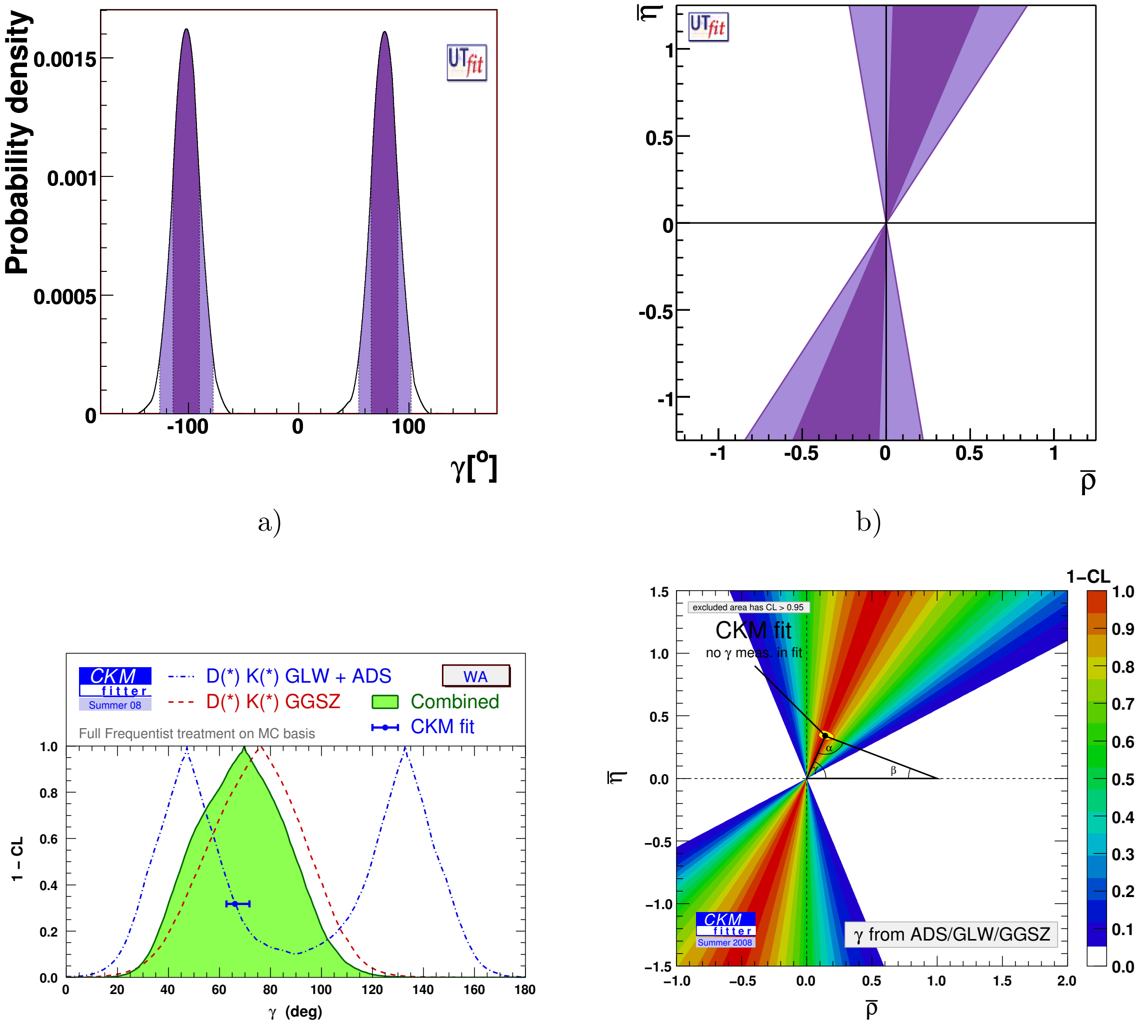

a)

b)

c)

d)

Figure A.10: *γ measurements from $B \to DK$ decays. Results of the GLW [28], ADS [29], GGSZ Dalitz [30] are combined to give: a),c) Probability Density Distribution; b),d) CKM Parameters $\bar{\eta}$ vs. $\bar{\rho}$ [23], [24]. For the UTFit, the values outside the darkly and lightly shaded regions are excluded at 68% and 95% levels, respectively. For the CKMfitter, the shaded regions denote a 95% CL, while the blue bar denotes the estimated value from all other measurements.*

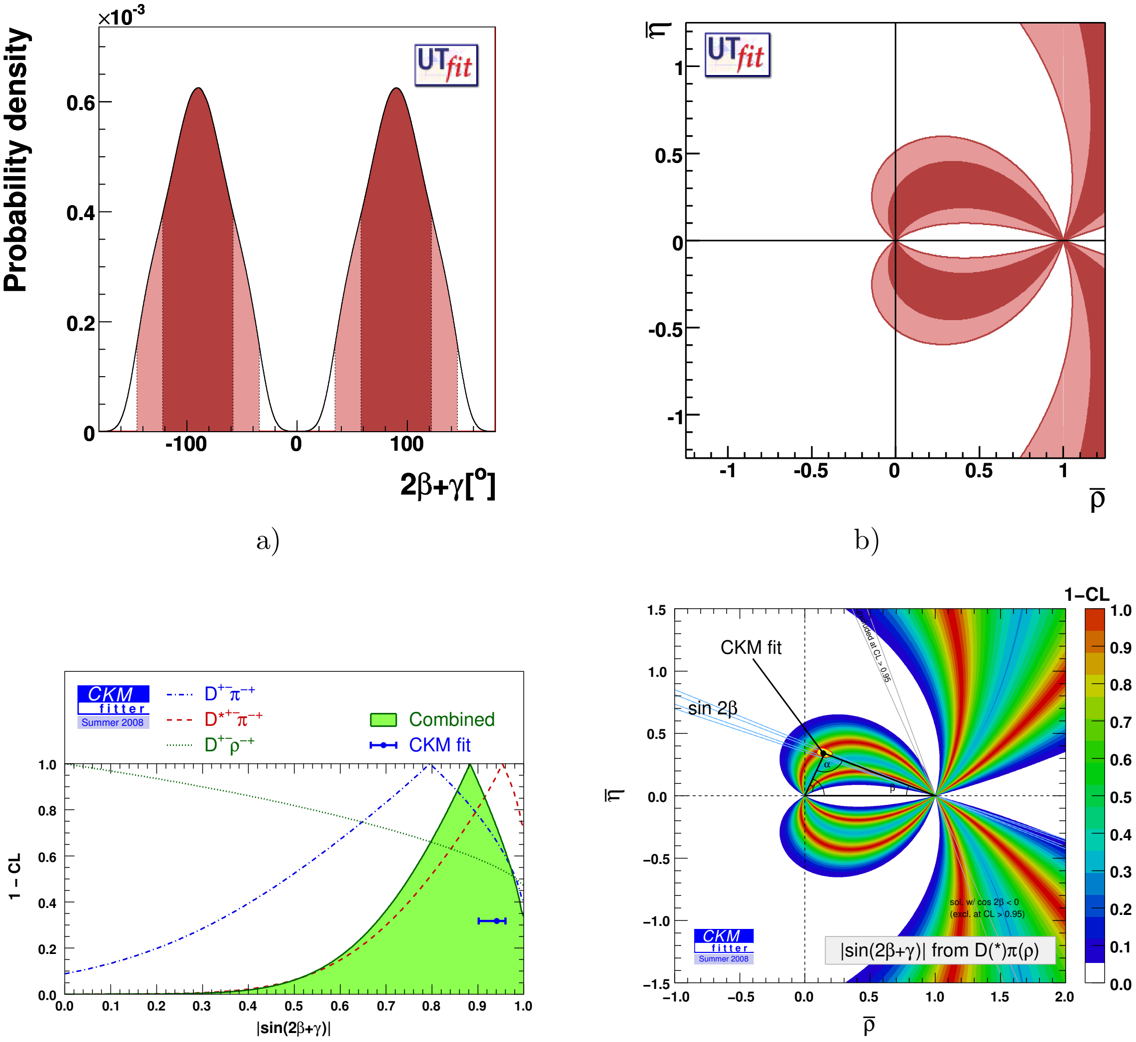

a)

b)

c)

d)

Figure A.11: $\sin(2\beta + \gamma)$ *measurements from* $B \rightarrow D\pi$ *decays for: a),c) Probability Density Distribution; b),d) CKM Parameters* $\bar{\eta}$ *vs.* $\bar{\rho}$ *[23], [24]. For the UTFit, the values outside the darkly and lightly shaded regions are excluded at 68% and 95% levels, respectively. For the CKMfitter, the shaded regions denote a 95% CL, while the blue bar denotes the estimated value from all other measurements.*

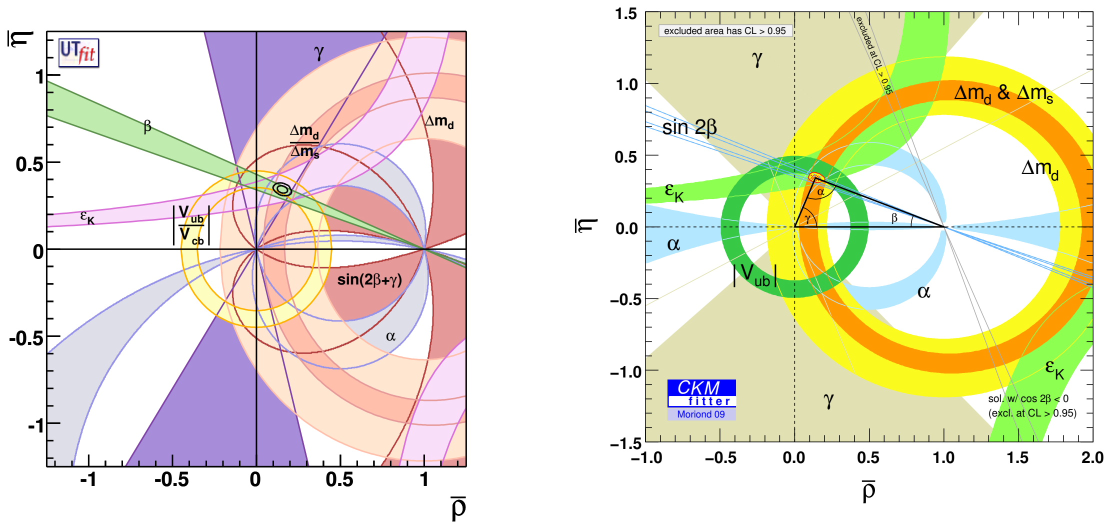

a) b)

Figure A.12: *Restrictions of CKM Parameters $\bar{\eta}$ vs. $\bar{\rho}$, utilizing all of the inputs, for: a) UTFit [23], b) CKMfitter [24]. The shaded regions denote a 95% CL.*

Appendix B

Energy Loss In Matter

When charged particles pass through the silicon wafers in the SVT and the gas mixture in the DCH, they lose energy due to interactions with the material. In the moderately relativistic range ($\beta\gamma \sim 1.0 - 10$) the loss is due to ionization and atomic excitation. It is modeled by the Bethe-Bloch (BB) equation [85]:

$$-\frac{dE}{dx} = \frac{Kz_i^2}{A}\frac{1}{\beta}\left(\frac{1}{2}\ln(\frac{2m_e c^2\beta^2\gamma^2 T_{max}}{I^2}) - \beta^2 - \frac{\delta}{2}\right), \tag{B.1}$$

where $K = 4\pi N_A r_e^2 m_e c^2 = 0.307\mathrm{MeV}\cdot\mathrm{cm}^2$, z_i is the charge of the incident particle, Z is the atomic number of the target, m_e is the electron mass, T_{max} is the maximum kinetic energy which can be imparted to a free electron in a single collision, I is the mean excitation energy and δ is the density effect correction due to the presence of the matter. Note that the energy loss has a relatively simple form ($-dE/dx = (\mathrm{C}_1\ln(\beta\gamma) - \mathrm{C}_2\beta^2 - \mathrm{C}_3)/\beta^2$, with the coefficients C_i depending only on the properties of the material and fundamental constants of nature), which is universal for all charged particles in the *BABAR* detector.

However, in practice momenta (rather than velocities) are measured for each track.

This results in distinct Bethe-Bloch curves for each particle type (Fig. B.1). By matching the dE/dx to the momentum for each collection of hits we are able to identify the corresponding particle type. Inversely, if the PID information is provided from other detector components, one can extract the momentum value from dE/dx (in the low $\beta\gamma$ region, where the function is monotonically decreasing). In order to accomplish these tasks, we combine the energy loss information from each hit along the track and match it to the particular BB curve.

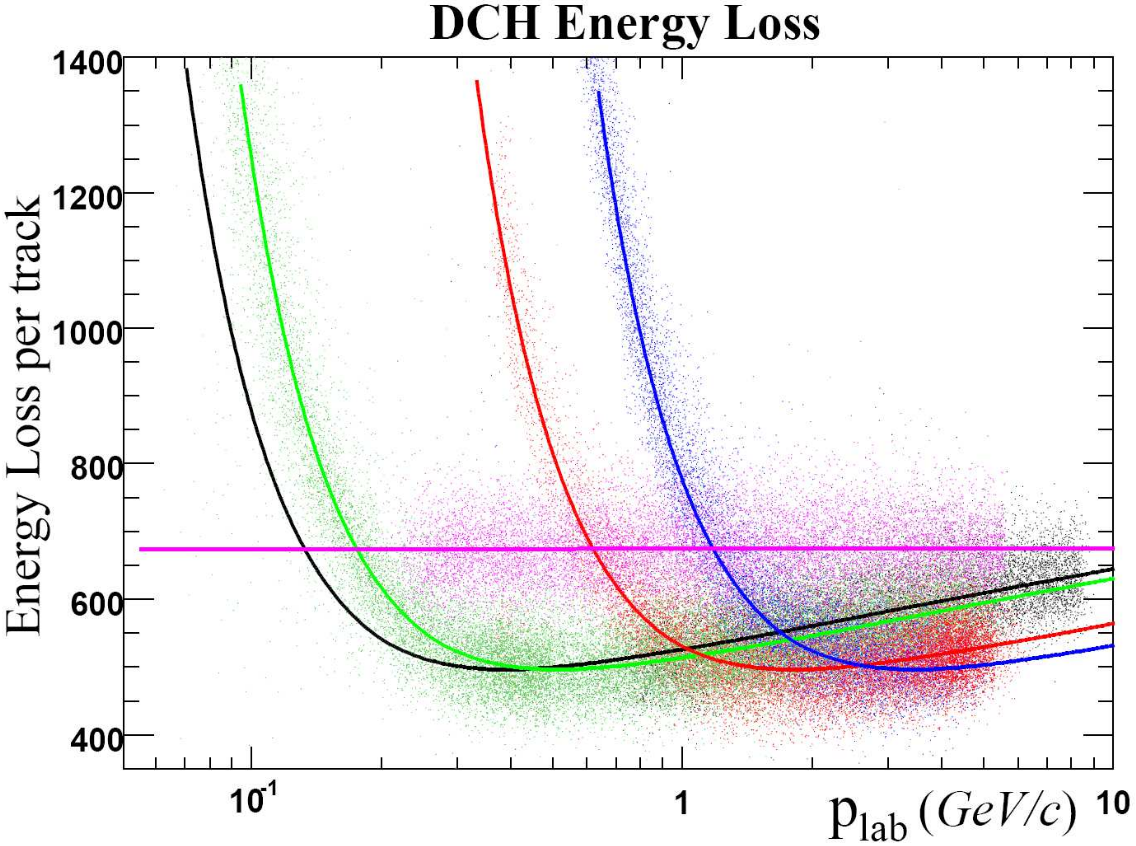

Figure B.1: *Bethe-Bloch curves for each particle type present in the BABAR detector [86]. Shown left to right (i.e. in order of increasing mass) are muons (black), pions (green), kaons (red) and protons (blue). The electrons are highly relativistic and the BB function is an (essentially) flat tail in this momentum range.*

B.1 Truncated Mean

The standard way to use the dE/dx information in *BABAR* is to implement the Truncated Mean algorithm. It relies on the approximation that the particle is moving sufficiently fast for the energy loss of each hit to be negligible compared to the overall momentum (which therefore assumed to be constant along the track). However, rather than having a Gaussian shape, the distribution (of the number of hits vs. dE/dx for a particular momentum value) has a Landau tail. We truncate it by removing the outliers with the highest energy (40% of the hits for the SVT and 20% for the DCH) as well as by throwing out the point with the lowest energy in the SVT, in order to reduce the error due to electronics noise [45]. An average dE/dx for track is then computed from the remaining values.

In practice, the situation is more complicated. The measured energy loss depends not only on velocity but also on track charge, its polar angle θ, its azimuthal angle ϕ as well as on how long the detector has been in service (*i.e.* run number). An example of such variations in dE/dx is shown in Fig. B.2. They have been parametrized to high precision by A.Telnov [86]. For instance, the modified Bethe-Bloch curve for the SVT is represented as:

$$-\frac{dE}{dx} = C_0(\theta) * (1 + C_7(\theta, \phi, x)) * (1 + C_1(\theta)x + C_2(\theta)x^2) * (1 + (C_4(\theta))^{-x})^{C_3(\theta)} \qquad \text{(B.2)}$$

for $x < 2$ (*i.e.* for all particles except electrons, which have $-\frac{dE}{dx} = C_5(\theta) + C_6(\theta) * (x - 3.0)$), where $x = \log_{10}(\beta\gamma)$; C_i are calibration constants, which are computed separately for each run number, each charge ($+1$ or -1) as well as for data vs. MC. It is also possible to compute the (approximate) inverse for the above equation, which is then be used to obtain momentum

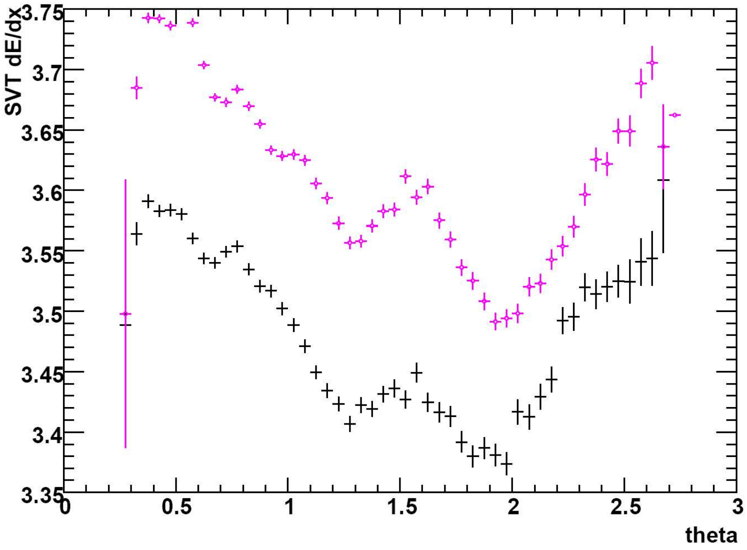

Figure B.2: *Measured energy loss in the SVT as a function of the polar angle theta shown for Run1 (bottom black markers) as well as for Run5 (top magenta markers with the circle through the center) data [86]. The discrepancies due to the imperfections in BABAR (i.e. the impact of electronics degradation, radiation damage, etc.) rather than detector physics.*

information from the dE/dx value (for a known particle type). I have incorporated both the Eq. (B.2) as well as its inverse into the *BABAR* software framework and they are available in Release 24 [87].

B.2 Hit Based Approach

As the energy of the particles decreases, the dE/dx goes up in accordance with Eq. (B.1). For sufficiently low momenta ($\sim$ 200 MeV/c) the truncated mean approximation breaks down since the changes in the track momentum (due to collisions with matter) can not be neglected. Therefore, the corresponding dE/dx values can no longer be averaged over the track and it is necessary to study each hit independently.

Developing the correct treatment is a work in progress, which requires isolating

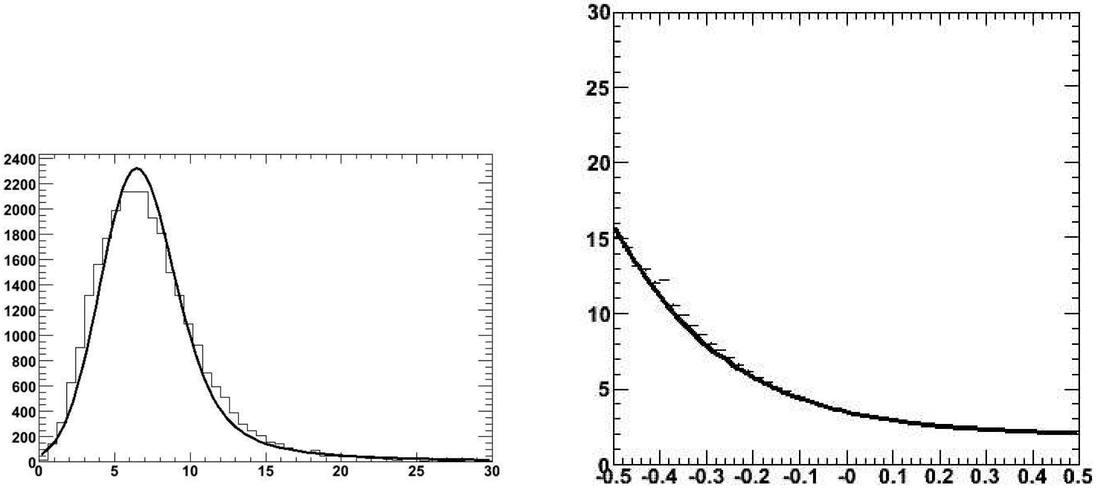

a) b)

Figure B.3: *Hit based studies. Shown is the proton data sample from Λ decays: a) Number of hits for a particular value of* $x = \log_{10}(\beta\gamma)$ *(*$-0.2 < x < 0.18$*), b) The most probable value as a function of* x*.*

sufficiently pure samples (*i.e.* samples where we know the particle mass) and studying their energy losses in the SVT. As shown in Fig. B.3, we fit the dE/dx values for a particular $\log_{10}(\beta\gamma)$ with a more complex function (a convolution of a Gaussian with a Landau PDF), where the peak values are parametrized via a formula resembling Eq. (B.2). While the truncated mean is still the standard for *BABAR* analyses, the new approach should improve track reconstruction, resolution and efficiency (and should be of particular relevance for PID, $B \rightarrow D^{*}\pi$ analyses, $\Upsilon(2S) \rightarrow \Upsilon(1S)\pi^{+}\pi^{-}$ analyses, *etc.*).

Appendix C

Event Shape Discriminants

C.1 Construction

The Event Shape Discriminants are designed to distinguish the 'jetty' quark-antiquark continuum background events from the more symmetric $B\overline{B}$ decays. When constructing them, we explicitly require $|\cos\theta_T| < 0.8$ (in order to reject a large portion of the background) and then combine the following variables:

1. The four Legendre monomials (split for charged and neutral particles), which describe the shape of the event : $L_0^{charged}$, $L_0^{neutral}$, $L_2^{charged}$, $L_2^{neutral}$.
2. The sum of the transverse momenta of all particles for the rest of the event (*i.e.* for all tracks other than the ones corresponding to the four charged pions), calculated with respect to the B direction : $\sum_r p_T$.
3. Additional geometric variables : $\cos\theta_{BT}$ (the cosine of the angle between the B thrust and the z axis), $\cos\theta_B$ (cosine of the B direction with respect to the beam), $cos\theta_T$

(cosine of the angle between the thrust of the rest of the event and the B thrust), shown in Figs. C.1(a)-C.1(f).

4. The vertex chi-squared, computed for 4 charged tracks : χ^2_{vtx} (or more precisely, the vertex convergence probability $p_{\mathrm{vtx}} = -\log(Prob(\chi^2_{\mathrm{vtx}}, 5))$), shown in Figs. C.1(g),(h).

The above observables are combined in a manner which optimizes the discriminating ability between the signal and background. Namely, we construct the shape variable which maximizes the ratio between the signal and background efficiency. The bulk of the task is accomplished by the Legendre monomials, while adding the remaining parameters refines the process even further (Fig. C.2).

C.1.1 Event Shape

The standard approach is to use an Artificial Neural Network (NN). This technique usually gives the greatest possible discriminating ability. It has also been used by a number of *BABAR* analyses in the past (*e.g.* [73]). Specifically, the NN nonlinearly combines the observables into one discriminant by assigning each variable (or combination of variables) a corresponding coefficient, which is determined by running the network on known signal and background events (*a.k.a.* training). In our case, we train the NN on the truth-matched signal Monte-Carlo as well as off-resonance data. The resulting acceptance rates for the continuum, given a set amount of signal, are shown in Table. C.1.

The distributions for the direct output of the NN are strongly peaking and difficult to fit (with enough precision to effectively distinguish between the PDFs). We resolve the problem by applying an inverse Fermi transformation ($\mathcal{L} \rightarrow -\ln(\frac{1}{\mathcal{L}} - 1)$) to it. The resulting

Table C.1: *Continuum efficiency vs. (longitudinally polarized) signal efficiency.*

Signal (%)	90	70	50	30	10
Background (%)	43.8	16.9	6.3	2.0	0.3

variable is referred to as $eShape$. It is generally fitted with a sum of three gaussians (two of which are asymmetric). The PDFs for the signal as well as of the backgrounds are shown in Figs. D.5, D.6.

C.1.2 Likelihood Shape

As an alternative to the NN multivariate discriminant, we form a likelihood-based discriminant

$$likeShape = \log \frac{\mathcal{L}_{\rm sig}}{\mathcal{L}_{\rm bkg}},$$

where $\mathcal{L}_{\rm sig}$ ($\mathcal{L}_{\rm bkg}$) is the multivariate event likelihood for signal (background) events. We use the same input variables and train it on the same samples as $eShape$. However, in this case the discriminant is constructed explicitly, rather than relying on the 'black box' Neural Net. Since there is a non-linear correlation between the Legendre monomials $L0$, $L2$ we remove it by transforming $L2$ (for both charged as well as neutral particles) via

$$L_{20} = \frac{\mu_{L2}(L0)}{\sigma_{L2}(L0)} L2,$$

where $\mu_{L2}(L0)$, $\sigma_{L2}(L0)$ are the mean and sigma of the $L2$ distribution as a function of $L0$ (shown in Fig. C.3). They are determined from the quadratic fit to be

$$\mu_{L2}(L0) = 0.03 - 0.085L0 - 0.041(L0)^2, \qquad \text{(C.1)}$$

$$\sigma_{L2}(L0) = 0.051L0 + 0.018(L0)^2.$$

We then combine the monomials with $\sum_r p_T$, account for the correlations with the $\cos\theta_T$ and construct the final Fisher variable

$$\mathcal{F}_6 = 0.931\, L_{20\,\mathrm{tracks}} + 1.1714\, L_{20\,\mathrm{neutrals}} + 0.0696 \sum_r p_T - 0.22|\cos\theta_T| + 4.61\cos^2\theta_T. \quad \text{(C.2)}$$

As shown in Fig. C.4, it is easily fitted with a gaussian distribution.

The likelihood discriminant *likeShape* is formed by combining $\mathcal{F}_6$, $|\cos\theta_T|$, $\cos\theta_B$, $\cos\theta_{BT}$ as well as p_{vtx}. (Note that unlike *eShape* we individually fit each variable to construct *likeShape*.) The distribution for the signal vs. the background events is shown in Fig. C.5. Its discriminating ability is nearly the same as that of *eShape* (Fig. C.2). However, the likelihood discriminant handles correlations better and the corresponding PDFs have a simpler form (Figs. D.7, D.8). For most modes they are be fitted by a sum of two gaussians (vs. three for the *eShape*), which reduces the systematic error due to PDF shape uncertainty.

C.2 Comparison Studies

Event Shape and Likelihood Shape discriminants are highly correlated ($\sim 95\%$) and we perform a complete comparison study in order to determine which one functions better. Namely, we fit the PDFs, construct the ML Fit, verify its functionality and obtain the results (*i.e.* repeat the analysis procedure of Chapter 4) for each discriminant, while all other variables remain the same. First, we used an incomplete dataset (Runs 1-5 with portions of Run 6) to examine the impact on the signal yield and CP parameter systematics, in order to determine which shape variable should be used in the final fit. The results of the study are summarized in Table. C.2. Its conclusions are:

Table C.2: *Uncertainties due to implementing the fitter with likeShape vs. eShape on the test dataset (Runs 1-5 with portions of Run 6). The σ_{Syst} refers to the systematic error due to the uncertainty in the discriminant PDF parameters.*

Parameter	σ_{Stat}	σ_{Syst}	σ_{Total}
$N^{\rho^0\rho^0}_{likeShape}$	25.71 ± 0.18	0.688	25.72
$N^{\rho^0\rho^0}_{eShape}$	25.81 ± 0.19	3.266	26.02
$S_{likeShape}$	1.04 ± 0.03	0.006	1.04
S_{eShape}	1.01 ± 0.03	0.022	1.01
$C_{likeShape}$	0.82 ± 0.03	0.044	0.82
C_{eShape}	0.83 ± 0.03	0.047	0.83

1. Using the likelihood-based discriminant reduces the systematic error due to PDF shape uncertainty by 2.6 events (*i.e.* it decreases from 3.266 to 0.688, as shown in Table C.2).

2. Statistical uncertainties dominate the overall error.

3. The collaboration chose to keep *eShape* as the default variable for the purposes of publication.

C.3 TDCP Fit Using The Likelihood Discriminant

We also perform the fit on the full dataset while using *likeShape*, instead of *eShape*. The raw results are shown in Section 4.7, Table 4.25. Since the fitter configuration has changed, several portions of the analysis had to have been repeated. Namely it was necessary to perform a new set of toy scans in order to determine fit bias. In this case we started with 63 longitudinal events and 27 transverse events (close to the results of the ML fit), and varied each yield around this value. The results are shown in Fig. C.6. The fitter bias is 5.02 ± 1.38 for longitudinal signal, -2.17 ± 0.73 for transverse signal and is roughly independent of the yield. Naturally, we also construct fits of S and C as a function of S, as shown in Fig. C.7. The bias in S and C is consistent with 0 (-0.14 ± 0.09 for S and -0.06 ± 0.04 for C), and all uncertainties are propagated into the systematic errors. The likelihood enhanced projections are used to ensure the validity of the fitter and are shown in Fig. E.14 (there are no discrepancies from what is expected).

The systematic error due to PDF shape uncertainty (for the discriminant component) drops from 3.02 to 0.54 events (as well as from 0.028 to 0.005 and 0.042 to 0.020 for S and C, respectively). The overall event yield fluctuates down to

$$N_{\rho^0\rho^0} = 85 \pm 34\,(\text{stat.}) \pm 14\,(\text{syst.}),$$

with statistical error dominating the result. Due to the lower signal event yield, we obtain higher (statistical) uncertainties for the CP coefficients (and f_L). They are determined to be:

$$S = 0.4 \pm 0.9\,(\text{stat.}) \pm 0.2\,(\text{syst.}),$$

$$C = 0.5 \pm 1.1\,(\text{stat.}) \pm 0.3\,(\text{syst.}).$$

Furthermore, the Branching Fraction and the fraction of longitudinal polarization are measured to be

$$\mathcal{B}_{\rho^0\rho^0} = (0.78 \pm 0.31\,(\text{stat.}) \pm 0.13\,(\text{syst.})) \times 10^{-6}, \tag{C.3}$$

$$f_L = 0.69 \pm 0.19\,(\text{stat.}) \pm 0.05\,(\text{syst.})$$

with the total significance (statistical+systematic) of 3.0σ, when *likeShape* is used. As expected, these results are consistent with the ones obtained using *eShape* (*i.e.* the default analysis described in Chapter 4).

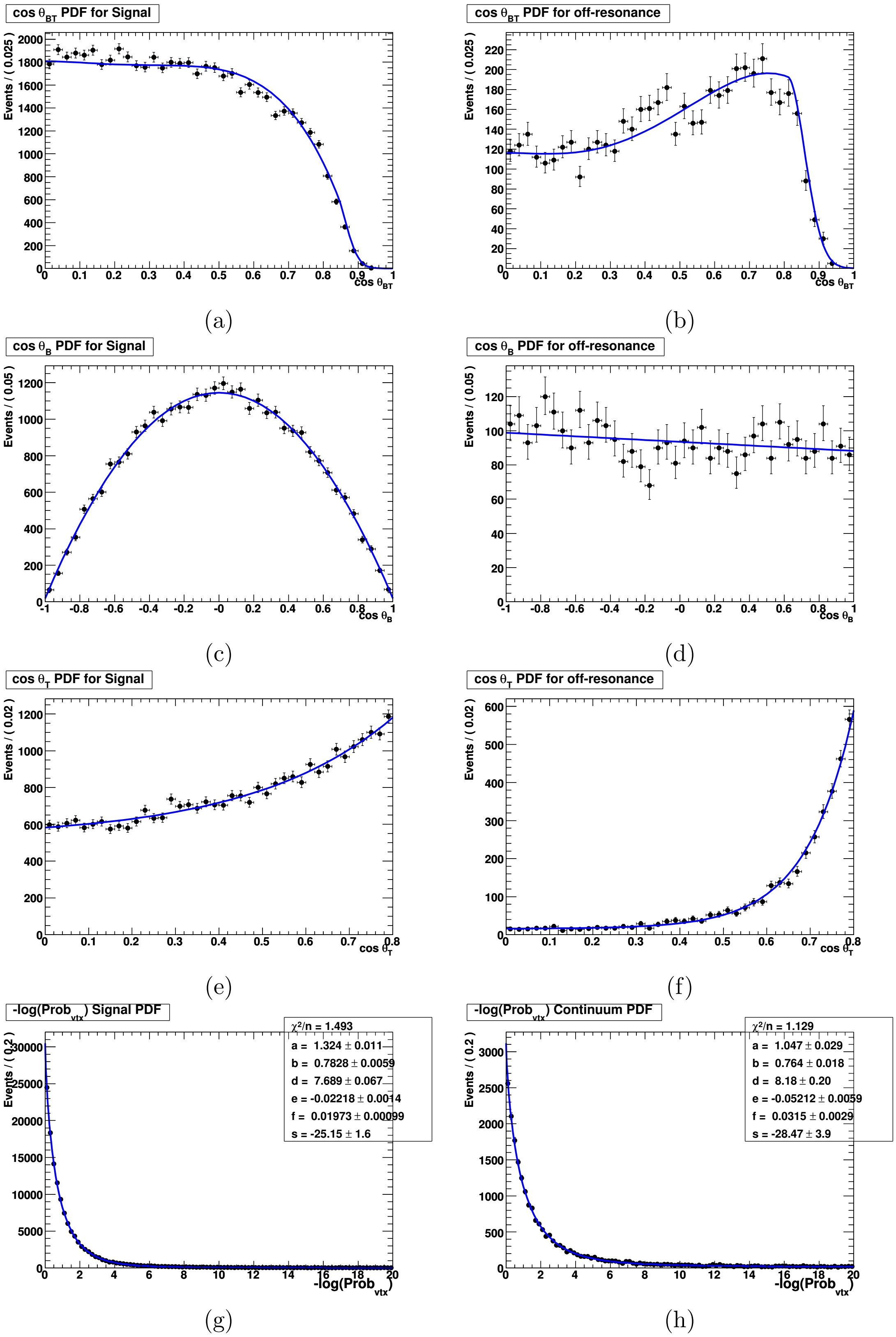

cos θ_{BT} PDF for Signal

(a)

cos θ_{BT} PDF for off-resonance

(b)

cos θ_B PDF for Signal

(c)

cos θ_B PDF for off-resonance

(d)

cos θ_T PDF for Signal

(e)

cos θ_T PDF for off-resonance

(f)

-log(Prob$_{\rm vtx}$) Signal PDF

(g)

-log(Prob$_{\rm vtx}$) Continuum PDF

(h)

Figure C.1: *Distributions of the additional geometric variables for: a)*$\cos\theta_{BT}$ *signal, b)*$\cos\theta_{BT}$ *off-resonance background; c)*$\cos\theta_B$ *signal, d)*$\cos\theta_B$ *off-resonance background; e)*$\cos\theta_T$ *signal, f)*$\cos\theta_T$ *off-resonance background; g)*$p_{\rm vtx}$ *signal, h)*$p_{\rm vtx}$ *off-resonance background.*

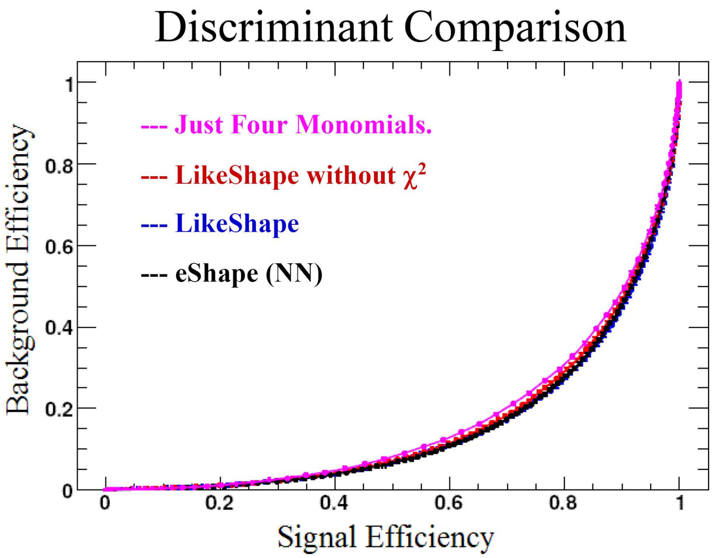

Figure C.2: *Background vs. signal efficiency for the shape discriminants.*

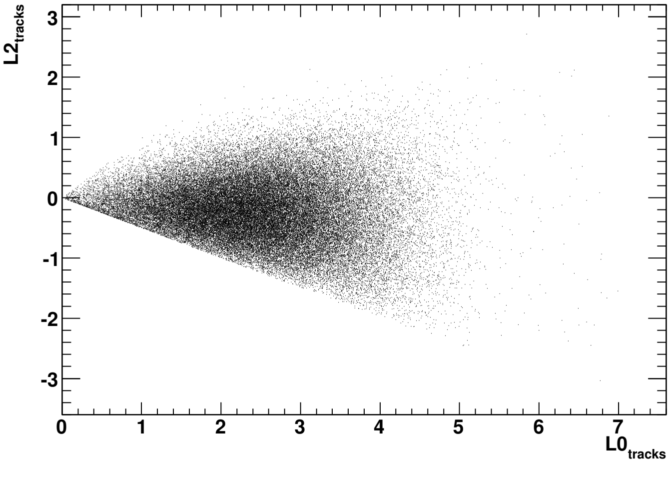

Figure C.3: *$L2$ monomial as a function of $L0$ monomial for $B^0 \to \rho^0\rho^0$ events (computed from charged tracks).*

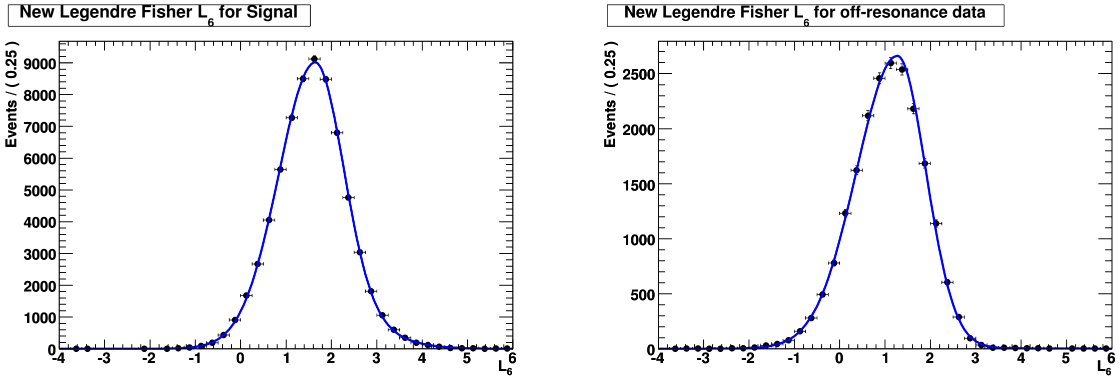

a) b)

Figure C.4: *$\mathcal{F}_6$ for a) signal, b) off-resonance data.*

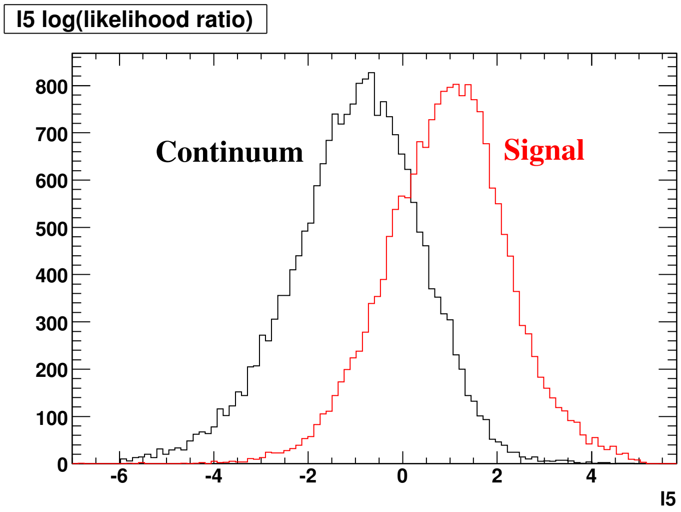

Figure C.5: *Distribution of the likelihood discriminant for signal (red) and background (black) events.*

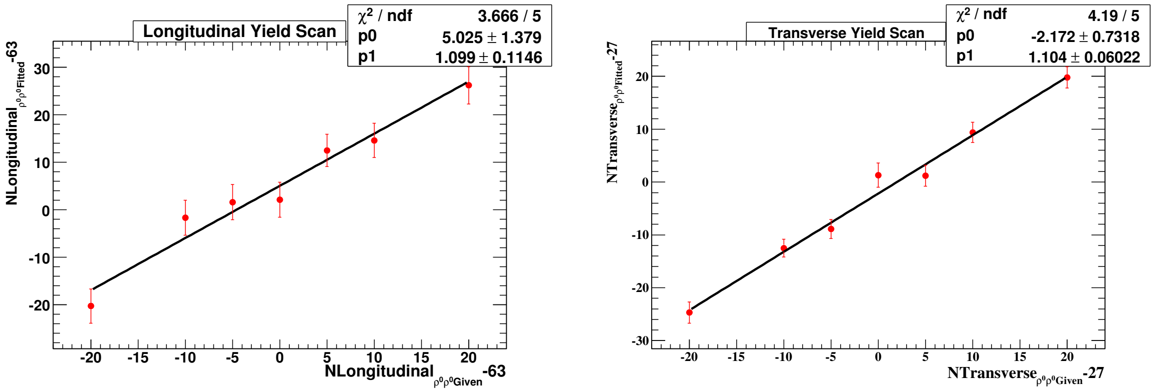

(a) (b)

Figure C.6: *Yield Scans around* $nSigL = 63$ *and* $nSigT = 27$ *for the fitter with the* $likeShape$ variable.

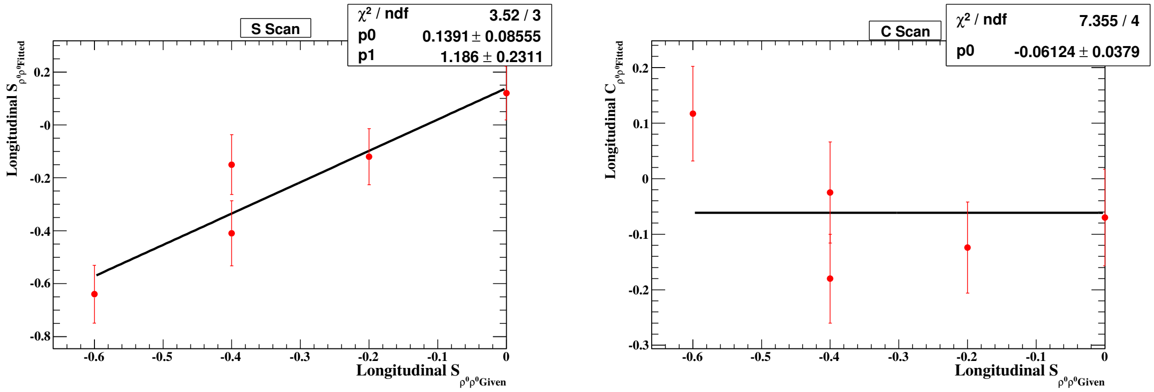

Figure C.7: $S_{fitted} - S_{expected}$ and C *as a function of* $S_{expected}$ *for the fitter with the* $likeShape$ *variable.*

Appendix D

PDFs

Probability Density Functions for each Maximum Likelihood Fit component, grouped by observables. The distributions are described in Section 4.5.3.

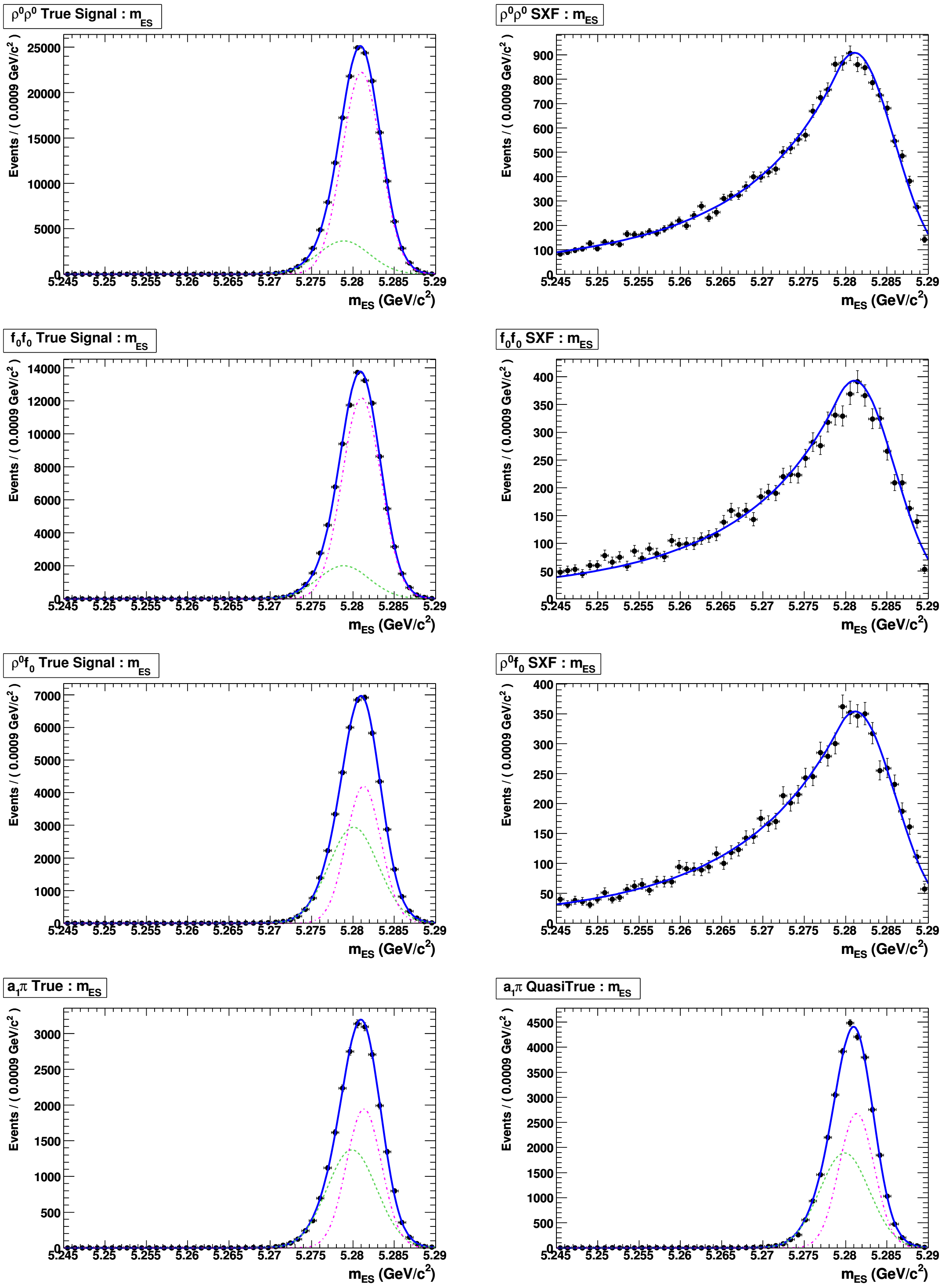

Figure D.1: m_{ES} *Distributions. Fitted to the Monte Carlo.*

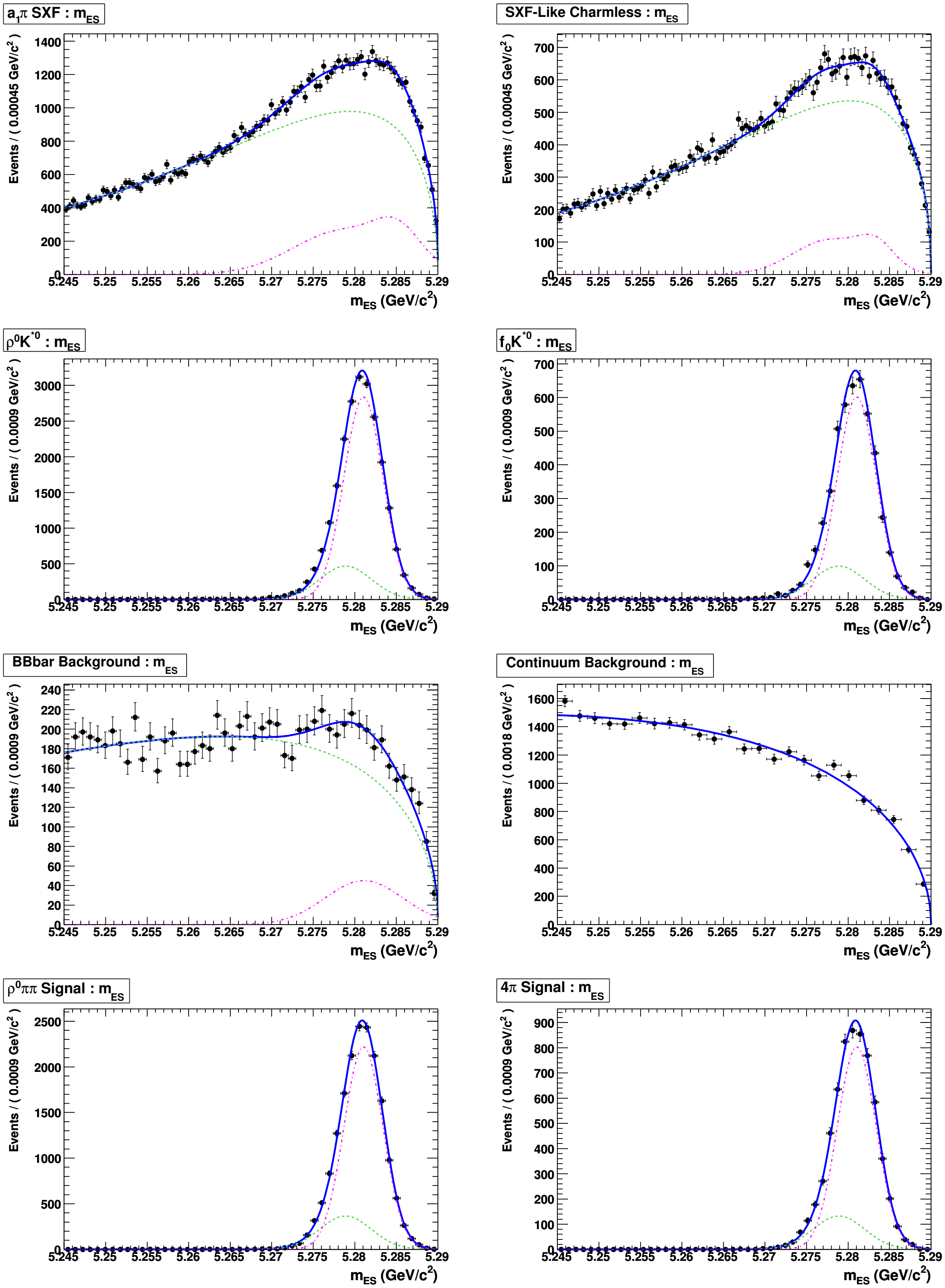

Figure D.2: m_{ES} *Distributions. Fitted to the Monte Carlo (or to the sideband for the Continuum).*

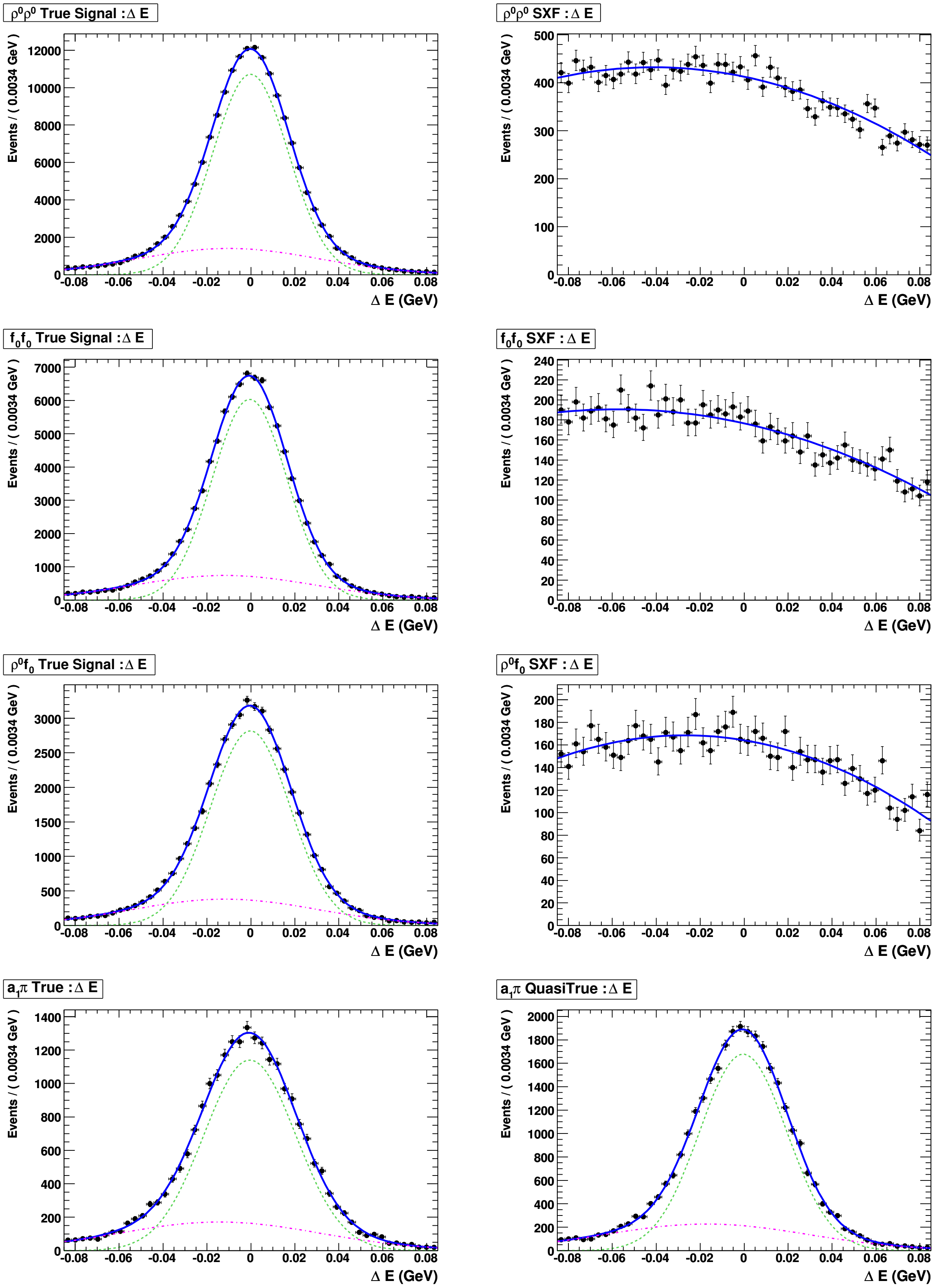

Figure D.3: ΔE *Distributions. Fitted to the Monte Carlo.*

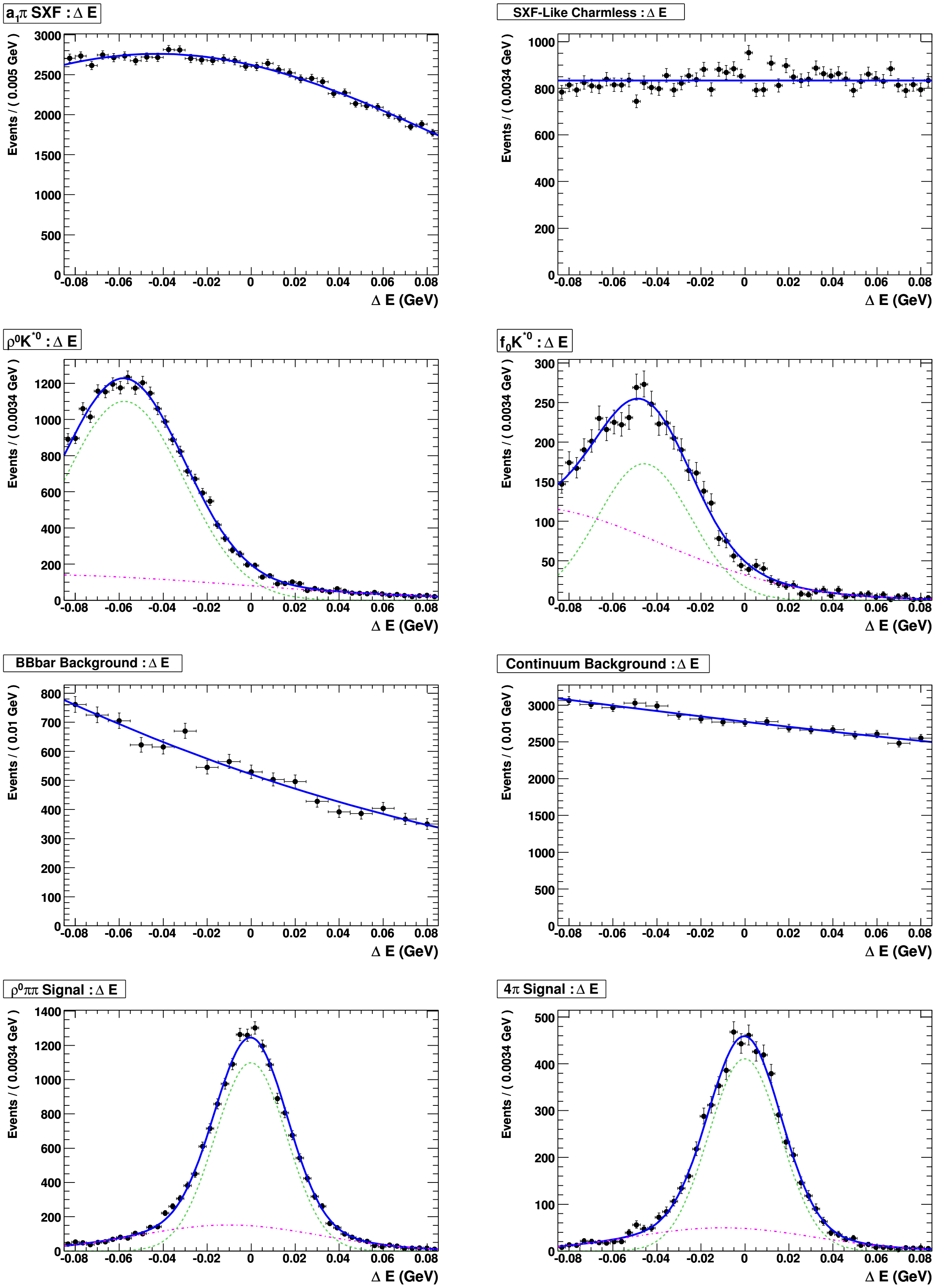

Figure D.4: ΔE *Distributions. Fitted to the Monte Carlo (or to the sideband for the Continuum).*

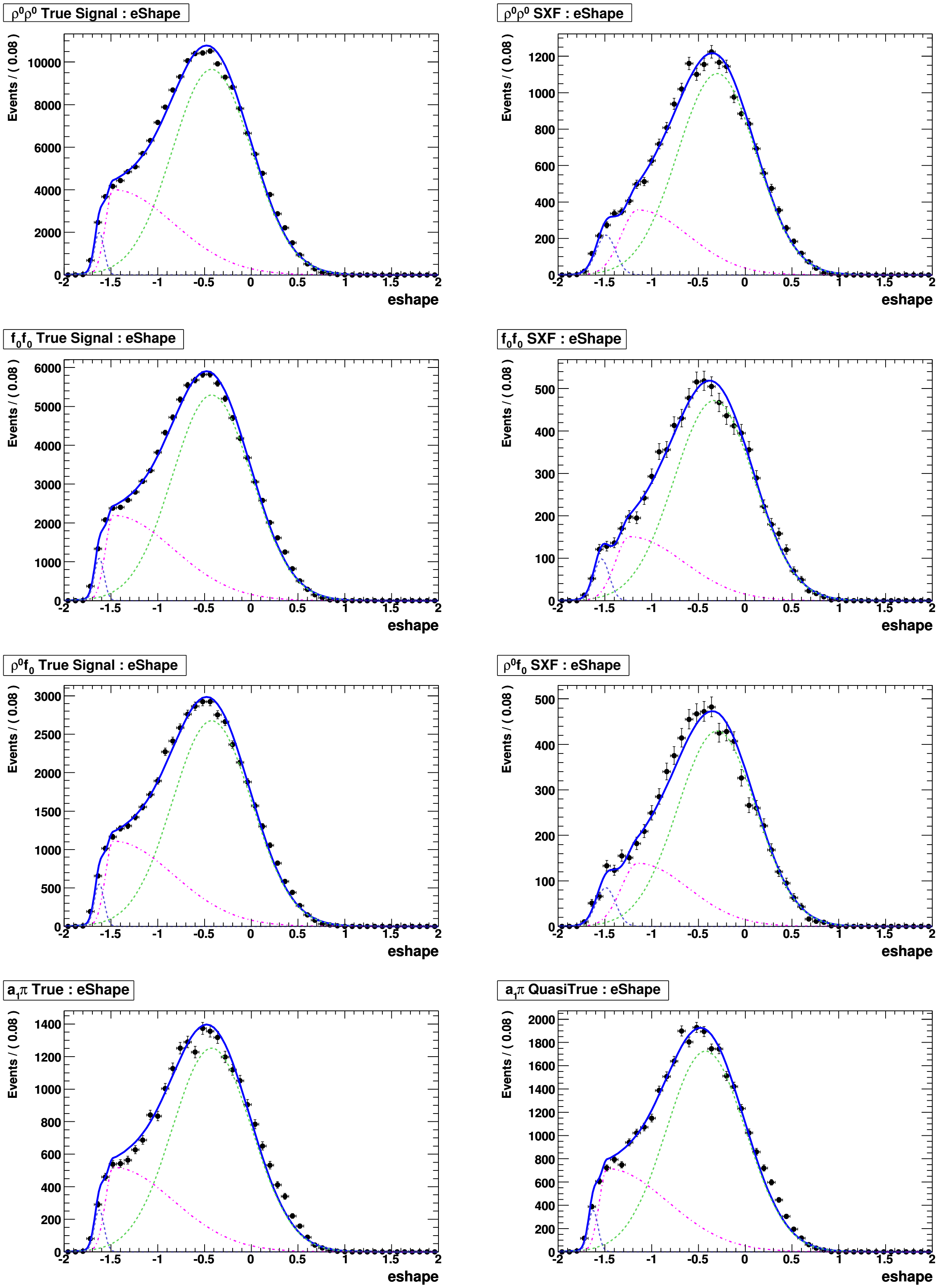

Figure D.5: *eShape Distributions. Fitted to the Monte Carlo.*

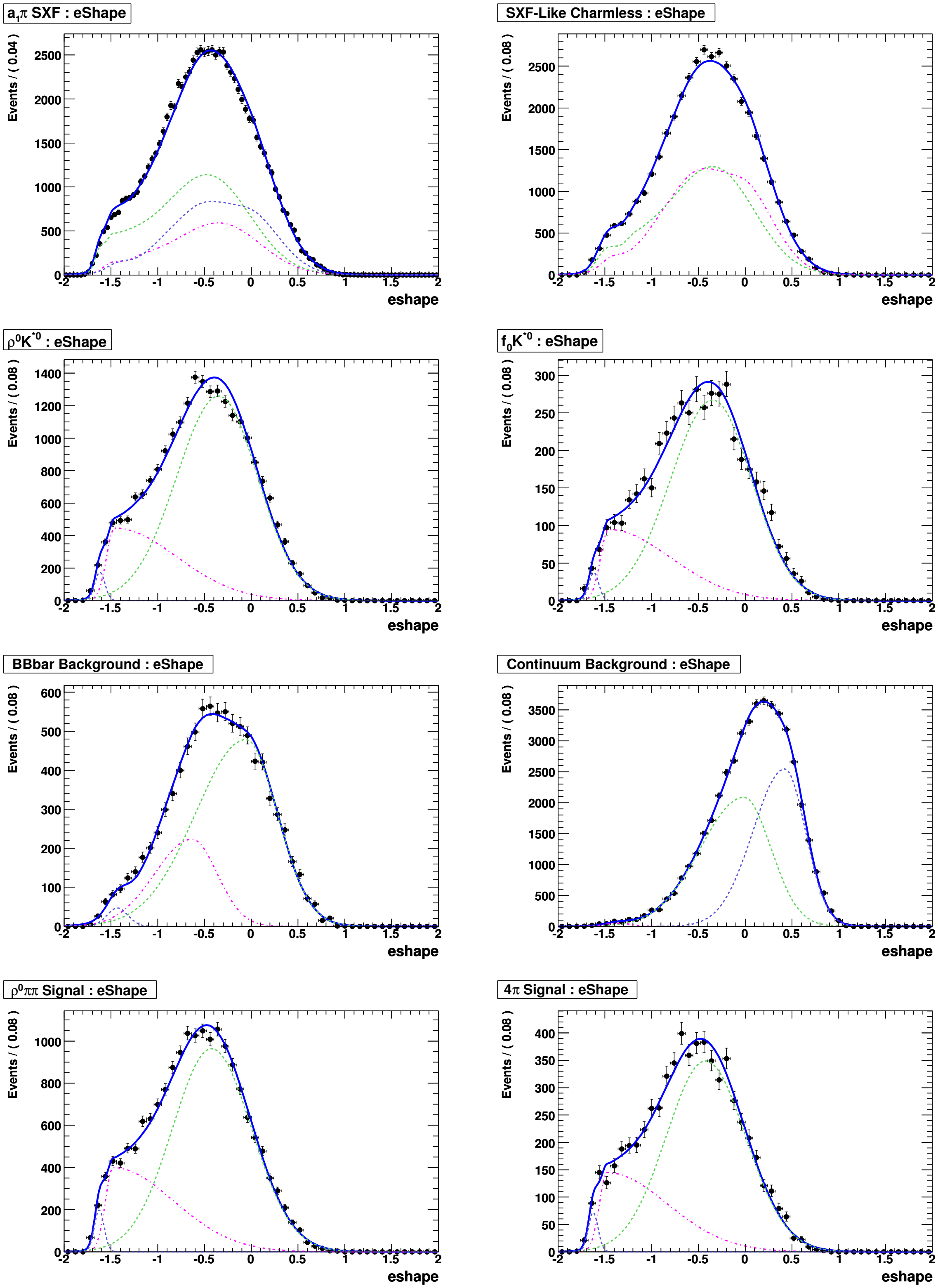

Figure D.6: *eShape Distributions. Fitted to the Monte Carlo (or to the sideband for the Continuum).*

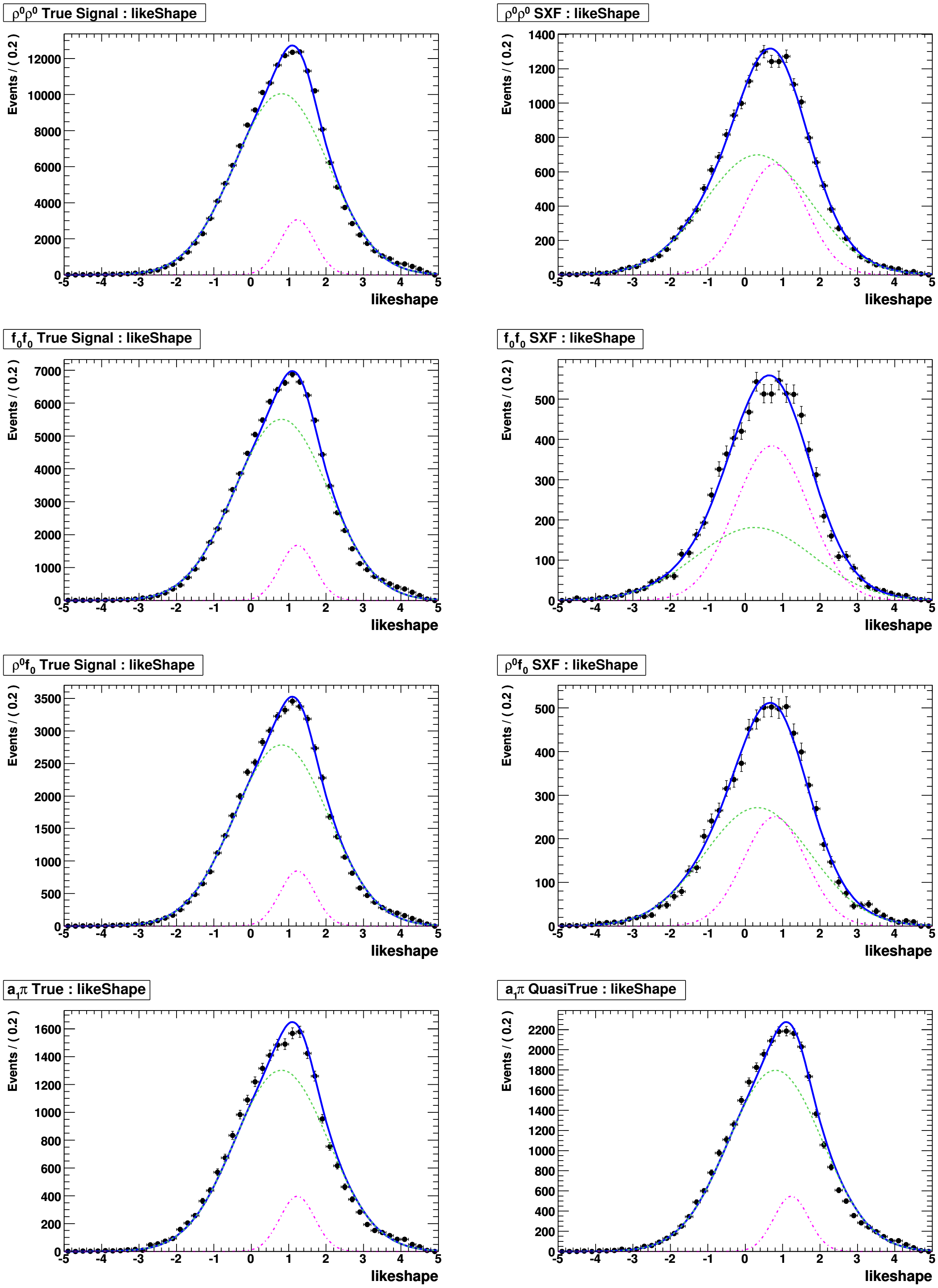

Figure D.7: *likeShape Distributions. Fitted to the Monte Carlo.*

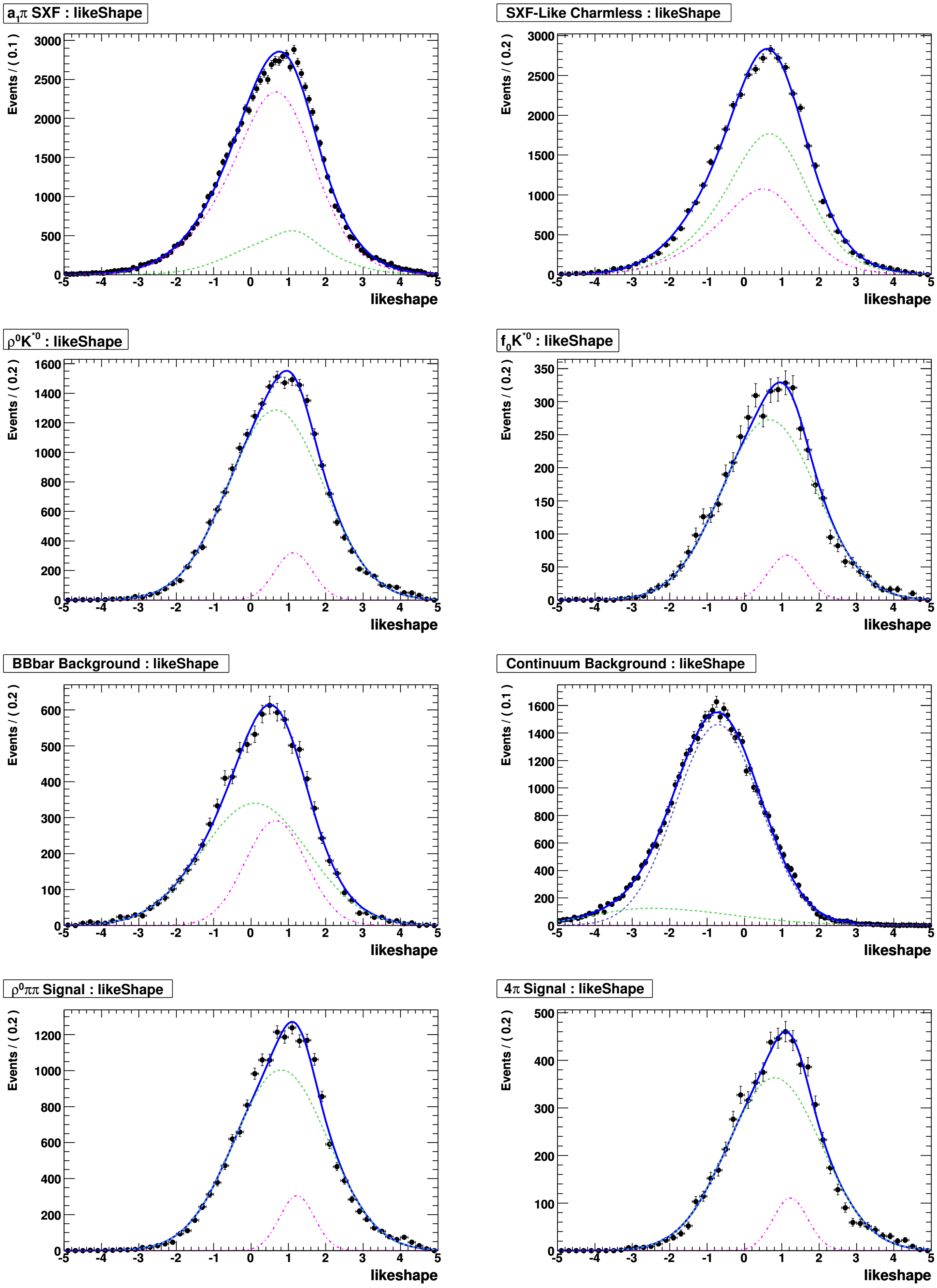

Figure D.8: *likeShape Distributions. Fitted to the Monte Carlo (or to the sideband for the Continuum).*

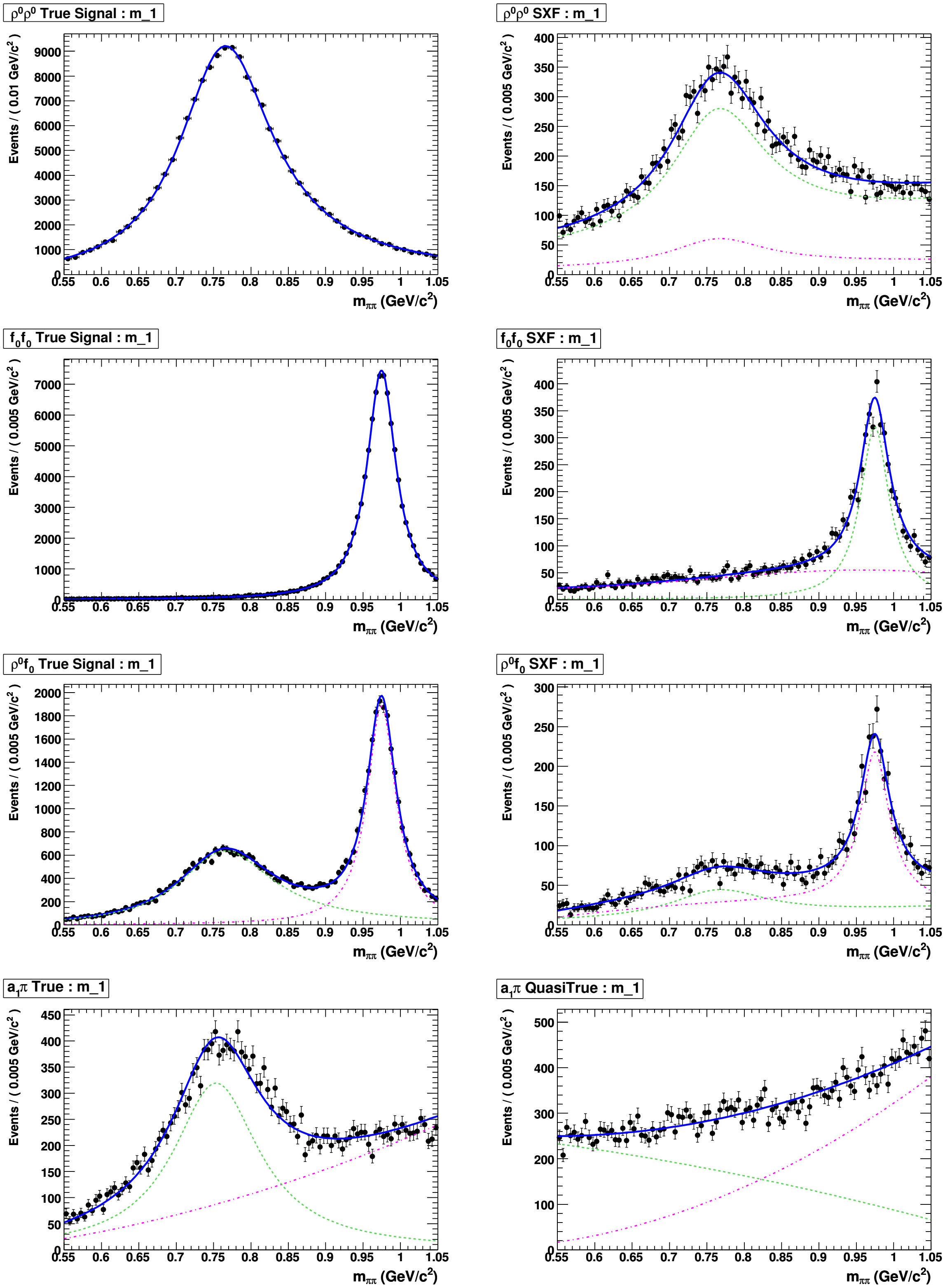

Figure D.9: m_1 *Distributions. Fitted to the Monte Carlo.*

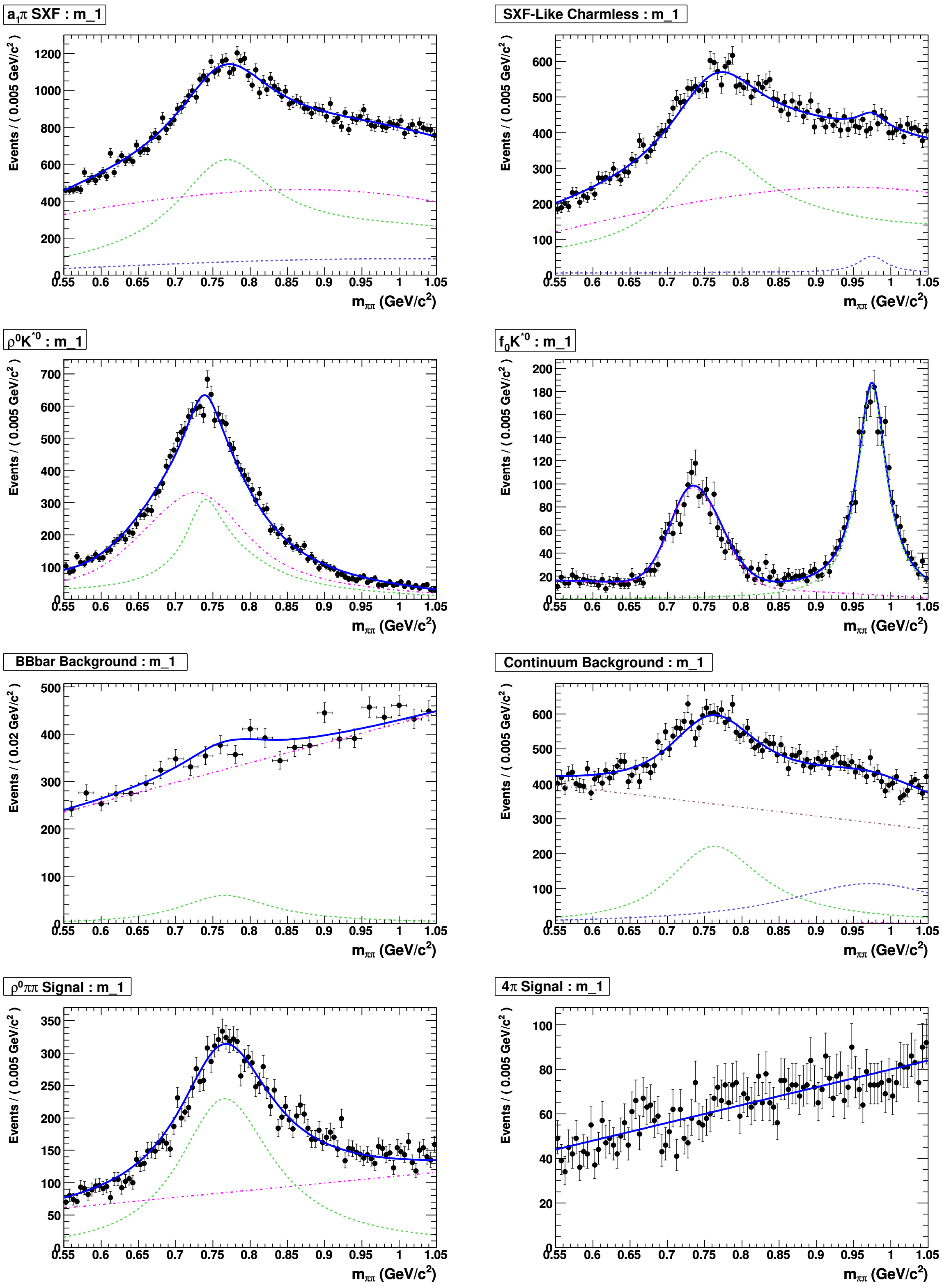

Figure D.10: m_1 *Distributions. Fitted to the Monte Carlo (or to the sideband for the Continuum).*

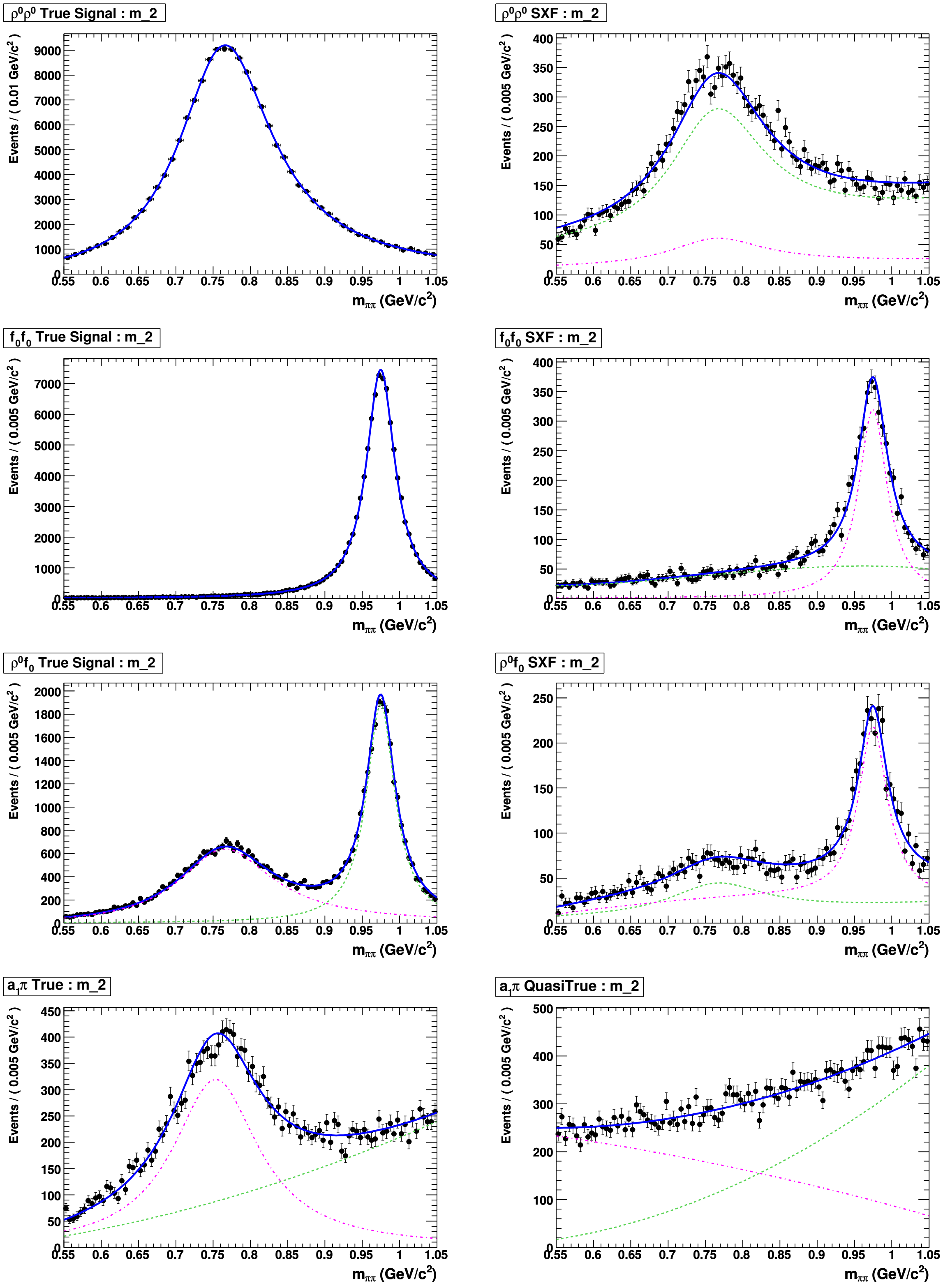

Figure D.11: m_2 *Distributions. Fitted to the Monte Carlo.*

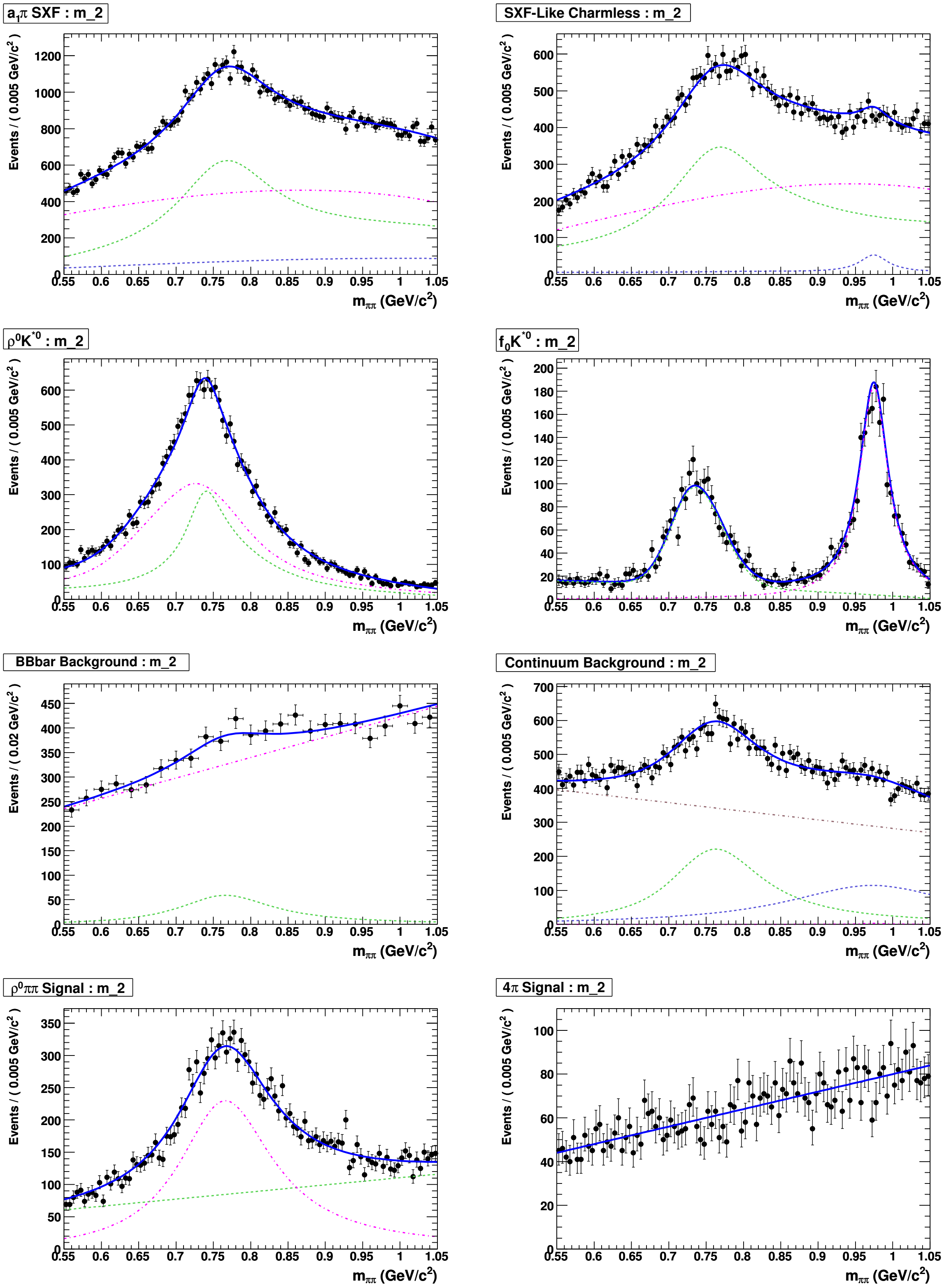

Figure D.12: m_2 *Distributions. Fitted to the Monte Carlo (or to the sideband for the Continuum).*

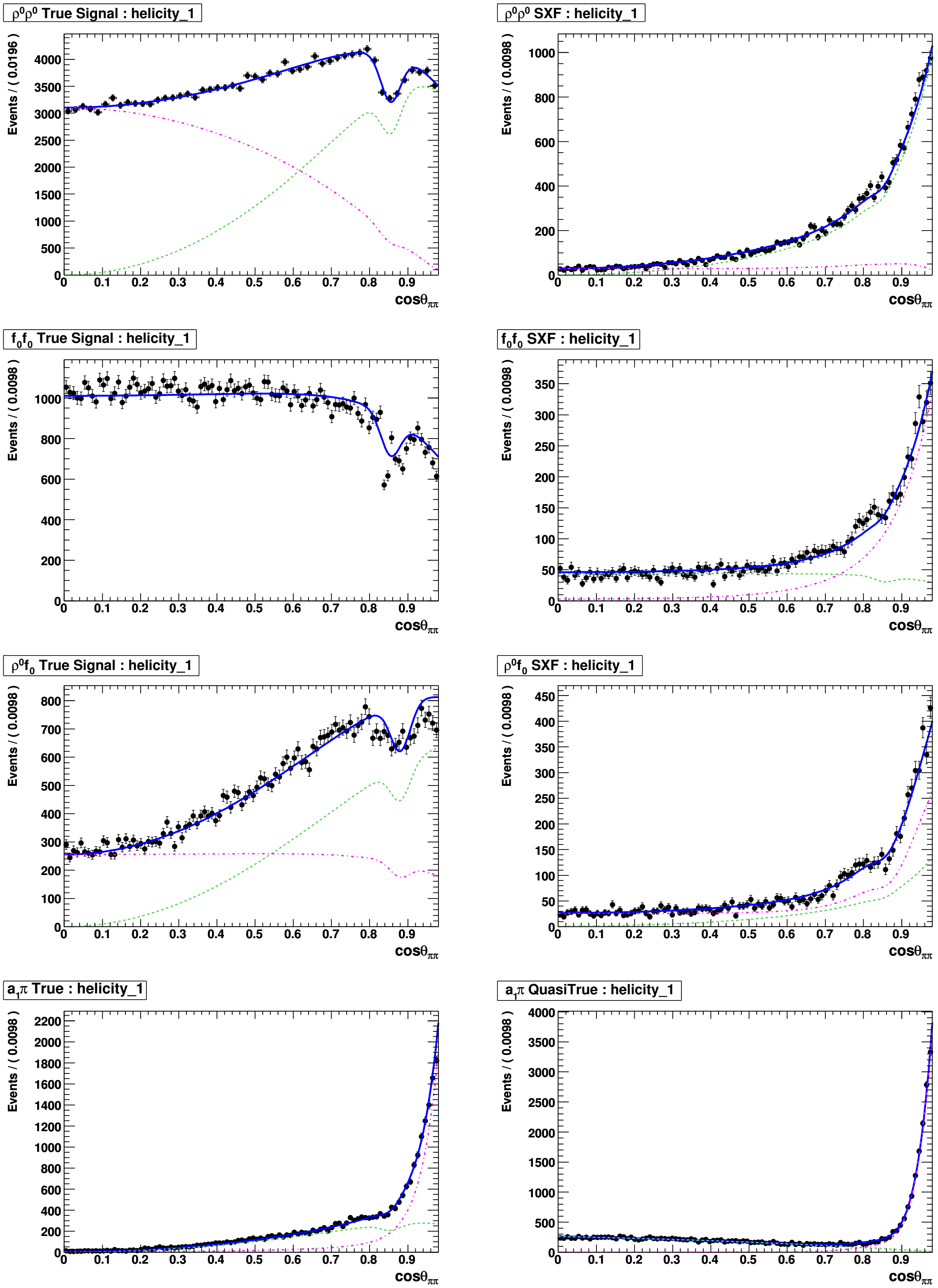

Figure D.13: $\cos\theta_1$ *Distributions. Fitted to the Monte Carlo.*

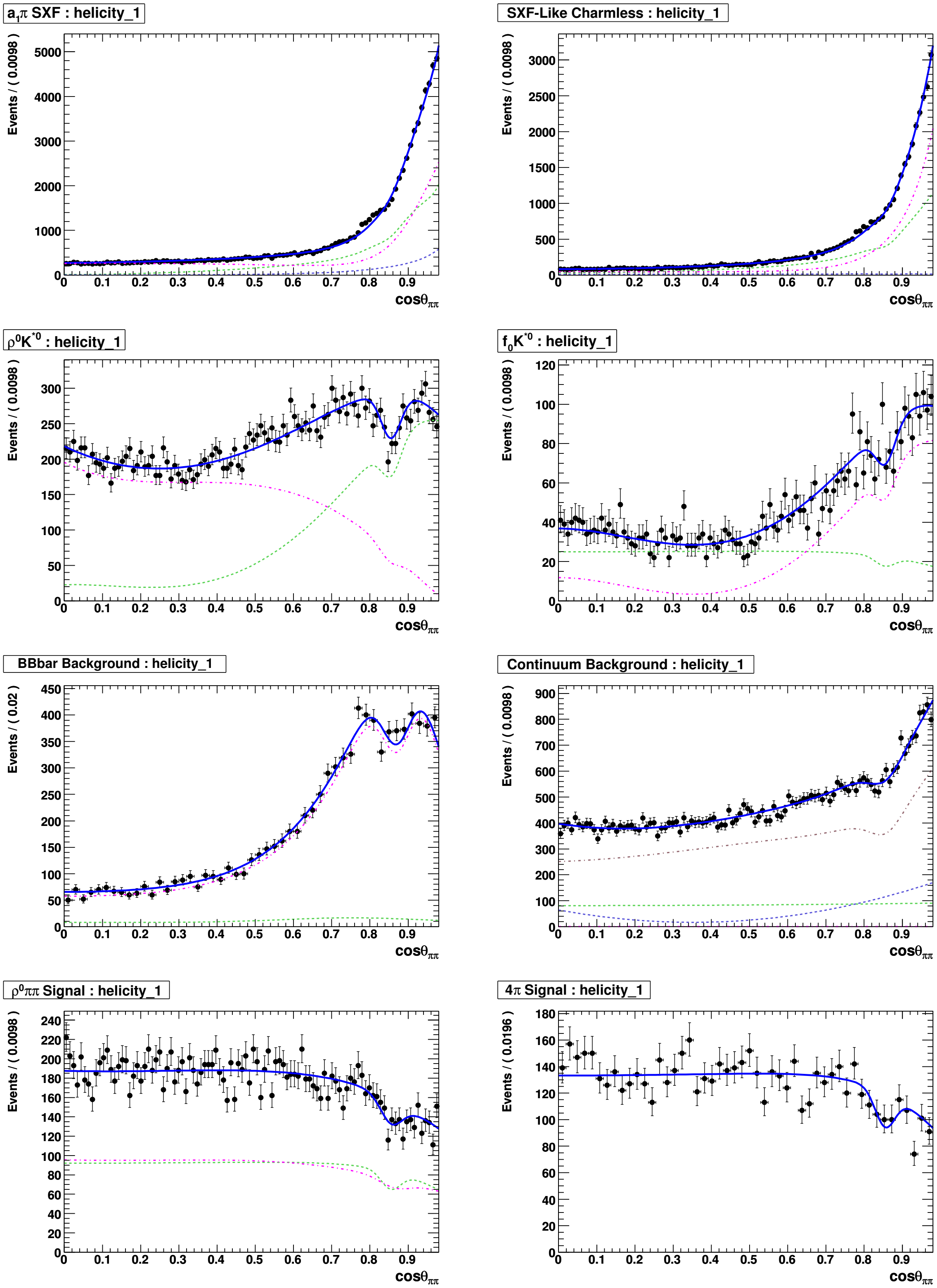

Figure D.14: $\cos\theta_1$ *Distributions. Fitted to the Monte Carlo (or to the sideband for the Continuum).*

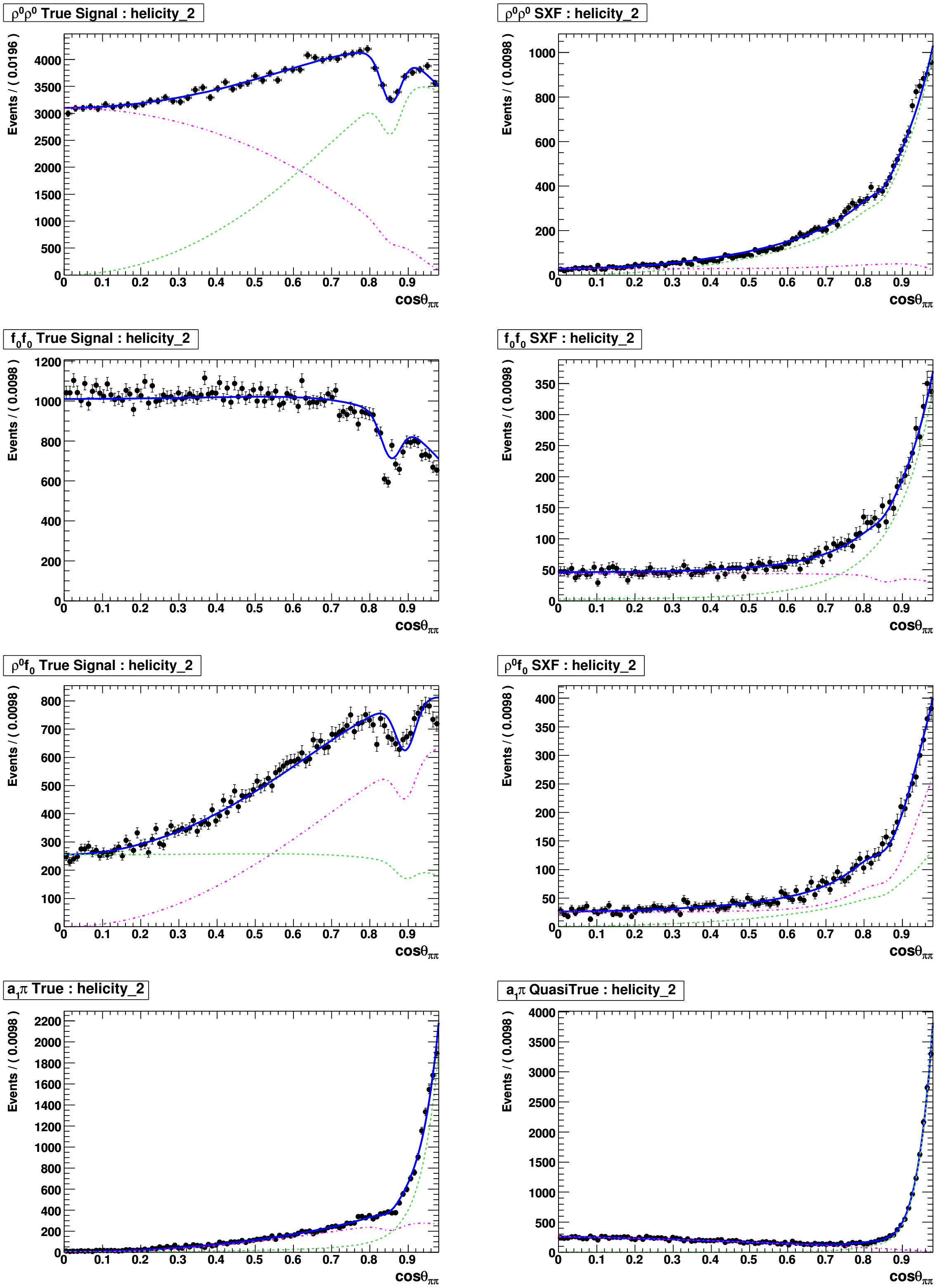

Figure D.15: $\cos\theta_2$ *Distributions. Fitted to the Monte Carlo.*

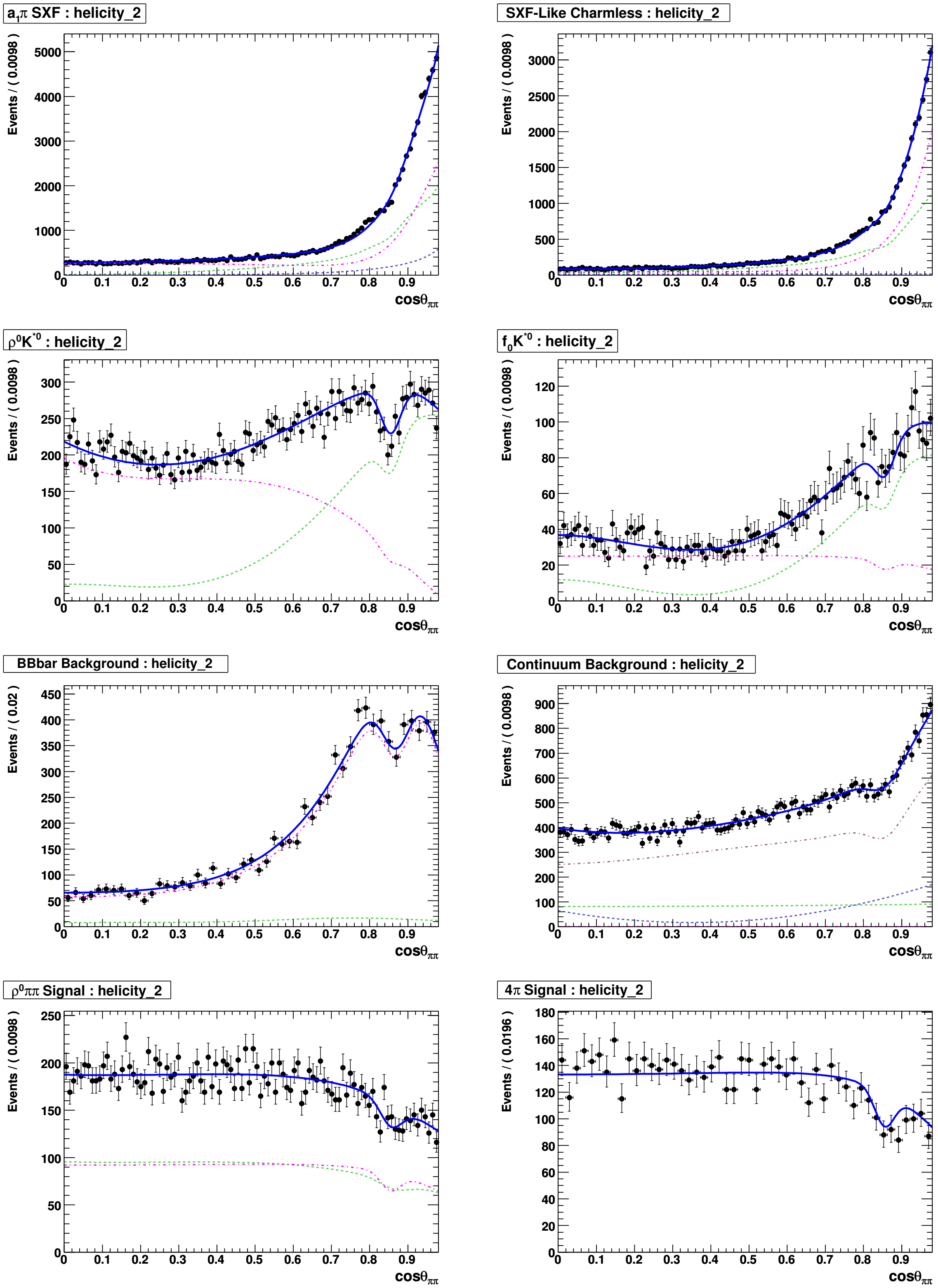

Figure D.16: $\cos\theta_2$ *Distributions. Fitted to the Monte Carlo (or to the sideband for the Continuum).*

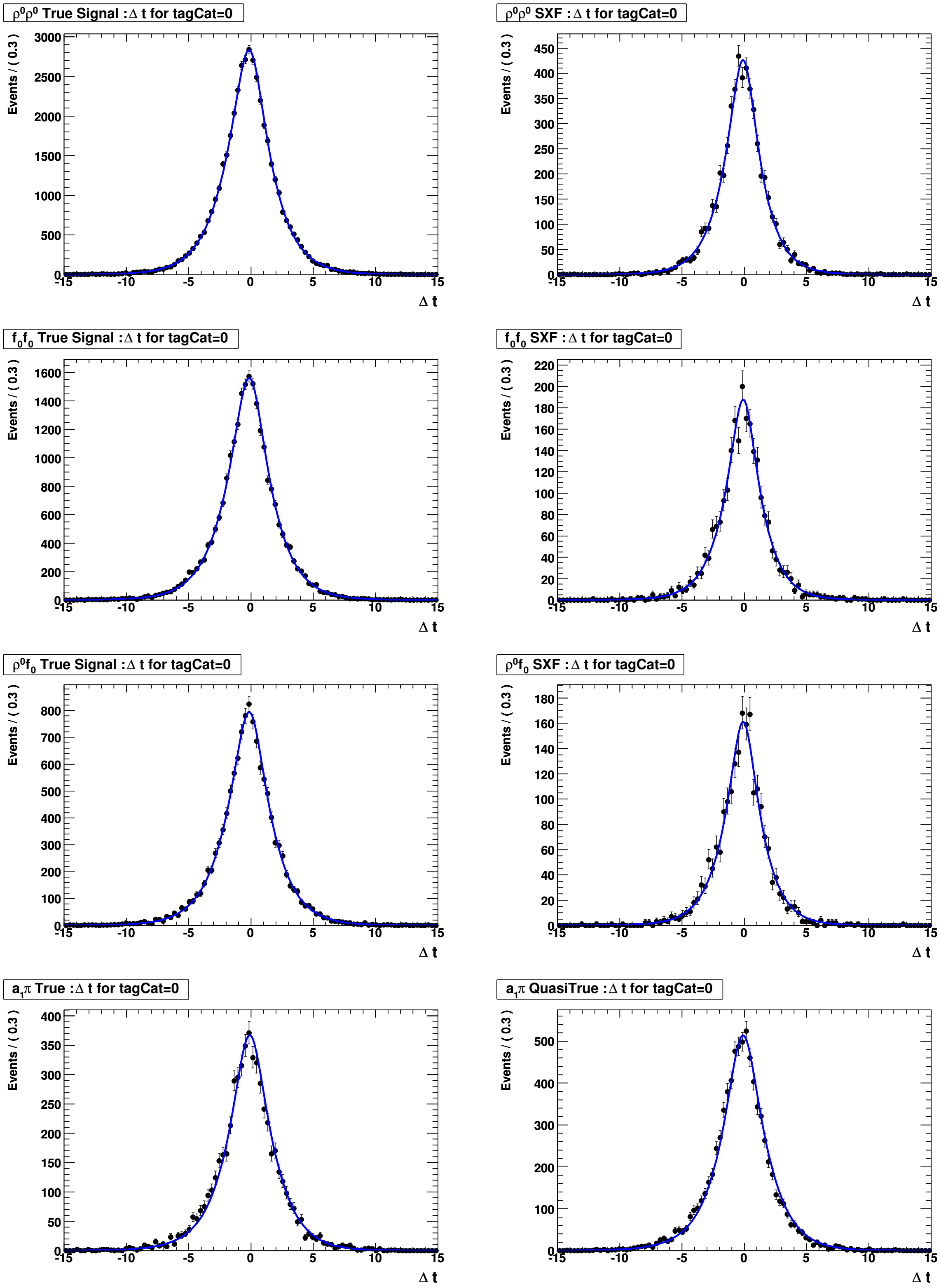

Figure D.17: Δt *for* $tagCat = 0$ *Distributions. Fitted to the Monte Carlo.*

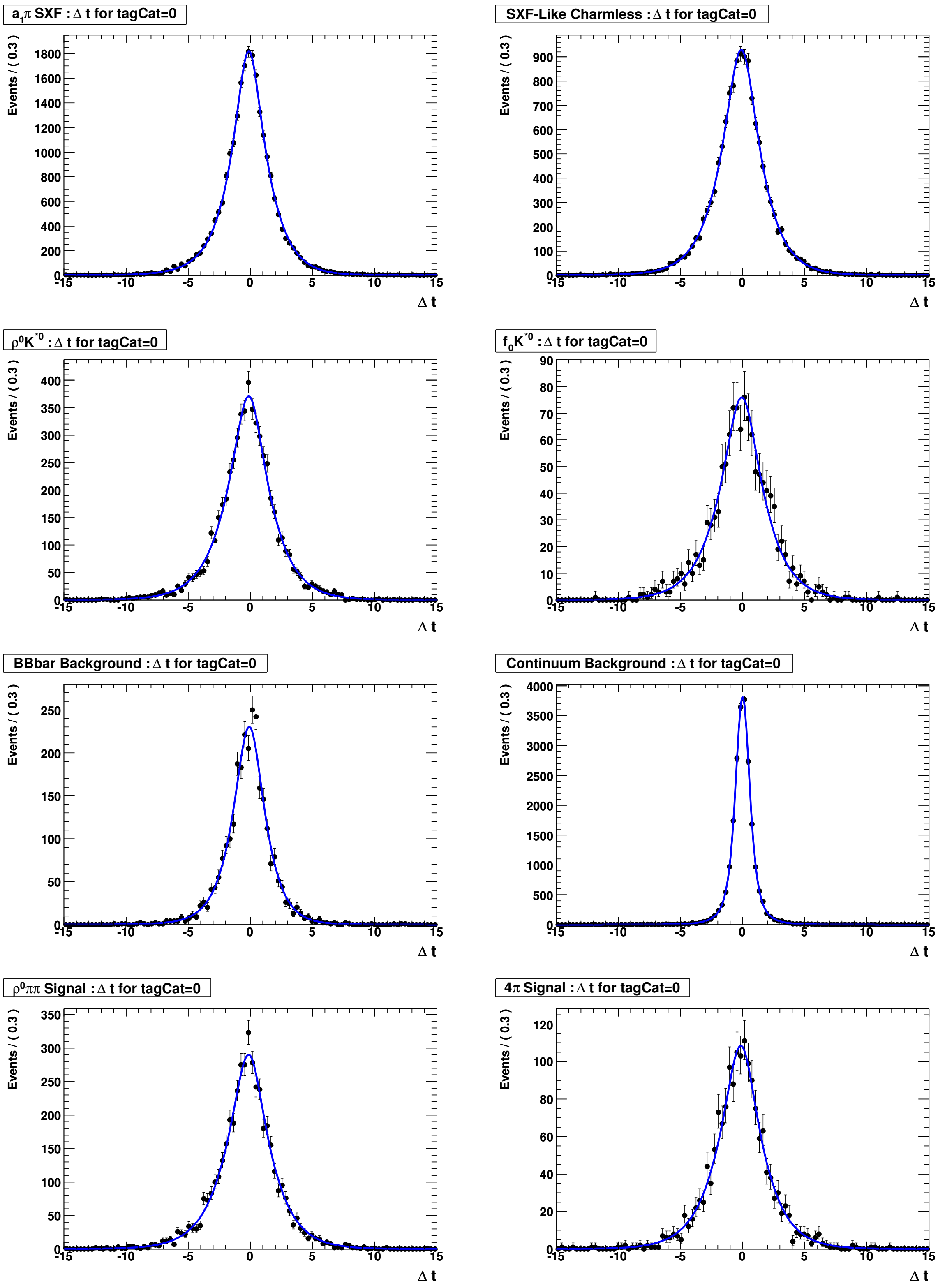

Figure D.18: Δt *for* $tagCat = 0$ *Distributions. Fitted to the Monte Carlo (or to the sideband for the Continuum).*

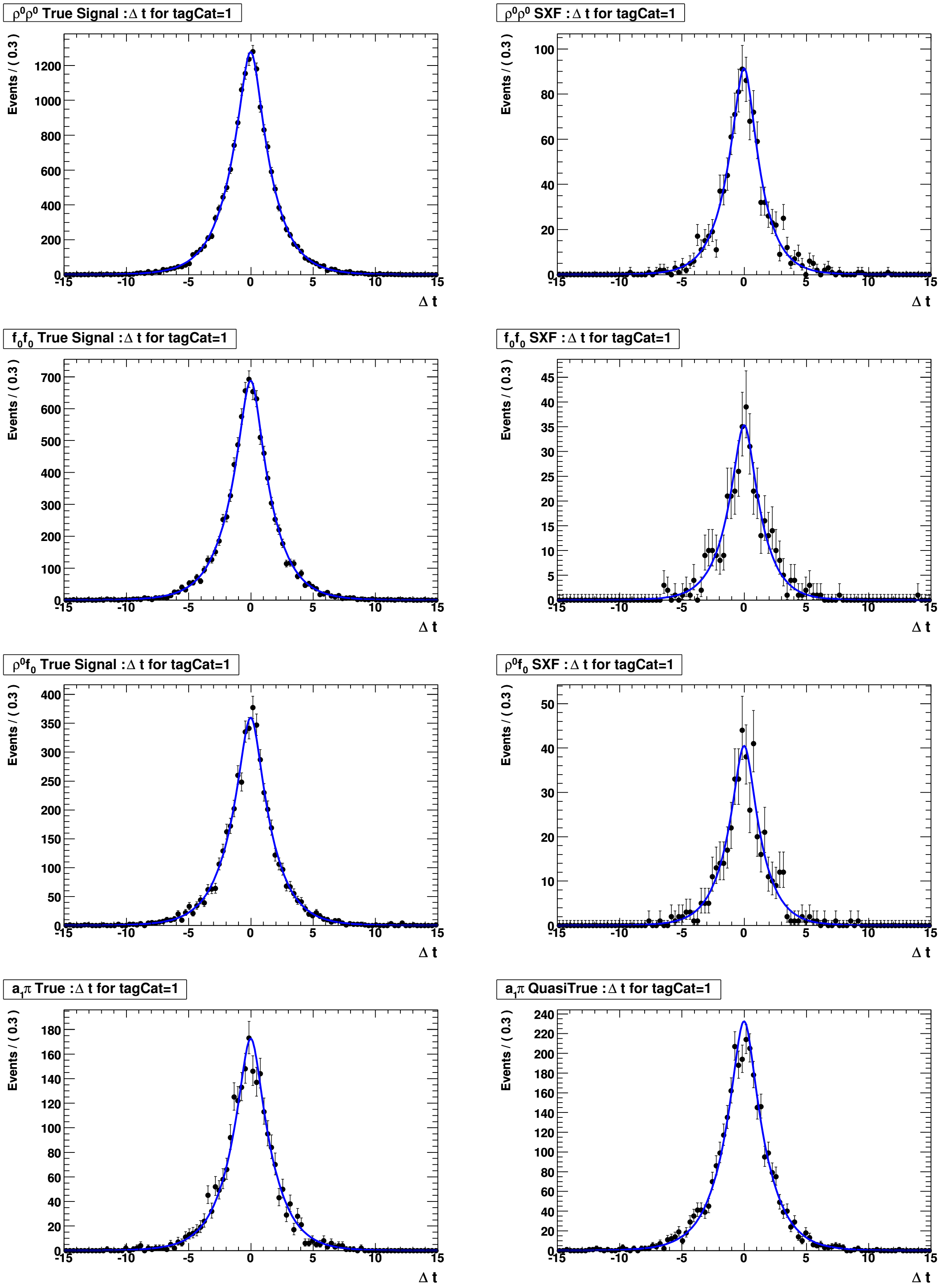

$\rho^0\rho^0$ True Signal : Δ t for tagCat=1

$\rho^0\rho^0$ SXF : Δ t for tagCat=1

f_0f_0 True Signal : Δ t for tagCat=1

f_0f_0 SXF : Δ t for tagCat=1

ρ^0f_0 True Signal : Δ t for tagCat=1

ρ^0f_0 SXF : Δ t for tagCat=1

$a_1\pi$ True : Δ t for tagCat=1

$a_1\pi$ QuasiTrue : Δ t for tagCat=1

Figure D.19: Δ*t for tagCat* = 1 *Distributions. Fitted to the Monte Carlo.*

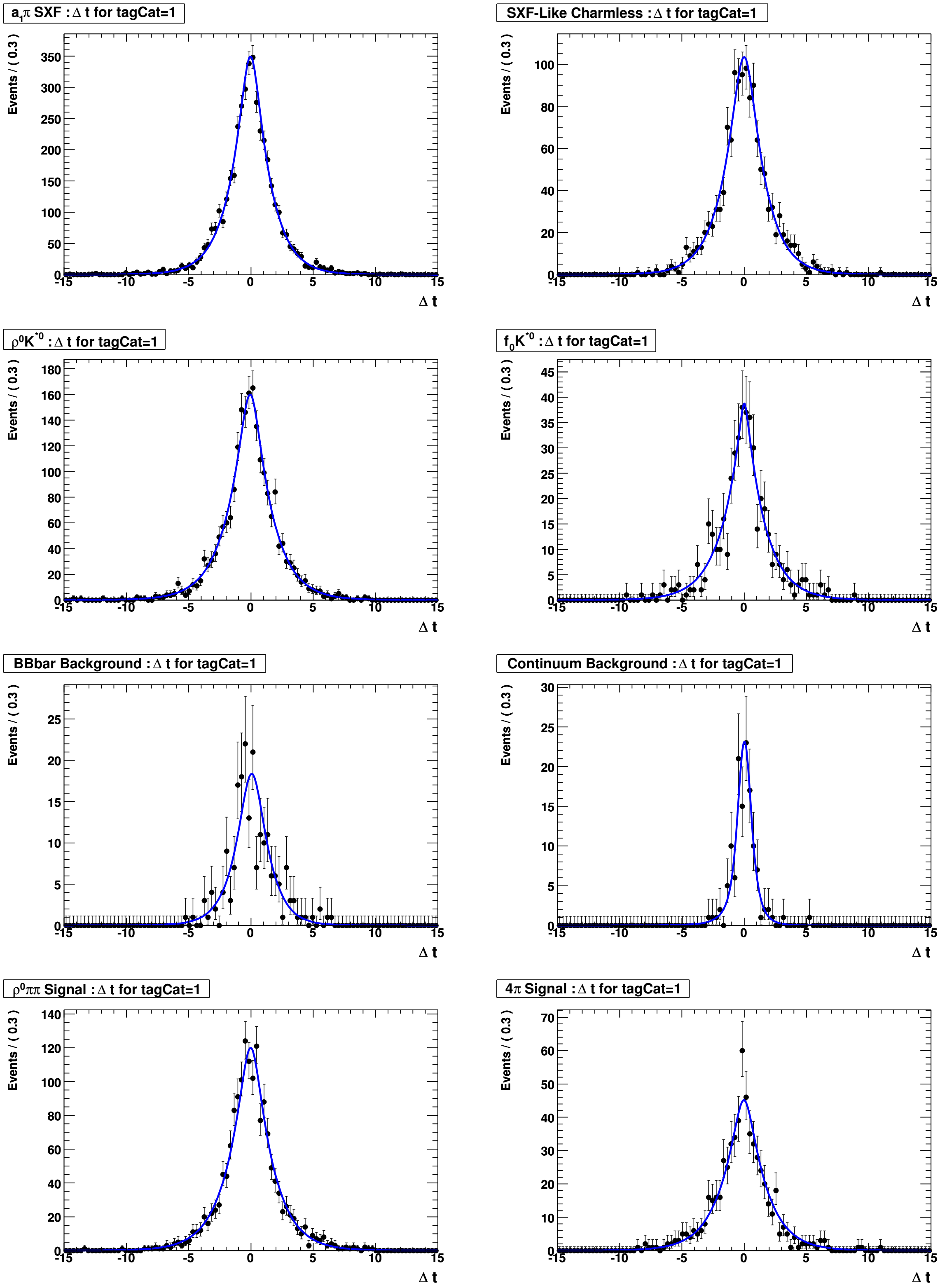

Figure D.20: Δt *for tagCat* = 1 *Distributions. Fitted to the Monte Carlo (or to the sideband for the Continuum).*

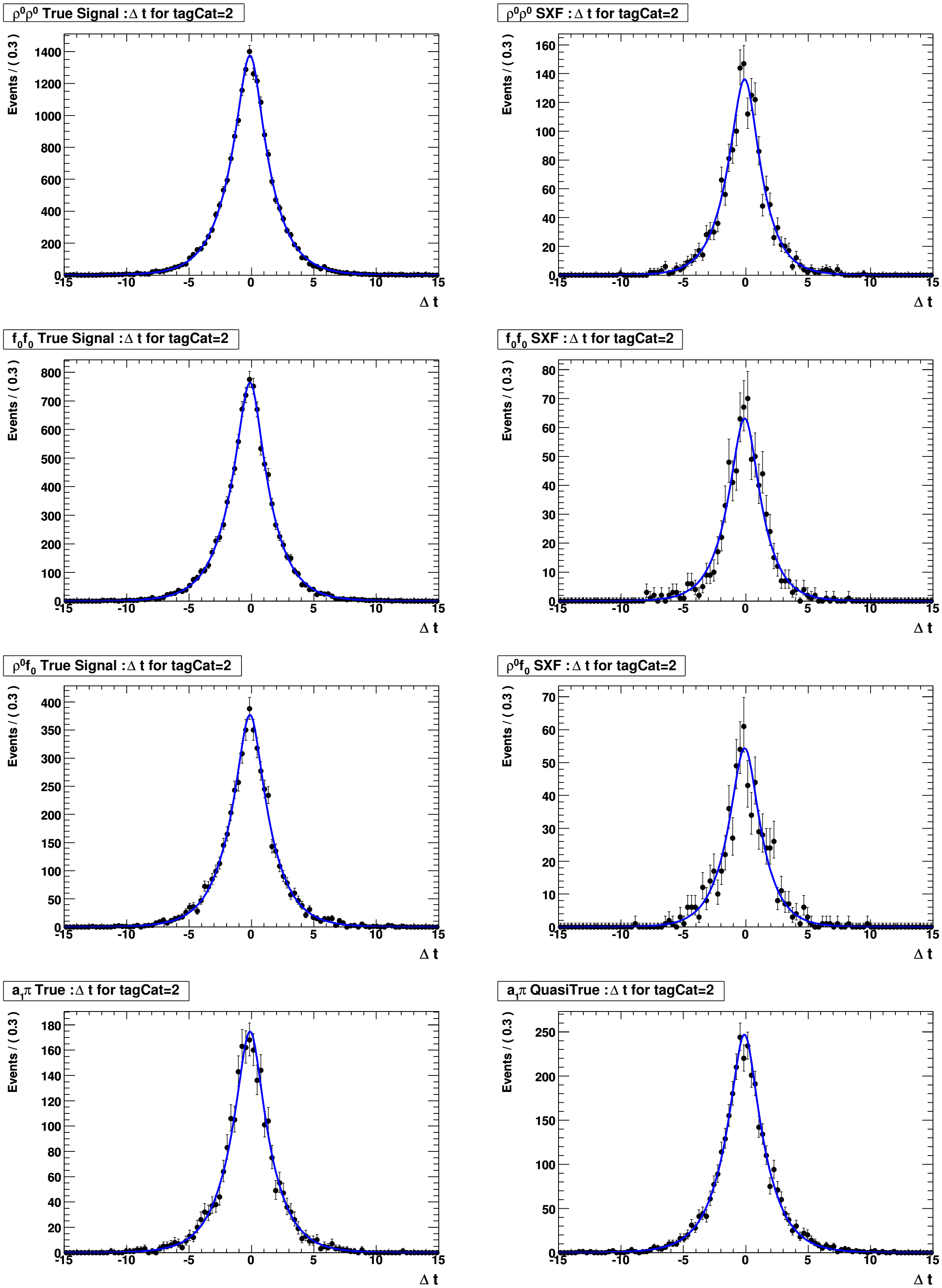

Figure D.21: Δt *for* $tagCat = 2$ *Distributions. Fitted to the Monte Carlo.*

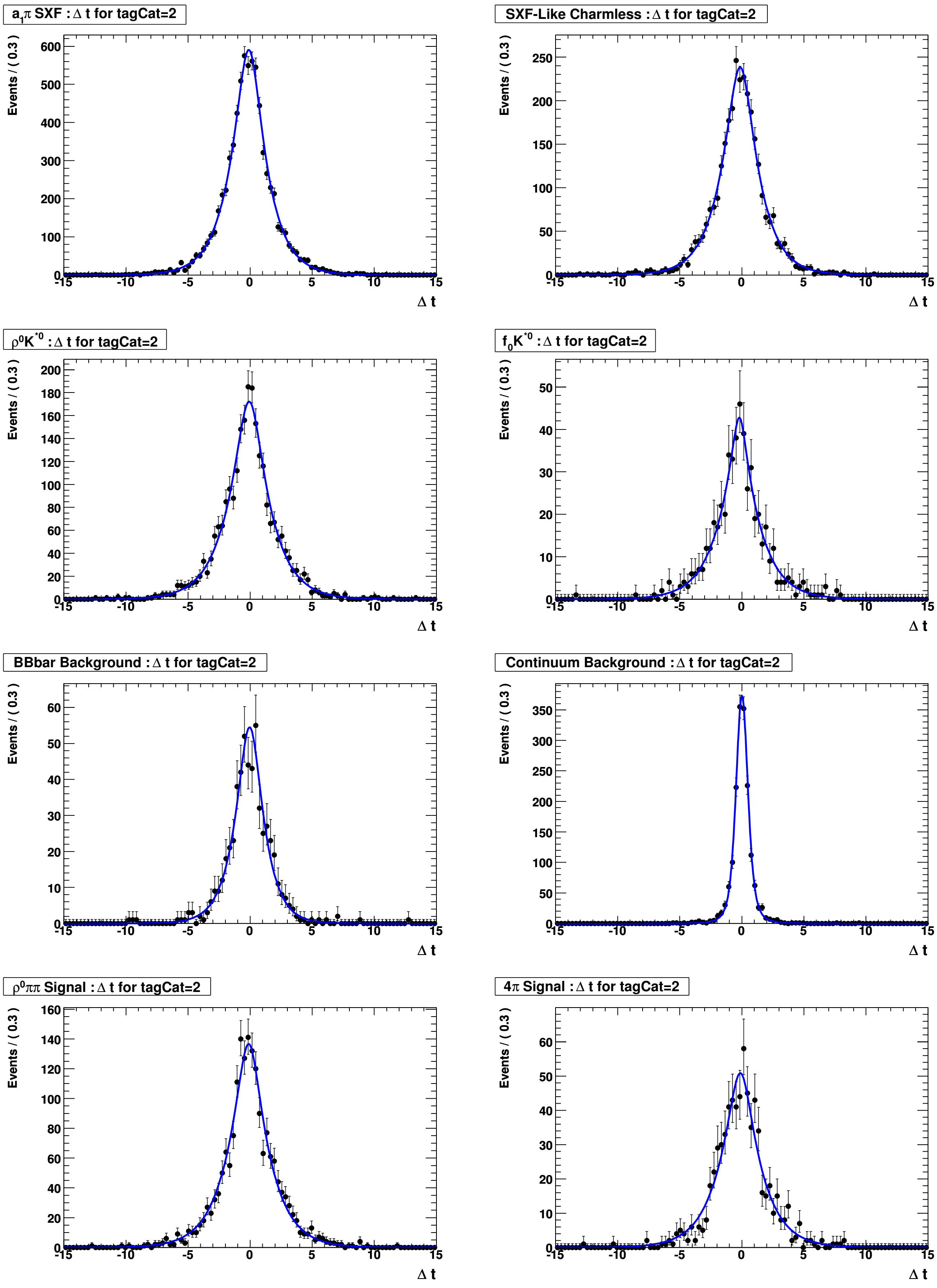

Figure D.22: Δt *for tagCat* = 2 *Distributions. Fitted to the Monte Carlo (or to the sideband for the Continuum).*

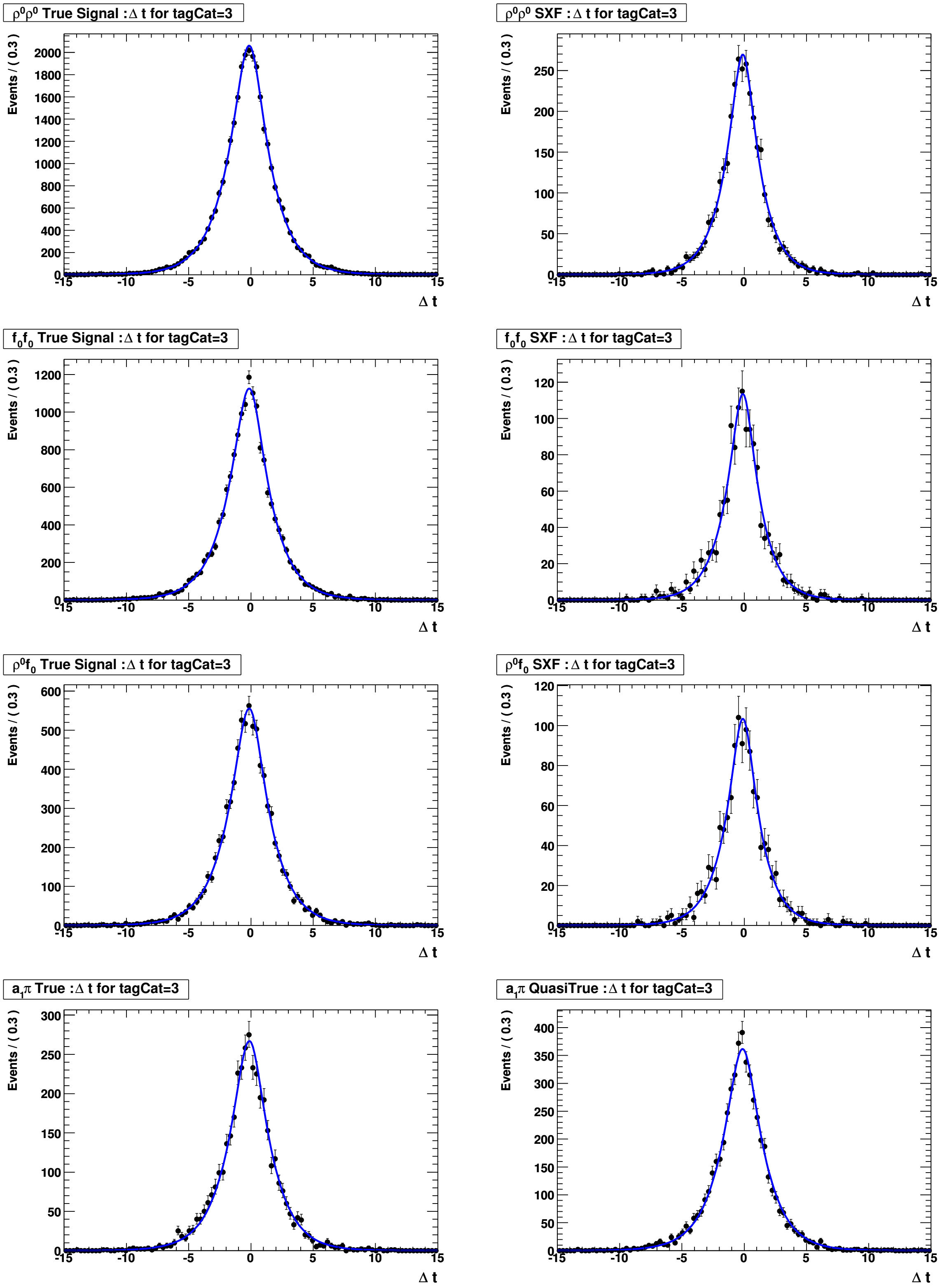

Figure D.23: Δt *for* $tagCat = 3$ *Distributions. Fitted to the Monte Carlo.*

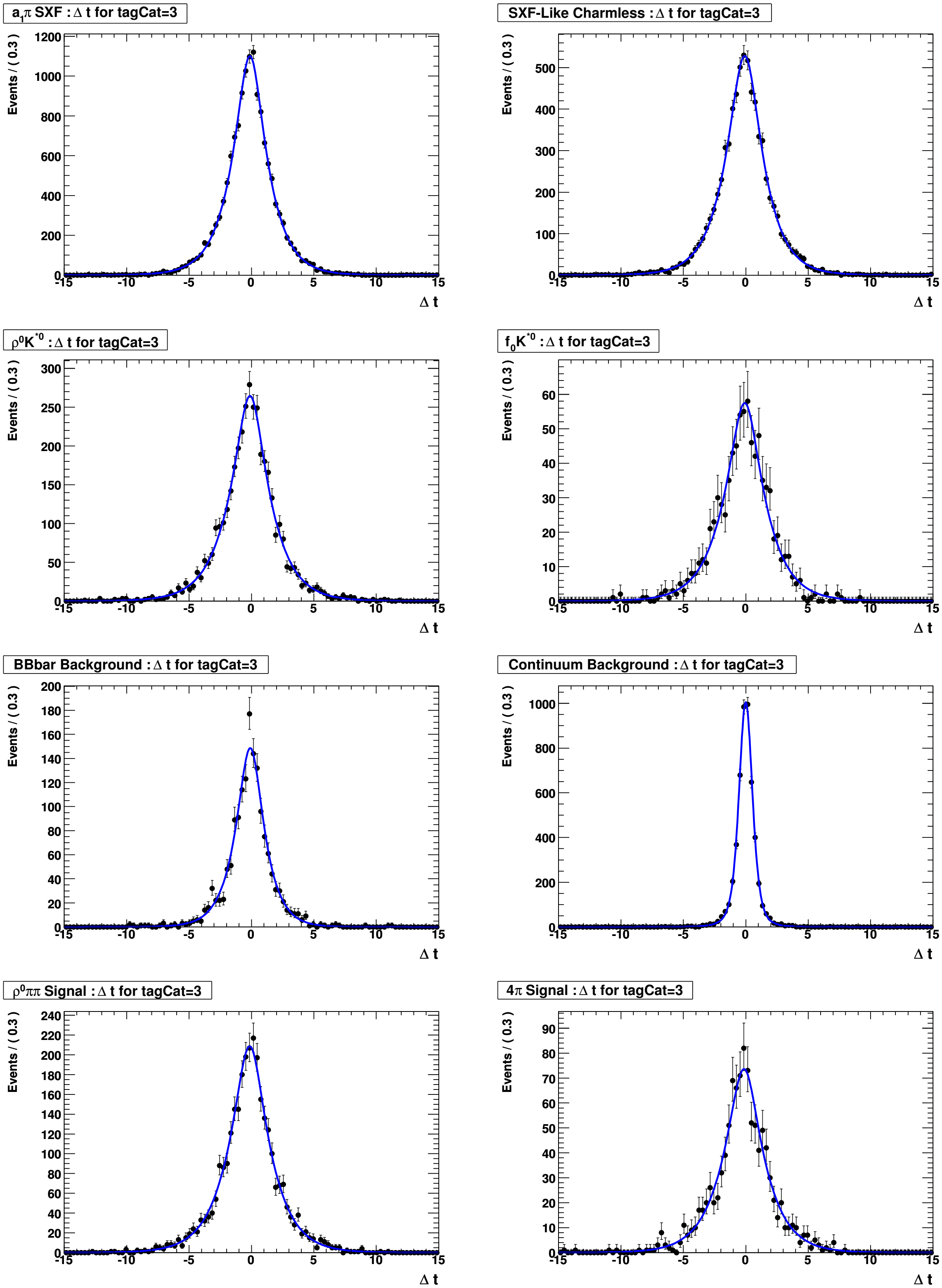

Figure D.24: Δt *for tagCat* $=$ 3 *Distributions. Fitted to the Monte Carlo (or to the sideband for the Continuum).*

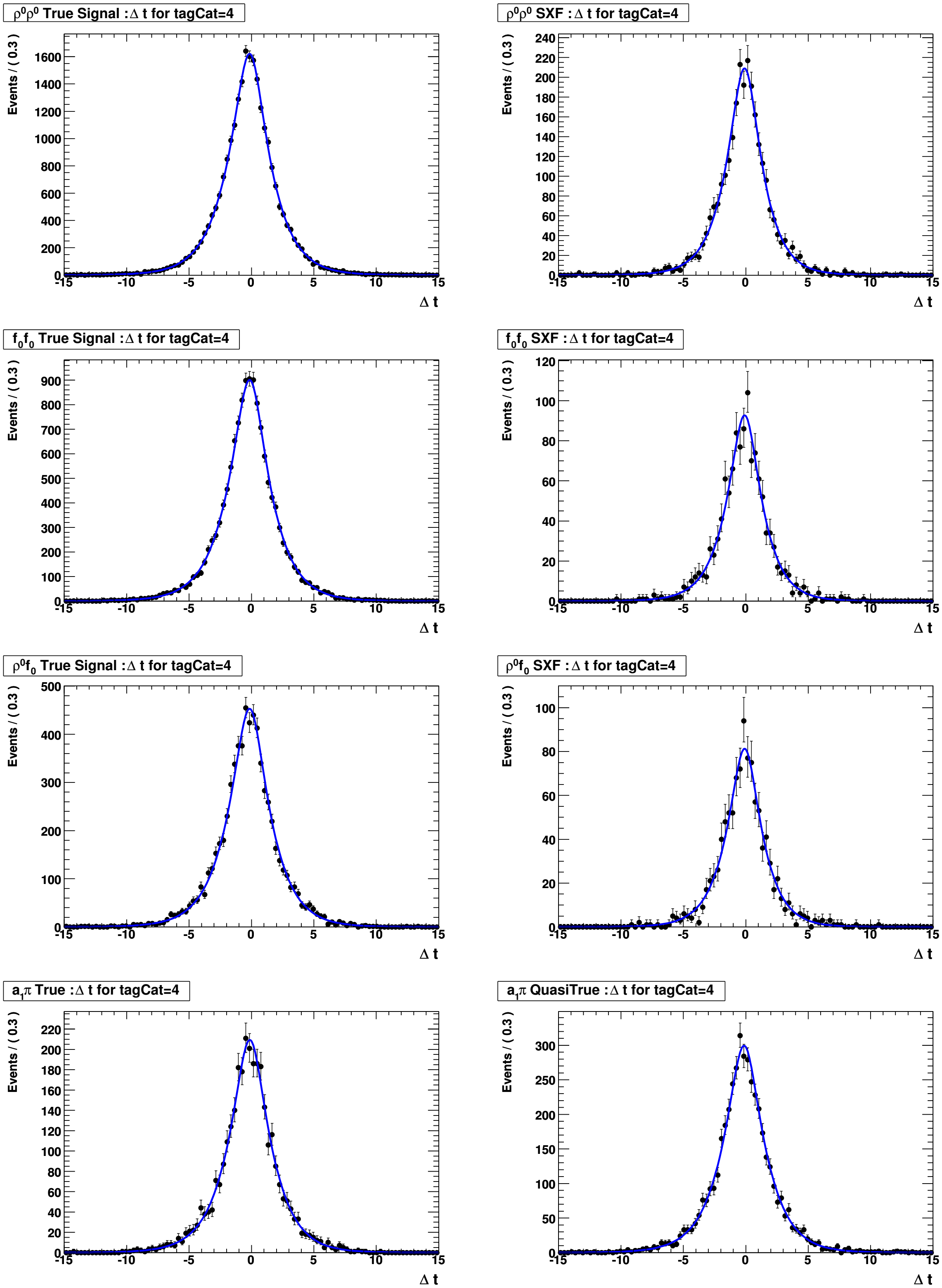

Figure D.25: Δt *for tagCat* $= 4$ *Distributions. Fitted to the Monte Carlo.*

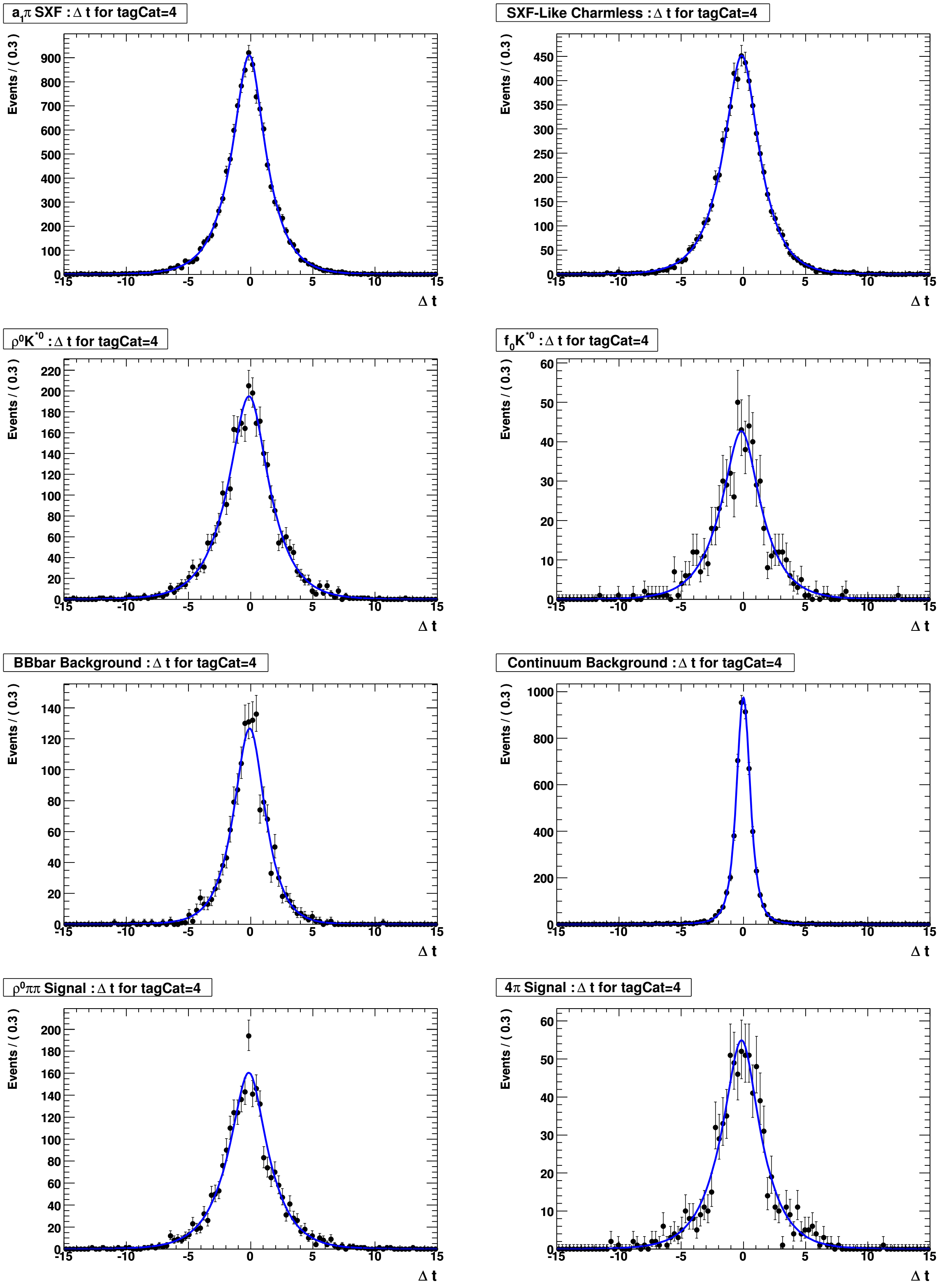

$a_1\pi$ SXF : Δ t for tagCat=4

SXF-Like Charmless : Δ t for tagCat=4

ρ^0K^{*0} : Δ t for tagCat=4

f_0K^{*0} : Δ t for tagCat=4

BBbar Background : Δ t for tagCat=4

Continuum Background : Δ t for tagCat=4

$\rho^0\pi\pi$ Signal : Δ t for tagCat=4

4π Signal : Δ t for tagCat=4

Figure D.26: Δt *for tagCat* = 4 *Distributions. Fitted to the Monte Carlo (or to the sideband for the Continuum).*

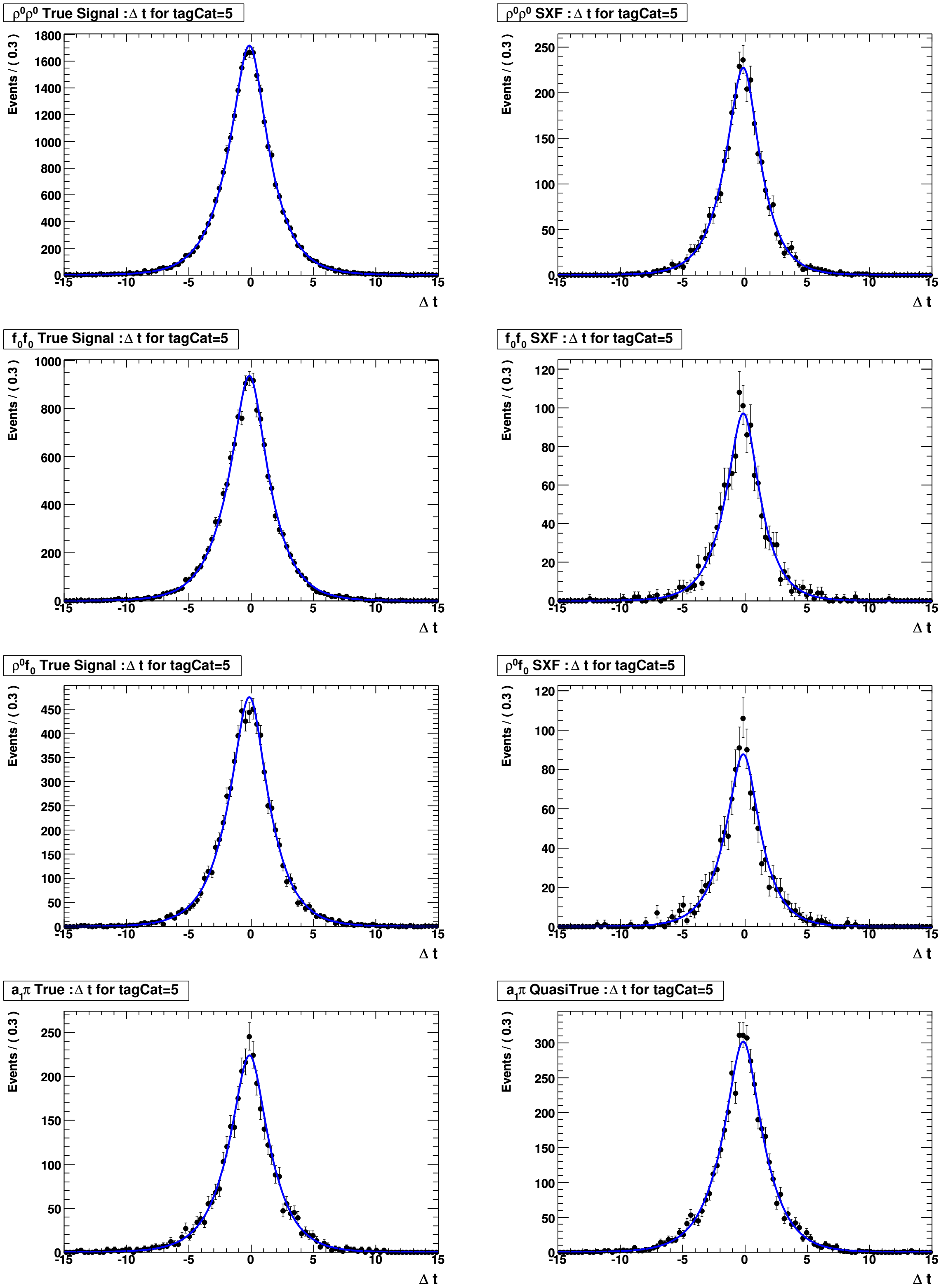

Figure D.27: Δt *for* $tagCat = 5$ *Distributions. Fitted to the Monte Carlo.*

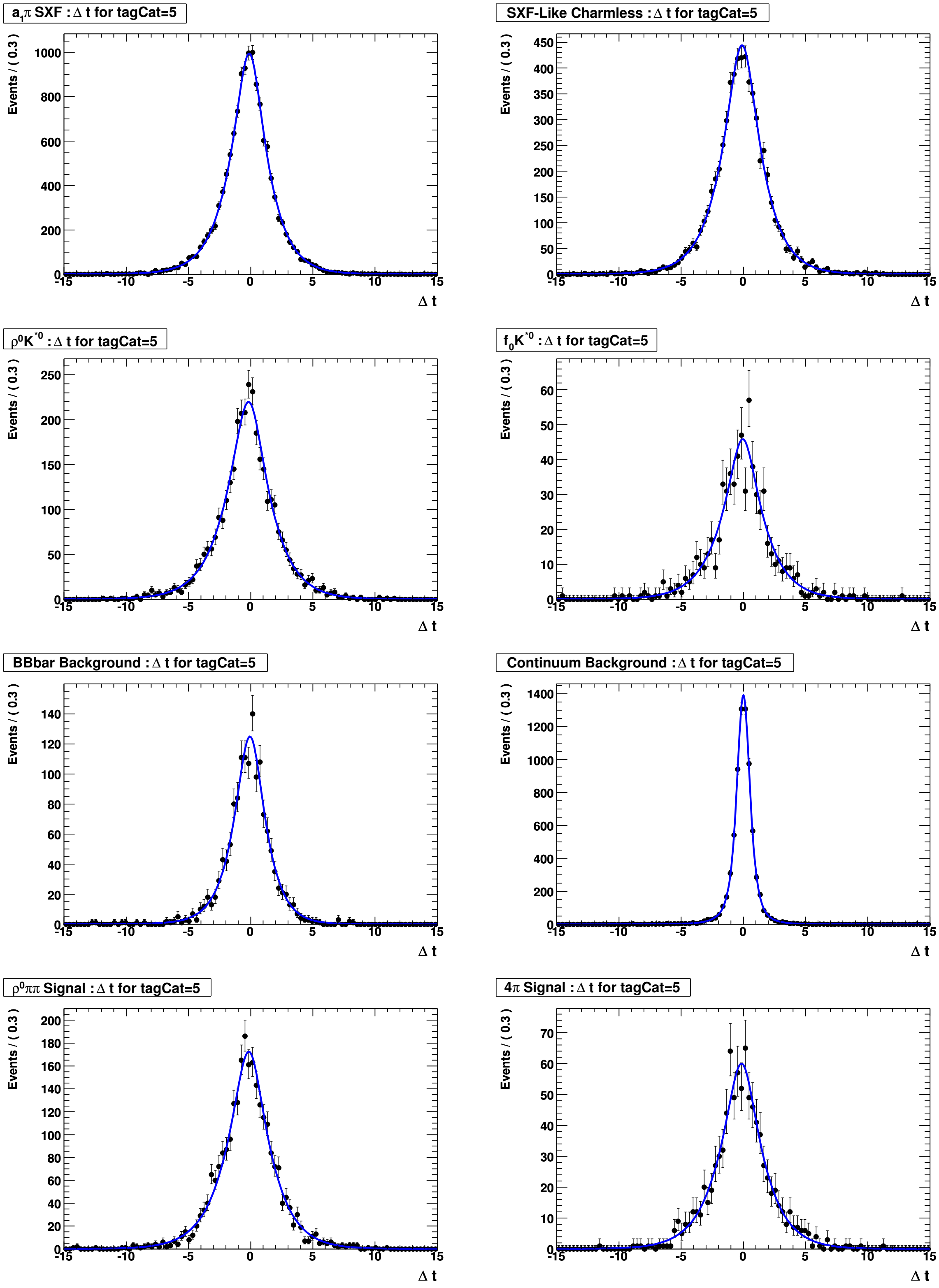

Figure D.28: Δt *for tagCat* = 5 *Distributions. Fitted to the Monte Carlo (or to the sideband for the Continuum).*

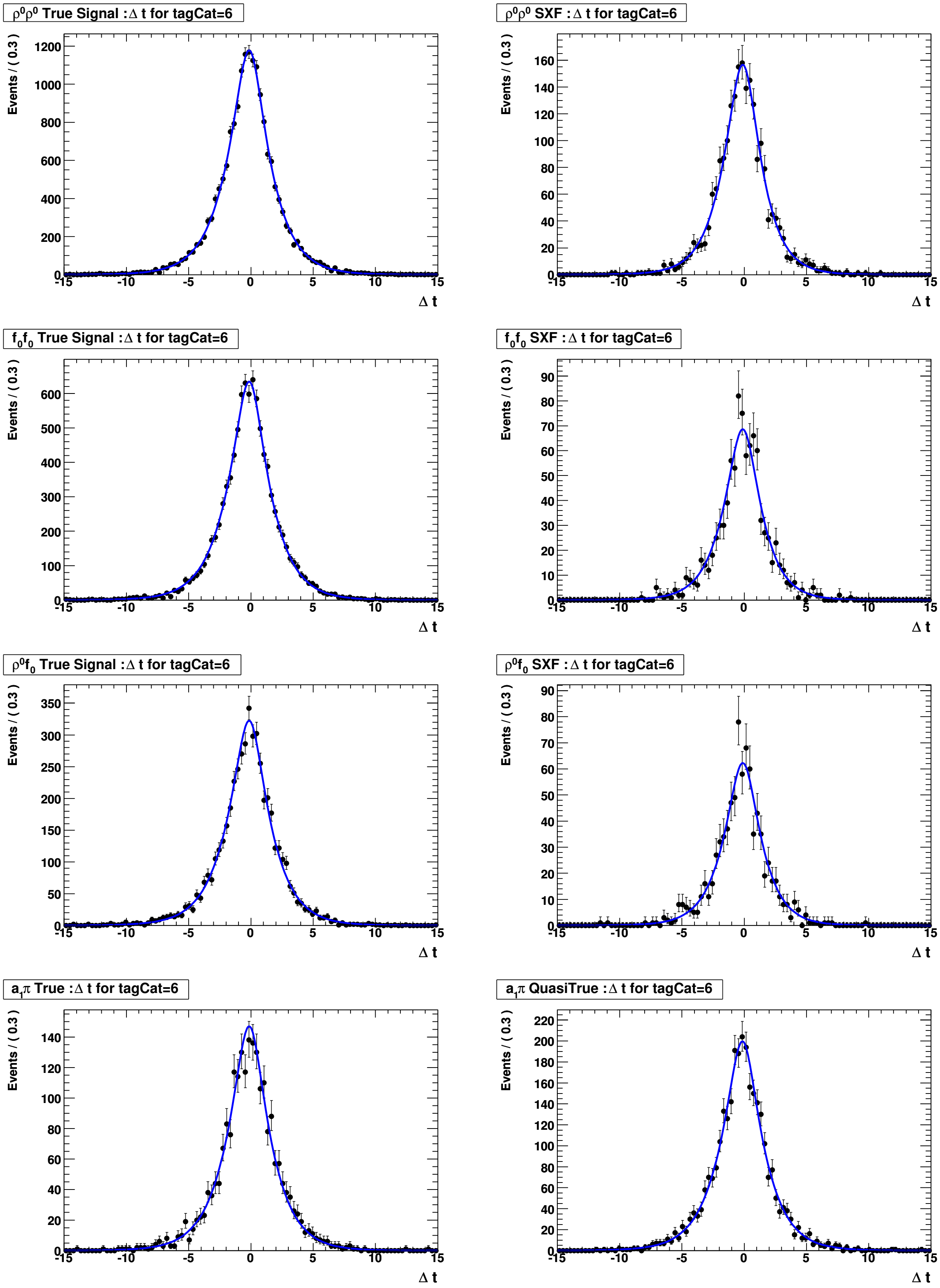

Figure D.29: Δt *for* $tagCat = 6$ *Distributions. Fitted to the Monte Carlo.*

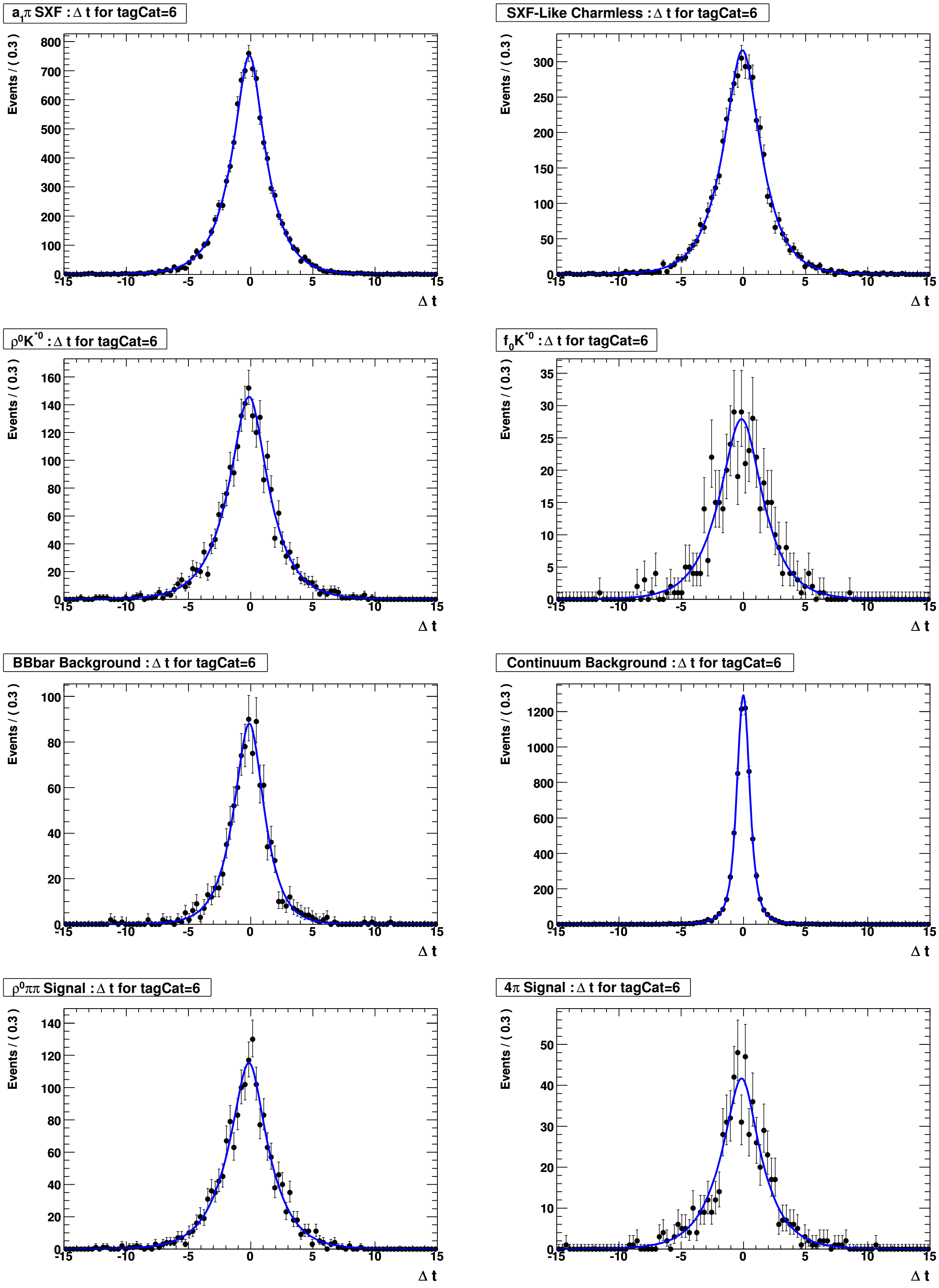

Figure D.30: Δt *for tagCat* $=6$ *Distributions. Fitted to the Monte Carlo (or to the sideband for the Continuum).*

Appendix E

Validations

The validation procedure involves multiple steps, including:

1. Ensuring that the fitter(s) return the correct event yields and CP parameters: Figs. E.1-E.4.
2. Comparing the default (*LBNL*) and *Saclay* fitters: Figs. E.5-E.6.
3. Generating sPlots: Figs. E.7-E.11.
4. Producing direct as well as (likelihood) enhanced projections: Figs. E.12-E.14.

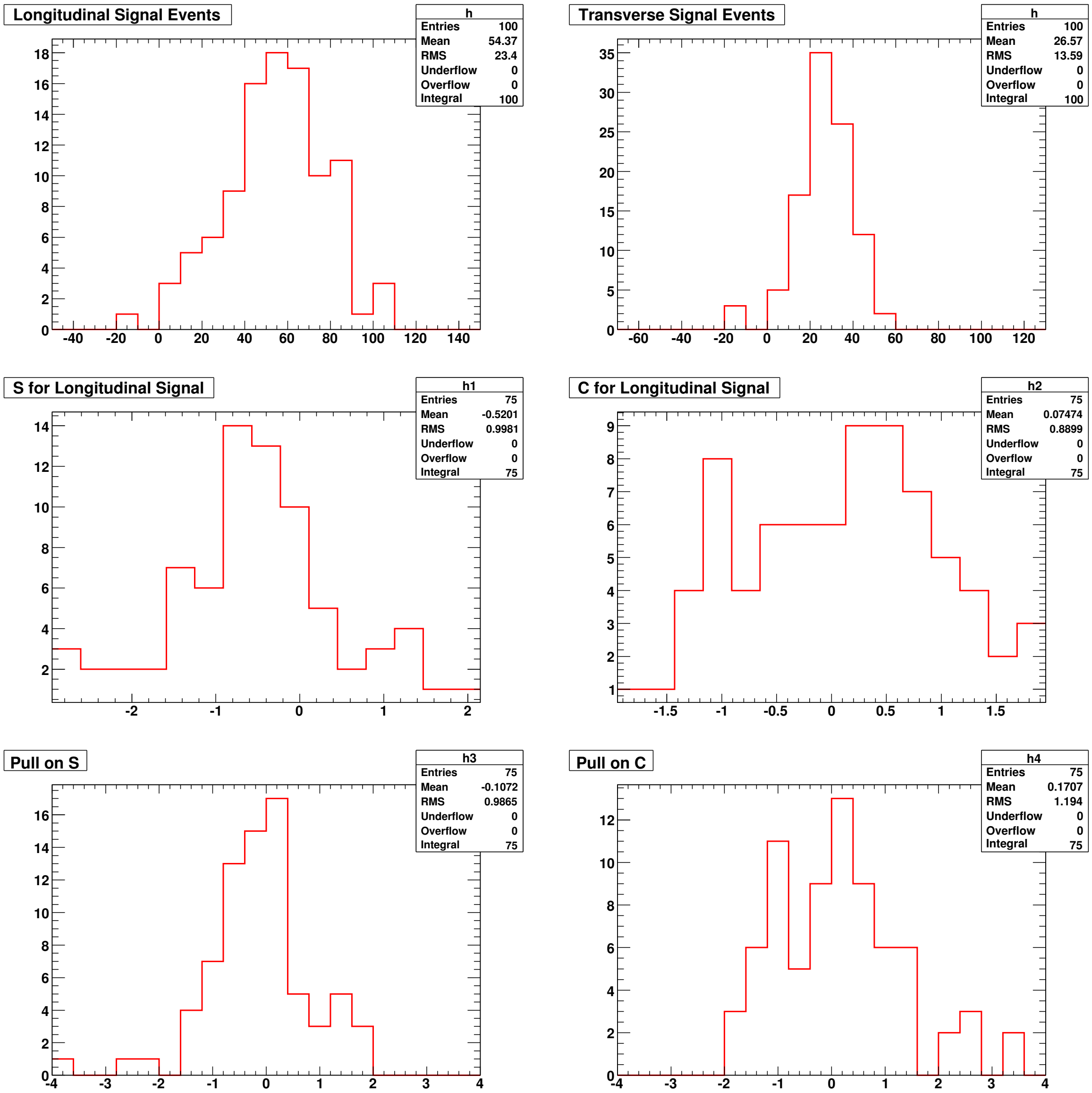

Figure E.1: *Basic Fitter event yields as a function of: Longitudinal Signal, Transverse Signal (row 1), S, C (row 2), S-Pull, C-Pull (row 3).*

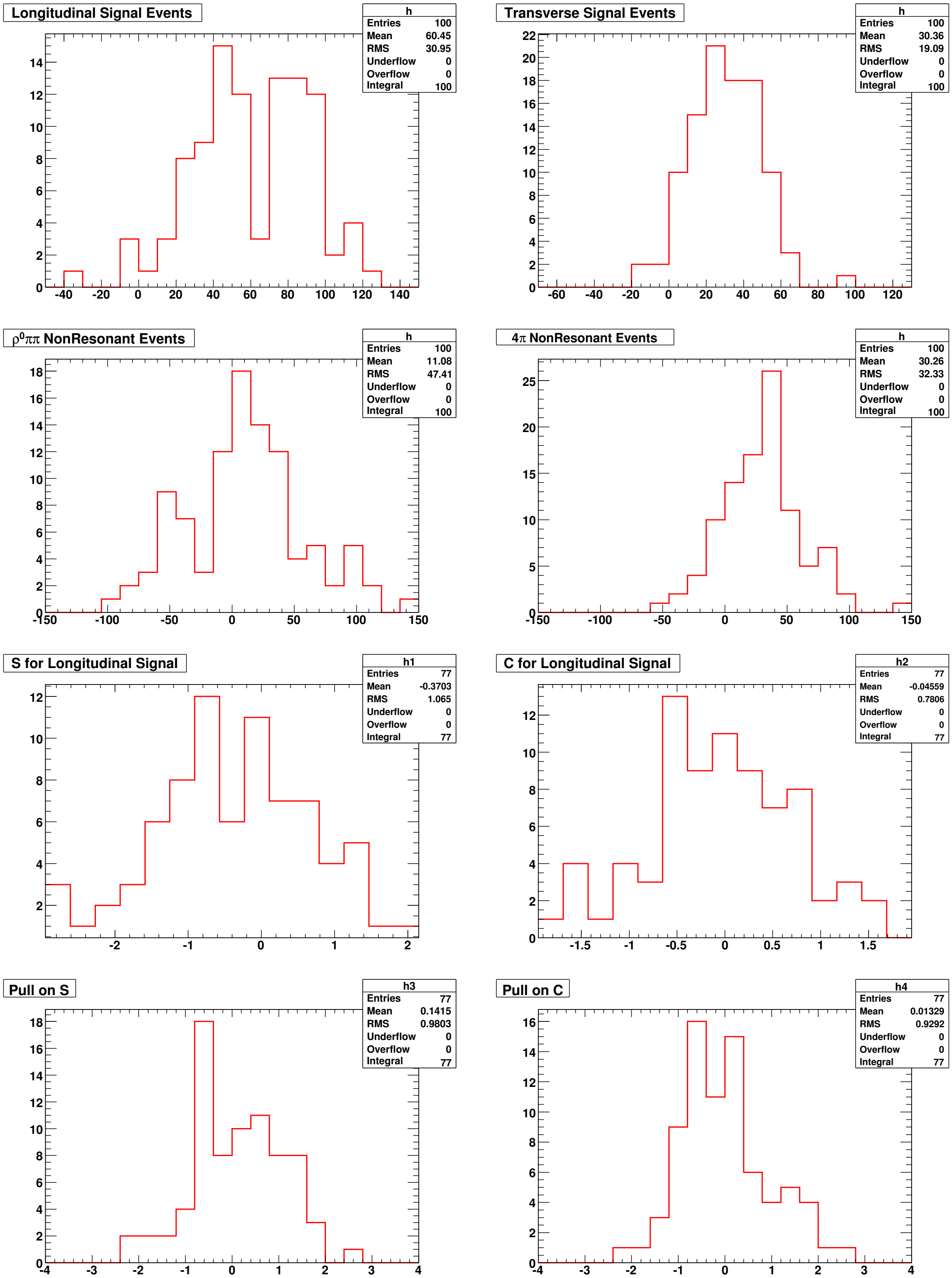

Figure E.2: *Full Fitter event yields plotted as a function of: Longitudinal Signal, Transverse Signal (row 1), $\rho^0\pi^+\pi^-$, $\pi^+\pi^-\pi^+\pi^-$ (row 2), S, C (row 3), S-Pull, C-Pull (row 4). The NR mode Yields are expected at to be at their upper limits.*

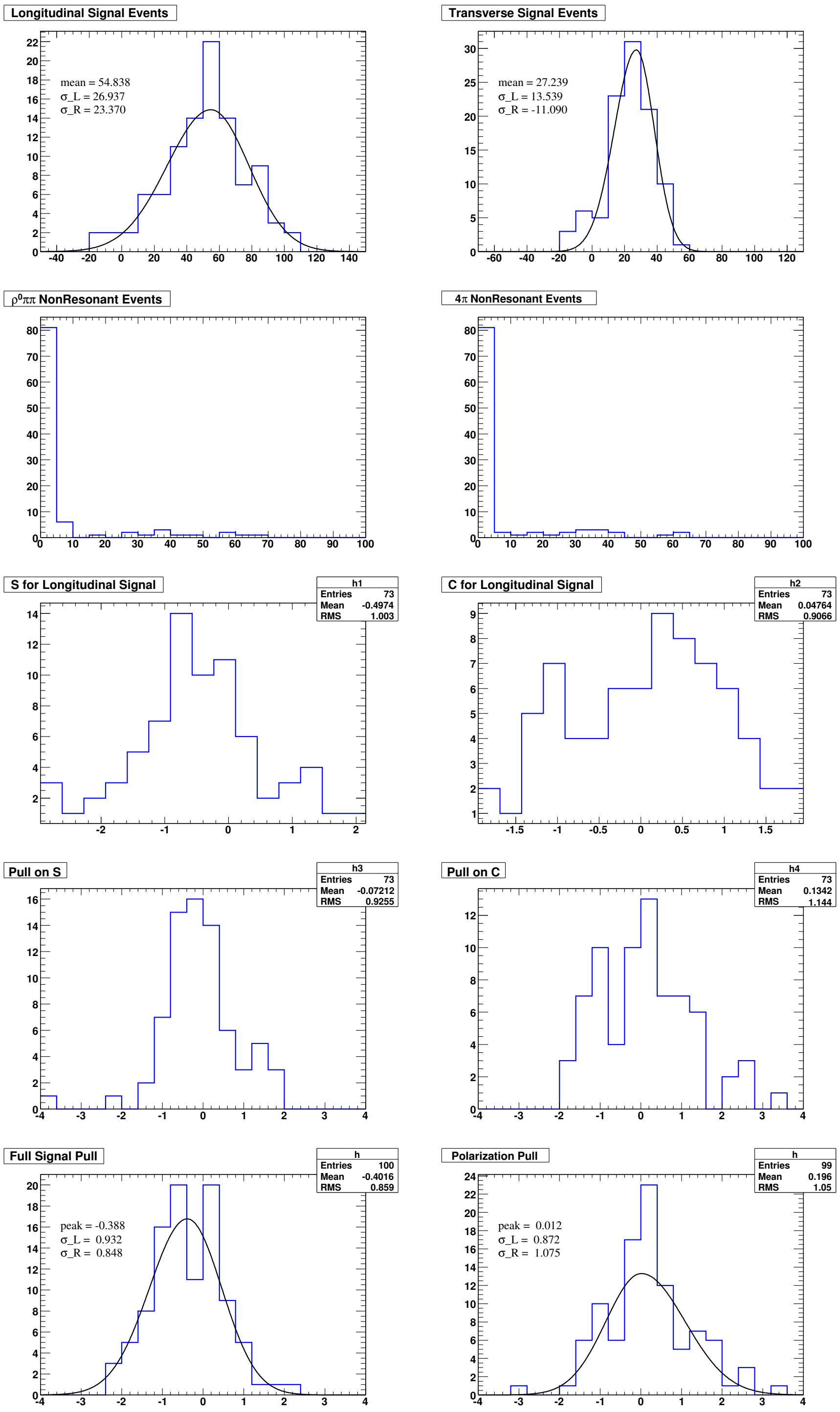

Figure E.3: *Full Fitter event yields plotted as a function of: Longitudinal Signal, Transverse Signal (row 1), $\rho^0\pi^+\pi^-$, $\pi^+\pi^-\pi^+\pi^-$ (row 2), S, C (row 3), S-Pull, C-Pull (row 4), Total Signal Pull, Polarization Pull (row 5). The NR mode Yields are embedded to be zero and the Fitted Yields are restricted to be above* 0.

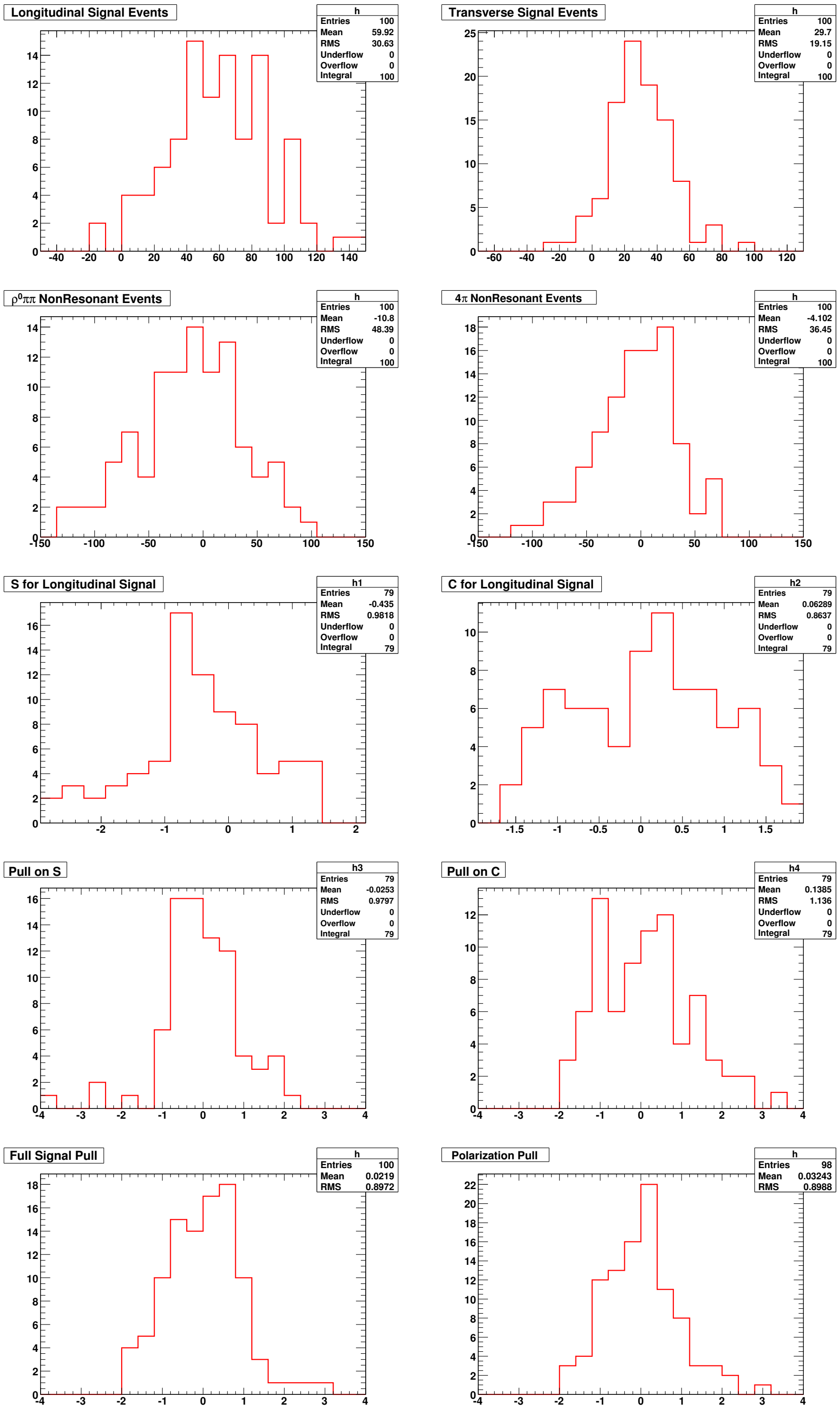

Figure E.4: *Full Fitter event yields plotted as a function of: Longitudinal Signal, Transverse Signal (row 1), $\rho^0\pi^+\pi^-$, $\pi^+\pi^-\pi^+\pi^-$ (row 2), S, C (row 3), S-Pull, C-Pull (row 4), Total Signal Pull, Polarization Pull (row 5). The NR mode Yields are expected at to be zero.*

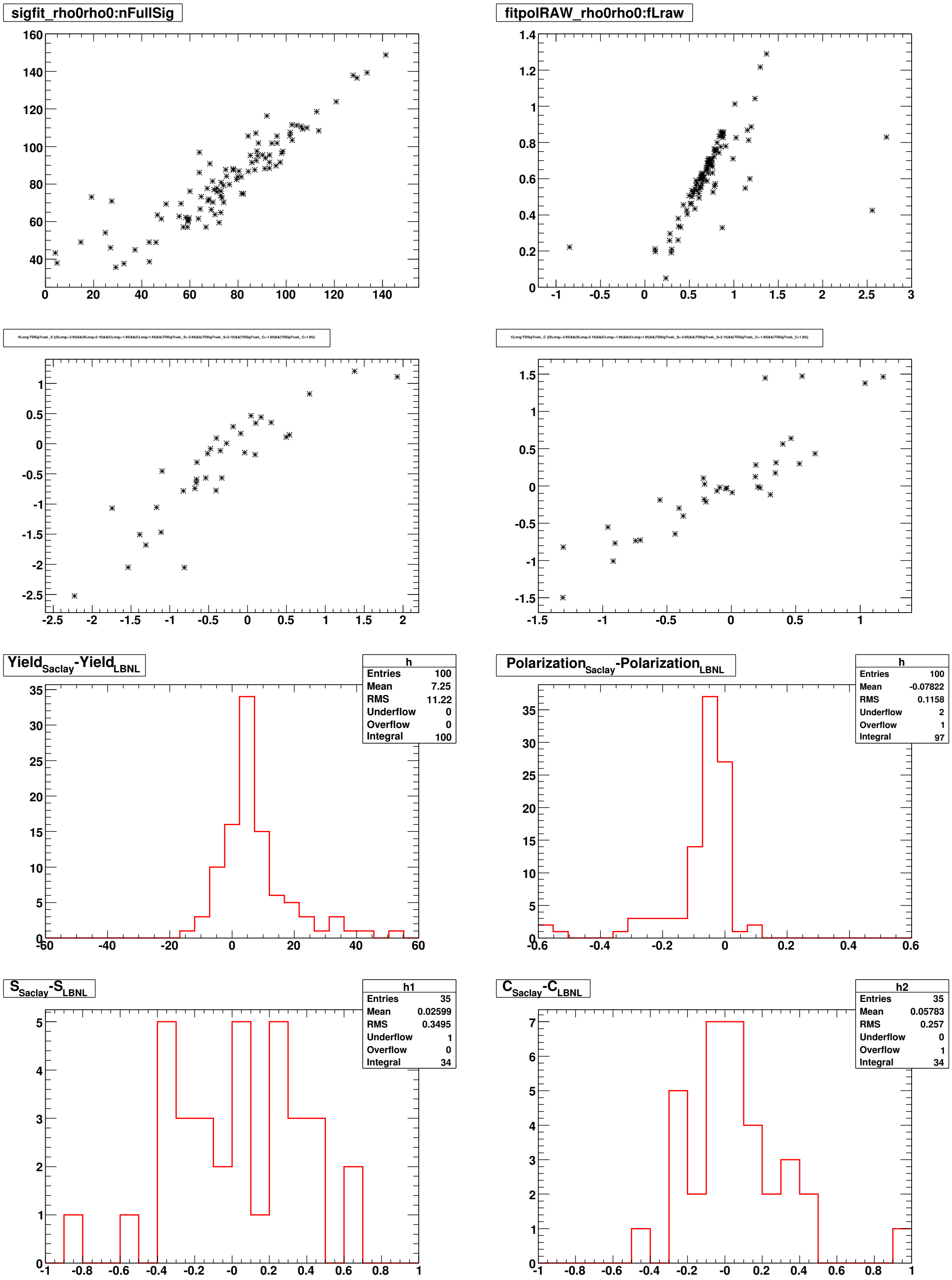

Figure E.5: *Fits on LBNL(our) generated Datasets for the Full Fitter. Saclay result vs. LBNL result for: Signal Yield and Polarization Fraction (row 1), S and C (row 2). Saclay result minus LBNL result for: Signal Yield and Polarization Fraction (row 3), S and C (row 4).*

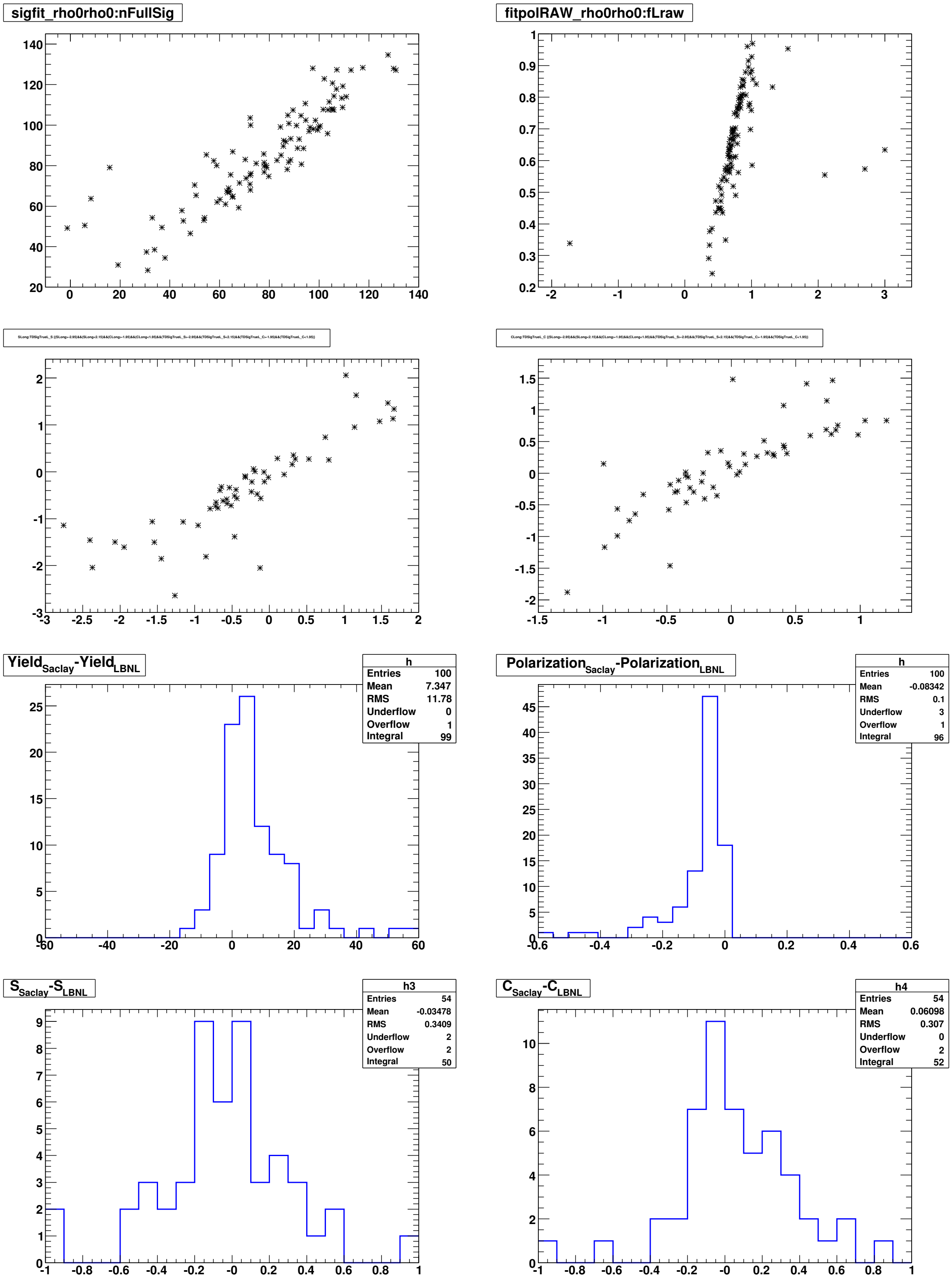

Figure E.6: *Fits on Saclay generated Datasets for the Full Fitter. Saclay result vs. LBNL result for: Signal Yield and Polarization Fraction (row 1), S and C (row 2). Saclay result minus LBNL result for: Signal Yield and Polarization Fraction (row 3), S and C (row 4).*

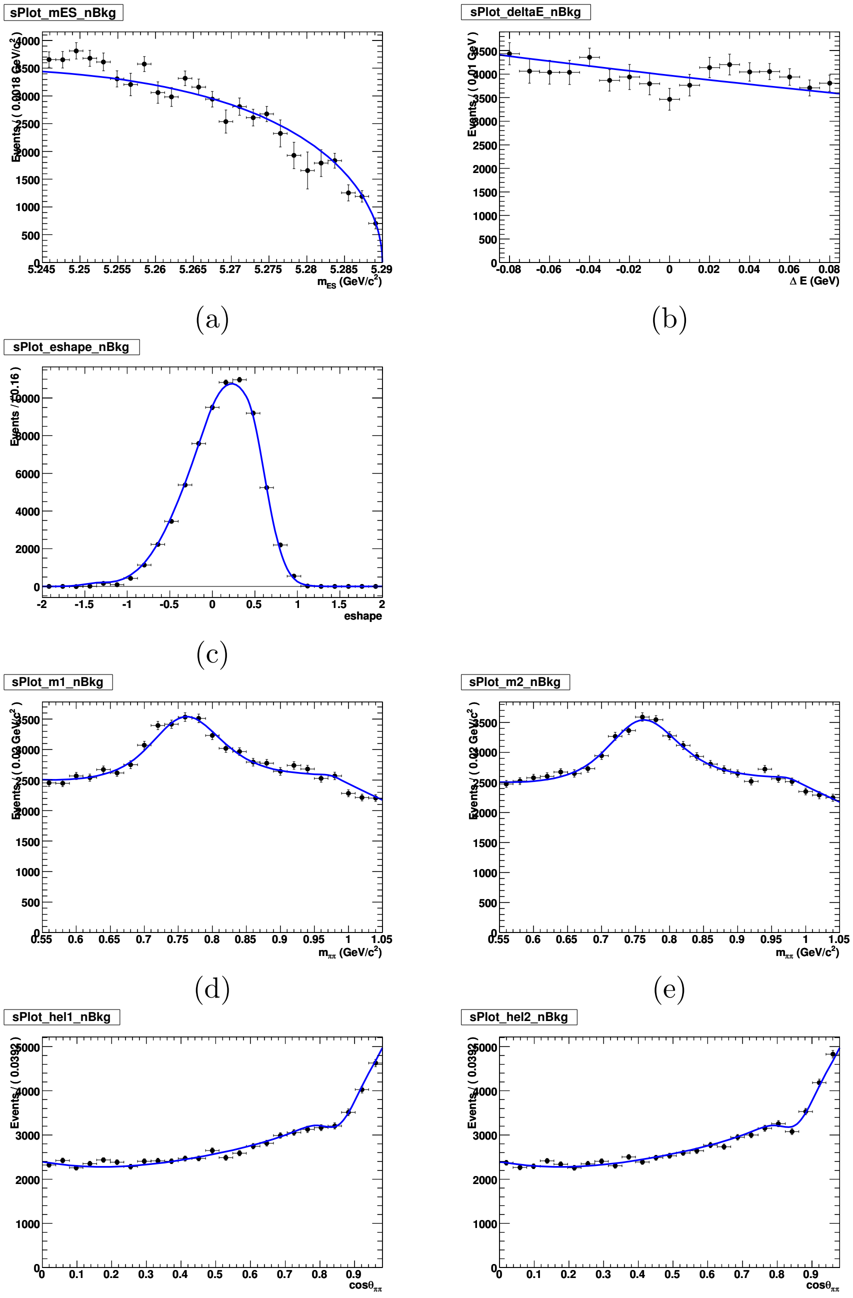

(a) (b)

(c)

(d) (e)

(f) (g)

Figure E.7: *Continuum Background sPlots. The black dots denote projections, while the blue lines are the (independently fitted) PDFs for the corresponding variable. Shown are projections onto a)* m_{ES}*, b)* ΔE*, c) eShape, d),e) two* $\pi\pi$ *invariant masses* $m_{\pi\pi,1}$*,* $m_{\pi\pi,2}$ *and f),g) two helicities* $\cos\theta_1$*,* $\cos\theta_2$*. When a mass or helicity is projected the other three mass-helicity variables are ignored.*

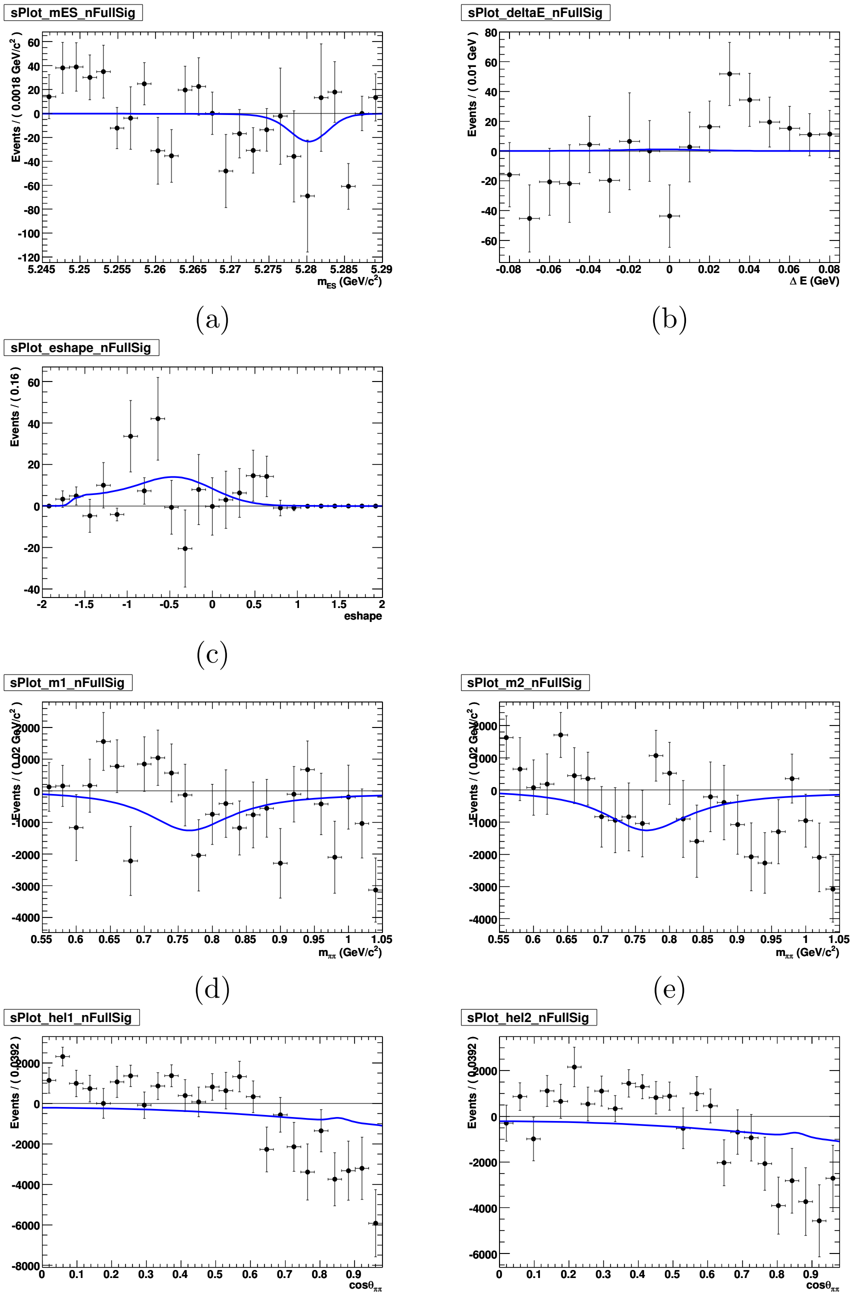

(a) (b)

(c)

(d) (e)

(f) (g)

Figure E.8: *$\rho^0\rho^0$ Signal sPlots. The black dots denote projections, while the blue lines are the (independently fitted) PDFs for the corresponding variable. Shown are projections onto a) $m_{\rm ES}$, b) ΔE, c) eShape, d),e) two $\pi\pi$ invariant masses $m_{\pi\pi,1}$, $m_{\pi\pi,2}$ and f),g) two helicities $\cos\theta_1$, $\cos\theta_2$. When a mass or helicity is projected the other three mass-helicity variables are ignored.*

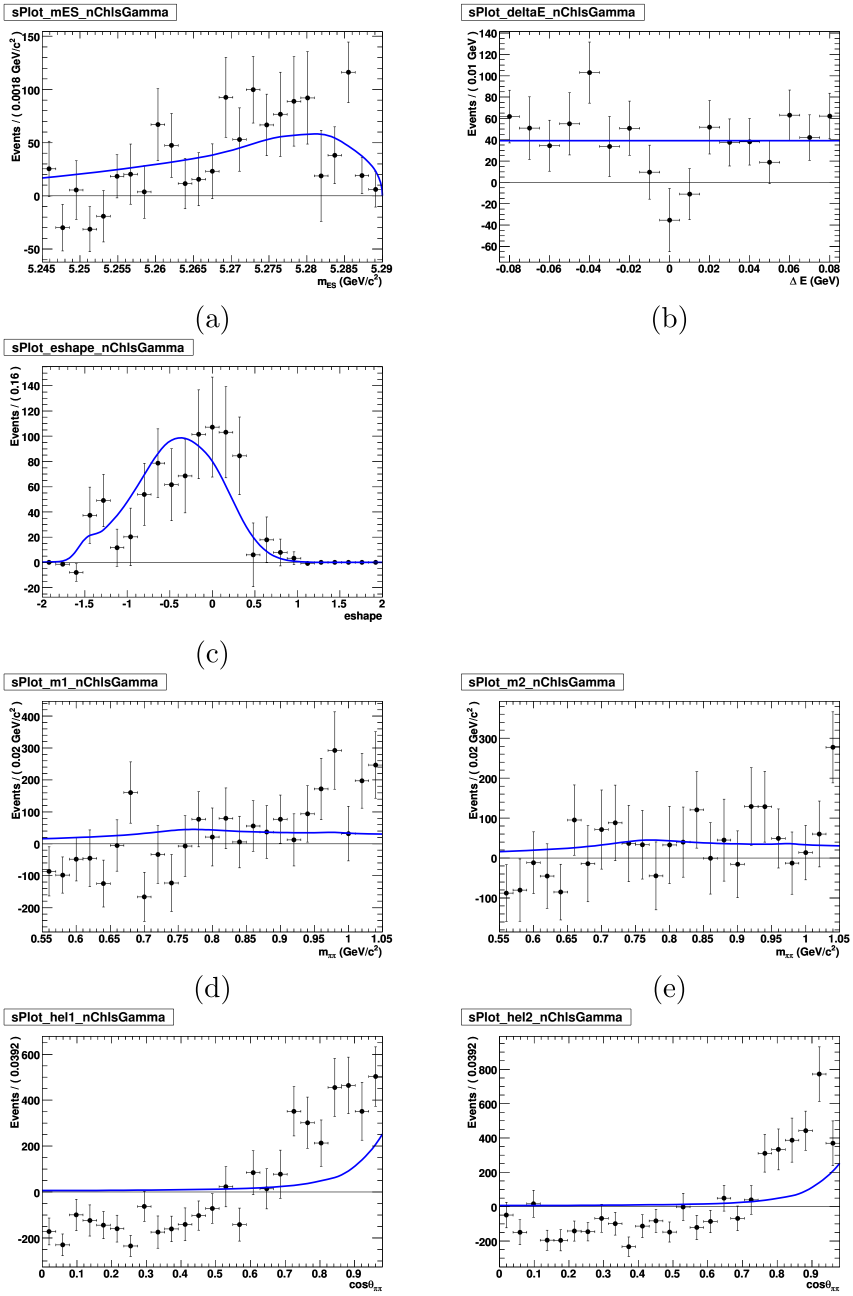

(a) (b) (c) (d) (e) (f) (g)

Figure E.9: *Charmless Background sPlots. The black dots denote projections, while the blue lines are the (independently fitted) PDFs for the corresponding variable. Shown are projections onto a)* m_{ES}*, b)* ΔE*, c) eShape, d),e) two* $\pi\pi$ *invariant masses* $m_{\pi\pi,1}$*,* $m_{\pi\pi,2}$ *and f),g) two helicities* $\cos\theta_1$*,* $\cos\theta_2$*.*

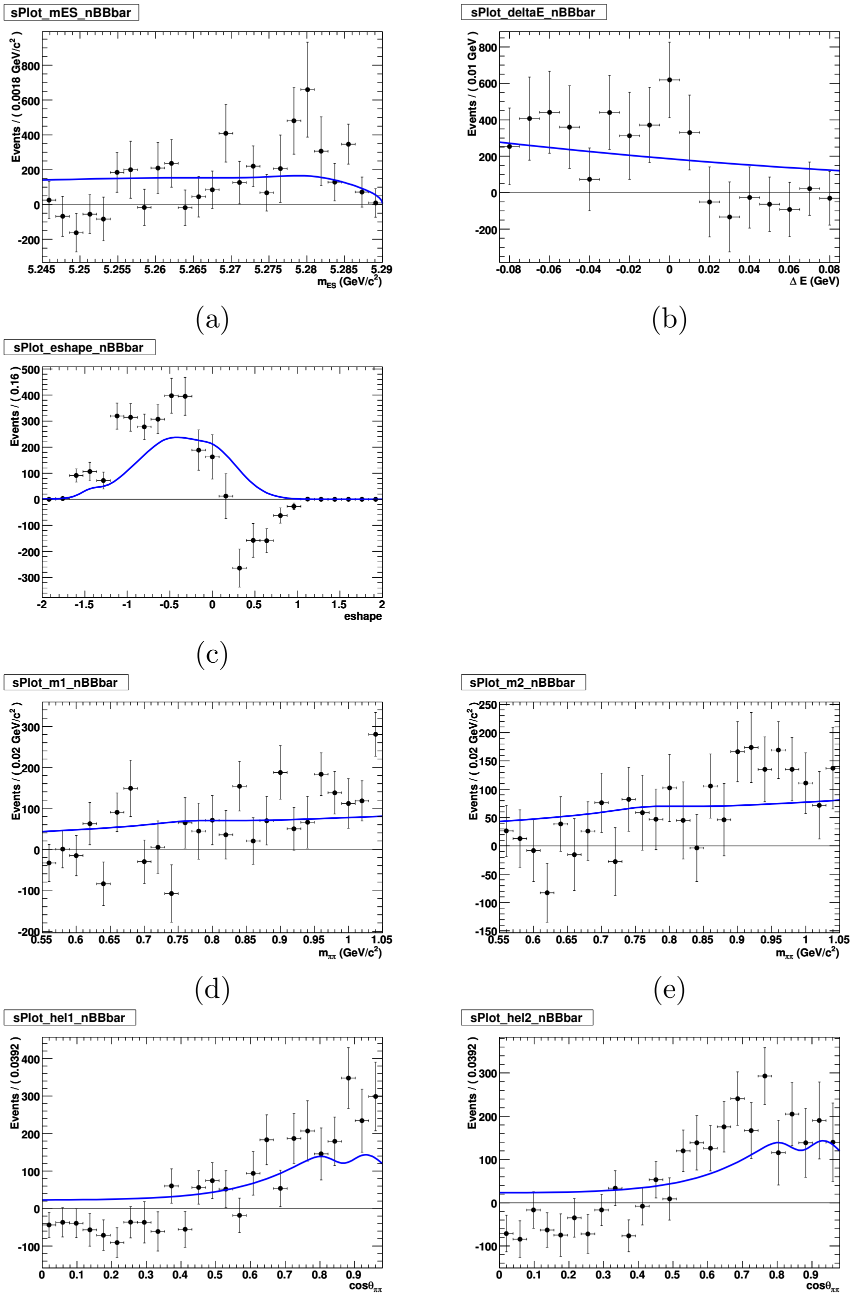

(a) (b) (c) (d) (e) (f) (g)

Figure E.10: $B\overline{B}$ *Background sPlots. The black dots denote projections, while the blue lines are the (independently fitted) PDFs for the corresponding variable. Shown are projections onto a)* m_{ES}*, b)* ΔE*, c) eShape, d),e) two* $\pi\pi$ *invariant masses* $m_{\pi\pi,1}$*,* $m_{\pi\pi,2}$ *and f),g) two helicities* $\cos\theta_1$*,* $\cos\theta_2$*.*

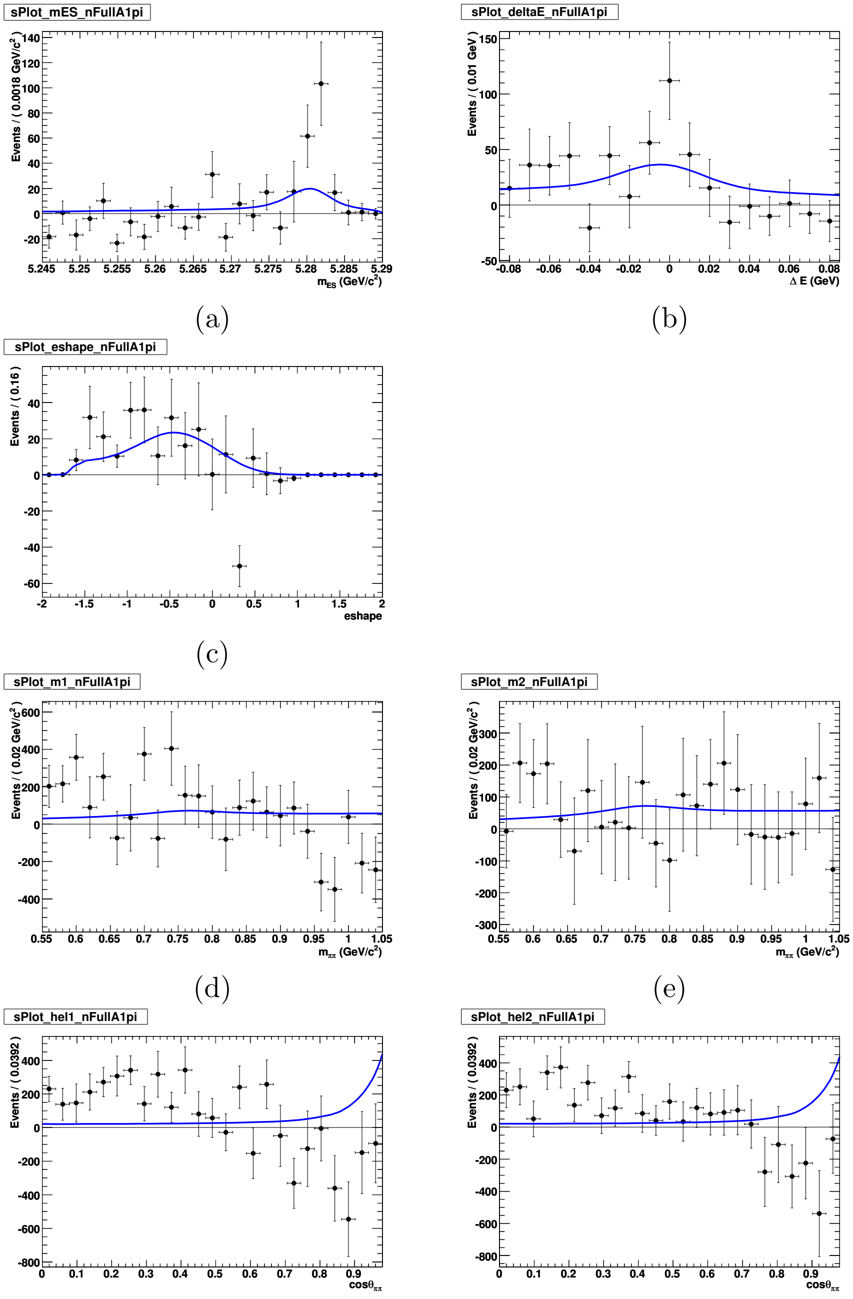

(a) (b)

(c)

(d) (e)

(f) (g)

Figure E.11: *$a_1\pi$ Background sPlots. The black dots denote projections, while the blue lines are the (independently fitted) PDFs for the corresponding variable. Shown are projections onto a) m_{ES}, b) ΔE, c) eShape, d),e) two $\pi\pi$ invariant masses $m_{\pi\pi,1}$, $m_{\pi\pi,2}$ and f),g) two helicities $\cos\theta_1$, $\cos\theta_2$.*

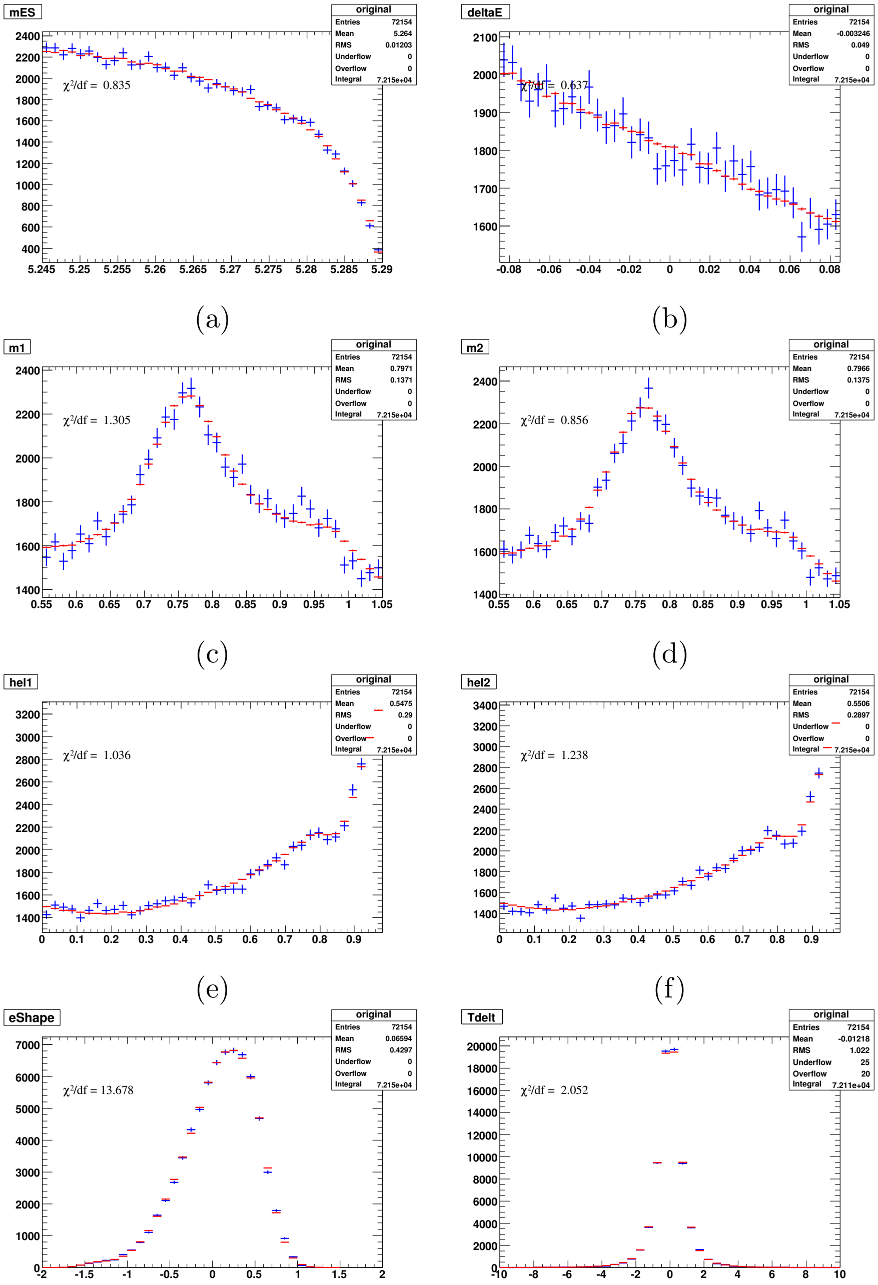

(a) (b)

(c) (d)

(e) (f)

(g) (h)

Figure E.12: *Projections in a)* m_{ES}*, b)* ΔE*, c),d) two* $\pi\pi$ *invariant masses* $m_{\pi\pi,1}$*,* $m_{\pi\pi,2}$*, e),f) two helicities* $\cos\theta_1$*,* $\cos\theta_2$*, g) eShape, h)* Δt*.*

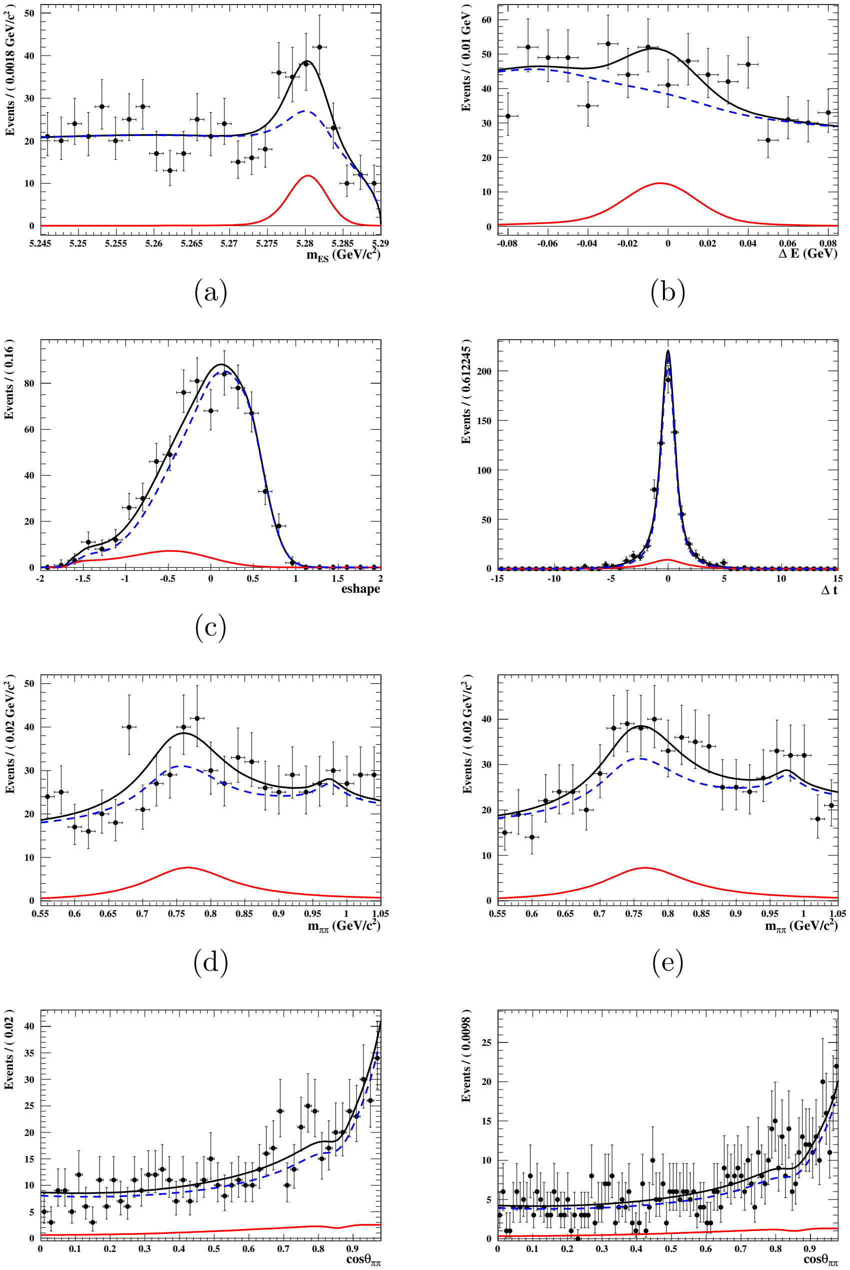

(a) (b)

(c) (d)

(e) (f)

(g)

Figure E.13: *Projection plots for the default fitter (which uses the eShape variable). Solid black line represents the full fit, solid red line shows the* $B^0 \to \rho^0\rho^0$ *component, and the blue hashed line represents the sum of all background components.* $B^0 \to \rho^0 f_0$ *and* $B^0 \to f_0 f_0$ *components are also shown, but are barely visible. A likelihood cut* $\mathcal{L}_{\rho^0\rho^0}/\mathcal{L}_{\text{total}} > 0.95$*, which enhances the signal component, is applied. Shown are projections onto a)* m_{ES}*, b)* ΔE*, c) eShape, d),e) two* $\pi\pi$ *invariant masses* $m_{\pi\pi,1}$*,* $m_{\pi\pi,2}$ *and f),g) two helicities* $\cos\theta_1$*,* $\cos\theta_2$.

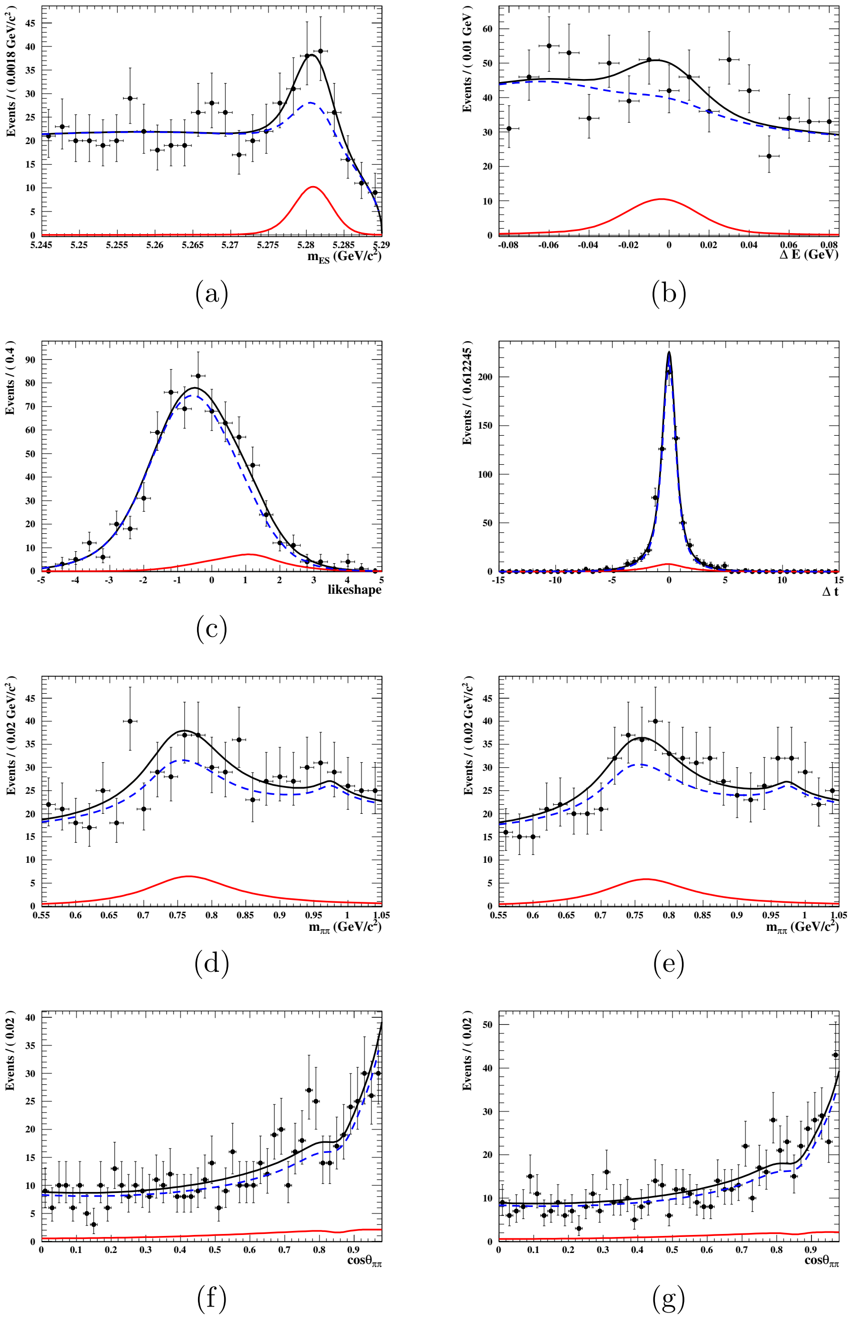

(a) (b) (c) (d) (e) (f) (g)

Figure E.14: *Projection plots for the fit using the likeShape variable. Solid black line represents the full fit, solid red line shows the* $B^0 \to \rho^0\rho^0$ *component, and the blue hashed line represents the sum of all background components.* $B^0 \to \rho^0 f_0$ *and* $B^0 \to f_0 f_0$ *components are also shown, but are barely visible. A likelihood cut* $\mathcal{L}_{\rho^0\rho^0}/\mathcal{L}_{\text{total}} > 0.95$*, which enhances the signal component, is applied. Shown are projections onto a)* m_{ES}*, b)* ΔE*, c) eShape, d),e) two* $\pi\pi$ *invariant masses* $m_{\pi\pi,1}$*,* $m_{\pi\pi,2}$ *and f),g) two helicities* $\cos\theta_1$*,* $\cos\theta_2$*.*